LASER ENGINEERING OF DEFECTS IN DIAMOND

FOR QUANTUM TECHNOLOGIES



By

BENJAMIN GRIFFITHS

A thesis submitted in fulfillment of
the requirements for the degree of

DOCTOR OF PHILOSOPHY

UNIVERSITY OF OXFORD
Department of Materials
Department of Engineering Science
St Peter's College
Supervisors: Prof. Jason Smith and Prof. Martin Booth

OCTOBER 2021

© Copyright by BENJAMIN GRIFFITHS, 2021
All Rights Reserved

ABSTRACT

Colour centre defects in diamond are promising candidates for many quantum technologies because they act as isolated two level systems in the solid-state that can be controlled and read-out through photonics [1] [2] [3]. Realisation of these technologies requires the placement of many highly coherent centres in a regular array with high positional accuracy and high fabrication yield [4]. Previous fabrication techniques have lacked the ability to produce high yields with high positional accuracy without causing irreparable damage to the lattice which reduced the quality of the spin and optical properties [5]. Ultra-fast laser writing has been shown to produce highly coherent nitrogen vacancy (NV) colour centres within the diamond lattice with positional accuracies of order hundreds of nanometers and a stochastic yield. In this case, the yield and positional accuracy is held back by the need to thermally anneal the diamond within a furnace to convert laser generated defects into colour centres; a fabrication step in which there is little to no control over individual site [6]. In this thesis, the ultra-fast pulsed laser writing technique is broached in detail from both a theoretical and experimental standpoint. The theory behind the highly non-linear light-matter interactions is studied and a hypothesis is developed for the energy transfer between photo-excited carriers and the lattice via the non-radiative recombination of self-trapped multi-excitonic states [7]. In addition, this thesis presents an expansion on the laser writing of colour centres through broaching the generation of different colour centres that have some preferential properties over the NV [8], and the development of a new engineering technique involving a local laser anneal [9]. The yield of generated centres is increased from stochastic to deterministic by replacing the global thermal anneal with the local laser anneal in combination with a fluorescence feedback mechanism. In addition, the use of the laser to locally anneal generated centres leads to a factor of five improvement in the positional accuracy due to the highly non-linear interaction of the laser with the material. These results culminate in

a key step forward in the development of a large scale quantum device and improved understanding of the highly dynamical processes that occur upon femtosecond laser interaction with a wide bandgap material.

ACKNOWLEDGMENT

This thesis would not have been possible without the Photonic Nanomaterials and Dynamic Optics and Photonics groups, both present and past members. There's too many of you to name in person but I would particularly like to thank Sam Johnson, Larry Chen and Laiyi Weng for excellent training on how to use the confocal microscopes and Patrick Salter for training on the ultra-fast laser systems. In addition I would like to thank Andrew Kirkpatrick and Shannon Nicley for lots of interesting discussions on optics and potential interaction mechanisms. For their work in the spin characterisation, photoluminesence excitation and EPR measurements I would like to thank Shazeaa Ishmael, Colin Stephen, Matt Mai, Jonas Becker, Helen Witkowska and Ben Green. Special thanks has to go towards Jason Smith, Martin Booth and Patrick Salter for the amazing opportunity to work on such an interesting and enthralling project. Your insights and guidance led towards lots of interesting discussions about science and have moulded me into a much better researcher.

Outside of work I would like to thank everyone who has made my time at Oxford special, especially the St Peter's College rowing team, the 6 am starts and camaraderie were exactly what was needed to motivate a long day in the lab or coding. The latter two years have not been a usual second half to a DPhil project, the global pandemic causing lab closures and restrictions that hindered research and daily life, unfortunately no pub trips, punting or cakes at Monday meetings (thanks Shazeaa) but its allowed for a unique experience and taken my project in new directions.

Finally, I would like to thank my family, my parents Gill and Phil, my brother, Sam and my girlfriend, Maggie for their love and support. Thank you for listening and pretending to look interested when I go off on a tangent about some random science topic that piques my interest and for supporting me throughout the project, I couldn't have done this without you.

PUBLICATIONS

Journal Articles

- *Laser Writing of Individual Nitrogen-Vacancy Defects in Diamond with Near-Unity Yield*, Y.C. Chen, **B. Griffiths**, L. Weng, S. Nicley, S. Ishmael, Y. Lekhai, S. Johnson, C. Stephen, B. Green, G. Morley, M. Newton, M. Booth, P. Salter, J. Smith, Optica Vol. 6, Issue 5, pp. 662-667 (2019) [6] - Many of the results in Chapter 8 are seen in this work

- *Microscopic Processes During Ultra-Fast Laser Generation of Frenkel Defects in Diamond,* **B. Griffiths**, A. Kirkpatrick, S. Nicley, R. Patel, J. Zajac, G. Morley, M. Booth, P. Salter, J. Smith, Phys. Rev. B 104, 174303 [7] - Many of the results in Chapters 5 and 6 are seen in this work

- *Generation of Dense Silicon Vacancy Ensembles in Diamond with Narrow Linewidth through Direct Laser Writing*, **B. Griffiths**, L. Weng, Z. Mai, Y.C. Chen, H. Witkowska, A. Kirkpatrick, S. Nicley, B. Green, J. Becker, M. Booth, P. Salter, J. Smith, *Manuscript in preparation* [8] - Many of the results in Chapter 7 are seen in this work

Conference Presentations

- *Laser Engineering of Quantum Devices Based on Coherent Colour Centres in Diamond*, **Quantum Technology International Conference - QTech 2020**, November 2020

- *Colour Centres in Diamond: A Scalable Solid-State Approach to Quantum Technology*, **Quantum Technologies Showcase 2020**, November 2020

- *Ultra-fast Laser Writing of Frenkel Defects in Diamond*, **Photon 2020**, September 2020

- *Deterministic Laser Writing and Laser Annealing of Colour Centres in Diamond*, **Photon 2020**, September 2020

Outreach and Science Communication

- *Supporting Space Startups and Scaleups*, **Round-table Parliamentary discussion**, July 2021
- *Quantum Computing: Present and Future*, **Invited lecture - Dezhou University**, May 2021
- *Quantum Computing: Physics party piece or genuine technological advance*, **Institute of Materials (IOM3) Young Lecturer Competition**, March 2021
- *Laser Engineering of Defects into Diamond for Quantum Technologies*, **Invited seminar - Element 6**, December 2020
- *Quantum Technologies with Diamond*, **Institute of Materials (IOM3) Young Lecturer Competition**, March 2019
- *Quantum Technologies: An overview*, **St Peter's College graduate seminar**, December 2018
- *Write your Own Qubit*, **Quantum Technologies Showcase 2018**, November 2018

Intellectual Property

- Patent Contributor, Laser writing of colour centres in crystals, PCT/GB2019/051358, Filed May 2018, Pending.
- Patent Contributor, Laser method and apparatus for analysing crystals, PCT/GB2019/052820, Filed October 2018, Pending.

TABLE OF CONTENTS

Page

ABSTRACT ii

ACKNOWLEDGMENT iv

PUBLICATIONS v

CHAPTER

1 Introduction 1
- 1.1 The promise of quantum technologies 1
- 1.2 Solid-state spin qubits in diamond 3
- 1.3 Engineering spin qubits in diamond 5
- 1.4 Thesis outline 6

2 Literature Review 9
- 2.1 Introduction 9
- 2.2 Review of colour centres 10
  - 2.2.1 Nitrogen vacancy centre 10
  - 2.2.2 Group IV - vacancy centres 14
  - 2.2.3 Applications 21
- 2.3 Fabrication techniques 24
  - 2.3.1 Growth 25
  - 2.3.2 Ion implantation 27
  - 2.3.3 Electron irradiation 31
  - 2.3.4 Laser writing 33
- 2.4 Summary 39

3 Theoretical Background 40
- 3.1 Introduction 40
- 3.2 Light-matter interactions 43
- 3.3 Carrier dynamics 50
- 3.4 Energy relaxation into the lattice and defect formation 55
- 3.5 Spin-photon behaviour 57

3.6 Summary . . . 59

4 Experimental Methods . . . 60
4.1 Introduction . . . 60
4.2 Laser writing . . . 60
4.2.1 Single pulse laser writing . . . 60
4.2.2 Laser annealing with fluorescence feedback apparatus . . . 64
4.2.3 Iterative aberration control . . . 66
4.3 Photoluminescence imaging and spectroscopy . . . 69
4.3.1 Auto-correlation measurements . . . 70
4.3.2 Polarisation measurements . . . 72
4.3.3 Spin coherence . . . 72
4.3.4 Photoluminescence excitation spectroscopy . . . 73
4.3.5 Electron paramagnetic resonance spectroscopy . . . 74
4.4 Summary . . . 74

5 Non-Linearity of the Laser Writing Process - Theoretical . . . 76
5.1 Introduction . . . 76
5.2 Partial differential equation model . . . 77
5.2.1 Modelling the laser pulse . . . 78
5.2.2 Free carrier distributions . . . 88
5.2.3 Excitonic states . . . 104
5.2.4 Lattice temperature distribution . . . 107
5.2.5 Hypothesis for Frenkel defect generation . . . 108
5.3 Limitations of the model . . . 112
5.4 Summary . . . 113

6 Non-Linearity of the Laser Writing Process - Results . . . 116
6.1 Introduction . . . 116
6.2 Varying pulse energy . . . 116
6.3 Varying initial parameters . . . 128
6.3.1 Varying numerical aperture . . . 128
6.3.2 Varying pulse duration . . . 131
6.3.3 Varying wavelength . . . 133
6.3.4 Varying nitrogen content . . . 136
6.3.5 Modelling focal aberrations . . . 138
6.4 Summary . . . 143

7 Enhancement of Silicon Vacancy Ensembles . . . 146
7.1 Introduction . . . 146
7.2 Method . . . 147
7.3 Results . . . 150

7.4 Discussion . . . 152
7.5 Summary . . . 158

8 Deterministic Engineering of Single Colour Centres . . . 160
8.1 Introduction . . . 160
8.2 Laser annealing . . . 161
8.3 Fluorescence feedback . . . 164
8.4 Characterisation . . . 167
8.5 Advanced processing control . . . 173
8.6 Fluorescence spiking study . . . 175
8.7 Proximal writing . . . 183
8.8 Dependence on dopant level . . . 186
8.9 Summary . . . 188

9 Conclusion and Future Outlook . . . 191
9.1 Conclusion . . . 191
9.2 Future Outlook . . . 193

REFERENCES . . . 195

APPENDIX

A PDE Model . . . 227
A.1 Light intensity distribution . . . 227
A.2 Carrier density distributions . . . 229
A.3 Excitonic density distribution . . . 234
A.4 Bi-excitonic density distribution . . . 236
A.5 Self-trapped bi-excitonic density distribution . . . 238
A.6 Defect density distribution . . . 239
A.7 Lattice temperature distribution . . . 240

Diamond

Etymology: Adamas - Greek - invincible/unchangeable

No-one told the Greeks about femtosecond lasers

"Technology has advanced more in the last thirty years than in the previous two thousand. The exponential increase in advancement will only continue."

- Niels Bohr

Chapter One

Introduction

1.1 The promise of quantum technologies

Quantum information processing, computing and sensing are emergent fields that have garnered a lot of attention in recent years due to advances in materials engineering leading to the increasing likelihood of realisable quantum technologies [5][10][11]. These technologies have promised to revolutionise many areas, whether it be modelling complex chemical reactions for drug development or developing ultra-secure cryptographic protocols for protecting consumer data from eavesdroppers. The main advantage of quantum technologies over their classical counterparts is the ability to find solutions to exponential problems in linear or polynomial time [12].

The fundamental building block of a quantum device is the quantum bit (qubit). These work from a completely different paradigm to classical bits enabling an entirely new way to tackle problems. Classical bits can exist in one of two states, 0 or 1. By combining strings of these bits together, sets of yes, no questions can be asked by logic gates in order to arrive at an answer for a problem. Crucially, classical bits can only represent one possible state at a given time.

A quantum object is described by a wavefunction, ψ which is a solution to the Schrödinger equation. The form of this wavefunction is generally rather complicated,

however in the special case that the quantum object is somewhat isolated from its surroundings and has two possible eigenstates, much of the complication can be forgotten and the two states labelled again as 0 and 1. It is useful to represent these as vectors [13].

$$|0\rangle = \begin{bmatrix} 1 \\ 0 \end{bmatrix}, |1\rangle = \begin{bmatrix} 0 \\ 1 \end{bmatrix} \tag{1.1}$$

Because wavefunctions are linear functions, a linear combination, known as a superposition is an allowed solution, the only constraint being that the square of the pre-factors add up to 1.

$$|\psi\rangle = a\,|0\rangle + b\,|1\rangle \tag{1.2}$$

$$a^2 + b^2 = 1 \tag{1.3}$$

These pre-factors can be any complex number such that the set of allowed qubit states sweeps out a unit sphere known as the Bloch sphere. The square of the pre-factors represents the probability of attaining the $|0\rangle$ state or the $|1\rangle$ state upon measurement. Computation is achieved by applying sets of gates which take the form of rotation matrices and the computational advantage comes from a process known as entanglement. Entanglement can be achieved by applying specific sets of gates to multiple qubits at the same time and enables the multiple qubits to become represented by a single vector that cannot be factorised into individual qubit vectors. Physically, this corresponds to the measurement outcome of each qubit being inherently tied to the measurement outcome of the others. A set of N maximally entangled qubits allows for the representation of 2^N states simultaneously, an exponential improvement over classical bits, hence a maximally entangled quantum state is able to achieve exponential operations in linear time. A caveat is that only the classical states can be

measured so one has to be clever with algorithm design such that the desired answer leads to a classical state and the superposition states are only used during calculation.

Useful algorithms that have been written require somewhere between a few hundred to a few million perfect "logical" qubits [14]. Real qubits are imperfect as no quantum object is truly isolated from the environment and can be represented simply as a 0 and 1. Therefore the quantum state bleeds into the environment overtime (known as decoherence) leading to a build up of error. A perfect qubit can be simulated with tens to millions of real-world qubits depending upon the error rate, therefore scalability is the key parameter in determining the architecture with which to build a quantum device [15].

At the time of writing, the most mature architecture uses superconducting circuits as qubits and is being pioneered by a mixture of commercial companies and academic institutes [10] [11]. These have displayed proof of principle calculations achieving maximally entangled states of tens of qubits. However, this is a far cry from the million or so that will be needed in order to achieve useful computation. The main barrier to scalability from this architecture is that superconducting qubits require temperatures of $\sim$ mK which requires specialist cryogenic equipment (a dilution refrigerator) that is expensive and bulky. Further, to date, it has been difficult to engineer numerous qubits onto a single chip such that the engineering of superconducting qubits themselves is a barrier to scalability. Other architectures utilise ions trapped within an electromagnetic field [16] or photonic circuits [17] as qubits but these are held back by the need for high vacuum and thus suffer similar setbacks in scalability.

1.2 Solid-state spin qubits in diamond

The ability to scale leads to two desired qualities of a potential qubit architecture: the ability to place millions of qubits within a single chip and a well isolated qubit state

such that the device can be operated at higher temperature without random thermal excitement leading to decoherence. These requirements point towards a solid-state device. Within the solid-state, colour centres in materials such as diamond and silicon carbide offer great potential for use as qubits due to their atomic scale and material properties which hold them in place and isolate them from decoherence [18] [19]. In this thesis the focus is upon colour centres in diamond. Diamond is an ideal host for atomic scale qubits due to its robust structure and spin-free environment. The type of qubit that the diamond hosts is a spin qubit. Atomic scale defects, usually of the form X-vacancy, where X is a dopant atom, add discrete electronic states into the bandgap of the material whereby spin interactions lead to two addressable states [20]. The dopant generally comes from group IV or V of the periodic table due to the similarity to the carbon lattice. The discrete spin states can then be labeled $|0\rangle$ and $|1\rangle$ and used as qubits with transitions typically in the microwave range of the spectrum.

Direct communication between spin qubits is difficult and requires very close proximity of order nanometres [18], therefore in practice, a "travelling qubit" or photon is used as a mediator to transfer quantum information between qubits and enable entanglement. The spin qubits in diamond typically have a ground to excited state optical transition at red or near infrared wavelengths enabling transfer of quantum information through fluorescence [21]. Quantum gates can be calculated by finding the perturbation to the qubit Hamiltonian that leads to the desired rotation around the Bloch sphere; often coming in the form of pulses of light or microwaves. Often the electron spin is less isolated from the environment than the spin states of nearby nuclei, therefore nuclei are used as storage qubits with the electron spin used for control and readout with communication between electrons and nuclei through the hyper-fine interaction [22].

The isolated electron spin-photon interface of colour centres makes them ideal candidates for use as nodes of quantum networks. A quantum network consists

of nodes of well controlled qubits which interact via photonic channels to form an entangled network that can be used for quantum information processing and quantum computing. The qubits can be encoded to store information or calculate complex computational problems. Entanglement with nuclear spins can also be used to develop long-term quantum memories [2] [23] [24].

The nodes are entangled together by first entangling each qubit with photons and then interfering the photons via a Hong-Ou-Mandel interference followed by detection which projects the entanglement onto the nodes [25]. The photonic channels that connect each qubit allow for the ability to use different types of nodes within the network because the qubits don't have to communicate directly. This gives flexibility and scalability to the quantum network idea and can be implemented in many ways such as chip-based systems or much larger systems using optical fibres. Entanglement is achieved when measuring the output state of the system, there is an equal probability that either node could have produced the photon, the path is erased, the idea initially proposed by Cabrillo et al in 1999 [26]. Barrett and Kok showed how this could be used to produce a high fidelity Bell state for scalable quantum networks in 2005 [25]. Entanglement between a two-node network within diamond was first reported by Hensen et al in 2013 using the NV- centre as both nodes at 1.3 km [27] and between a 3 node network was reported in 2021, again using NV centres [28].

1.3 Engineering spin qubits in diamond

In order to develop a quantum device based on these centres, robust engineering techniques need to be developed such that devices can be reliably engineered containing millions of high-quality qubits. The quality of the qubit is both measured by its isolation from the environment and the ability to be able to control and readout via a strong spin-photon interface [18]. A number of engineering techniques have

been developed for the generation of colour centres within diamond which will be outlined in the following chapter. Recently, the use of a femtosecond laser has enabled significant progression in this field allowing for a stochastic generation of high-quality colour centres with great positional accuracy in all three dimensions and allows for the versatility to generate centres at a range of depths within the bulk [6].

Within diamond, laser engineering has traditionally been used to generate sp^2 hybridised graphitic tracks for use as optical wave-guides , radiation detectors and stress generation [29]. More recently, advances in laser engineering at lower fluences in diamond alongside advances in adaptive optics have allowed for the generation of specific colour centres [6][30] displaying great optical and spin qualities and a high positional accuracy rivaling alternative engineering techniques and nearing the quality of native colour centres.

1.4 Thesis outline

This thesis will explore the mechanisms behind the laser engineering of these centres in more detail in conjunction with the development of a new engineering technique that takes the yield of laser generated single nitrogen vacancy centres from stochastic to deterministic as well as using the laser to generate other interesting colour centres. The thesis will be structured as follows:

Chapter 2 : Literature Review

A review of colour centres in diamond will first be discussed with a focus on the nitrogen vacancy and group IV vacancy centres which are most promising for quantum technologies. This chapter will review current methods used to generate centres including growth processes, annealing, ion-implantation, electron irradiation and the current progress of colour centre generation using a femtosecond pulsed laser.

Chapter 3: Theoretical Background

This chapter will discuss some of the processes that take place when a femtosecond laser pulse interacts with a semiconductor from a theoretical standpoint starting with the light-matter interactions and followed by mechanisms by which the energy relaxes into the crystal. In addition, a theoretical description of spin-photon interactions will be discussed.

Chapter 4: Experimental Methods

This chapter will outline the experimental apparatus used both for the engineering of colour centres through laser writing and for the characterisation of laser written centres. In addition, it will outline methods for varying the writing parameters and different characterisation techniques.

Chapter 5: Non-Linearity of the Laser Writing Process - Theoretical

This chapter regards the development of a coupled non-linear integro-differential equation model of laser interaction with diamond and presents a new hypothesis for the mechanism by which energy is delivered to individual lattice sites to generate vacancies.

Chapter 6: Non-Linearity of the Laser Writing Process - Results

This chapter regards an experimental and theoretical study in which the parameters of the laser processing are varied to determine how these affect the fabrication within the material. Experimentally laser parameters are varied and theoretically the partial differential equations developed in chapter 5 are solved numerically and fitted to experimental data to discuss the viability of the model to describe the experiment.

Chapter 7: Enhancement of Silicon Vacancy Ensembles

This chapter regards the use of laser writing for the enhancement of ensemble silicon vacancy centres in diamond without losing optical properties. Hypotheses about the mechanisms for formation of these ensembles are discussed.

Chapter 8: Deterministic Engineering of Single Colour Centres

This chapter will describe a new experimental method to deterministically generate

single colour centres into diamond utilising a femtosecond pulsed laser both to generate vacancies and to diffuse them in the material. In addition a study involving the how the fluorescent properties of centres behave during processing is undertaken and how this is influenced by laser parameters.

Chapter 9: Conclusions and Future Outlook

Here the thesis will be summarised and the future outlook will be also discussed.

Chapter Two

Literature Review

2.1 Introduction

Wide bandgap materials such as diamond and silicon carbide have been found to be host to a range of colour centre defects that are of potential use for quantum technologies [31]. These are of interest for many technological applications due to the ability to produce stable single photon sources and control and readout the spin state at room temperature with relative ease. Different spin states give different electric transition dipoles, thus allowing for control over the spin state via optical, microwave and radio frequencies.

Diamond provides the ideal environment for hosting colour centres due to its nuclear-spin free environment and sturdy structure [32]. It forms in a tetrahedral face centred cubic structure from carbon atoms with a lattice constant of $\frac{1}{4}$ which gives 8 atoms in the unit cell. Due to its spin-free structure, isolated electron spins can reach coherence times of around a millisecond at room temperature and close to a second when cooled to cryogenic temperatures [33] [34]. Nitrogen is a common impurity in diamond and two classifications have been devised to classify its prevalence. Type I diamond constitutes of nitrogen impurities of more than 20 ppm (parts per million) and type II diamond contains no detectable nitrogen impurities. Type Ib is defined

as where the nitrogen atoms are concentrated in isolated sites of the diamond with other areas being devoid of impurities. Type IIa is where the diamond contains no impurities and type IIb is where there are very few nitrogen impurities but other impurities such as Boron are present [35].

2.2 Review of colour centres

There are a range of colour centres that can exist in the diamond lattice and display stable single photon emission [21]. Many of these have only been identified via spectroscopy; their internal state structure and physical structure is currently unknown. Of those that are known a range of colour centres have displayed the ability to control the spin state making them useful for quantum applications. They generally have the form of a dopant that lies near to carbon in the periodic table as nearest neighbor to a lattice vacancy or laying between lattice sites generating a split vacancy [36].

2.2.1 Nitrogen vacancy centre

The most mature of these is the nitrogen vacancy (NV) centre first detected in 1965 after the diamond had been radiated with electrons and annealed at 600^{o}C [37]. Its structure was identified in 1977 via electron paramagnetic resonance (EPR) measurements [38] as is shown in Figure 2.1. The nitrogen atom has five valence electrons, three of which covalently bond to the surrounding carbon atoms leaving two un-bonded as a lone pair. The vacancy has three valence electrons; two of these form quasi-covalent bonds with the surrounding structure leaving a single un-bonded electron.

The three remaining electrons couple together in an axial C_{3V} symmetry, continuously exchanging roles. Two charge states of the NV centre emerge, a neutral and a negatively charged centre. In the NV^{-} variation, an extra electron is added to the

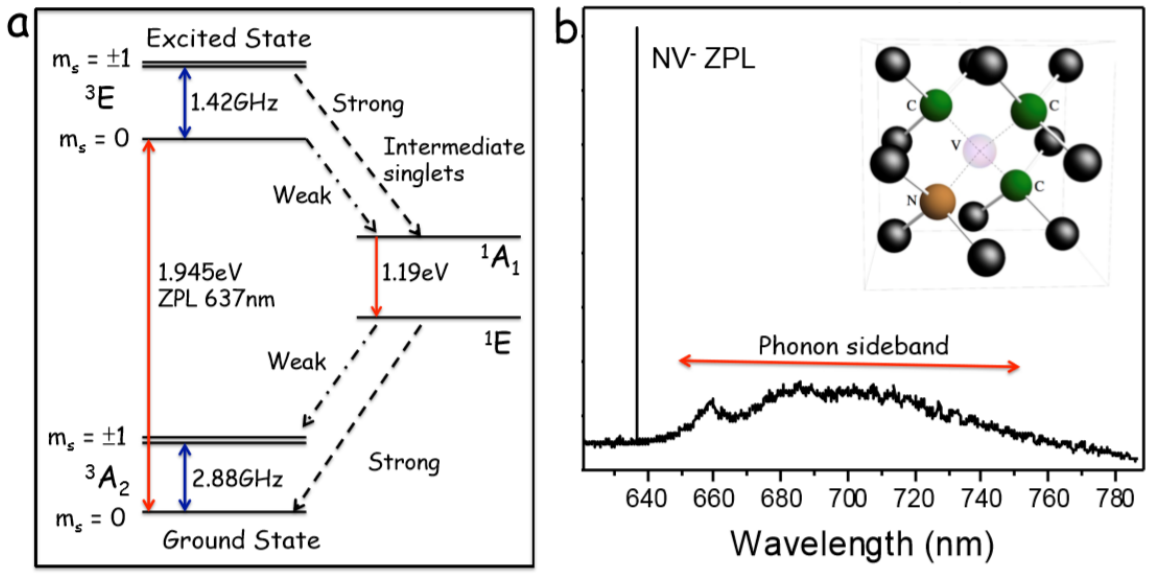


Figure 2.1 a. The energy level structure of the negatively charged nitrogen vacancy centre. The optical transition between the ground and excited states is at 637 nm with ground state $m_s = 0$ and $m_s = \pm 1$ separated by D = 2.87 GHz and excited state split by D = 1.42 GHz. Intermediate singlet states exist with a singlet ZPL of 1044 nm [31]. b. A fluorescence spectrum of the NV^- centre measured at a temperature of 4 K. ZPL at 637 nm with a broad phonon sideband at longer wavelengths. The inset shows the physical structure of the NV centre. Figure from ref. [31].

vacancy region forming an S=1 pair with the other valence vacancy electron leading to discrete energy levels within the bandgap [31]. Spin-spin interactions generate a triplet ground state $^3A_2$, which can be split into an $m_s = 0$ level and two spin levels of $m_s = \pm 1$ separated by D = 2.87 GHz and a triplet excited state 3E also split into $m_s = 0$ and ± 1 states these split by D = 1.42 GHz. Two singlet states also exist between the triplet states which are meta-stable and decays to these are weak. The energy levels of the NV^- centre can be seen in Figure 2.1a [38].

An optical transition occurs between the $m_s = 0$ ground and excited states leading to a zero-phonon line (ZPL) transition at 637 nm. Interactions with lattice phonons also lead to optical transitions at longer wavelengths. This leads to a broad peak and wavelengths greater than the ZPL as shown in Figure 2.1b. Approximately 4% of the transitional energy goes through the ZPL as indicated by the Debye-Waller parameter

(0.04 for NV^-).

As the ground state is non-degenerate and split with zero applied field, microwaves can be used to excite between different spin states. Coupling to the meta-stable intermediate singlets through inter-system crossing occurs more readily when the centre is in the $m_s = \pm 1$ states, the meta-stable states have lifetimes of tens of nanoseconds compared with the 12 ns for the $m_s = 0$ excited state lifetime leading to a quenching of the fluorescence intensity for the $m_s = \pm 1$ states [39] [40] [41] [42]. This optical spin-polarisation mechanism allows for initialisation into a pure state easily, which is key for all quantum applications [43]. The spin dependent fluorescence intensity thereby allows for optically detected magnetic resonance (ODMR) measurements allowing control and readout of the spin state [44] [45]. ODMR signals from single centres were detected in 1997 through confocal microscopy following improvements to electron irradiation techniques [46]. This was then verified to be a single photon emitter through autocorrelation measurements with a Hanbury Brown Twiss (HBT) interferometer in the year 2000 by Kurtseifer et al [47].

Rabi oscillations of a single electron spin state from the NV^- centre in bulk diamond were first detected at room temperature in 2004 by Jelezko et al who also measured the spin coherence times (T_2) of 2 μs, it was from here that the NV^- centre was identified as a credible candidate for networked quantum computing due to its long spin coherence time and ability to optically readout the spin state [3]. Following improvements in engineering, spin coherence times of order hundreds of microseconds at room temperature have been achieved [48] and at low temperature alongside dynamic decoupling methods, spin coherence times approaching a second has been achieved [33]. Isotopes of carbon such as ^{13}C have been found to couple to the NV^- and give preferential properties. ^{13}C has a nuclear spin of spin $\frac{1}{2}$ and thus couples to the electron spin of the NV^- and induces hyper-fine splitting. Scharfenberger et al theoretically tested how optical and magnetic control of the NV^- centre changes in the

presence of an adjacent ^{13}C finding that the hyperfine splitting allowed for high fidelity between quantum states during optical and magnetic control [49]. This hyperfine splitting separates the spin states of the NV^- from the spin bath of substitutional 14N nuclei, thus vastly increasing the coherence time [50]. In addition, the nuclear spin has a much longer coherence time than the electron spin of the NV^- and through spin-spin dipolar coupling the information can be transferred and stored in the nucleus [51][52]. Using this method, long term quantum memories can be achieved and to date the longest coherence time of a coupled nuclear spin using dynamic decoupling methods is nearly 2 minutes [53] and entanglement between the nuclear spins has been achieved for over 10 seconds [52]. It was found by Balasubramanian et al in 2009 that the T_2 time of single NV^- centres can be extended to beyond 1.8 ms by reducing the concentration of ^{13}C from its natural level (1.1%) to 0.3% indicating that the spin $\frac{1}{2}$ ^{13}C is the main source of electron decoherence due to spin $\frac{1}{2}$ coupling [34]. In 2019, Bradley et al coupled the NV^- to 8 surrounding nuclear spins from ^{13}C through the hyper-fine interaction allowing for spin coherence times lasting tens of seconds [52].

The NV^- centre has an excited state lifetime of 12 ns giving a ZPL linewidth of 13 MHz [54]. Togan et al first demonstrated spin-photon entanglement between a photon and an NV^- in 2010 by utilising the fact that the excited level of the $|A_2\rangle$ level is an entangled state of $|m_s = \pm 1\rangle$ spins and orbital $|E\pm\rangle$ angular momentum states and thus will decay with equal probability to the ground state [55] [56]. Entanglement between two single NV^- centres at a distance of 1.3km was achieved by Hensen et al in 2015, which is the first work that demonstrates loophole-free Bell inequality violation for both detection and locality and therefore demonstrates that the entangled centres can be used to solve quantum problems [27]. This was achieved through the Barrett and Kok scheme where the indistinguishable photons were interfered through Hong-Ou-Mandel interference and photon detection leading to entanglement through path erasure. In order to achieve entanglement via this regime, a high flux

of indistinguishable photons are needed. Strain around the emitter can lead to stark shifts lifting the indistinguishability. However Tamarat et al found that the Stark effect can be utilised by applying electric fields, tuning the excited state energy, hence tuning of the ZPL wavelength which is critical for being able to obtain quantum interference between centres and entanglement [54]. In 2021 Pompilli et al demonstrated the first 3 node quantum network using 3 NV centres entangled through photonics with a fidelity of $\sim$ 85 % [28].

The other stumbling block to entanglement is the low photon flux of ZPL photons from the emitter. This can be improved either through extracting more photons from the diamond or forcing more photons through the ZPL. In 2010, Hadden et al integrated solid immersion lenses into the diamond surface which allowed for lower refraction losses at the surface of the diamond. This allowed for NV^- centres to be placed further from the surface for the same amount of light detection, which allows for better coherence preservation [57]. In 2015, Johnson et al coupled the NV^- centre to an open optical micro-cavity at 4K so that the ZPL emission resonated and was amplified, whilst also suppressing emission from the phonon side-band thus increasing the Debye-Waller factor and giving more light for quantum applications [58]. In 2020 Ruf et al resonantly excited Purcell enhanced NV^- centres in a micro-cavity allowing for faster spin-entanglement times [59].

2.2.2 Group IV - vacancy centres

More recently a host of group IV elements (silicon, tin, germanium and lead), in conjunction with a lattice vacancy, have been found to also display spin control alongside stable single photon emission. These have sparked a flurry of new research activity in the area of solid-state spin qubits [60] as they offer some advantages over the NV centre such as a much larger Debye Waller factor allowing a much faster

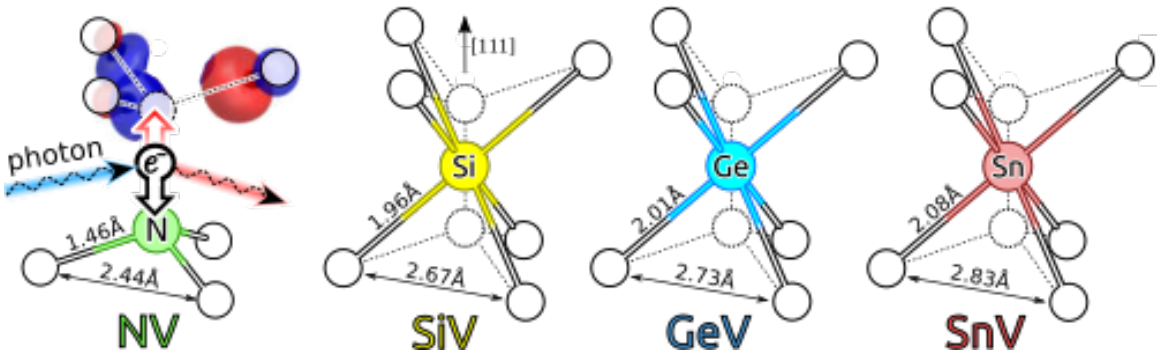


Figure 2.2 Physical geometry of the nitrogen vacancy (NV), silicon vacancy (SiV), germanium vacancy (GeV), and tin vacancy (SnV) centres [36]. The NV consists of nearest neighbor substitutional dopant and a lattice vacancy, the group IV centres consist of the dopant located in an interstitial location surrounded by a split vacancy. The lead vacancy (PbV) (not shown) also takes this configuration. Figure from ref. [36].

transfer of quantum information to photonics, one of the key stumbling blocks of the NV centre [36].

Group IV dopant elements sit between lattice sites rather than in a substitutional location [36]. The vacancy is then split, surrounding the dopant atom aligned along the [111] axis and has D^{3d} inversion symmetric point group symmetry, this differs to the geometry of the NV centre as shown in Figure 2.2.

This geometry leads to degenerate doublet ground and excited states within the bandgap [61]. Spin-orbit coupling then acts to lift the degeneracy leading to four discrete states and four possible ZPL transitions. The strength of the spin-orbit coupling differs for different defects leading to differing coherence behaviours. A larger splitting exponentially reduces the probability of thermal excitation through phonon coupling allowing coherent behaviour at higher temperatures. The basic electronic structure for this geometry and the degree of spin orbit coupling against state splitting is shown in Figure 2.3 [60] [62]. The inversion symmetry of these centres protects these spectral lines from first-order Stark shifts vastly reducing homogeneous broadening and allowing for transform limited linewidths during experiment [63].

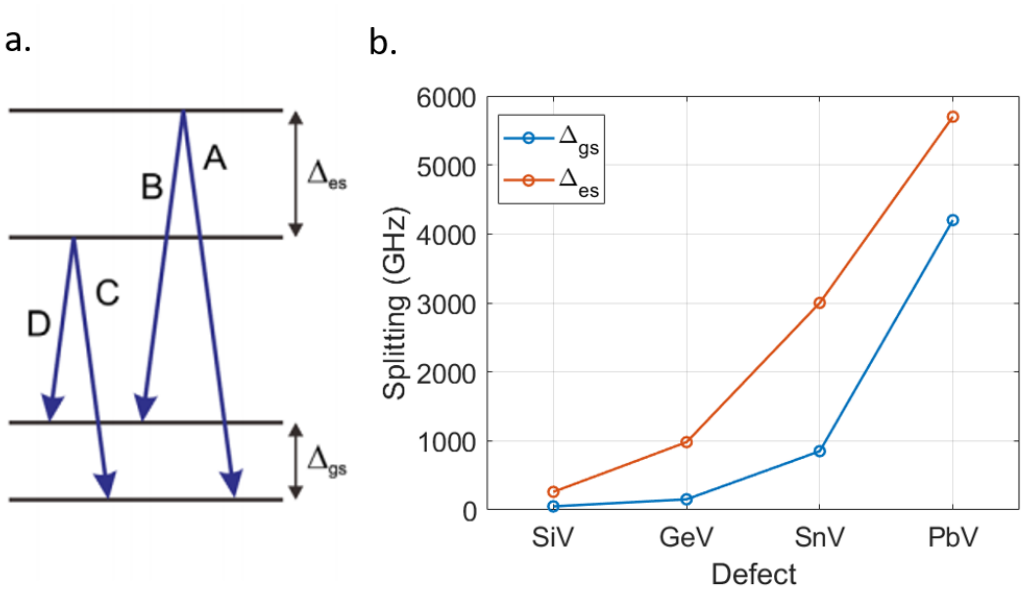


Figure 2.3 a. Electronic structure of the group IV vacancy centres. Doublet ground and excited states form due to the spin-orbit coupling [62]. This structure leads to four zero-phonon line transitions. b. The amount of ground and excited state splitting for different defects. Larger splitting leads to an exponential decrease in thermal coupling allowing coherence at higher temperatures. Data taken from references [60] and [62].

The most researched of the group IV centres is the silicon vacancy (SiV) centre. Like the NV centre, the SiV has neutral and negative charge states, both of which have been identified as useful for quantum applications. The negatively charged ZPL consists of spin-orbit split orbital doublet ground and excited states within the diamond bandgap centred at 737 nm with a ground state splitting of 50 GHz and excited state splitting of 260 GHz. These four states allow for four optical fine structure transitions [64]. This centre offers advantage over the NV centre due to a high Debye-Waller factor of 0.7-0.8, [65] [66] offering an efficient spin-photon interface making it easier to strongly couple to nanocavities. Due to the lack of spectral diffusion from Stark shifts, near-lifetime limited linewidths of between 125-400 MHz have been consistently observed from single centres [63] [67] [68] [69] , and indistinguishable photons from separate SiV's have been observed, without the need of external frequency tuning [70]. Linewidths of 5-50 GHz are typical for ensemble centres, limited by inhomogeneities in crystal strain [71] [72] [73]. The SiV^- centre is a spin-1/2 system and couples efficiently to the surrounding nuclear and electron spin bath of dopant atoms, in addition to efficient spin-phonon coupling hence displays spin coherence times of $T_2^* = 38$ - 48 ns at 4 K, much shorter than the NV [74] [75] [76] [77]. Spin-phonon coupling can be somewhat mitigated through operating at mK temperatures allowing improvement in spin relaxation times by a factor of 300 and enhancement of the spin coherence by a factor of 5 [78]. Ultrafast optical control [75] and readout or microwave based control [79] of the spin state alongside the efficient spin-photon interface allows for the development of a coupled spin quantum network connected through photonics [24] [80].

Fluorescence of the SiV^- centre was first observed in 1981 by Vavilov et al by conducting a cathodoluminescence investigation into polycrystalline diamond grown via chemical vapour deposition [81] and in 1995, it was verified to contain silicon [82]. The electronic structure of the SiV^- was identified in 1996 [83]. Initial attempts

to fabricate SiV^- within diamond by ion implantation proved unsuccessful due to photoluminescence lifetimes of $\sim$ 1 ns and poor quantum efficiency of $\sim$ 0.05 [84]. This is likely due to significant damage surrounding the defect created by the ion implantation process. More successful attempts followed in 2011 by SiV^- centres generated during CVD growth [65]. Successfully ion implanted SiV^- centres with high quantum efficiencies, high positional accuracy and yield were generated in 2011 following which, a wealth of literature has emerged in the area of ion implanted SiV defects [63] [68]. Ultra-fast optical and microwave control of the spin state at helium and milliKelvin temperatures was demonstrated in 2016 [75] and 2017 [79] respectively. Spin polarisation of SiV in the neutral charge state was demonstrated in 2017 [85]. The formation of SiV through laser ablation of silicon nanoballs on the surface of diamond was demonstrated in 2019 [86].

The neutrally charged centre has more recently emerged as a potential qubit candidate [87] first identified in 2011 [88]. Identified via near infrared ZPL transitions at 946 nm and 951 nm, it combines the advantages of high Debye Waller factor of the SiV^- and long spin coherence times of the NV^-. In 2018, Rose et al. found that 90 $\pm$ 10% of optical transitions of the SiV^0 went via the ZPL, measured electron spin coherence times of $T_2 = 250$ ms at 15 K with dynamical decoupling techniques and spin relaxation times of $T_1 = 43 \pm 2$ s [89]. Utilising the nuclear spin of the silicon atom, they also achieved nuclear spin coherence times approaching 1 s. The electronic structure of the SiV^0 was identified by Green et al. in 2019 to include triplet ground and excited states and a singlet excited state [87]. Initialisation and readout of the spin state has been proposed via a small application of strain to the emitter, however, the magnitude of this strain is currently unknown [87]. This is the current stumbling block for this emitter.

The charge state that the SiV is stable in depends upon the local electronic environment around the emitter. This can be manipulated by altering the Fermi

level through the adding of dopants. Significant doping of group V elements such as nitrogen or phosphorous raises the Fermi level making the negative charge state preferable. Doping of group III elements such as boron leads to the opposite, lowering the Fermi level and making the neutral charge state preferable. Driving the Fermi level further in either direction leads to stable double negative and positive charge states respectively [90]. These do no contain optical transitions due to all the levels being full/empty but the presence of these charge states potentially allows for a quenching mechanism.

The other three group IV colour centres that have been identified as potentially useful for quantum applications are the germanium, tin and lead vacancy centres (GeV, SnV and PbV). All three display transitions in the optical region of the spectrum and have large Debye Waller factors. Germanium vacancy centres have a ZPL transition at 602.7 nm displaying a Debye Waller factor of ~ 0.6 [92]. The electronic structure contains two ground and excited states with twofold degeneracy. Spin-orbit coupling partially lifts the degeneracy producing four levels, two ground and two excited, much like the SiV^- centre. This leads to four line structure of the ZPL with a ground state splitting of 152 GHz and an excited state splitting of 981 GHz [93]. The GeV couples well to phonons giving it similar spin coherence times to that of the SiV^- (T_2=19 $\pm$ 1 ns at 2 K) [91] meaning ultra-fast control or milliKelvin temperatures are needed for use as a spin qubit. ZPL linewidths of 42 MHz have been recorded from single GeV centres [91]. The theoretical excited state lifetime is 6 ns which gives a transform limited linewidth of 26 MHz [93]. The small difference between the theoretical and experimentally measured linewidths gives some indication of other damage surrounding the centre, likely generated in ion implantation used to generate these centres.

Negatively charged tin vacancy centres have a ZPL transition at 619 nm which resolves into four transitions at low temperature [62]. A ground state splitting of $\sim$ 850 GHz is observed and excited state splitting of over 3 THz, much larger than that

of the other group IV colour centres [62]. As the probability of population decreases exponentially with the size of the splitting, two of the transition lines are weak, yielding a "doublet" ZPL. Excited state lifetimes of 5 ns have been measured giving a generally fast fluorescence cycle and narrow ZPL linewidths over 18 MHz [94]. The large splitting of the ground state reduces phonon coupling leading to predicted spin coherence times of order milliseconds without cooling down to milliKelvin temperatures, a huge advantage over the SiV and GeV centres [62]. Early spin coherence measurements revealed T_1 times of greater than 10 ms [95] and an electron spin decoherence time of $T_2 = 1.3$ μs at 1.7 K revealing an which was extended to $T_2 = 330$ μs with two pulse dynamical decoupling methods [96]. To date, these centres have been engineered via ion implantation techniques followed by a high temperature global anneal to heal unwanted damage and allow diffusion of vacancies to the implanted ion.

Lead vacancy (PbV) centres have also emerged as another potential spin qubit in diamond. The electronic structure of the PbV is similar to that of the other group IV centre, a doublet ground state and doublet excited state leading to four optical transitions. The spin-orbit coupling leads to severe splitting of the doublets meaning that two of the ZPL transitions are centred at 520 nm with a splitting of 5.7 THz and the further two can be seen at 552 nm, split by 4.2 THz. The large splitting of both doublets means that phonon coupling is weak meaning coherent spin states can be achieved at higher temperatures (> 1 K). To date, spin control of lead vacancies is yet to be demonstrated [97]. The excited state lifetime was found via autocorrelation measurements to be 3 ns [60].

Each of these group IV vacancy centres is somewhat tuneable by applying strain to the emitter. The strain leads to further splitting of the ground and excited state doublets leading to suppression of spin dephasing as the splitting moves further from phonon resonant frequencies [98] allowing for coherent states to be extended to higher temperatures. Strain engineering has enabled a six times enhancement of the spin

coherence time from SiV^- centres at T = 4 K and achieving the same spin coherence as an unstrained centre at 100 mK ($T_2 = 0.25 \pm 0.02$ μs) [98]. Recent works have involved ion implantation and fabrication of nanostructures such as nanopillars in order to engineer the strain surrounding these defects [98]. Nanopillars have also been used to engineer single defects whereby the ion implantation technique is not sensitive enough to allow for single defect engineering by spatially confining single ions to individual nanopillars [97].

There has been less research done into the group IV vacancy complexes than the NV^- centre as group VI elements occurs less often in natural diamond than nitrogen but with the onset of synthetic diamond, they have become possible colour centre for quantum applications. However, as the atoms preferentially sit between lattice sites, the group IV vacancy defects are the most stable form of atoms within the lattice. This makes it difficult to exhibit strong control over the amount of dopant that lays in the lattice and artificial engineering processes lead to either too many centres or virtually none. A step towards robust engineering of useful group IV defects would be the ability to passivate unwanted centres.

2.2.3 Applications

A colour centre surrounded by nearby carbon-13 nuclei has been proposed as a node in a solid-state quantum computer [52]. Most proposals involve an NV spin but can be converted to use the group IV vacancy centres if lower temperatures and faster control systems are used to combat the strong spin dephasing. The centre acts as the initialisation and readout qubit via its ZPL and is able to pass information to nuclear spins for computation and storage via entanglement [99]. The advantage of these over alternative architectures is the ability to position potentially millions of qubits onto a single chip and the ability to maintain coherence at relatively high temperatures.

Coupling of electron-nuclear spin nodes together could be achieved either through spin-spin dipolar interactions between the centres or through an off-chip photonics network. Spin-spin dipole interactions are ideal and efficient even allowing for quantum computation to occur at room temperature, however the spin-spin coupling requires that the centres be < 50 nm apart from each other which requires significant materials engineering improvements to scale to more than a few qubits.

Coupling through photonics requires transferring the quantum information to a photon which can be addressed off-chip and entangled through the Barrett and Kok scheme [25]. This approach utilises the single photon emission behaviour of the colour centre where the quantum information is carried by photons emitted via the ZPL. This allows for the flexibility of coupling centres together at great distances allowing for much more leeway in the materials engineering required [18]. To date entanglement between nodes placed 1.3 km apart in separate laboratories has been achieved [27]. However a caveat is that low temperature (4 K for NV, mK for most group IV vacancy centres) is required to suppress phonon coupling [18]. For NV centres, this is easily achieved with regular cryogenics though, so dilution refrigerators are not needed, for other centres, dilution refrigerators or significant strain would be required. In addition, due to the small Debye Waller factor of the NV^- centre (0.04), only a small amount of the fluorescent light emitted carries the quantum information and is useful for quantum information processing. Therefore entanglement via photons is inefficient and often difficult to achieve before decoherence occurs. The group IV vacancy centres have higher Debye Waller factors but generally shorter coherence times, even at mK temperatures leading to similar issues in entanglement efficiency. These inefficiencies can be mitigated by engineering micro-structures around the centre which confine the optical modes that it is allowed to emit into. One such structure is a Fabry Perot micro-cavity which creates a resonance with the ZPL emission enhancing the Debye Waller factor by upto a factor of five [58][59]. By squeezing the optical density of states,

the lifetime of the emitter can also be shortened, allowing for single photon emission at a faster rate. Alternatively, entanglement and quantum information processing can be accelerated by extracting more photons from the device. Diamond is a high refractive index dielectric, ergo, there is a lot of reflection and refraction from interfaces and surfaces. By shaping the surface of the diamond around the emitter such that the interface is normal to the emission (a solid immersion lens) [57], more light can be extracted and hence information processing procedures can occur faster. Another way to deal with photon loss is to generate multidimensional photon cluster states that are resilient to loss. Here the state is shared between multiple entangled photons. These can be realised by utilising the entanglement between successive photons if gates are applied to the spin state between emission cycles or through some non-linear entangled pair generation mechanism such as spontaneous parametric down conversion [100].

Under the presence of an electromagnetic field, the fine structure of the NV^- centre changes via Zeeman and Stark shifts [54]. The ability to readout the spin-state means that these shifts can be detected and the centre can be used to detect weak electromagnetic fields. One such detector that has been proposed is by combining the colour centres with a nano-scale probe, the colour centre being the magnetometer and the probe allowing for high spatial resolution [101]. The sensor utilises the spin properties of the NV^- centre which Zeeman split under an applied magnetic field. By measuring the change in energy of transitions between spin states, the strength of the magnetic field can be determined. An ensemble of centres can be entangled using the spin-photon interface to form a quantum network which allows for higher sensitivity. Sensing and imaging of weak magnetic fields is a growing field and has a host of applications ranging from medical imaging to navigation systems. Recent advances in quantum sensing using NV ensembles have shown sensitivity of $(310 \pm 20)\ pT/\sqrt{Hz}$ in the frequency range of 10-150 Hz [102].

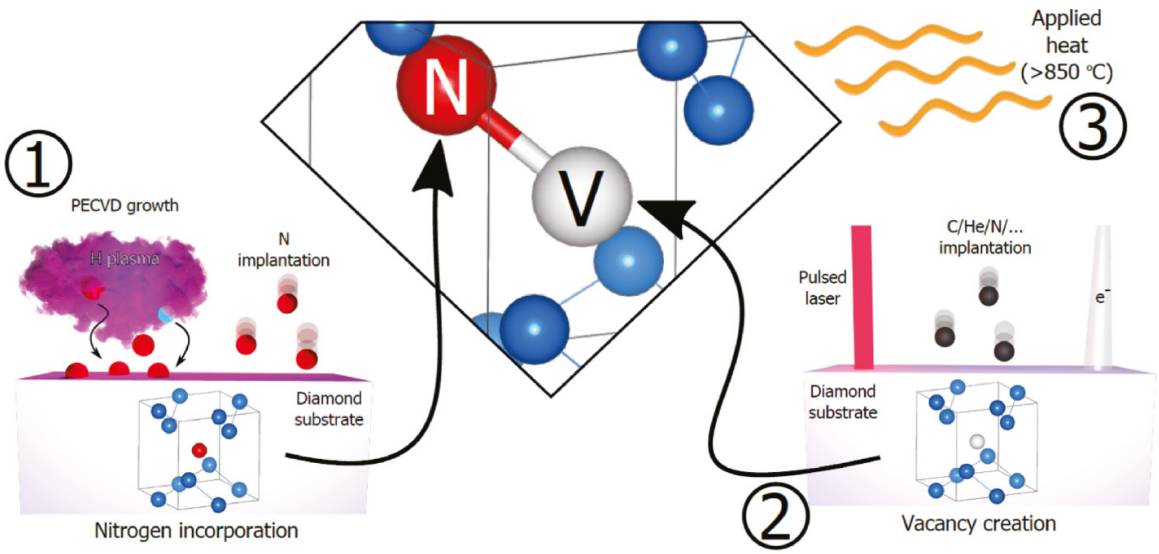


Figure 2.4 The three stages involved in the generation of nitrogen-vacancy colour centres in diamond (nitrogen incorporation, vacancy generation, heat application) and various approaches to each stage. Figure from ref. [105].

2.3 Fabrication techniques

To provide scalable quantum technologies based on colour centres in diamond, it is necessary to be able to engineer the centres in a controlled manner with an accuracy of less than a micron such that control hardware can be robustly engineered [63] [103].

Research into colour centres has occurred since the 1950's, however, until ∼25 years ago the research was carried out on native defects in naturally grown diamond. This meant that there was no control over the positioning of the defect within the diamond or the levels of impurities surrounding the defect. In 1953, it was demonstrated that diamonds could be grown synthetically in a lab allowing for control over the levels of impurities within the diamond [104]. In addition, techniques have been created that allow for control in the creation and placement of new colour centres.

In order to engineer colour centres into the material, three stages are required; the incorporation of dopant atoms into the material, the generation of a vacancy, and some applied heat to allow diffusion of the two defects together [105]. This is displayed for the example of the NV centre in Figure 2.4

The following sub-sections will review the work that has been done to date on developing each of these techniques.

2.3.1 Growth

Nitrogen can be introduced into the diamond lattice during the growth process of synthetic diamond with a significant degree of control such that most diamond used for industrial applications is synthetic, grown with the desired level of impurities. Two main techniques are used to grow diamond, chemical vapour deposition (CVD) and high pressure, high temperature (HPHT) growth. CVD diamond is grown by gas deposition of carbon onto a substrate. The gases used are usually hydrogen and methane. The hydrogen gas is used to selectively create diamond rather than graphite as atomic hydrogen etches graphite, breaking its bonds. Impurities such as nitrogen can be added and their concentration carefully controlled by feeding the gas with the desired impurity in gas form [106]. Silicon can also be incorporated in a similar manner to nitrogen but with much lower levels of control at the time of writing. Typically when impurities are introduced, many of them form colour centres, randomly distributed throughout the material [107]. For academic studies, this random distribution works well but for a device where a regular array is needed, these are more a hindrance. Careful annealing post growth can quench or destroy these defects leaving a fluorescence-free platform with which to generate centre through post growth mechanisms [107]. Alternatively the diamond can be grown to be as pure as possible with little to no impurities (less than 1 part per billion (ppb) of nitrogen and boron), following which, the impurities can be introduced post growth [103]. In addition CVD growth can allow for an artificially low level of carbon-13 atoms throughout the lattice, enabling enhanced spin coherence [103].

In HPHT growth, the starting material is graphite and the pressure and temperature

are increased until double carbon bonds are broken and converted into single bonds [108]. HPHT diamonds generally exhibit very low amounts of strain, but control over impurities is very difficult leading to concentrations typically over 100 ppm, limiting NV coherence to sub microseconds [103]. In addition, HPHT diamonds typically contain complexes of dislocations that are difficult to anneal out. CVD growth currently sets the benchmark for creating diamonds of high purity needed for many applications. CVD also gives the advantage of being able to grow monocrystalline diamond rather than polycrystalline which allows for greater control over the orientation of defects as well as improving coherence times and levels of optical control [106].

Substitutional nitrogen within the diamond provides a spin $\frac{1}{2}$ bath which couples to colour centres, reducing coherence properties. Therefore good quality NV^- centres are seldom found in diamond containing high levels of nitrogen. However it is easier to artificially produce NV^- defects in diamond containing higher nitrogen content due to the greater chance of locating a nitrogen atom. This leads to a trade-off between ease of fabrication and quality of the defects. The level of impurities within a CVD grown sample can be carefully controlled by varying the composition of the desired impurity within the growth gas. As the diamond is grown layer by layer, it is possible to grow very pure diamond that sandwiches a layer of heavily doped diamond by introducing N_2 gas into the chamber during growth. This is known as delta doping and the layer of doped diamond can be as thin as 2 nm [109]. Delta doping is useful as it can be combined with other fabrication techniques to produce high amounts of impurities for fabrication in the desired area but leaving most of the diamond impurity free, thus keeping the inherent spin bath of the diamond to a minimum. It has been demonstrated that native NV defects preferentially grow along the [111] plane when the synthetic diamond is grown in this direction with a probability of 95% [110]. Control over the orientation of the defects will be useful in creating devices as the NV^- dipoles can then be excited equally by light polarised along the [111] direction.

Introduction of other impurities allows for some level of control over the Fermi level allowing some level of control of the charge state of defects within the material. For example, for quantum applications, the NV^- is preferable over the NV^0. Adding group V elements such as phosphorous to the material raise the Fermi level and provide extra electrons to maintain charge stability [111][112]. Alternatively if the neutral or positive charge states of a defect were preferred, boron or other group III elements can be added during the growth process to lower the Fermi level [111][112]. The amount of doping must be carefully controlled as these dopants will add strain to the lattice and couple to the spin of the colour centre, reducing coherence [111][112]. Recently the use of n-type doping with phosphorous has allowed extension of NV spin coherence times by a factor of four [113].

Many applications require very thin films and membranes of diamond of order 100 nm, however, growth of these presents a challenge as current growth techniques require a substrate [114]. Membranes have been instead developed growing bulk material, laser cutting and mechanical polishing followed by reactive ion etching down to the desired thickness. These membranes generally have non-uniform thickness due to the inaccuracy of the technique which leads to losses during coupling of defects to micro-cavities. Therefore improvement in the fabrication of membranes is vital. Surface roughness' of around 4 nm are typically leading to scattering of optical modes or accidental destruction of the centres when the defects are orientated within nanometres of the surface, however this can be improved to an rms surface roughness of 0.6 nm [115].

2.3.2 Ion implantation

Rather than introducing impurities during growth, implantation of the desired impurity into the purest diamond allows for introduction of dopants and generates lattice

vacancies during the implantation process, fulfilling two of the stages required for colour centre generation [116] [117] [105] [118]. Historically, ion implantation is the fabrication technique with the highest positional accuracy and is therefore most commonly used [5] . For NV^- centres, a nitrogen ion beam is used to bombard diamond leading to a track of nitrogen impurities introduced into the diamond to depths of micrometers, as well as knocking many carbon atoms into interstitial sites creating neutrally charged lattice vacancies. For SiV, the ion beam fires silicon atoms into the material and each of the other group IV elements for GeV, SnV, and PbV [60]. For the group IV elements, control of the dopant level during growth is low therefore ion implantation has typically been used over growth processes to introduce the dopant to the material [105].

The implantation depth is determined by the energy of the incoming ions following a Bragg curve, with the highest energy ions able to reach upto a micron into the material [105][21]. However there is a trade-off, as higher energy ions create more damage to the material [105] and straggle significantly more leading to a loss of lateral positional accuracy [5]. Lower energy ions implant closer to the surface and have achieved depths as shallow as 1 nm [119] useful for applications such as magnetic sensing. A schematic showing the implantation depth against level of straggling and excess damage is shown in Figure 2.5.

The increase in straggle leads to a severe reduction in lateral positional accuracy and more damage as the ion passes through. Lattice vacancies and sometimes voids and dislocations are generated in the wake of the ion as the energy is passed into the material.

There are three ways in which an incident ion can dissipate energy within the diamond: Rutherford scattering, knock-on atoms and ionisation. Rutherford process is from direct ion-ion scattering and subsequent displacement of a carbon atom into an interstitial site. Knock-on displacements occur when a displaced carbon causes further

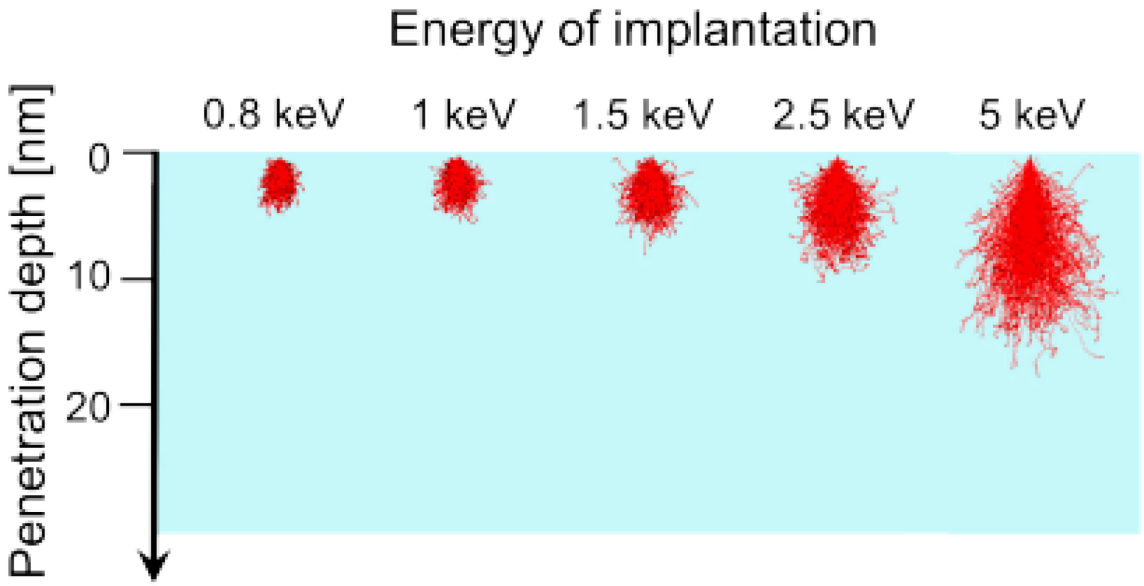


Figure 2.5 A schematic showing how implantation depth changes with the ion's initial energy as well as the increase in straggling. Figure from ref. [5].

lattice damage. The third way ions can dissipate energy is in the form of ionisation through the generation of electron-hole pairs in the diamond which then relax and lead to vacancy formation [120]. If the initial ion energy is too high ($\sim$ 100 keV), graphitic material can form [5]. In addition, channelling can happen if the material is weaker in one direction than another, preferentially implanting in a particular direction.

The implantation stage is often followed by an annealing step of above 600°C, which causes the vacancies to diffuse throughout the diamond. Many interstitial carbon atoms will then recombine with their lattice sites, but a few percent diffuse far enough away to be a stable vacancy. Some will diffuse out through the surface but a few will remain in the material. If a vacancy encounters the dopant atom, the vacancy becomes trapped by the dopant atom forming a colour centre [118] [121]. However, many vacancies are often still left within the material which can have detrimental consequences on the quality of the centres. This is a further trade off of initial ion energy, where the yield of colour centres generated increases for higher energies but at the cost of coherence [5]. In addition the probability of forming ensemble centres also

increases which is undesirable for many applications [99].

By implementing a mask during the implantation process, very high lateral positioning accuracies can be achieved. One method involves use of a Polymethyl methacrylate (PMMA) mask to cover the diamond and which is etched to form a mask via electron beam lithography. Following this, ions are implanted but can only enter the material through the holes in the mask allowing positional accuracies limited only by the lithography of order nanometres [122]. These masks fail to maintain high positional accuracies for higher implantation depths due to the level of straggle [105]. Alternatively, a method that achieves a positioning accuracy of around 20 nm is achieved by focusing the ion beam into a pierced AFM tip and using low energy ions (5 keV) [21].

The yield of successful sites is typically low at around 5% for the best quality centres [21]. This can be increased by increasing implantation energies but is still limited by the Poissonian nature of the annealing stage. An upper limit of 37% is achieved for the generation of single colour centres [105]. A few "deterministic" approaches have improved upon this by detecting the ion pre/post impact with the substrate through the collection of secondary electrons from the substrate or electron-hole pairs generated around the ion. This allows tracking of the ion and therefore an improvement in the yield but requires significant signal processing and slows down the implantation significantly [123]. The Poissonian nature of the process also means that some ensembles will form regardless of the care put into processing. This is not ideal for generating dense arrays of single colour centres [122] [118]. Another major stumbling block is the inability to implant deep within bulk material giving limitations to device design. Axial positioning accuracy can be inaccurate as a track of vacancies is created from the surface to the deepest implantation depth meaning that post annealing, the centre can migrate closer to the surface [5]. To tackle the shallow implantation depths that achieve the best quality centres, overgrowth of pure

CVD material is often used [124]. The yield of defect creation can also be increased by combining ion implantation with delta doping during growth at the desired depth. Here the implantation is a vacancy creation mechanism.

The quantum properties of ion implanted NV^- centres such as coherence time and line-width of the ZPL have been optimised to approach those seen in native centres although have not yet reached that level due to surrounding damage to the material. Gaebel et al showed that an NV^- centre created by ion implantation can achieve coherence times of $\sim$350 μs although coherence times of under 100 μs are more prevalent [125]. To date, the longest coherence time measured from an ion implanted NV centre is 428 μs [126]. Linewidths of 13 MHz of the ZPL from ion implanted NV^-'s have been reported in diamond allowing the production of indistinguishable photons [127].

Focused silicon ion beams followed by global annealing have been used to engineer SiV centres into the material achieving high spatial accuracy but low yield [63]. This technique remains the main method for generating SiV defects due to the difficulty of introducing silicon into diamond during growth. To date, all studies on other group IV colour centres (PbV, GeV and SnV) have engineered the defects into the material via ion implantation [128] [97] [62] [96] [94].

2.3.3 Electron irradiation

An alternative approach to vacancy formation can be achieved through irradiating the surface with electrons [129]. In this approach, the dopant atom is grown into the material and vacancies are generated through irradiation with an electron beam. The mechanism behind vacancy generation is similar to that of ion implantation, however the electron has a much smaller cross-section hence produces less strailing. In addition, the smaller mass allows electron irradiation to generate vacancies at much greater

depths than ion implantation, upto hundreds of microns in depth [129][105]. This technique was the first used to generate NV centres into diamond in 1965 [37].

Similarly to ion implantation, vacancy formation can take place via either Rutherford scattering, knock-on scattering or electron-hole pair relaxation [130]. A minimum initial kinetic energy for electron irradiation of 145 keV has been found for Rutherford scattering [131]. Vacancies are generated throughout the material upto a set depth determined by the initial kinetic energy of the electrons. Following vacancy formation, the diamond is annealed at a temperature above 600°C, allowing the vacancies to diffuse. These then meet the impurity dopants and form colour centres throughout the crystal.

Electron irradiation is able to produce NV centres with coherence times equal to that of native centres and produce lateral positional accuracies of ~ 50 nm. The axial positional accuracy on the other hand is very low with vacancies being produced throughout the entire depth of the material down to the deepest depth determined to an accuracy of $\sim 1\mu$m by the initial electron energy. For this reason, electron irradiation is often used when lots of vacancies are wanted or high densities of NV centres, but positional accuracy is less important. An example would be for an ultra-sensitive magnetometer [102] where the important parameter is NV density. Lower energy irradiation leads to better coherence properties of generated colour centres and is capable of creating ensembles of highly coherent NV's. The coherence times measured from NV ensembles generated by this technique is limited by coupling to surrounding NV spins [132].

Control over the depth of electron generated colour centres can be achieved by combining electron irradiation with delta-doped diamond. If a tunnelling electron microscope (TEM) is used for the irradiation, the lateral positional accuracy can be of order tens of nanometers without the need of masking. Recently, a TEM with low energy electron irradiance of ~ 145 keV has been shown to produce reproducibly long

coherence NV centres in the diamond lattice [131]. Electron irradiation has enabled the generation of NV centres with T_2 times approaching 1 ms and lateral positional accuracy only limited by the diffusion length during annealing. Axial positional accuracy has been localised to less than 4 nm through use of delta-doping [131].

2.3.4 Laser writing

An alternative method to generate colour centres into diamond is through the use of laser writing on a doped diamond material, followed by an annealing step. Ultra-fast laser processing of transparent materials is a mature field allowing for the modification of bulk structures for various applications, whether it be generating wave-guides through refractive index modification, surface modification or a vast array of other optical applications [29][133] [134] [135]. It is only recently that it has been explored as a route to the controlled formation of defect complexes and colour centres. Ultra-fast laser processing can be separated into three distinct practices, direct laser writing, where the laser is focused deep within the bulk, laser ablation, where the laser removes surface material and laser facilitated electron irradiation, whereby the laser is focused above the surface and ionises the air above a material, the electrons of which then get accelerated at the surface [136].

The use of a femtosecond laser to facilitate generation of colour centres into diamond was first pioneered in 2013 [137]. Here, a Ti:Sapphire 800 nm laser was focused 1 μm above the surface of a type Ib diamond, causing visible surface damage. Annealing in air at 680°C oxidised the defects and ensemble NV^- fluorescence was observed. The laser processing in this case was indirect, with the pulsed laser ionising the oxygen and nitrogen in the air creating free electrons which in turn created vacancies within the diamond [138]. Pre-annealing no fluorescence was observed, therefore it is possible that the free electrons converted native NV^0 into the NV^-.

Direct laser writing involves the focusing of the laser into the material and producing significantly high focal intensities such that modification of the material can take place. The high intensity sub-bandgap laser light interacts non-linearly with valence electrons (i.e. interaction involves absorption of multiple photons per electron) promoting a high density of carriers into the conduction band [134]. Relaxation of these carriers leads to the generation of vacancy-interstitial pairs, known as Frenkel defects. A full theoretical model for the laser interaction with diamond has yet to be validated with experimental data, the concept of which shall be explored in chapters five and six. If the laser generated vacancy is diffused through an annealing step, colour centres can be generated using this method. If multiple laser pulses are used, laser induced defects act as absorption centres and lead to efficient generation of further damage. Most work involving direct laser writing in diamond has focused on generating significant bulk modification and the formation of sp^2 hybridised graphitic material to fabricate electrically conductive wires and significant strain within the material for use in optical waveguides and particle detectors [139] [140] [141] [142]. However, in some works, where samples were thermally annealed after laser processing, the creation of NV centres near the graphitised region was observed as a result of the migration of vacancies from the damaged region to bind to nitrogen present in the diamond lattice [143].

Pimenov et al found that ensemble NV^- centres could be created within type IIa CVD diamond by applying multiple pulses of a pico-second pulsed laser into the diamond. The laser created vacancies within the lattice and also increased the temperature within the focal volume to 1600°C which allowed for diffusion of the vacancies to reach a nitrogen atom and form NV^- [143]. However, as well as generating many NV colour centres of both charge states, a large amount of residual damage was created. Kurita et al showed that through tuning the pulse duration, the ratio of ensemble centres to graphitic formation could be increased with short pulse durations

generating high density ensemble NV with a low probability of forming graphitic material [144].

In 2017, it was demonstrated that single ultra-short pulses of an aberration corrected laser focused into the bulk diamond material followed by an annealing step at 1000°C for 3 hours, allowed for controlled generation of single NV^- centres with high positioning accuracy and low residual damage and demonstrated that these centres produce the best coherence and optical properties of any synthetically produced NV^- centre [6] [145]. Yields of single centres followed Poissonian statistics due to the random walk annealing stage [6]. They also found that the laser written NV^- centres displayed good optical properties and spin coherence times equal to that seen in native centres ($\sim$ 800 μs [145]). The laser written centres also displayed transform limited ZPL linewidths suggesting that inhomogeneous broadening of the centres is low, and the centres can produce indistinguishable photons. The freedom of this technique allows for the generation of 3D arrays of single NV^- centres [145]. Integration of laser written NV centres with laser written waveguides was demonstrated in 2018 [146]. Yurgens et al recently showed that by focusing light through a solid immersion lens (t-SIL) rather than a planar diamond surface, the pulse energy threshold for vacancy and therefore NV formation is significantly reduced and allow for generation of colour centres close to the diamond surface [147]. This is not normally possible using traditional optical methods as to achieve a high enough optical intensity, an oil immersion objective lens is used. Near surface processing boils the immersion oil which causes significant phase aberrations during focusing so no processing occurs [6]. Single pulse direct laser writing has recently been shown to produce single and ensemble colour centres in a range of other materials including SiV centres in silicon carbide and the RL centre in gallium nitride [148] [149] [150] [151] as well as luminescent centres in cubic boron nitride [152].

The use of a femtosecond laser to nano-ablate the diamond surface has also been

used to generate colour centres. Kononenko et al showed that a train of infrared pulses focused upon the surface of the diamond led to the generation of ensemble NV centres around the crater [153] [154]. They showed that the density of ensembles scaled logarithmically with the pulse energy of the multiple pulses. Rong et al showed that nanoablation of a diamond surface that has been coated in silicon nanoballs led to the generation of single and ensemble SiV centres in the nanoablated crater [86]. The mechanism behind surface processing is somewhat similar to the high energy regime of bulk processing however rather than forming graphitic material, the material is blasted away leaving a crater. Areas nearby that received a lower energy density from the laser experience generation and diffusion of vacancies leading to colour centre formation.

A significant advantage of direct laser processing over other post-growth methods for materials engineering is that the non-linearity of the interaction provides a route to localisation in three dimensions such that complex 3D micro-structures can be generated with high positional accuracy. Here, the magnitude of the non-linearity is defined as the gradient of a slope on a dual logarithmic plot with the pulse energy/focal intensity on the x-axis and the response of the material on the y-axis. A theoretical discussion of the processes involved during laser processing will be discussed in chapters three, five and six.

Annealing

An annealing stage is often required following many fabrication methods to heal residual damage to the lattice and allow vacancy migration to form the desired centre. Annealing describes heating of the sample such that vacancies and interstitial atoms within the lattice diffuse and recombine as well as other damage being broken apart via thermal diffusion. A low level of residual damage is vital for gaining high optical and spin coherence from defects. As all known fabrication processes generate residual

damage, annealing is key to reduce this. Various defects within the material have different threshold energies for diffusion, therefore careful control of the temperature allows for control over which defects anneal away and which remain within the lattice.

Defects within diamond start to diffuse dependent upon their activation energy within the lattice. Diffusion can be modelled with the heat equation where the diffusion coefficient, D, is a variable that depends upon the activation energy and the temperature of the anneal.

$$D = D_0 \exp\left(\frac{-E_A}{kT}\right) \tag{2.1}$$

Where E_A is the activation energy for diffusion, k is the Boltzmann constant, T is the temperature of anneal and D_0 is a normalisation coefficient [155]. The activation energy for neutral vacancies has been estimated to be 2.3 ± 0.3 eV with a diffusion normalisation coefficient of 3.1×10^{-6} cm^2 s^{-1} allowing vacancy diffusion at temperatures above $\sim$ 600 °C [156] [157]. Split-interstitial carbon atoms have a lower activation energy of 1.6 ± 0.02 eV [155] making them mobile at room temperature with a diffusion coefficient of 1×10^{-6} cm^2 s^{-1}. Dopant atoms will also become mobile at hotter temperatures, for example a substitutional nitrogen has an activation energy of 5 ± 0.3 eV [156] [158]. Diffusing the dopant atoms is rarely done though as vacancies are mobile at lower temperatures. Under the assumption of no or homogeneous strain, diffusion will be isotropic and can be described by a spherically symmetric function [159]

$$N(r,t) = N_0 r \exp\left(\frac{-r^2}{4Dt}\right) \tag{2.2}$$

where $N(r,t)$ is the concentration of defects that diffuse within a radius r and time t. N_0 is a normalization constant and D is the diffusion coefficient. The distance a defect can diffuse can be approximated by taking the square root of the product of the

diffusion coefficient and the annealing time [155]. Annealing works by a random walk of the dopant and hence will produce a stochastic Poissonian yield of colour centres if a dopant atom is within the radius of diffusion during an anneal [160]. In addition, other conglomerate defects such as di-vacancies can form, also stochastically, and reduce the probability of forming the desired centre [156]. Strain within the material will lead to a preferential diffusion direction, a full analysis of diffusion would require knowledge of the strain in the material [160].

Whilst vacancies are mobile at $\sim$ 600 °C, iterative studies have shown that the yield of colour centres can be optimised by annealing at a higher temperature and for differing periods of time. Chen et al studied the yield of laser written single NV centres against different annealing times and temperatures following laser generation of vacancy clusters, finding that an anneal at 1000 °C for 3 hours provided the highest yield [159]. Chu et al also studied the yield of NV centres given differing anneal temperatures and lengths of time following ion irradiation of the material. Here the best results were obtained from annealing for four hours at 400 °C, followed by two hours at 800 °C, and finally two hours at 1200 °C, with a one hour ramp up to each temperature [161].

Annealing at temperatures above 2100°C can lead to breaking of the bonds holding an NV^- centre together and leads to dissociation of the centre [162]. Thus, annealing can also be used to destroy colour centres and return the lattice to a pure state. This is important as annealing can also be used to break apart other agglomerations of defects in the lattice such as dislocations or graphitic material which would lead to decoherence if an NV^- was used for quantum purposes.

2.4 Summary

In this chapter colour centres within diamond as a platform for quantum technologies has been reviewed with a brief overview of various architectures based on these centres. In addition, a variety of engineering techniques for generating colour centre defects in diamond have been summarised. Each fabrication technique has a variety of advantages and disadvantages. Ion implantation followed by annealing has been demonstrated to produce highly coherent colour centres with high positional accuracy but has a very low yield and leaves a track of vacancies and shallower depths along the implantation track which makes it difficult for fabricating large scale devices. Electron irradiation produces centres that rival native defects in quality but has little to no positional control and laser writing followed by annealing has demonstrated colour centre generation with high optical and spin coherence and high positional accuracy but displays a Poissonian yield.

Chapter Three

Theoretical Background

3.1 Introduction

Ultra-fast laser writing into bulk diamond has been observed to exhibit three regimes experimentally under high, mid and low pulse energies; an induction into sp^2 hybridised graphite [29][133][163], a slightly lower energy regime whereupon a pulse knocks individual carbon atoms into interstitial sites creating vacancies but leaving most of the material untouched [6] [151], and a low energy regime in which the laser pulses cause the diffusion of defects within the material but do not create further damage (chapters five and eight) [9]. In chapter eight it will be shown that a pulse which creates a small number of vacancies, followed by a train of lower energy pulses allows for deterministic generation of single NV centres with greater positional accuracy than the focal volume of the laser, a key step towards the development of a solid-state quantum device [9]. The mechanisms in which the laser interacts with the diamond is critical for effective engineering of devices, but are not yet fully understood.

It is understood that when a sub-bandgap laser pulse interacts with a semiconductor, it generates a high density of non-equilibrium charge carriers through a combination of multi-photon absorption, Zener breakdown and avalanche processes, the relative strengths of each are highly non-linear with respect to the focal intensity [134] [164]

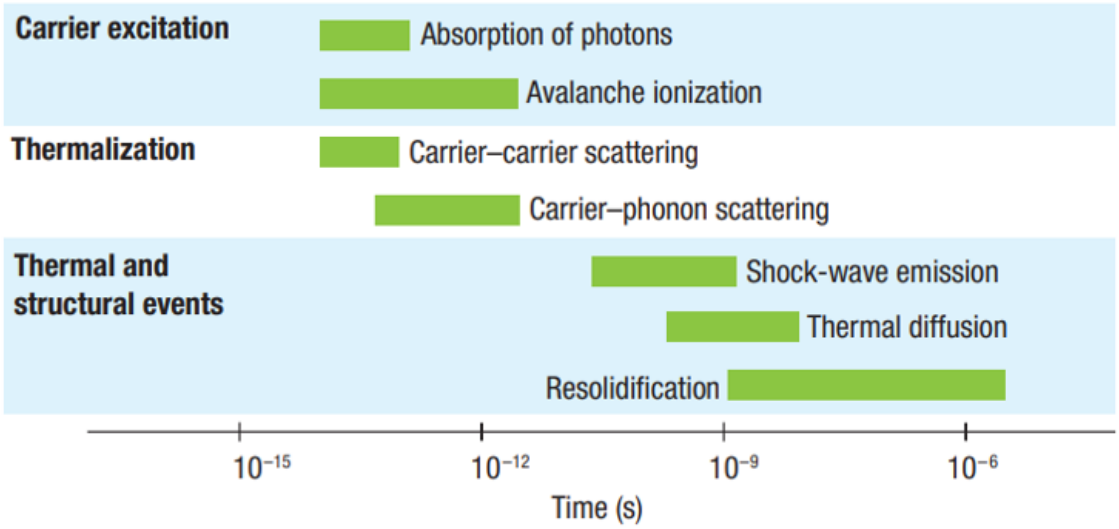


Figure 3.1 Timescale of the physical phenomena associated with the interaction of a femtosecond laser pulse with transparent materials. The green bars represent typical timescales for the relevant process. Figure from ref. [134].

[165] [166]. Following the pulse, carriers thermalise very fast through carrier-carrier scattering to a temperature much higher than the lattice [167]. Scattering with optical and acoustic phonons follows such that the excess energy is dissipated into the lattice and the two approach a quasi-equilibrium temperature [168] [169] [170] [171] with an arbitrarily high density of carriers determined by the laser pulse. The non-equilibrium nature of this system allows for some unusual states of matter including dense excitonic states and at a low enough temperature, condensation into an electron-hole liquid [167]. Such states are long lasting and eventually decay through recombination processes. The associated timescales of these processes are nicely summarised in the following figure from Gattas *et al.* [134].

Gatass *et al.* split the laser processing of transparent materials into three categories: carrier excitation, thermalisation, and thermal and structural events. The latter of these is known to produce large scale damage, voids and dislocations. In diamond

in addition to thermal structural changes, it has been shown theoretically and in agreement with experiment that high energy pulses generate carrier densities of a significant proportion of the atomic density, and above a threshold carrier density ($\sim$ 9% ρ_A), there is a significant shift in the potential energy surface such that a non-thermal melting occurs through a Coulomb explosion on timescales of $\sim$ 10-100 fs [172] [173]. Re-solidification of this material leads to the formation of sp^2 carbon and voids which become frozen in. In addition, longer duration pulses allow for collisions of high energy carriers with lattice ions, which facilitates a thermal melting followed by re-solidification as graphitic material [174]. Similarly to ultra-fast phase changes, ablation of surface material can be explained by a Coulomb explosion when the carrier density becomes high enough that valence electrons can no longer hold the ions together [153].

Lower energy pulses are known to form defects spanning single atomic sites. The formation of single-site defects necessarily requires the energy dissipation into the lattice to undergo some non-thermal process. Single defect creation within semiconductors must occur through some localisation process of carrier energy to a single atomic site for which various mechanisms have been proposed such as the formation of polarons, charge trapping via an existing lattice defect or voids frozen in during re-solidification following ultra-fast melting [136]. Within certain dielectrics such as Alkali Halides and SiO_2, the non-radiative relaxation of excitons is known to form photolytic defects [175] [176]. The existence of excitons and poly-excitons within diamond has been found through luminescence experiments [177] and self trapping of bi-excitonic states has been shown to apply a significant deformation potential to a single atomic site [178] but a quantitative study between poly-excitonic states and defect formation in diamond is yet to be done.

Density functional theory (DFT) calculations reveal that introducing a vacancy into a perfect diamond lattice requires an energy input of 7.14 eV [156], however

molecular dynamics simulations reveal a significantly higher activation energy for defect formation with a minimum at 30 eV and a weighted average energy of around 70 eV [179]. Such a large range of theoretical estimates on the formation energy make estimations of formation mechanisms difficult to determine.

To date, laser processing within diamond has mostly been studied considering the non-linearity of the initial photoionisation process under the assumption that the energy relaxation leading to defect creation is a linear process [180] [181]. In the high energy regime, where lattice damage and breakdown is proportional to the total carrier density, these models are able to explain experimental data, but in the lower energy regime lattice damage is not proportional to electron density such that more complex interactions become important. It should be noted that models of some of these interactions exist in the literature, often focusing upon the conduction band electron dynamics, however these models are generally simplified so that the equations can be solved analytically such as ignoring the spatial dependence of carriers and energy transfer to the lattice [168] [182]. Furthermore many consider the multi-photon processes as a simple power-law relationship with regards to the focal intensity, not considering the band structure or non-linear propagation of the light through the material. Lagomarsino *et al.* showed that degeneracy between valance bands leads to a non-perturbative enhancement of photoionisation leading to higher non-linearities than would be expected in the generation of free carriers [180].

3.2 Light-matter interactions

The initial process that occurs when light is absorbed by a material is the generation of photo-electrons through photoionisation. This consists of valence-band electrons being promoted across the bandgap into the conduction band. The large bandgap of diamond means that single photons do not have enough energy to promote electrons across the

potential barrier; generation must occur through non-linear processes involving the simultaneous absorption of multiple photons and band bending.

The electron wavefunctions within a material can be characterised as a superposition of all states.

$$\Psi_0 = c_1\psi_1 + c_2\psi_2 + ... + c_n\psi_n \tag{3.1}$$

Which is normalised such that the total probability is equal to 1. An incoming pulse of light can be thought of as a perturbation to the Hamiltonian potential such that the pre-factors change corresponding to a transition of the electron into a different state. The form that the perturbation takes is related to the electric field vector and the choice of gauge. Commonly the length gauge is selected such that the potential is given by.

$$V_{int} = eEr \tag{3.2}$$

Where V_{int} is the perturbation potential, e is the electron charge, E is the electric field strength and r is the distance the electron is perturbed by.

This perturbation represents the formation of dipoles within the material in response to the incoming electric field. The wavelength of light is much larger than the inter-atomic distance such that the long wavelength approximation holds. In this case, the temporal and spatial dependence of the electric field can be separated and each atom can be evaluated as if it has a uniform spatial field. The temporal dependence of the electric field can be approximated as a Gaussian multiplied by a sinusoid with the oscillation frequency of the field, ω_0.

$$E(t) = E_0 \exp\left(\frac{(t-\mu)^2}{2\sigma^2}\right) e^{i\omega_0 t} \tag{3.3}$$

Where E_0 is the maximum amplitude of the field, t is the time, μ is the peak time

and σ is the standard deviation of the Gaussian corresponding to the pulse duration.

The probability of transition is then governed by substituting this into the Schrödinger equation and integrating over all momenta, p.

$$W = \int_{-\infty}^{\infty} \left| \frac{-i}{\hbar} \int_{-\infty}^{\infty} \langle \Psi_P | V_{int} | \Psi_0 \rangle \ dt \right|^2 d^3p \tag{3.4}$$

Where W is the density of promoted carriers, $\hbar$ is the reduced Planck's constant, i is the imaginary number and Ψ_P is the electron canonical momentum gained by the field and can be represented by a non-relativistic Bloch-Volkov function [183].

A more useful parameter, such that pulses of arbitrary duration can be studied, is the differential of this with respect to time which gives the rate at which electrons transition across bands. This is given by

$$\begin{aligned} \frac{dW}{dt}(t) = \int_{-\infty}^{\infty} \Bigg| \frac{-i}{\hbar} \langle \Psi_P(t) | V_{int}(t) | \Psi_0(t) \rangle \\ \cdot \exp\left(\frac{iT}{\hbar} \left[\frac{p^2}{2m} + I_p + U_p \right] \right) \Bigg|^2 d^3p \end{aligned} \tag{3.5}$$

Which can be deduced from symmetry arguments evaluating at a time $t+T$ where T is the oscillation period. I_p is the effective ionisation potential and U_p is the average ponderomotive energy of electrons within the field.

Evaluating this integral is difficult and changes depending upon the polarisation of the light and the structure of the bands. A first solution to this integral was determined by Keldysh in 1965 [164] by assuming a direct gap and linear dispersion.

The Keldysh solution leads to the following set of equations.

$$\frac{dW}{dt}_{PI} = \frac{2\omega_0}{9\pi} \left(\frac{\omega_0 m}{\hbar \gamma_1} \right)^{\frac{3}{2}} Q(\gamma, x) \exp\left[-\pi \langle x+1 \rangle \frac{K(\gamma_1) - E(\gamma_1)}{E(\gamma_2)} \right] \tag{3.6}$$

Where

$$\gamma = \frac{\omega_0}{\omega_t} = \frac{\omega_0}{e} \left(\frac{m' c n \epsilon_0 \mathcal{E}_g}{I} \right)^{\frac{1}{2}} \tag{3.7}$$

$$\gamma_1 = \frac{\gamma}{\sqrt{1+\gamma^2}} \tag{3.8}$$

$$\gamma_2 = \frac{\gamma_1}{\gamma} \tag{3.9}$$

$$x = \frac{2\mathcal{E}_g}{\pi\gamma_1\hbar\omega_0}E(\gamma_2) \tag{3.10}$$

$$Q(\gamma,x) = \sqrt{\frac{\pi}{2K(\gamma_2)}}\sum_{n=0}^{\infty}\exp\left[-\pi n\frac{K(\gamma_1)-E(\gamma_1)}{E(\gamma_2)}\right]\Phi\left[\sqrt{\frac{\pi^2(2\langle x+1\rangle-2x)+n)}{2K(\gamma_2)E(\gamma_2)}}\right] \tag{3.11}$$

Where e is the charge of the electron, m' is the reduced exciton mass, c is the speed of light, n is the refractive index of the medium, ϵ_0 is the permittivity of free space, $\mathcal{E}_g$ is bandgap energy and I is optical intensity. K and E are the elliptical integrals of the first and second kind and $\Phi(z)$ is the Dawson Integral. The $\langle x\rangle$ notation refers to the integer part of x.

The important parameter is γ, known as the Keldysh parameter which compares the optical frequency ω_0 to the frequency required to tunnel ω_t. When $\gamma \gg 1$, the function corresponds to the simultaneous absorption of multiple photons by an electron within the valence band which transitions to an energy state within the conduction band. Light has very little momentum compared with electrons so transitions only occur vertically without transferring momentum. In energy space, this is represented by a delta function at an energy corresponding to the number of photons absorbed given by $\langle x+1\rangle$.

For values of $\gamma \ll 1$, the electromagnetic field is strong enough that the bands bend down and the momentum gained by valence electrons is large causing an adiabatic horizontal shift of the bands. The empty conduction band orbitals do not shift due to no momentum gain. These two effects cause the conduction and valence orbitals to

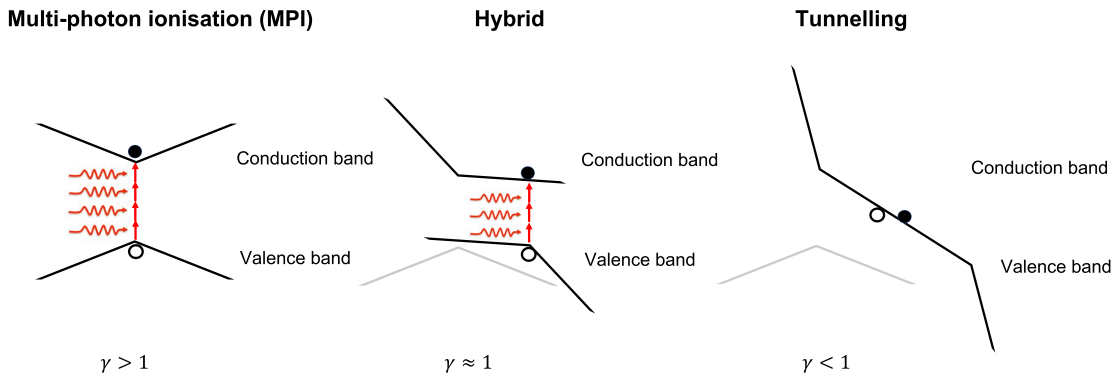


Figure 3.2 A schematic showing the three solutions to the Keldysh equation dependent upon the value of γ. For large γ's, little momentum is gained by valence electrons and transitions occur vertically via multi-photon ionisation. For small values of γ, valence electrons gain a large momentum shift and the band edges bend due to the field causing the valence and conduction orbitals to overlap allowing transitions to occur via tunnelling. The transition between these two occurs at values of $\gamma = 1$ where a hybrid of multi-photon and tunnelling processes occur. In grey is the zero field position of the valence band which is adiabatically shifted due to the canonical momentum of the field.

overlap allowing the electron to tunnel between them. Neglecting γ terms, this set of equations reduces down to the standard equations for tunnelling under a strong electric field.

When $\gamma \approx 1$, both tunneling and multi-photon absorption occur. Therefore transitions occur vertically upon a dispersion diagram after the valence bands are adiabatically horizontally translated due to the canonical momentum of the field. Figure 3.2 displays a schematic of each of these regimes.

When considering multi-photon effects alone, an effective ionisation potential, Δ, can be defined to account for the change to the bandgap due to the momentum gained by the field. This is given by

$$\Delta = \frac{2\mathcal{E}_g}{\pi\gamma_1 E(\gamma_2)} \tag{3.12}$$

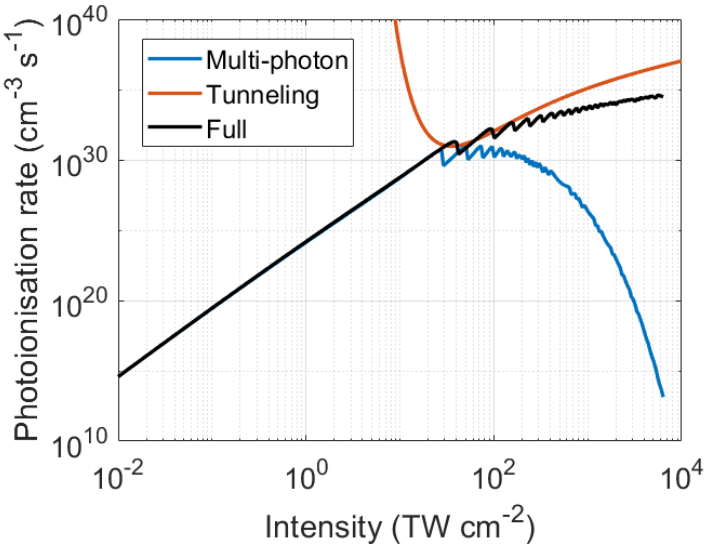


Figure 3.3 The rates of photo-ionisation calculated via the Keldysh equations as a function of laser intensity at for a bandgap of $\mathcal{E}_g = 7.1eV$. The full distribution follows the multi-photon distribution for low pulse energies with tunnelling taking precedence at $\sim$ 100 TW cm^{-2}.

And is substituted in place of $\mathcal{E}_g$ in the Keldysh equations. Inputting the direct bandgap of diamond (7.1 eV) and refractive index (2.4) of diamond into the full Keldysh equations and solving numerically achieves the relation with increasing intensity displayed in black in Figure 3.3. The rate calculated from the multi-photon approximation is shown in blue and the tunnelling approximation shown in red.

Keldysh theory gives a rate of photo-ionisation given an intensity value, a direct energy gap and monochromatic wavelength under the assumption of a linear dispersion relation. Inputting the direct bandgap of diamond, it predicts a power law at lower intensities representing 5 photon absorption. At intensities above $\sim$ 100 TW cm^{-2}, tunneling starts to dominate.

The Keldysh approach is vastly successful and is often applied when evaluating photoionisation in semiconductors under a strong electric field producing results which somewhat emulate experimental results for a wide range of materials. However, a number of issues arise due to some of the principle assumptions. The assumption

of monochromatic light becomes an issue for pulses shorter than $\sim$ 20 fs due to a significant spectral width allowing multi-photon processes involving photons of different energies. In addition, the assumption of a direct gap and linear dispersion means that the Keldysh solution is inaccurate for indirect semiconductors and inaccurate at calculating photoionisation away from the Γ point.

Since Keldysh evaluated the integral in equation 3.5, solutions have been found for simple geometric shaped band-structures including a cosine and parabolic band structure [184]. These lead to some severe changes the relationship with field intensity indicating that an accurate band-structure is vital for an accurate calculation of the photoionisation. Real world band-structures are more complex than the geometric shapes that have been evaluated analytically. A different approach is therefore needed to account for this complexity. Analytical solutions are yet to be found for real world and-structures however, Monte Carlo simulations across band-structures calculated via DFT have enabled progress in this field. Within diamond, Lagomarsino *et al.* employed a Monte Carlo technique including the band structure of diamond to track the multi-photon rates for a diamond crystal as a function of momentum [180]. They found a non-linearity that varied significantly with laser intensity for the total multi-photon rate in diamond over a 30 fs pulse, with a maximum non-linearity of order 9. The deviation from 5 photons to 9 photons is explained due to the momentum gain of the valence bands allowing photoionisation to take place away from the centre of the Brillouin zone where the bandgap is much larger. In addition they found that degeneracy in the valence bands at the Γ point led to a nonperturbative quantum interference causing higher harmonic generation within the polarisation density of the crystal, significantly increasing the photoionisation rate at k states further from the centre of the Brillouin zone [180].

3.3 Carrier dynamics

Once electrons have been promoted to the conduction band, they will not stay at the same energy states. Many scattering events can then take place which change the electron distribution. The electron-phonon coupling will cause the phonon subsystem to react to the non-equilibrium distribution of electrons generating longitudinal optical and acoustic phonons. Elastic electron-phonon scattering leads to momentum relaxation and will distribute the carriers more evenly across the Brillouin zone. Inelastic scattering leads to energy relaxation and will ultimately bring the carriers back towards equilibrium with the lattice. In addition, carrier-carrier scattering leads to a thermalisation of the electron gas such that it resembles an equilibrium distribution given by an electron temperature.

The system is driven such that it is out of equilibrium by the photoionisation, thus a non-equilibrium equation should be considered to model how the electron distribution changes over time and at $t = 0$ and $t = \infty$ the distribution should be given by Fermi-Dirac statistics. Non-equilibrium dynamics of a quantum gas can be described fully by the quantum Boltzmann equation where each individual collision is considered separately through collision integrals. The Boltzmann equation is a non-linear integro-differential equation which cannot be solved analytically in all but the simplest cases, however various approximations and numerical approaches have yielded accurate results given a set of assumptions.

The Boltzmann equation models the change to the distribution f as a sum of all processes in phase space.

$$\frac{df}{dt}(r,k,t) = \sum_i \left[\frac{\partial f}{\partial t}\right]_i (r,k,t) \tag{3.13}$$

Where there are separate terms for various scattering process and terms for electron gain and loss processes and diffusion. This approach yields 7 dimensions for each

function, 3 for space that are compactly written as r, 3 for momentum written as k and a dimension for time. This is often written as the following statement [185].

$$\frac{df}{dt} + \frac{\mathbf{p}}{m} \cdot \nabla f + \mathbf{F} \cdot \frac{df}{d\mathbf{p}} = \left(\frac{df}{dt}\right)_{coll} \tag{3.14}$$

Where collision terms are described on the right-hand side and the left-hand side describes changes in the size of the distribution, diffusion and the external forces, $\mathbf{F}$ acting on the particles. Collisions are evaluated through collision integrals considering energy and momentum conservation and the form of these integrals depends upon the nature of the scattering particles and the interaction between them. For example scattering between carriers occurs through the screened Coulomb interaction where the level of screening is determined by the Debye screening length in turn dependent upon parameters such as carrier density and temperature. The transfer of momentum between carriers is dependent upon the angle of collision and the collision integral integrates across this for scattering from all directions. These integrals are often impossible to solve analytically, therefore a number of simplifications have been developed that are accurate under certain conditions. The most developed of these simplifications are the collision time and the relaxation time approximation. These both act to model the effect of many collisions which are known to take the distribution towards equilibrium. The relaxation time, also known as the Bhatnagar, Gross and Krook approximation considers the difference between the current distribution and a Maxwellian equilibrium distribution, acting to bring the distribution towards equilibrium in a relaxation time [185].

$$\left(\frac{df}{dt}\right)_{coll} = \frac{(f_0 - f)}{\tau_{relax}} \tag{3.15}$$

Where f_0 is the equilibrium distribution and τ_{relax} is the relaxation time. Many collision terms are combined into a single term which assumes that they act to drive

the system towards an equilibrium state over a given relaxation time. This linearises the equation and distributions exponentially decay towards equilibrium given no driving terms. Given a steady state driving term such as a uniform electric field that varies slowly with time, the system can reach a quasi-equilibrium and the relaxation time approximation does a good job of describing this. However, given a dynamical situation such as the interaction with a pulse of light, this linearisation does not hold [185].

The collision time approximation likewise considers the average effect of collisions. Rather than integrating each collision integral separately as in the full Boltzmann equation, an assumption is made that the average collision randomises the motion of the scattering particles such that there is no "path memory". For this to work, constraints must be imposed such as the conservation of total momentum and energy for elastic collisions. Particles are deemed to scatter in an empirical time τ_{coll}. By making the assumption that the distribution is homogeneous across momentum, the dimensionality can be reduced from 7 to 5 [168]. This assumption is valid in the limit of many collisions as carriers exchange differing amounts of momentum with each other dependent upon the angle of collision, thus homogenise over time as collisions occur over a range of angles. In the collision time approximation, the average effect is considered equivalent to stating all angles occur equally [185]. This approach is often utilised in the Drude-Sommerfield model. Various scattering processes are characterised by an average collision time and the collision times add according to Matthiessen's rule. The model treats particles classically and describes how the energy of an average carrier at a particular energy state changes as a function of time. The exact form of the equation governing the change to the distribution is dependent upon the type of collision. For example, the change to the distribution given an elastic collision leads to a homogenisation of the momentum distribution whilst total energy is conserved. Therefore this can be modelled as $\frac{\partial f}{\partial \mathcal{E}} \frac{\partial \mathcal{E}}{\partial t}$ which can be written as

$$\frac{df}{dt}(\mathcal{E}) = \frac{1}{\tau_{coll}} \int_0^\infty \int_0^\infty \frac{f(\mathcal{E}_1) f(\mathcal{E}_2)}{\mathcal{E}_1 + \mathcal{E}_2} \, d\mathcal{E}_1 \, d\mathcal{E}_2 - f(\mathcal{E}) \text{ for } \mathcal{E} \leq \mathcal{E}_1 + \mathcal{E}_2 \tag{3.16}$$

Where τ_{coll} is the elastic collision time, $\mathcal{E}_1$ and $\mathcal{E}_2$ are dummy variables across energy to integrate over to calculate the change to the function f. This often gives a reasonably accurate description of average semiconductor dynamics but often gives inaccurate values for certain measurable variables such as conductivity. Including empirical parameters into the model can negate this [185].

A schematic showing different processes that can occur to a conduction band electron is shown in Figure 3.4. The diagram shows a direct gap material with linear dispersion for clarity. Diamond being an indirect semiconductor requires momentum transfer or larger energies for transitions across the gap. Each of these processes can be calculated via a scattering term in the Boltzmann equation. Often these processes are modelled independently considering the total population density but not considering energy dynamics within the conduction and valence bands [134][165] [171] [186] [187] [188] [189]. This simplification vastly reduces the complexity of the equations and can relatively accurately predict the density of carriers that are generated but also can lead to over or underestimates of the relative importance of particular processes [168].

These scattering terms can be modelled through density and energy conservation arguments utilising a collision time approximation given empirical input parameters for scattering times. A more in-depth discussion on this will be covered in chapter five. For electrons, f is given by $\frac{\rho_e(\mathcal{E})}{n}$ where n is the total number of conduction band electrons, however the normalisation can be neglected by carefully adding the total density into the denominators of scattering terms.

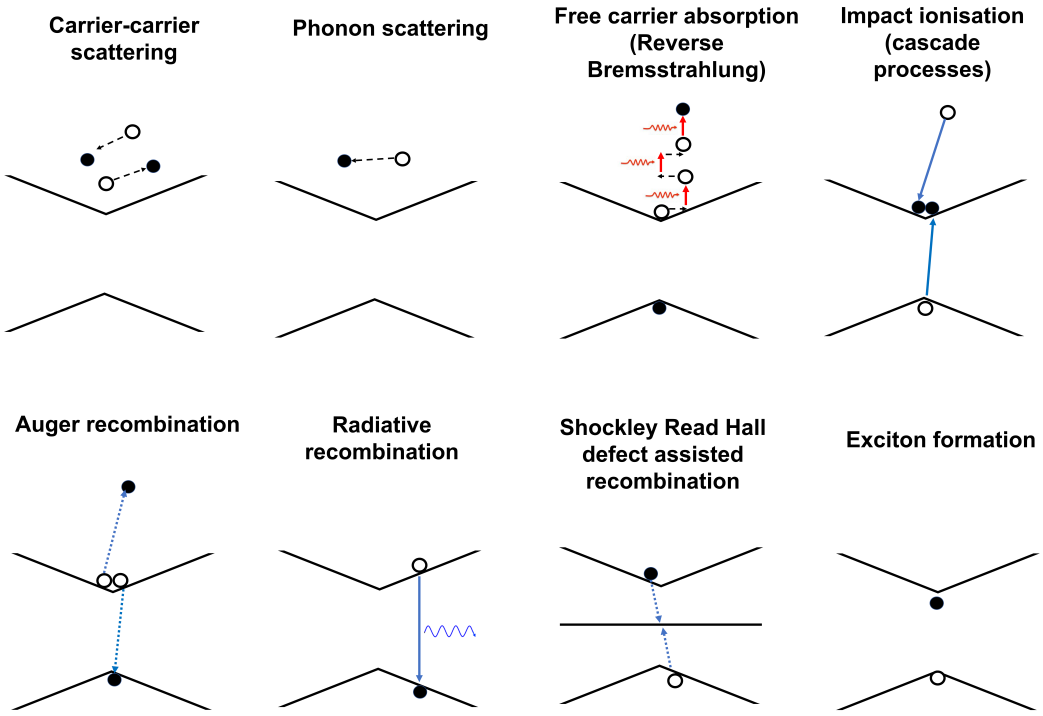


Figure 3.4 The different scattering processes that can occur to a conduction band electron during and after the laser pulse shown for a direct gap linearly dispersing semiconductor. Scattering can occur with other carriers and phonons leading to momentum transfer or with photons leading to energy gain. Excess energy can be passed to valence electrons leading to impact ionisation. The reverse process (Auger recombination) can occur at high densities. Other potential recombination routes are direct via emission of photons or defect assisted through the Shockley-Read-Hall effect. Electrons can also bind to valence band holes forming excitonic states.

3.4 Energy relaxation into the lattice and defect formation

The relaxation of energy from photoionised carriers is often neglected in discussions of atomic scale defect formation in diamond with the majority of work being done on calculating the photoionisation process. This approach is often successful at modelling the total carrier generation from an ultra-fast laser pulse and gives accurate results for high energy laser damage where Coulomb explosions drive non-thermal melting processes and are dependent only upon the carrier density generated. For lower energy mechanisms, the carriers must deposit their energy more locally into the lattice and the energy relaxation must be looked at in more detail. During the cooling of the carrier plasma generated by the pulse, dense excitonic states, electron-hole plasmas and electron-hole liquids can form [167] [177]. Studies of these states are often undertaken at low temperatures to allow for long lasting states and a high chance of recording luminescence from the radiative recombination of such states. Within diamond at least, the link between excitonic states and atomic scale defect formation has not been studied, however in a number of other wide bandgap materials it has been shown that atomic scale defects form from the self trapping of dense excitonic states [176].

Excitonic self trapping in semiconductors occurs due to coupling between excitonic states and the surrounding phonon bath. The exciton provides a local deformation potential to the lattice with the strength of this deformation potential being dependent upon the coupling strength and the localisation of the exciton. Given a highly localised state, the deformation potential can become strong enough that a significant potential well forms prohibiting motion of the exciton. The deformation potential alters the equilibrium positions of nearby nuclei and if strong enough can push nuclei to interstitial sites. This is the key mechanism behind Frenkel defect formation in SiO_2 from pulsed laser irradiation [176].

A rudimentary theoretical approach to the generation of Frenkel defects in diamond is to assume that the number of defects created scales as the volume of the diamond in which the energy density is above a threshold for defect creation [159]. In this approach, the mechanisms behind defect formation are not considered, rather, there is an assumption that the number formed scales linearly with the energy density once above a threshold. Here the assumption was that the point-spread-function of the pulsed laser in diamond can be approximated as a cylindrically symmetric Gaussian beam distribution. Under the assumption that the number of defects created scales as the volume in which the energy density is above a threshold for defect creation, the number of defects would scale as

$$N_D \propto V_{>th} \rightarrow N_D = A\sqrt{\frac{E_P}{E_{P_{th}}} - 1} \cdot ln\left(\frac{E_P}{E_{P_{th}}}\right) \tag{3.17}$$

where $V_{>th}$ is the volume in which the energy density is above the threshold for defect creation, A is a proportionality constant, E_P is the laser pulse energy and $E_{P_{th}}$ refers to the threshold pulse energy for defect creation [159]. The fluorescence intensity should be proportional to this under the assumption that each vacancy radiates a uniform amount. Chen explained this as the expected behaviour if photoionisation processes underwent tunnelling but found that vacancy generation does not follow this approach with a rudimentary least squares analysis only fitting over a very small region of parameter space. The reasoning for this is likely that at the high intensities required for the Keldysh parameter to be less than one, significant plasma generation will occur and modify the focal volume such that it is no longer accurately described by a Gaussian beam. In addition, this approach does not give any insight as to the underlying physics of the defect formation, rather, gives a top down approach to attempting to describe the laser mechanism.

3.5 Spin-photon behaviour

For many quantum applications, engineered colour centres need to be single centres rather than ensembles. Single colour centres have a fluorescence cycle from an electron and will give out single photons at a rate given by the lifetime of the excited state in a Fock state. Emission through the ZPL is entangled to the spin of the centre and can allow for the quantum information to be transported to another site allowing communication between multiple qubits. If the photon emission is split between two photodiodes in a Hanbury Brown and Twiss interferometer, a single photon cannot travel down both paths and be detected by both photodiodes. Therefore, a single photon emitter such as an NV^- centre will produce an anti-bunching dip in a histogram of the time delay between photon detection events on each photodiode at zero time delay and is an efficient test to make sure that the engineered site contains a single photon emitter. The width of the dip gives information about the lifetime of the emitter. Coherent light such as that from a laser will produce no anti-bunching as photon events are random. The NV^- centre is a three-level system with a meta-stable state of a longer lifetime. Pumping the emitter under higher excitation power leads to further excitation into the meta-stable state produce bunching effects around the anti-bunching dip.

In general, the auto-correlation function for a Hanbury Brown and Twiss (HBT) interferometer is given by [190]

$$g^{(2)}(\tau) = \frac{\langle I(t)I(t+\tau)\rangle}{\langle I(t)\rangle\langle I(t+\tau)\rangle} \tag{3.18}$$

where the brackets $\langle ...\rangle$ denote the time averaged value. The value at zero time delay is denoted $g^{(2)}(0)$ and the value of this should equal

$$g^{(2)}(0) = \frac{\langle N(N-1)\rangle}{\langle N\rangle^2} \tag{3.19}$$

where N is the Fock state of the light. A perfect single photon emitter should therefore give a $g^{(2)}(0)$ of zero, however, real world emitters are imperfect, perhaps due to non-radiative pathways for relaxation from the excited state from imperfections in the crystal. In addition, background fluorescence from the sample such as the Raman signal and potentially reflected excitation light also couple into the interferometer adding noise which will increase the baseline from zero. For a sufficiently large signal to noise ratio, the baseline should be close to zero. If a site contains two single photon emitters (i.e. two NV centres), $g^{(2)}(0)$ should be greater than or equal to 0.5. The general solution for the second order autocorrelation function for the three-level system depends upon the excited state and meta-stable state lifetimes, τ_1 and τ_2 and is given by [47]

$$g^{(2)}(\tau) = 1 + c_1 e^{-\frac{\tau}{t_1}} + c_2 e^{-\frac{\tau}{t_2}} \tag{3.20}$$

where c_1 and c_2 are scaling constants. Background signals can be measured by recording the fluorescence signal from the bulk diamond misaligned from the laser writing site, which can then used to calculate the baseline for the autocorrelation data-set according to the function

$$a = 1 - \big(\frac{S}{S+B}\big)^2 \tag{3.21}$$

[9] where S and B are the photon count rates for the emitter and background fluorescence, respectively. The raw data-sets, $g^{(2)}_{raw}(\tau)$ can then corrected for this baseline according to

$$g^{(2)}(\tau) = \frac{g^{(2)}_{raw}(\tau) - a}{1 - a} \tag{3.22}$$

3.6 Summary

In this chapter some of the ideas behind pulsed laser interaction with semiconductors have been addressed starting with the light matter interactions and delving into carrier dynamics and the Boltzmann equation. In addition, quantum statistics of luminescence has been outlined, giving a method by which the Fock state of light can be determined and an ability to determine whether a particular luminescent site within diamond is a single or multiple colour centre.

Chapter Four

Experimental Methods

4.1 Introduction

The experimental procedures within this thesis can be broadly broken down into two constituents, laser fabrication of atomic scale defects within bulk diamond and characterisation of these defects. This chapter will outline the experimental apparatus and methodology used for both of these procedures.

4.2 Laser writing

To generate the colour centres within the material, direct laser writing was used. Moreover, two regimes were used, single pulse and multiple pulse direct laser writing both within the bulk material.

4.2.1 Single pulse laser writing

Initially single pulse laser writing was undertaken using a regeneratively amplified Ti:Sapphire laser (Spectra Physics Mai Tai and Spectra Physics Solstice amplifier). A schematic of the laser writing apparatus is shown in Figure 4.1. The Mai Tai Ti:Sapphire generates an 80 MHz train of 100 fs pulses which are input into the Solstice

regenerative amplifier undergoing chirped pulse amplification (CPA) to achieve intense ultra-short pulses that are above the breakdown threshold of the laser cavity. The amplified pulses are output at a 1 kHz repetition rate. A trigger enabled the emission of single pulses at a time or a steady stream of pulses at 1kHz. The output laser pulses were initially expanded onto a liquid crystal phase-only spatial light modulator (SLM) (Hamamatsu X10468-02) for iterative aberration control, and then imaged in a 4f system onto the back aperture of a $\times$60 1.4NA oil immersion objective lens (Olympus PlanApo). The beam was expanded such that the intensity profile at the back aperture was a top hat function. Diamond samples were mounted on precision translation air bearing sample stages (Aerotech x-y: ABL10100; z: ANT95-3-V) which provide movements in all three directions. A LED transmission microscope was built alongside and imaged onto a CCD to monitor the sample during the laser processing. A linear polariser was placed in the beam path for polarisation control.

The pulse energy was controlled through rotation of a half-wavelength wave-plate and measured either via a 50:50 beamsplitter into a power meter for which a multiplication factor was then applied to calculate the power at the back focal plane of the objective lens. In order to obtain an accurate pulse energy measurement, the average power was detected from a stream of many pulses and dividing by the repetition rate gave an average energy per pulse. Single pulses were directed at the sample in regular arrays which could be programmed into G code allowing automated motion of the stages and gating of the laser. At low pulse energies, the laser written sites are invisible in transmission microscopy, therefore heavy graphitic tracks that scatter light and thus appear dark in transmission were also written at the same depth for orientation. These were given some asymmetry to allow easy orientation accounting for potential imaging imperfections such as mirroring or rotation. An example of a transmission image of graphitic wires and point orientation marks surrounding laser written NV centres at the same depth can be seen in Figure 4.2. Graphitic tracks

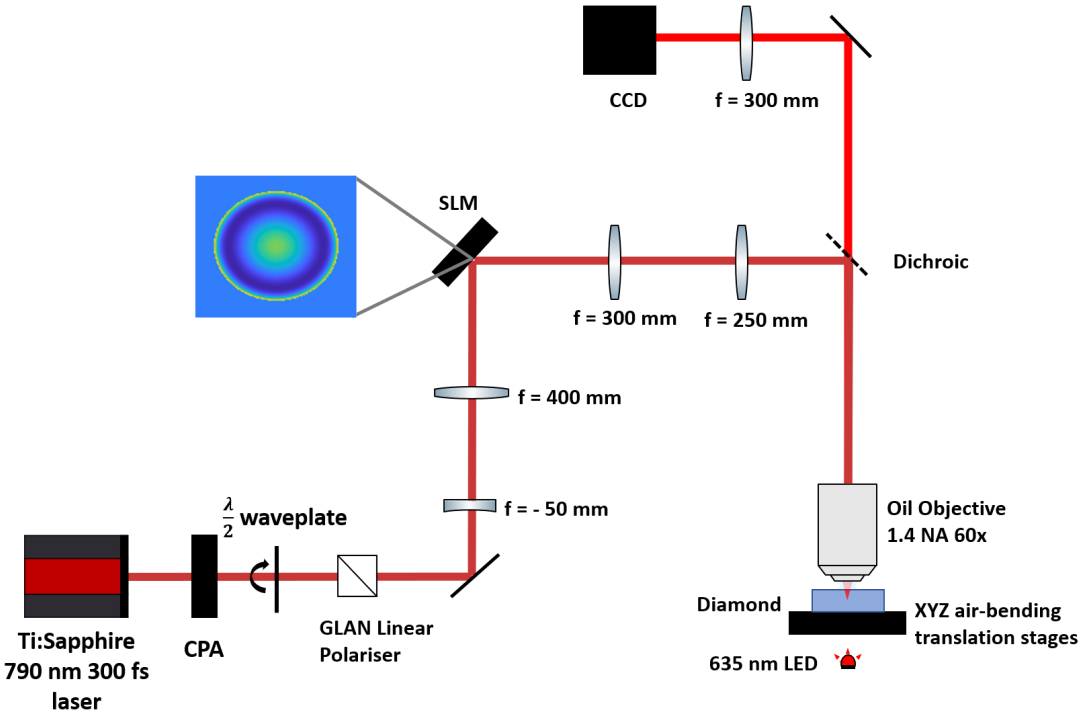


Figure 4.1 Schematic of the Ti:Sapphire laser processing optical set-up. Pulses of a Gaussian temporal shape are focused into a diamond through a 60× oil immersion objective lens. Pre-focusing the pulses are reflected off a spatial light modulator for adaptive aberration control [7].

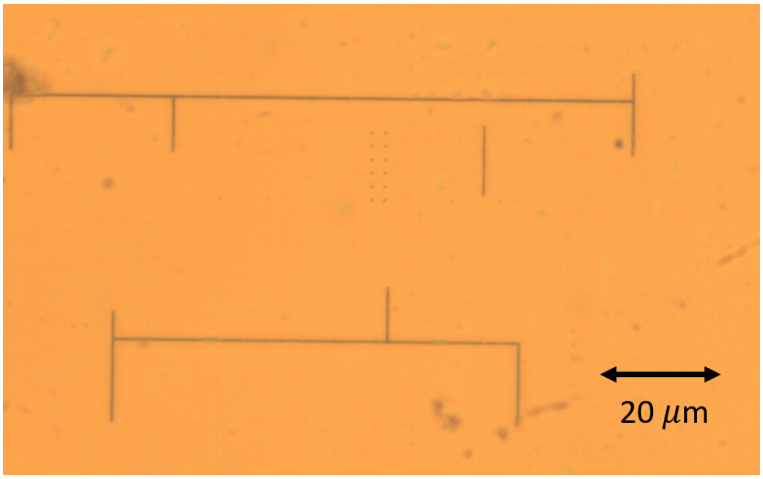


Figure 4.2 A transmission microscope image of graphitic orientation markers surrounding an array of single NV centres. The graphitic markers scatter light allowing for easy orientation. The microscope should be aligned to these markers, and following fluorescence imaging and optimisation, single colour centres become visible in fluorescence microscopy.

fluoresce brightly over a broad range of wavelengths so are easy to see in fluorescence microscopes.

Through tuning the compression of the pulse as it passes through the chirped pulse amplifier, the pulse duration can be varied experimentally between $\sim$ 120 fs and 1 ps. Pulse durations were then measured using spectral phase interferometry for direct electric-field reconstruction (SPIDER). Sampling of the optical intensity detected from many pulses at different delay times through varying the path length of the interferometer gives a time-dependent map of the pulse duration. The pulse duration at focus will be slightly longer than that measured by the SPIDER due to dispersion passing through the pre-sample optics and into focus due to the spectral bandwidth. The duration of the laser pulse has a significant affect on the size of the fabrication region. For nanosecond or longer pulses, thermal processes dominate the damage generation mechanism because the pulse duration is comparable with the characteristics time of thermal diffusion (ns) [134]. The diffused heat will melt the material and generate damage outside the focal volume of laser. In contrast, the

duration of ultra-fast lasers (with picosecond or femtosecond pulse length) is shorter than the timescale of thermal diffusion. Thus, most of the pulse energy is delivered to the focal volume before it can diffuse away as heat, leading to a limit of the feature size smaller than the focal volume of the pulsed laser beam.

Single pulse laser writing was also conducted with a different laser (Pharos Light Conversion Ytterbium femtosecond laser) in order to study the wavelength dependence of the laser processing. This laser outputs 1030 nm 170 fs light at 1 MHz repetition rate which was frequency doubled by second harmonic generation to 515 nm. The optical path from this laser was similar to the Ti:Sapphire, however a different SLM was used, tailored to green light rather than infrared, the same model but with a differing dielectric coating (Hamamatsu X10468-02). Single pulses could be selected or a train of pulses at 1 MHz and pulse energy was controlled through rotation of a half wavelength wave-plate.

4.2.2 Laser annealing with fluorescence feedback apparatus

For the work in chapter eight of this thesis, it was desirable to monitor the fluorescence from a location on the sample at the same time as processing using the Ti:Sapphire writing apparatus. A confocal microscope was added to the optical apparatus from Figure 4.1. This presents a challenge as not only do the excitation and collection regions need to be confocal, they also need to be confocal with the focal volume of the writing laser. Figure 4.3 shows the optical apparatus for laser processing with fluorescence feedback.

The laser processing was performed using the same Spectra Physics Solstice Ti:Sapphire and multiple pulsing was carried out at a 1 kHz pulse repetition rate. Fluorescence feedback was measured using a custom-built beam scanning confocal photoluminescence microscope, integrated into the laser writing system. A dichroic

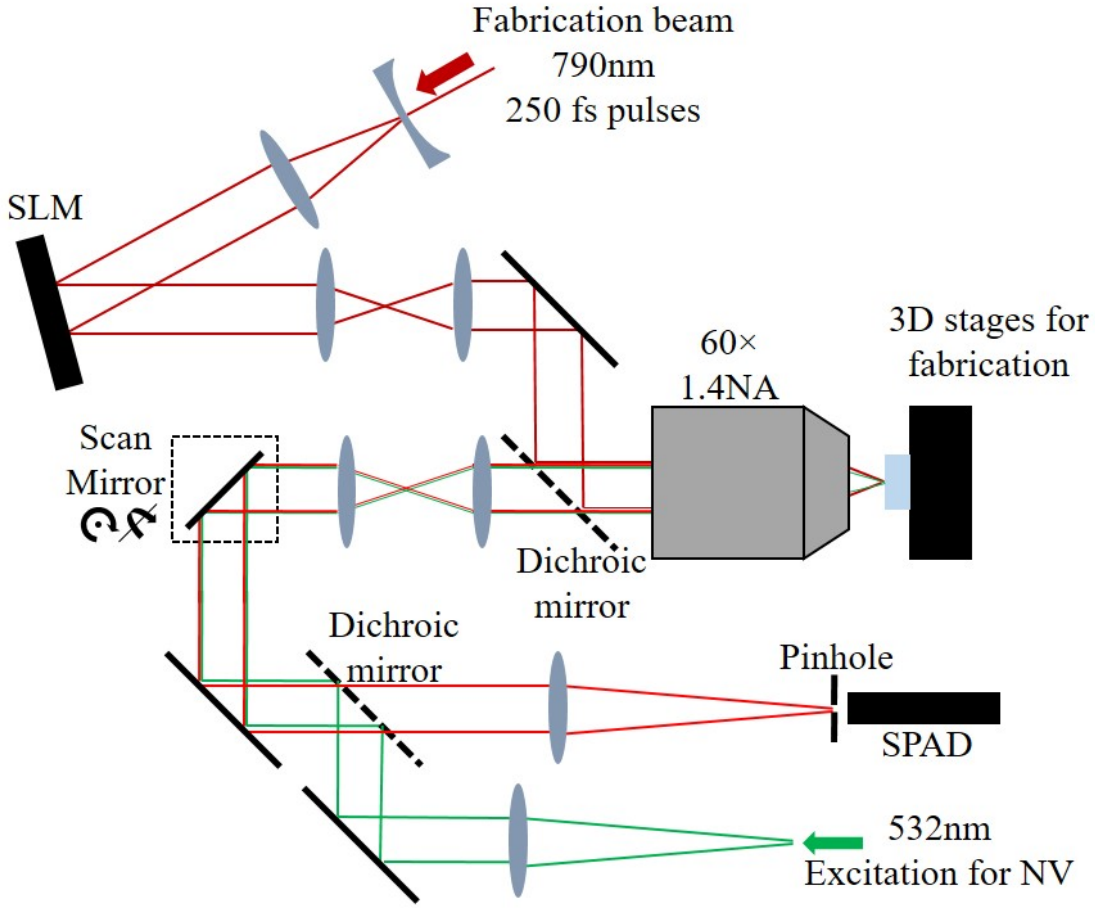


Figure 4.3 Experimental system for laser writing of defects inside a crystal with fluorescence feedback [9].

mirror coupled excitation light at a wavelength of 532 nm and power 2 mW into the same objective lens as used for the laser processing. Photoluminescence was collected in epiconfiguration and detected after a confocal pinhole using a silicon single photon avalanche diode (Excelitas) at a sampling frequency of 1 kHz. A bandpass spectral filter transmitting wavelengths between 650 and 750 nm isolated fluorescence from negatively charged NV centres, cutting out light from both the fabrication laser and Raman signal associated with the confocal excitation. The confocal microscope was aligned to the laser writing system such that it only detected fluorescence generated from within the focal region of the fabrication laser.

Initially, a single "seed" pulse of a high enough energy to generate a small number of vacancies within the focal region was used. The pulse energy for this was chosen to be just below the visibility threshold for GR1 fluorescence with an oil immersion lens which has previously been shown to produce the best quality laser written NV centres [6]. Following this, a train of lower energy "diffusion pulses" were used at a 1 kHz repetition rate. Processing was continued until the fluorescent signal corresponding to a single NV centre was detected, at which time the 1 kHz pulse train was ceased. The methodology behind this experiment will be discussed in more detail in chapter eight.

4.2.3 Iterative aberration control

The effect of the laser processing on the diamond lattice is very sensitive to the optical intensity at a particular location. Minimising the size of the focal volume is therefore critical in attaining precision and control over the fabrication process. In order to minimise the fabrication volume, a high numerical aperture objective lens is used. However, focusing the laser deep into the diamond material with a high numerical aperture introduces a significant spherical aberration due to the mismatch of the refractive indices between the immersion oil and diamond, causing strong refraction

at the interface. This spherical aberration plays havoc with the focal volume and vastly reduces the focal intensity. In addition, any misalignment in the optical path is amplified by the high numerical aperture and difference in refractive index leading to potentially large astigmatisms and coma aberrations. These effects have a profound effect and reduce the intensity such that the laser can no longer modify the material. Advances in adaptive optics have allowed for the correction of these aberrations by applying the conjugate phase shifts to the beam pre-focusing [191]. An arbitrary aberration can be described by a superposition of any set of orthogonal polynomials on the unit disk. The set of Zernike polynomials are commonly used. Modelling focal aberrations will be described in more detail in the following chapter when modelling the focal volume. Experimentally a phase pattern consisting of a superposition of Zernike modes was applied to the spatial light modulator in the beam path and this was iteratively altered such that the energy to generate visible graphitic marks in the diamond bulk was minimised. This can be described mathematically by

$$\phi_{SLM}(r,\theta) = \sum_{n,m} C_n^m Z_n^m(r,\theta) \tag{4.1}$$

Where C is a scaling factor, Z is the Zernike polynomial and m and n are indices to indicate which polynomial is being addressed. Later in this thesis, these polynomials are addressed in both Cartesian coordinates and polar coordinates dependent upon whichever makes the mathematics easier. The dominant aberration to control for is the spherical aberration due to the large refractive index mismatch at the oil/diamond interface. Through this iterative aberration correction technique, diffraction limited laser writing has achieved generation of graphitic tracks and generation of vacancy-interstitial pairs at depths down to 220 μm, limited only by the working distance of the lens [29]. Near surface writing is difficult as the laser intensity becomes high enough to boil the immersion oil which adds random aberrations and stops the fabrication

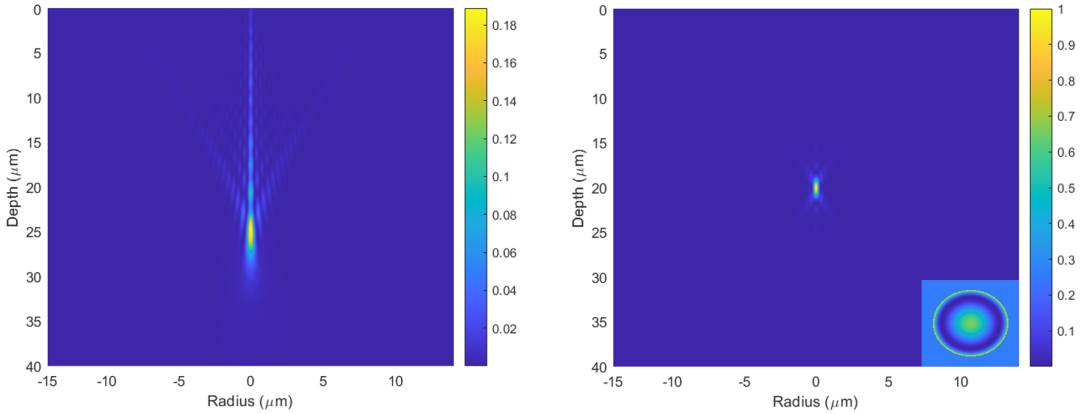


Figure 4.4 The effect of the aberration correction on the laser focal intensity distribution when focused through the interface between the immersion oil and diamond to a depth of 20 μm. The left graph shows that the focus is significantly elongated in z axis by a spherical aberration without aberration correction. The corrected focus, shown on the right, has a much smaller focal volume allowing for much higher focal intensities. The phase distribution of the laser beam pre-focus is modified by the liquid crystal phase-only spatial light modulator (inset) to correct the aberrations in the system and those introduced by focusing into the diamond.

process. Due to this reason, direct laser writing is limited to depths deeper than $\sim$ 2 μm. It is estimated using this iterative aberration control method, Strehl ratios nearing unity can be achieved.

Figure 4.4 displays a time-integrated rz slice of the focal volume from a focus at 20 μm with no correction applied (spherically aberrated) and a perfectly corrected focal volume where the laser is irradiated from above. The inset of the right-hand figure shows the phase pattern applied to achieve the correction. The modelling required to achieve this diagram is discussed in chapter five.

The effect of aberration correction is twofold. It minimises the size of the focal volume and therefore increases the focal intensity. In the figure the only aberration shown is spherical due to the mismatch of refractive indices, this is the dominant correction needed, other aberrations could potentially need correcting due to misalignment of

the optical path or imperfections of the focusing optics.

The laser interaction with the material is highly non-linear with regards to the focal intensity. Therefore the true interaction region is much smaller than the focal volume which is great for positional accuracy but also amplifies the need for aberration control as a small reduction in focal intensity is amplified significantly from the non-linear interaction.

4.3 Photoluminescence imaging and spectroscopy

After processing, a home-built beam-scanning room-temperature confocal fluorescence microscope with an excitation of 532 nm at 1.1 mW was used for fluorescence imaging of laser written features. Fluorescence was collected between 580 nm and 900 nm through the use of long-pass and bandpass filters. A schematic of the microscope used is shown in Figure 4.5. The diamond samples were placed onto XY translation stage (Thorlabs) and an oil immersion objective placed in a z translation stage (Thorlabs) to allow for focusing into the material. A Laser Quantum Gem 532 nm laser of maximum power 300 mW was directed through polarisation optics (either linear or circularly polarised dependent upon the type of characterisation desired) and directed towards the region of interest and directed to locations of interest with a fast steering mirror. The photoluminescence was then directed to a single photon photodiode (Excelitas) for photon counting or toward a Spectrograph (Princeton Instruments Spectograph 2500i) fitted with a back-illuminated CCD camera (Princeton Spec-10 100B) to characterise a point of interest through spectroscopy. In addition, a 50:50 fibre beam splitter could be added to split the fluorescent signal to perform auto-correlation measurements. The sample was illuminated from below with a white light LED for transmission microscopy and imaged onto a CCD (Thorlabs) to allow for accurate sample positioning to regions of interest. Laser written colour centres are invisible

in the LED transmission microscope, however, the graphitic tracks and heavy laser damage scatter the light and appear dark in transmission and were used for orientation. Initially, the graphitic marks were bought into focus within the transmission microscope, following which the sample was imaged in photoluminescence where the graphitic tracks appear bright. Tweaking the direction of the beam to optimise the photon count rate from the graphitic tracks followed by another fluorescence image allowed for the fluorescence for the lower energy laser written point defects to be seen. Iterating through this optimisation procedure allowed for high-quality fluorescence images to be taken.

4.3.1 Auto-correlation measurements

To determine the photon statistics of fluorescent laser written sites, auto-correlation measurements were performed through Hanbury, Brown and Twiss interferometry. To split the photoluminescence emission evenly between two single photon avalanche photodiodes, a 1×2 50:50 fibre splitter (Thorlabs) was used. Upon detection of a photon on photodiode A, a timer started which stopped following detection of a photon on the second channel at $t = \tau$. A histogram of correlation intensity was built up as the function of the delay time τ between the photon detection events allowing for determination of whether the emission displays single photon statistics, coherence or thermal light. The position of the excitation beam was re-optimised every five minutes using a peak finding algorithm applied to the scanning mirror whereby the beam was deflected and a 1 μm^2 image around the region was taken following which a 2D Gaussian was fit and the beam centred to the peak of the Gaussian. During this, the fluorescence would be collected from areas surrounding the emitter which would add to the baseline, however, this process allows for compensation of sample drift and for data-sets to be collected over periods of many hours. The signal to noise ratio was high

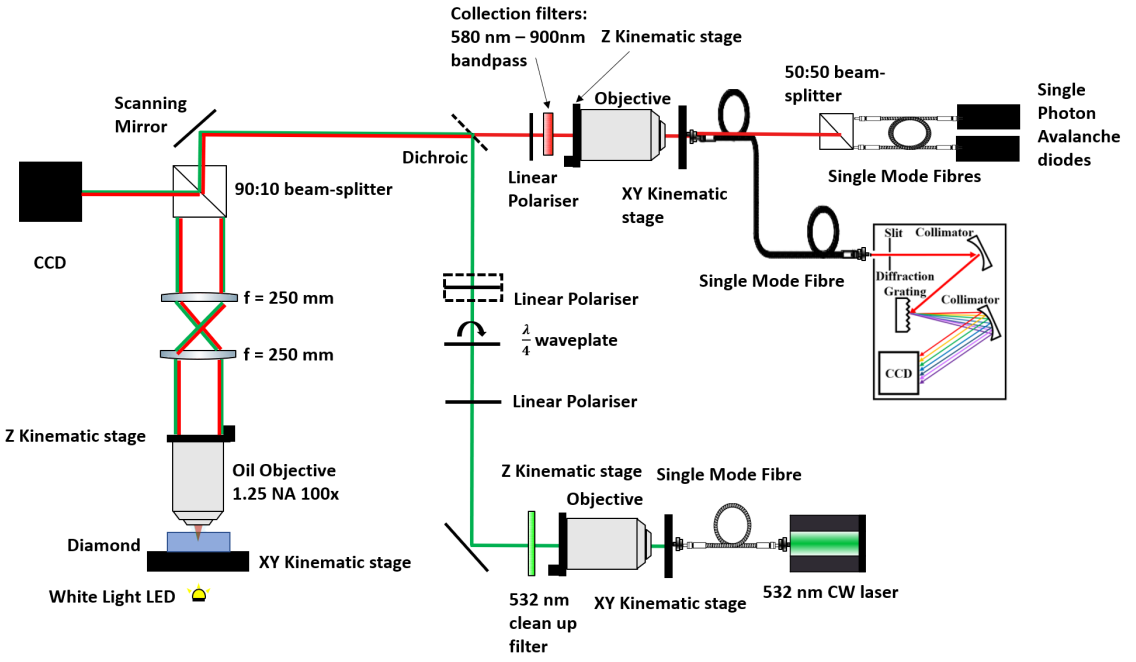


Figure 4.5 Schematic set-up of the home-built room-temperature confocal microscope apparatus. The 532 nm continuous wave (CW) GEM laser is either linearly or circularly polarised depending on experimental requirements. The dichroic of 550 nm allows the excitation and photoluminescence to be separated and the oil immersion objective lens has an NA of 1.25 and a magnification of 100. Coupling of the emission into a single mode fibre allows for fluorescence to be directed either towards one or two single photon avalanche diodes for imaging and autocorrelation measurements or towards a spectrograph for spectroscopy. When performing spectroscopy, the filters in the collection path are removed. The linear polariser in the dashed rectangle after the quarter waveplate is used only to characterise if the beam is linearly or circularly polarised and removed for normal use.

enough that the addition to the baseline could be considered negligible. Excitation of the emitters during these experiments was undertaken below the saturation point of the emitter to minimise any bunching around the anti-bunching behaviour which can make normalisation difficult.

4.3.2 Polarisation measurements

Polarisation measurements were undertaken during photoluminescence imaging through rotation of a linear polariser within the collection path. The excitation path of the confocal microscope was altered to produce a circularly polarised excitation beam such that all orientations are excited equally. Circular polarisation can be achieved by placing a combination of linear polarisers and wave-plates within the excitation beam. Initially placing two linear polarisers orthogonal to each other in the excitation beam cuts out all light. Adding a quarter wavelength wave-plate between the two at a 45° angle causes the beam to become circularly polarised. The second linear polariser can then be removed. A high degree of polarisability indicates that the axis of the dipole of the emitter lies in the plane of the objective lens whilst a low degree of polarisability indicates that the emitter is out of the plane or the presence of multiple dipoles.

4.3.3 Spin coherence

Hahn echo measurements were performed to determine electron spin coherence times of single emitters. A biasing DC magnetic field was applied parallel to the axis of an NV centre to split the $m_s = \pm 1$ levels in the electronic ground state. The 532 nm laser was coupled through an Isomet 1250C acousto-optic modulator to produce pulsed light. This was operated with a custom driver to eliminate the leakage of green laser light. The sample was mounted onto a co-planar waveguide board, and microwaves were delivered to the sample using a 20 μm copper wire over the surface.

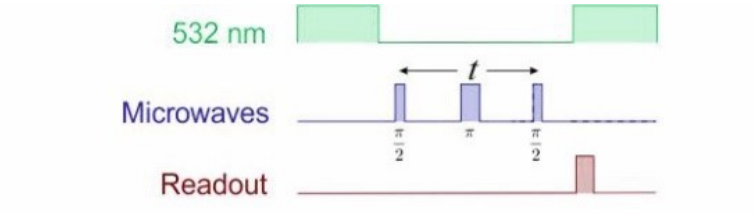


Figure 4.6 Pulse sequence for Hahn echo measurements used to record spin coherence from laser-processed NV centres [9].

A Keysight N5172B source was switched using a Swabian Instruments PulseStreamer and subsequently amplified with a MiniCircuits ZHL-16W-43-S+ amplifier. The spin echo signal was fitted to a stretched exponential decay function

$$f(t) = e^{-\frac{t}{T_2}^{\alpha}} \tag{4.2}$$

where t is the total free-precession time, T_2 is the electron spin-coherence time, and α is a free-parameter related to the dynamics of the spin environment. Figure 4.6 displays a schematic of the pulse sequence used to perform Hahn echo measurements.

4.3.4 Photoluminescence excitation spectroscopy

Photoluminescence excitation (PLE) spectroscopy was used to probe the ZPL's of laser written colour centres at a temperature of $T = 4.2$ K. To perform low temperature spectroscopy and PLE measurements, the room-temperature confocal microscope was modified such that the sample was placed in a liquid helium bath cryostat. Here the steering mirror and dichroic mirror were placed on-top of the helium dewar and the sample, objective lens and telecentric 4f system placed inside the vacuum pumped tube and cooled to 4 K. PLE requires that the excitation is resonant with the ZPL. For PLE of SiV^- ensembles, a home built self seeded external cavity tapered amplifier was scanned through resonance with the SiV^- ZPL at a wavelength of 737 nm, and the exact wavelength was measured directly using a wavemeter (High Finesse WSU-30).

Fluorescence was collected from the phonon side-band of the emitter and the data interpolated to determine the ZPL linewidth.

4.3.5 Electron paramagnetic resonance spectroscopy

In order to determine the concentrations of non-fluorescent spin defects within the bulk material used in chapter seven, electron paramagnetic resonance (EPR) spectroscopy was undertaken. Here, a biasing magnetic field was applied to the material causing a Zeeman splitting of paramagnetic defects. The splitting of zero field degenerate states when a magnetic field is applied is given by

$$\Delta E = g_e \mu_B B \tag{4.3}$$

where g_e is the Lande g-factor, μ_B is the magnetic moment of the state and B is applied field. Microwave light was then incident upon the Zeeman split states and the level of absorption measured. This was repeated for a range of magnetic field strengths. If the microwave frequency is resonant with ΔE, a photon is absorbed causing a peak in the absorption spectrum against magnetic field strength. Taking the first derivative of the absorption spectrum allows for measurement of how absorption changes. Hyper-fine coupling to nuclear spin states leads to multiple absorption peaks in quick succession. Analysis of the locations of peaks within the spectrum allows for identification of the concentrations of various spin defects throughout the material.

4.4 Summary

This chapter has outlined the apparatus used for the experimental studies outlined later in this thesis. The various laser writing apparatus for single and multiple pulse processing has been fully described and the method for minimising the focal aberrations in the laser writing apparatus has been presented. The apparatus for

monitoring fluorescence during processing as an optical feedback mechanism has also been discussed, and will be discussed in further detail in chapter eight.

The experimental apparatus of the custom-built confocal microscope which was used to investigate the optical properties of the laser-generated sites has been presented. In addition, an overview of the experimental methods of photoluminescence spectroscopy, autocorrelation measurements, polarisation, spin control, photoluminescence excitation and electron paramagnetic resonance spectroscopy have been discussed.

Much of the equipment and microscopes that were used for laser writing and characterisation were pre-existing and just needed various amounts of alignment. The fluorescence confocal microscope that was added to the laser writing system for fluorescence feedback was built by myself alongside Laiyi Weng, Patrick Salter and Sam Johnson. A more recent upgrade to this that is integrated directly into the laser writing set-up rather than as an temporary addition has been built by Andrew Kirkpatrick.

Chapter Five

Non-Linearity of the Laser Writing Process - Theoretical

5.1 Introduction

Understanding the mechanisms by which the laser interacts with the diamond during laser processing is critical for effective engineering of devices. However, they are not yet fully understood with most current descriptions able to explain part of the process and provide only qualitative comparison to experiment. Much of the work on laser fabrication has studied effects for pulses which produce dielectric breakdown and significant restructuring of the material. The threshold for dielectric breakdown is often treated as a Heaviside step-function with regards to pulse energy above which structural modification occurs and below which the energy dissipates thermally throughout the material producing little structural change. For diamond, this is given by the photo-excited carrier density reaching $\sim 9\%$ of the atomic density. Some qualitative analysis has linked colour centre formation to lower energy laser pulses previously but as yet there are no quantitative studies of centre formation in agreement with experiment.

The transition to breakdown is unlikely to be a perfect step-function and much

of the interesting physics lies in this transition region. It is likely that the formation of individual lattice vacancies occurs at pulse energies just below the threshold. The goal of the next two chapters is to develop a quantitative understanding of Frenkel defect generation in diamond by comparing the results of a coupled rate equation model with experiments performed using laser processing. It will be shown that defect generation via the non-radiative recombination of multi-excitonic states predicts a defect distribution in agreement with experiment.

5.2 Partial differential equation model

Non-equilibrium dynamics of a quantum gas can be described fully by a Boltzmann equation [185]. The Boltzmann equation models the change to a distribution f as a sum of all processes that act upon that distribution in phase space.

$$\frac{df}{dt}(r,k,t) = \sum_i \left[\frac{\partial f}{\partial t}\right]_i (r,k,t) \tag{5.1}$$

Interactions are evaluated through collision integrals considering energy and momentum conservation and the form of these integrals depends upon the nature of the interaction. Many of these integrals are analytically unsolvable, however, collision time approximations allow for a simplification where processes are characterised by a characteristic timescale. The disadvantage of this approach is that it neglects nuances of individual interactions, showing the average effect given a large number of interactions. In addition, the collision time parameter has to be determined empirically rather than evolving naturally from the equations.

Despite this, a Boltzmann equation approach with collision time approximations for various terms was utilised with interaction times determined empirically from a range of sources. To simplify the analysis, an assumption that the carriers are homogeneous with respect to momenta was made meaning that all the terms of the

Boltzmann equation can be constructed purely in terms of energy, space and time. While this is untrue for short timescales (Photoionisation produces a non-uniform momentum distribution [180]), carrier scattering quickly homogenises the momentum distribution across the Brillouin zone after a few scattering events such that this approximation gives reasonably accurate results. A set of 8 coupled equations was developed keeping track of the light intensity, carrier and excitonic densities, lattice temperature, and defect density as a function of space, time and energy. These will be outlined throughout this chapter and a summary showing all terms in all the equations can be found in Appendix A. Results of the numerical simulations and the comparisons to experiments are shown in chapter 6.

5.2.1 Modelling the laser pulse

In order to model how the laser interacts with the semiconductor, one must define the region of space and time to simulate over and then find an analytical expression for the laser intensity across that region, $I(x, y, z, t)$.

Pulsed laser light propagates according to a inhomogeneous wave equation, however this can be simplified using the slow varying envelope approximation to a homogeneous wave equation and multiplied by an envelope of the pulse width. This approximation will be valid for pulses in which the pulse duration is of order several oscillatory periods (i.e. the spectral bandwidth is narrow). The homogeneous wave equation is given by [192]

$$\left(\nabla^2 - \frac{n}{c^2}\frac{\partial^2}{\partial t^2}\right) E(x, y, z, t) = 0; \tag{5.2}$$

Through separation of variables, this can be split into two separate equations, one dependent upon time and one dependent upon space and these are equal which is only true if they are equal to a constant.

$$E(x, y, z, t) = \psi(x, y, z)T(t); \tag{5.3}$$

$$\frac{\nabla^2\psi(x, y, z)}{\psi(x, y, z)} = -k^2 \tag{5.4}$$

$$\frac{n}{c^2T(t)}\frac{\partial^2 T(t)}{\partial t^2} = -k^2 \tag{5.5}$$

In reality, the wave equation is inhomogeneous and only approximately homogeneous, therefore this constant will be a spread of wave-vectors corresponding to the spectral width. The time-independent equation is known as the Helmholtz equation and a general solution can be calculated considering an weighted superposition of plane waves.

$$\psi(x, y, z) = \int_{-\infty}^{\infty}\int_{-\infty}^{\infty} \Psi_0(k_x, k_y)e^{-i(k_x x + k_y y)}e^{i(z-z_0)\sqrt{k^2-k_x^2-k_y^2}}\, dk_x\, dk_y \tag{5.6}$$

[192] where z_0 is axial position of the focal plane and k_x and k_y are coordinates regarding the conjugate plane of the focal plane. This approach can be thought of as taking the Fourier transform of the wave-vectors and applying various phase shifts to find the electric field distribution at different depths. In the normalised case, the intensity distribution is simply the square of the electric field distribution. This approach is a scalar approximation of the vectorial modelling required to obtain the true electric field in the focus of a high numerical aperture objective lens, however, the difference in the solutions for the two approaches is negligible for all but the highest numerical apertures.

In the experimental apparatus, the laser pulse is expanded such that the electric field distribution at the back focal plane of the objective lens is a top-hat function.

$$I(k_x, k_y)_{BFP} = \begin{cases} 1 & \text{if } k_x^2 + k_y^2 \leq R_{pupil} \\ 0 & \text{otherwise} \end{cases} \tag{5.7}$$

Where R_{pupil} is the pupil radius. Taking the Fourier transform gives the in-plane intensity distribution at the focal depth and adding phase shifts allows for calculation of the intensity distribution at various depths and with various aberrations where $k(x, y) = \phi(x, y)$.

$$I_V(x, y, z) = \int_{-\infty}^{\infty} \int_{-\infty}^{\infty} I(k_x, k_y)_{BFP} e^{i\phi(x,y)(z-z_0)} e^{-i(k_x x + k_y y)} \, dk_x \, dk_y \tag{5.8}$$

The large change in refractive index by focusing into a diamond produces a large spherical aberration. Misalignment of optics can also introduce further aberrations such as coma or astigmatism. ϕ is then given by a superposition of all aberrations and any phase pattern that is added to an optical element pre-focusing. With a spatial light modulator (SLM) as the optical element, the total phase is expressed as

$$\phi(x, y) = \phi_{Ab}(x, y) + \phi_{SLM}(x, y) \tag{5.9}$$

Assuming the optics are perfectly aligned, the general aberration given no adaptive optical element includes defocus and spherical aberration. This is given by

$$\phi_{Ab}(x, y) = -I(k_x, k_y)_{BFP} \cdot \frac{2\pi}{\lambda} \cdot NA \cdot \left[\sqrt{\left(\frac{n_2}{NA} \right)^2 - r^2} - \sqrt{\left(\frac{n_1}{NA} \right)^2 - r^2} \right] \tag{5.10}$$

Where $r = \sqrt{x^2 + y^2}$, n_1 is the refractive index above the surface of the diamond, n_2 is the refractive index of the diamond and NA is the numerical aperture of the lens. An oil immersion objective lens was used for processing with the immersion oil having a refractive index of $n_1 = 1.51$ and the diamond, a refractive index of $n_2 = 2.4$. It is useful to be able to separate out the phase aberration into individual components

such that individual aberrations can be addressed with the SLM [191]. This can be separated into defocus,

$$\phi_{Defocus}(x,y) = I(k_x,k_y)_{BFP} \cdot \frac{2\pi}{\lambda} \cdot NA \cdot \sqrt{\left(\frac{n_2}{NA}\right)^2 - r^2} \tag{5.11}$$

and the defocus-free spherical aberration.

$$\phi_{Sph}(x,y) = \phi_{Ab} - \frac{\langle \phi'_{Ab}, \phi'_{Defocus} \rangle}{\langle \phi'_{Defocus}, \phi'_{Defocus} \rangle} \phi_{Defocus} \tag{5.12}$$

Where $\langle , \rangle$ denotes the inner product and the $'$ notation represents the aberrations with subtracted mean values [191].

$$\langle \phi'_{Ab}, \phi'_{Defocus} \rangle = \frac{1}{N} \Sigma_r \phi'_{Ab} \phi'_{Defocus} \tag{5.13}$$

$$\phi'_{Ab}(x,y) = \phi_{Ab}(x,y) - \frac{1}{N} \Sigma_r \phi'_{Ab} \tag{5.14}$$

$$\phi'_{Sph}(x,y) = \phi_{Sph}(x,y) - \frac{1}{N} \Sigma_r \phi'_{Sph} \tag{5.15}$$

The phase term in equations 5.8 and 5.9 can now be rewritten as

$$\phi(x,y) = \phi_{Sph}(x,y) + \phi_{Defocus}(x,y) + \phi_{SLM}(x,y) \tag{5.16}$$

For perfect spherical aberration correction, the conjugate of ϕ_{Sph} is applied to the SLM.

$$\phi_{SLM}(x,y) = -\phi_{Sph}(x,y) \tag{5.17}$$

In practice, other aberrations such as coma and astigmatism are applied to compensate for misalignment of the laser writing system through thermal drift. The

functional form of these can be added to the phase factor to calculate how the distribution changes.

$$\phi_{SLM}(r,\theta) = \sum_{n,m} C_n^m Z_n^m(r,\theta) \tag{5.18}$$

Separating the equations in this form is convoluted but is useful from an experimental viewpoint to calculate the phase to apply to an adaptive optical element. It is also useful for simulation work as it allows modelling of laser fabrication from an aberrated focus.

The above equations give the functional form of the focal volume with no time dependence, the Helmholtz solution. The general solution for the time dependence of the intensity of light coming from the laser can similarly be found through a weighted superposition of plane waves in frequency space. However rather than integrating across the spectral width, one can consider the time dependence separately. The range of frequencies that make up the pulse superpose to make an ultra-short pulse with a phase that shows the colour evolution through time. For a sufficiently small spectral width, this can be approximated by a Gaussian function of the appropriate width where the colour evolution does not change throughout the pulse. The time dependence can be modelled as a Gaussian multiplied by a sinusoid of the laser frequency, ω_0.

$$I_t(t) = \mathrm{Re}\left[\exp\left[\frac{-(t-\mu)^2}{2\sigma^2} \right] e^{i\omega_0 t} \right]^2 \tag{5.19}$$

where sigma is defined such that the full-width-half-maximum (FWHM) of the square of the Gaussian is equal to the pulse duration. The full normalised intensity distribution $I(x,y,z,t)$ arises by multiplying together the spatial and time dependences, however as there is some spectral width to the pulse, there will be a spatial variation to the time dependence, hence the homogeneous wave equation approach breaks down. The spatial variation of the time dependence manifests as a varying phase

velocity which can be found through multiplying the wave vector by the speed of propagation to form the dispersion relation $\omega = \frac{ck}{n}$. As before, $k(x, y) = \phi(x, y)$ and an additional term denoting the spatial variation of the time dependence can be calculated by comparing ω with ω_0 and calculating the difference in the number of oscillatory periods as a function of position. In addition, the pulse propagates at a speed of $\frac{c}{n}$ and this propagation accumulates phase which is included in the addition.

$$I_0(x, y, z, t) = I_V(x, y, z) \cdot I_t\left(t + \frac{\omega_0 n^2(z_0 - z)}{c^2\phi(x, y)}\right) \tag{5.20}$$

Given no non-spherical aberrations, the equations can be simplified by the azimuthal symmetry into $I(r, z, t)$. Rotating by 2π about the depth axis gives the full distribution. Figure 5.1a shows how the simulated intensity distribution changes as a function of time and Figure 5.1b shows an r,z slice of the distribution at the peak time given no plasma effects and no spherical aberrations. This is plotted with the laser pulse coming from the left-hand side. The banding that can be seen corresponds to the individual wave peaks of the sinusoid showing points of equal time.

Multiplying by a scaling factor allows simulation of laser pulses of different pulse energies.

$$\text{Pulse Energy (J)} = 2\pi \int_0^\infty \int_0^\infty I_0(r, z_0, t)\ r\ dr\ dt \tag{5.21}$$

The differential of the intensity function with respect to time gives the first term in the first of the set of coupled non-linear differential equations.

$$\frac{dI}{dt}(r, z, t) = \left[\frac{\partial I}{\partial t}\right]_0 + \left[\frac{\partial I}{\partial t}\right]_{eh} \tag{5.22}$$

where

$$\left[\frac{\partial I}{\partial t}\right]_0 (r, z, t) = \frac{I_0(r, z, t + dt) - I_0(r, z, t)}{dt} \tag{5.23}$$

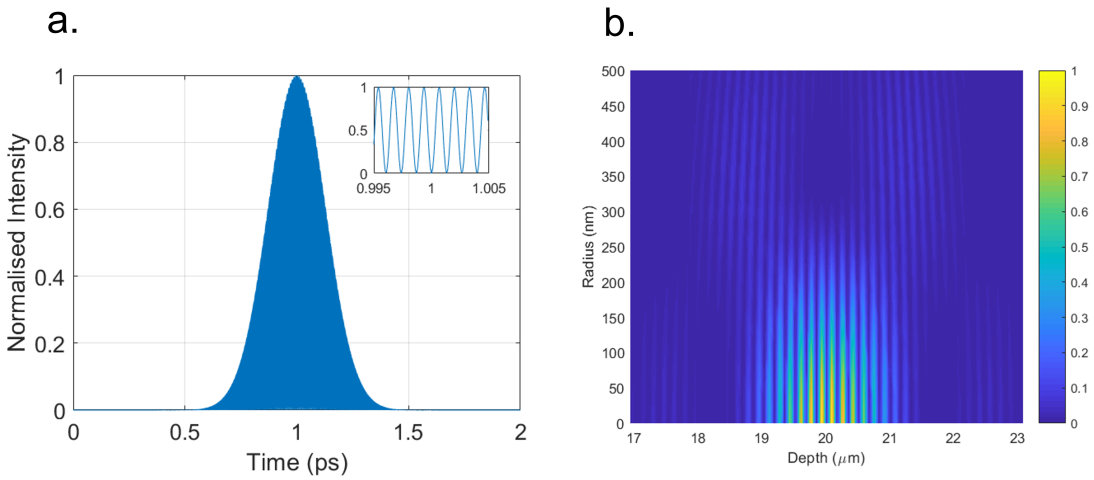


Figure 5.1 a. A normalised intensity distribution as a function of time with a pulse duration of 300 fs. Inset shows a zoom in, indicating the sinusoidal nature of the oscillation. b. A normalised intensity distribution as a function of r and z with a focal depth at 20 um and perfect aberration correction at peak time.

The second term in equation 5.22 regards the changes to this distribution due to the absorption of photons by electrons within the material and the changes to how the pulse propagates due to the generated electron plasma. This is non-trivial to calculate as several processes occur that affect this term, namely photoionisation, free carrier absorption, plasma resonance, beam attenuation, self focusing and filamentation [171] [193]. In order to calculate this, one must model the light-matter interactions and how they change the electron distribution within the material addressed in section 5.2.2. The efficient generation of high densities of carriers leads to a metallic behaviour of the crystal [168] [171] [194]. This changes the focusing of the incoming light leading to absorption at shallower depths and attenuation of the beam. The spatial variation of the refractive index, which becomes complex, also leads to self focusing and strong absorption with the consequence that breakdown can occur at lower pulse energies than one would expect. In addition, the changing refractive index affects the rates of photoionisation and scattering processes. At very high densities, the carrier plasma

causes reflection of the incoming beam [195]. The feedback loop between carrier generation and the intensity distribution means that the intensity and carrier density must be calculated in parallel.

The plasma frequency, ω_p of the carriers is given by

$$\omega_p(r,z,t) = \sqrt{\frac{(\rho_e(r,z,t) + \rho_h(r,z,t)) \cdot e^2}{m\epsilon_0}} \tag{5.24}$$

where ρ_e and ρ_h are electron and hole densities respectively. The real and imaginary parts of the relative dielectric constant, ϵ_r are then given by

$$\mathrm{Re}[\epsilon_r(r,z,t)] = \frac{\omega_p(r,z,t)^2\tau_{coll}^2}{1+(\omega_0^2\tau_{coll}^2)},\ \mathrm{Im}[\epsilon_r(r,z,t)] = \frac{\omega_p(r,z,t)^2\tau_{coll}}{\omega_0(1+(\omega_0^2\tau_{coll}^2))} \tag{5.25}$$

τ_{coll} is the average collision time and the relative change to the real, n_r and imaginary parts, κ_r of the refractive index are given by

$$n_r(r,z,t) = \sqrt{\mathrm{Re}[\epsilon_r(r,z,t)]^2 \cdot \mathrm{Im}[\epsilon_r(r,z,t)]^2} + \frac{\mathrm{Re}[\epsilon_r(r,z,t)]}{2} \tag{5.26}$$

$$\kappa_r(r,z,t) = \sqrt{\mathrm{Re}[\epsilon_r(r,z,t)]^2 \cdot \mathrm{Im}[\epsilon_r(r,z,t)]^2} - \frac{\mathrm{Re}[\epsilon_r(r,z,t)]}{2} \tag{5.27}$$

n_r is multiplied by the standard $n_2 = 2.4$ refractive index of diamond to get the real part of the total refractive index. This manifests as a spatially dependent phase shift leading to self focusing and filamentation and also ties into the photoionisation equations and scattering functions outlined later, hence drastically change how the laser interacts with the matter.

Substituting $i\kappa_r$ into the wave equation leads to an exponentially decaying wave with the attenuation coefficient becoming large as the plasma frequency approaches that of the laser frequency. As photoionisation and scattering functions are highly dependent upon laser intensity, this also drastically affects the dynamics of the system.

In addition, at any change in refractive index, part of the wave will become reflected. This interferes with the incoming pulse and alters how the light focuses.

These effects can be summarised in a single term, the second term in equation 5.22 which is added to the intensity distribution calculated given no interaction. Due to the reflection interfering with the incoming light, it is necessary to calculate the change to the electric field distribution and convert into an intensity distribution to find this term.

$$\left[\frac{\partial I}{\partial t}\right]_{eh}(r,z,t) = \left(\left[\frac{\partial E}{\partial t}\right]_{eh}(r,z,t)\right)^2 \cdot \frac{cn_2\epsilon_0}{2} \tag{5.28}$$

where

$$\begin{aligned}\left[\frac{\partial E}{\partial t}(r,z,t)\right]_{eh} = E_0\left(r,z,t+\int_0^z \frac{\Delta\phi(r,Z,t)(Z-z)n_2}{c}\,dZ\right)\left(\prod_0^z \exp\left[-\alpha(r,Z,t)\frac{\omega_0}{c}\right]\right) \\ -\int_0^\infty\int_z^\infty R(r,z,t)E\left(X,Z,t-\frac{n_2n_r(r,z,t)\sqrt{(r-X)^2+(z-Z)^2}}{c}\right) \\ \left(\frac{dr^2}{(r-X)^2+(z-Z)^2}\right)dXdZ - E_0(r,z,t)\end{aligned} \tag{5.29}$$

Z and X are dummy variables to integrate over across depth and radius, $\Delta\phi$ is the path dependent phase shift

$$\Delta\phi(r,z,t) = \frac{\omega_0(n_2-(n_2n_r(r,z,t)))}{c\phi(r)} \tag{5.30}$$

α is the attenuation coefficient

$$\alpha(r,z,t) = \kappa_r\left(r+\int_0^z \Delta\phi(r,z,t)(Z-z)\,dZ, z, t+\int_0^z \frac{\Delta\phi(r,z,t)(Z-z)n_2}{c}\,dZ\right) \tag{5.31}$$

and R is the reflectively coefficient.

$$R(r,z,t) = \left|\frac{n_2n_r(r,z,t)-n_2n_r(r,z-dz,t)}{n_2n_r(r,z,t)+n_2n_r(r,z-dz,t)}\right|^2 \tag{5.32}$$

The first term in equation 5.29 describes the change to the electric field due to the phase shift induced to the propagating wave by an altered refractive index, the exponential describes the attenuation of the beam and the product of these exponential terms denotes that the exponential reduction in intensity at some depth Z compared with the no plasma case is dependent upon all of the pixels that the light has passed through until that point. Fresnel's equations are used to calculate the proportion of the light that is reflected with a simplification that the reflected proportion is calculated for normal incidence. The reflected wave is then calculated through Huygens' principle as a weighted superposition of spherical wave-fronts. This is subtracted as the wave undergoes a π phase rotation upon reflection. The reflection term is negligible for all but the highest electron densities where the real part of the effective refractive index becomes large.

The plasma effect is non-uniform across the profile of the beam such that the centre can become reflective with whilst other radii could still be transparent or strongly absorbing. This leads to a significant shift in the absorption profile at very high intensities. As the shift in refractive index is non-uniform across the radius of the beam, it also causes self focusing effects and filamentation. These two processes compete against each other leading to a non-trivial intensity and carrier distribution to calculate.

Figure 5.2 compares the spatial intensity distribution at the peak intensity when the effect of carriers is considered for three different pulse energies. Figure a is below the threshold in which the plasma has much effect, a small attenuation can be seen just below the focal depth. In contrast, high energy pulses produce a significant enough density of carriers that the effect on the incoming beam is drastic and around the threshold attenuation starts to dominate. The reflected wave also interferes with the incoming wave leading to variation just above focus and the increase in phase velocity at the absorbing region can clearly be seen to bend the rays. These plots are plotted

across a full diameter rather than radius as it is clearer to see the shifts in phase and spatial dependence of the attenuation. The attenuation is made clearer by plotting the term in the second bracket of equation 5.29 on its own shown in Figure 5.2d.

As well as changing the shape of the intensity distribution, plasma effects quench the pulse such that the relationship between pulse energy and peak intensity is no longer linear. In fact, for pulses significantly greater than the threshold, the plasma is generated at shallower depths, before the pulse reaches the focal depth, such that the highest intensities are not reached due to attenuation of the beam.

Figure 5.3a and b shows the time dependence of the intensity distribution at the central pixel of focus after plasma effects are taken into consideration for a pulse above breakdown threshold and for a pulse just below. The second of these corresponds to the pulse energy required to produce a single Frenkel defect given the hypothesis outlined in the rest of this chapter. Plasma effects start to distort the distribution once the focal intensity reaches ~ 40 TWcm^{-2} and leads to attenuation of the beam. The effect of this is emphasised in these figures as the centre of the focal volume which decays quickly as the attenuation leads to the peak intensity moving to shallower depths. Plotting the maximum intensity within the focal volume as a function of time for the same two cases leads to the distributions seen in Figure 5.3 c and d. For high pulse energies, the shift to shallower depths is accentuated by the fact that the attenuation occurs before the mid-point of the Gaussian in time when the pulse is still sweeping into the focal region and the majority of the energy is above focus.

5.2.2 Free carrier distributions

The second rate equation concerns the density of electrons, ρ_e within the conduction band as a function of space, time and energy.

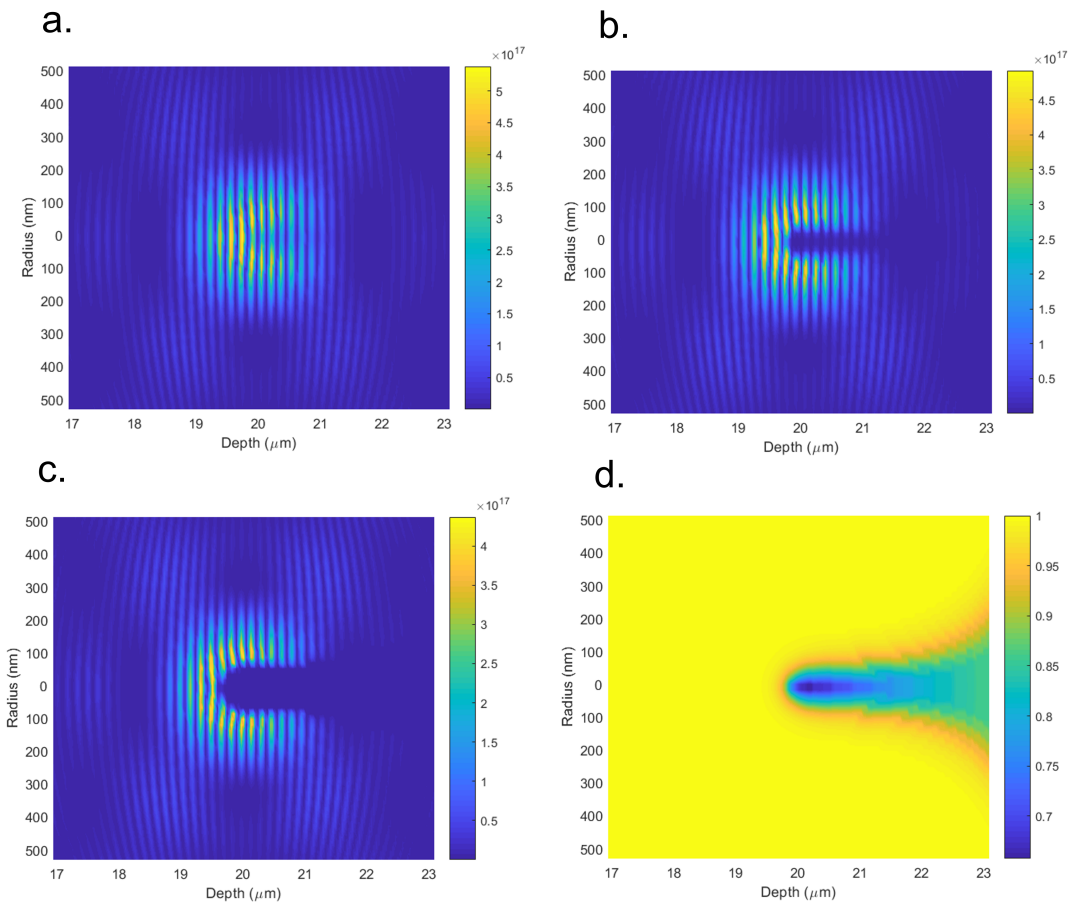


Figure 5.2 The spatial dependence of the light intensity at the peak time considering a. A low energy pulse where the carrier generation has only a small effect b. A pulse at which the threshold where plasma effects start to dominate c. A high energy pulse where carrier generation leads to significant attenuation of the beam. d. The reduction in focal intensity as a function of position showing the attenuation of the incoming light due to the plasma. Here the product of the exponential functions is shown.

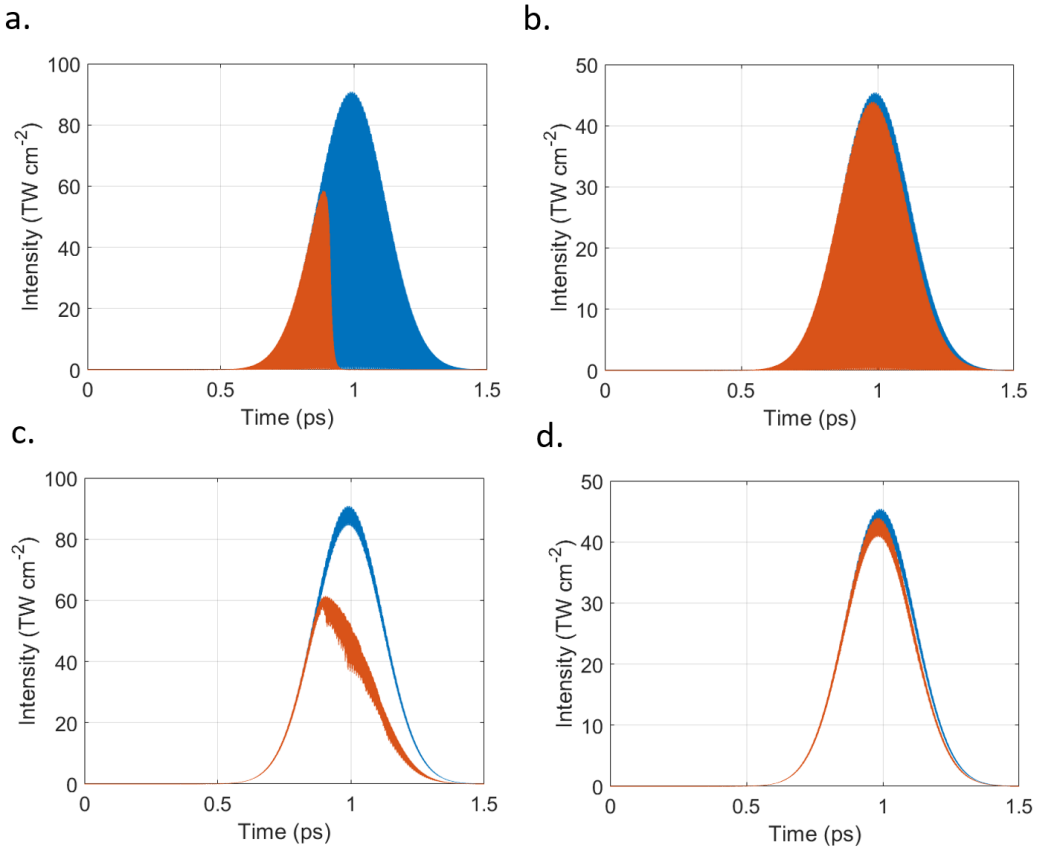


Figure 5.3 Change to the time variation of the intensity distribution when plasma effects are considered. a. The time component to the intensity for a high energy pulse above breakdown at the pixel corresponding to the centre of focus. b. The time component for a lower energy pulse at the central pixel. c. The maximum intensity within the simulated region as a function of time for a high energy pulse. d. The maximum intensity within the simulated region for a lower energy pulse.

$$\frac{d\rho_e}{dt}(r,z,t,\mathcal{E}) = \left[\frac{\partial\rho_e}{\partial t}\right]_{PI} + \left[\frac{\partial\rho_e}{\partial t}\right]_{epp} + \left[\frac{\partial\rho_e}{\partial t}\right]_{e-ph} + \left[\frac{\partial\rho_e}{\partial t}\right]_{cc} + \left[\frac{\partial\rho_e}{\partial t}\right]_{Casc} - \left[\frac{\partial\rho_e}{\partial t}\right]_{Auger} - \left[\frac{\partial\rho_e}{\partial t}\right]_{Rad} + \left[\frac{\partial\rho_e}{\partial t}\right]_{Diff} - \left[\frac{\partial\rho_e}{\partial t}\right]_{Exc} + \left[\frac{\partial\rho_e}{\partial t}\right]_{Exc_{Diss}} \tag{5.33}$$

The first term within this equation corresponds to the photoionisation of electrons across the bandgap. The second, third and fourth terms refer to energy change processes through collisions via free carrier absorption through electron-phonon-photon collisions, electron-phonon coupling and carrier-carrier scattering respectively. The fifth term refers to cascade or avalanche multiplication of the carrier density and the sixth and seventh terms regard losses to the electron density through Auger and radiative recombination processes. The eighth term regards diffusion of electrons and the latter two terms regard the formation and dissociation of excitons. An additional term including Shockley-Read-Hall recombination should also be included, however for this analysis, I make the assumption that the crystal is intrinsic and this term is negligible.

Through charge neutrality, the density of holes, ρ_h generated through photoionisation is equal to the electron generation such that an identical equation exists for holes as for electrons although the rates of various scattering terms are different.

$$\frac{d\rho_h}{dt}(r,z,t,\mathcal{E}) = \left[\frac{\partial\rho_h}{\partial t}\right]_{PI} + \left[\frac{\partial\rho_h}{\partial t}\right]_{hpp} + \left[\left[\frac{\partial\rho_e}{\partial t}\right]_{h-ph} + \left[\frac{\partial\rho_h}{\partial t}\right]_{cc} + \left[\frac{\partial\rho_h}{\partial t}\right]_{Casc} - \left[\frac{\partial\rho_h}{\partial t}\right]_{Auger} - \left[\frac{\partial\rho_h}{\partial t}\right]_{Rad} + \left[\frac{\partial\rho_h}{\partial t}\right]_{Diff} - \left[\frac{\partial\rho_h}{\partial t}\right]_{Exc} + \left[\frac{\partial\rho_h}{\partial t}\right]_{Exc_{Diss}} \tag{5.34}$$

Equations governing each of the terms in these equations will be outlined in the following subsections.

Modified Photoionisation

Photoionisation (PI) is often modelled using the Keldysh formula outlined in chapter three. However, this is inaccurate for diamond as the Keldysh approach assumes a perfectly linear dispersion and a direct gap. The true band-structure of diamond is more complicated, it is an indirect semiconductor and the bands have curvature. To find the true rate of photoionisation, the integral in equation 3.5 needs to be evaluated over the Brillouin zone of the crystal. For all but the most simple band-structures, this becomes analytically impossible such that a Monte Carlo approach is needed for accurate photoionisation rates [180]. A full Monte Carlo simulation of the Brillouin zone is computationally expensive therefore, in order to model other effects at the same time, a simplification must be found which keeps the accuracy but is easier to calculate.

Rather than solving the integral, by making use of points of high symmetry, here it is shown that a hybrid approach between standard Keldysh theory and the Monte Carlo approach allows for accurate photoionisation rates to be calculated.

The band structure of diamond was calculated using DFT via CASTEP [196]. Simulations were of a 3×3×3 supercell of diamond, in order to reduce the effects of the periodic boundary conditions, and employed the PBE exchange-correlation functional [197]. The simulation used the formation energy of the NV^0 centre as a convergence parameter to determine an appropriate Monkhorst-Pack grid spacing and plane wave basis size. This was calculated by Andrew Kirkpatrick and is shown in Figure 5.4.

When the light interacts with the material, it perturbs the wavefunctions, electrons oscillate with the field obtaining canonical momentum which alters the positions of the bands within the Brillouin zone, hence the photoionisation behaviour. The electron momentum gained by the field is given by the magnitude of the vector potential multiplied by the charge of the electron [183].

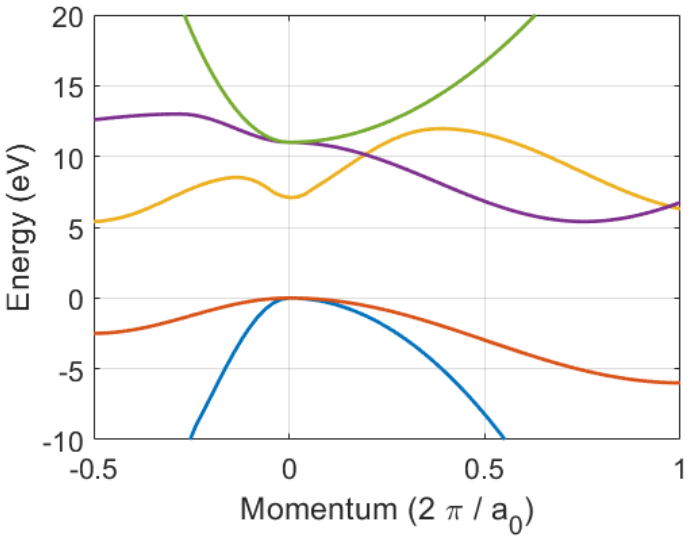


Figure 5.4 A simplified diagram of the band-structure of diamond showing the closest bands to the bandgap calculated via CaStep. a_0 is the bulk lattice constant for diamond at 3.57 Å.

$$p(t) = \hbar k(t) = p_0 + e|A(t)| \tag{5.35}$$

Where the vector potential, A has no spatial dependence in the long wavelength approximation and hence its relation to the electric field reduces to.

$$A(t) = -\int E(t)\ dt \tag{5.36}$$

The momentum gained by the field corresponds to an adiabatic horizontal shift of the valence bands in k space whilst leaving the conduction bands stationary allowing for photoionisation to take place away from the Γ point.

For a small enough region of momentum space, and given an empirical ionisation potential, Keldysh theory should give a good approximation. Therefore after applying a horizontal shift to the valence bands by the appropriate canonical momentum, conventional Keldysh theory (equations 3.6 to 3.11) can be utilised replacing the effective ionisation potential with the energy gap between the maximum point of the

shifted bands to the unshifted conduction bands at the same momentum state. By defining the polarisation density empirically to include the non-perturbative higher harmonic generation an effective instantaneous intensity felt by an electron including this harmonic generation can be calculated and used in place of the variable for intensity in the Keldysh equations.

$$P(t) = (n^2 - 1)E_0 \exp\left[\frac{(t-\mu)^2}{(2\sigma)^2}\right]\Big(\exp[i\omega t] + B\exp[3i\omega t] + C\exp[5i\omega t]\Big) \tag{5.37}$$

$$D = \epsilon_0 E + P \tag{5.38}$$

$$I_{eff}(t) = Re\big[E(t)\cdot D(t)\big]\frac{c}{n} \tag{5.39}$$

Whilst this approach neglects some possible transitions, it captures most as the probability for transition is greatest at the point corresponding to the shifted gamma point due to the high density of states from high curvature of the bands. Iterating this for the entire duration of the pulse reveals close agreement with the Monte Carlo approach as can be see by comparing Figure 5.5 with Figure 11 of [180].

This agrees well with Lagomarsino's work suggesting that the approximation of only using points of high symmetry and using standard Keldysh theory for different energy gaps is a valid simplification. The energy distribution of conduction band states due to photoionisation correspond to near delta functions at the energy corresponding to the band locations at the momenta at which transition occurred. In the approximation calculated above, these will be pure delta functions.

Figure 5.6 shows the energy distributions following 300 fs pulses of differing intensities assuming that the carriers do not change energy state post photoionisation. At low intensities, transitions occur fairly close to the centre of the Brillouin zone yielding a sharp peak centred $\sim$ 1.5 eV above the conduction band edge, however

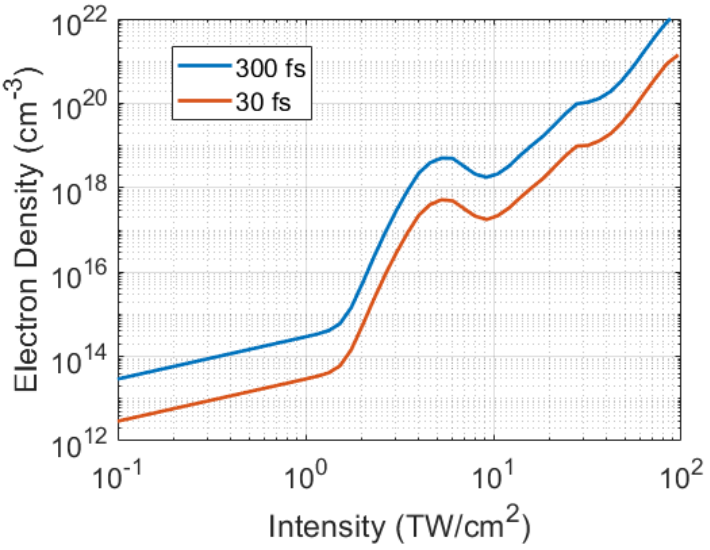


Figure 5.5 The electron distribution generated via photo-ionisation only as a function of laser intensity after a laser pulse of 300 fs and 30 fs.

at higher intensities, transitions favour states further away from the centre of the Brillouin zone yielding higher energy distributions as the bandgap is larger at those locations. Transitions also occur to higher energy bands corresponding to the second peak in the lowest intensity figure. The probability of this is much lower owing to the larger energy gap such that the density generated is significantly lower.

The energy distribution of photoionised carriers is additionally non-linear with respect to pulse energy than the total electron density which has profound implications on processes that depend upon the energies of carriers such as avalanche ionisation and scattering.

It is important to note that the rate of photoionisation includes the refractive index, which varies with time and is spatially inhomogeneous due to plasma effects. Once scattering processes and second carrier generation are taken into account, the refractive index varies significantly within the focal region such that an independent calculation of photoionisation is not accurate. As with the focal intensity, this needs to be calculated in parallel with other terms due to the inherently linked nature of

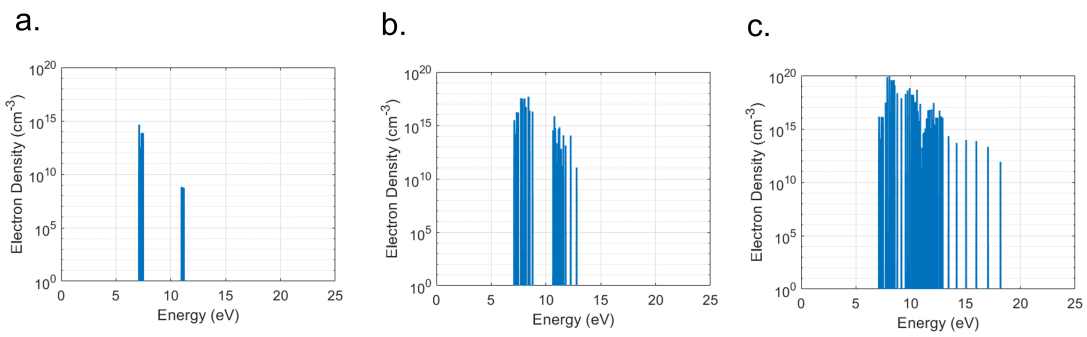


Figure 5.6 The electron distribution generated via photo-ionisation as a function of energy after a 300 fs laser pulse for peak laser intensities of 1.5 TW cm^{-2}, 10 TW cm^{-2} and 50 TW cm^{-2}.

the light-matter interactions.

Scattering processes

The energy distribution of conduction band states due to photoionisation correspond to near delta functions at the energy corresponding to the band locations at the momenta at which transition occurred. Many scattering events then take place which change the carrier distribution towards and away from equilibrium. Elastic scattering leads to momentum relaxation and will distribute the carriers more evenly across the Brillouin zone and inelastic scattering leads to energy relaxation and will ultimately bring the carriers back towards equilibrium with the lattice [185]. Given no driving field, collisional energy losses average out such that the distribution thermalises through screened Coulomb interaction carrier-carrier collisions to an effective temperature much hotter than the lattice. Electron-phonon coupling causes the phonon subsystem to react to the non-equilibrium distribution of electrons generating longitudinal optical and acoustic phonons which are emitted from carriers transferring energy to the lattice [198]. The carrier-phonon coupling strength in the conduction band is much stronger than in the valence band; holes relax over a longer timescale [199]. These scattering events lead to cooling of the carrier density to the Fermi-Dirac distribution

in equilibrium with the lattice. Under a driving electric field, carriers can absorb photons if their oscillation is knocked out of phase with the incoming field [182]. This is known as reverse Bremsstrahlung or carrier-phonon-photon scattering which leads to an efficient energy gain of carriers, skewing the distribution away from equilibrium. The photoionisation and reverse Bremsstrahlung processes compete with the phonon and carrier scattering leading to a skewed thermal distribution.

Within the model, the rates of each of these terms as a function of space, time and energy are approximated by using a mixture of collision time approximations, Drude theory and energy and momentum conservation [171] [195]. The average carrier-carrier collision time is calculated using the change to the carrier mobility as a function of carrier density under the assumption that each scattering event randomises the motion [200]. The dependence of the electron mobility due to carrier-carrier scattering has been measured experimentally by Kozak *et al.*. This yielded the following relationship in units of $m^2V^{-1}s^{-1}$[200].

$$\mu_{cc}(r,z,t) = \frac{aT(r,z,t)^{\frac{2}{3}}}{N_{carr}(r,z,t)\ln(1+bT(r,z,t)^2(1\times10^{-4}\cdot N_{carr}(r,z,t))^{-\frac{2}{3}})} \tag{5.40}$$

Where a and b are empirical parameters determined to be 4.1×10^{15} and 5×10^5 respectively, T is the lattice temperature, N_{carr} is the total carrier density inclusive of electrons, holes and their bound states and the subscript cc refers to carrier-carrier scattering. This can be converted from mobility to collision rate via

$$\tau_{cc}(r,z,t) = \mu_{cc}(r,z,t)\cdot\frac{m}{e} \tag{5.41}$$

under the assumption that each collision randomises the motion. As there is no carrier energy dependence to the rate of scattering of an individual carrier, the total energy dependence is based purely upon the density distribution. Carrier scattering is elastic; the total energy is conserved but the scattering acts to homogenise the

momentum distribution across the Brillouin zone and leads to thermalisation towards a Boltzmann distribution. This effect can be calculated considering carrier scattering between two carriers with the constraint that the total energy must be conserved and integrating across energy. This is complicated slightly by the density of states which limits the states which electrons can scatter into at high densities. The change to the electron distribution due to carrier-carrier scattering is given by

$$\left[\frac{\partial \rho_e}{\partial t}\right]_{cc}(r,z,t,\mathcal{E}) = \frac{1}{\tau_{cc}(r,z,t)}\left[\int_{\mathcal{E}_C}^{\infty}\int_{\mathcal{E}_C}^{\infty}\frac{\rho_e(r,z,t,\mathcal{E}_1)}{\mathcal{E}_1+\mathcal{E}_2-\mathcal{E}_C}\frac{\rho_e(r,z,t,\mathcal{E}_2)}{N_{carr}(r,z,t)}\,d\mathcal{E}_1\,d\mathcal{E}_2 - \rho_e(r,z,t,\mathcal{E})\right] \text{ for } \mathcal{E} \leq \mathcal{E}_1+\mathcal{E}_2-\mathcal{E}_C \tag{5.42}$$

Under the condition that

$$\rho_e(r,z,t,\mathcal{E}) + \left[\frac{\partial \rho_e}{\partial t}\right]_{cc}(r,z,t,\mathcal{E})\cdot\Delta t < D(\mathcal{E}) \tag{5.43}$$

Where $D(\mathcal{E})$ is the density of states at a given energy, $\mathcal{E}_C$ is the energy of the conduction band minimum, $\mathcal{E}_1$ is an initial electron energy and $\mathcal{E}_2$ is the initial energy of the scattering carrier. If the condition is not met, the electron cannot scatter into the energy state, $\mathcal{E}$ as it is full. The carrier-carrier scattering acts to drive the electron distribution towards a Boltzmann distribution at a raised electron temperature above the lattice energy given many scattering events. The density dependent nature of this term means that it is negligible at low densities with timescales of order tens of pico-seconds for carrier densities of 10^{17} cm^{-3} but dominates at high carrier densities where the timescale is reduced to less than a femtosecond for carrier densities of $\sim 10^{21}$ cm^{-3}.

The density of states is found by integrating the momentum states from the band structure over energy and calculating energy iso-surfaces shown in Figure 5.7.

Electron-phonon scattering acts to bring the electron-lattice system towards equilibrium taking energy from the electrons. Scattering with acoustic phonons is an elastic

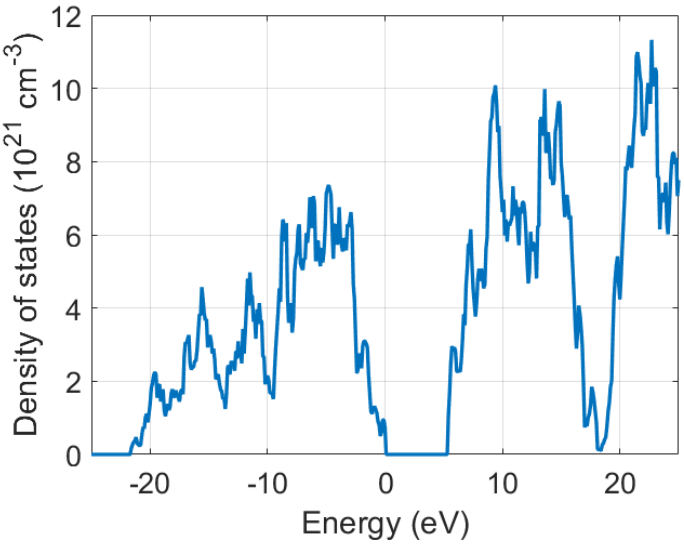


Figure 5.7 The density of states of the electron distribution in the valence and conduction bands. This was calculated by finding energy iso-surfaces across the band-structure.

process and cannot change the carrier energy significantly whereas optical phonons scatter inelastically with carriers and dominate energy transfer [185]. In the limit of many collisions a collision time approximation can be utilised given an empirical scattering rate. Tandon *et al.* used DFT to calculate the average carrier-phonon scattering rate as a function of energy inclusive of both emission and absorption within the valence and conduction bands [198]. They found that the average phonon scattering time, $\tau_{e-ph_{tot}}$ is proportional to the density of electron states at a particular energy.

$$\tau_{e-ph_{tot}}(\mathcal{E}) = \frac{1}{aD(\mathcal{E})} \tag{5.44}$$

With a proportionality constant of $a = 1 \times 10^{-12}$ s^{-1}m^3. Monserrat *et al.* used DFT to calculate the phonon energies [199]. In this work, these are averaged to find an optical phonon energy of 0.15 eV and 0.08 eV for acoustic phonons. The ratio of phonon emission to absorption is found by comparing the lattice temperature, T_L, to the electron temperature, T_e where the electron temperature is calculated by fitting a

best-fit exponential function to the electron energy distribution. This then allows for calculation of phonon emission and phonon absorption times given by

$$\tau_{e-ph_{emit}}(r,z,t,\mathcal{E}) = \tau_{e-ph_{tot}}(\mathcal{E})\frac{T_e(r,z,t)+T_L(r,z,t)}{T_e(r,z,t)} \tag{5.45}$$

$$\tau_{e-ph_{abs}}(r,z,t,\mathcal{E}) = \tau_{e-ph_{tot}}(\mathcal{E})\frac{T_e(r,z,t)+T_L(r,z,t)}{T_L(r,z,t)} \tag{5.46}$$

A proportion of the carriers at a given energy then moves to a higher or lower energy dependent upon whether the phonon is absorbed or emitted.

$$\begin{aligned}\left[\frac{\partial \rho_e}{\partial t}\right]_{e-ph}(r,z,t,\mathcal{E}) = -\frac{\rho_e(r,z,t,\mathcal{E})}{\tau_{e-ph_{tot}}(r,z,t,\mathcal{E})} \\ +\frac{\rho_e(r,z,t,\mathcal{E}-\mathcal{E}_{ph})}{\tau_{ep_{abs}}(r,z,t,\mathcal{E}-\mathcal{E}_{ph})} + \frac{\rho_e(r,z,t,\mathcal{E}+\mathcal{E}_{ph})}{\tau_{e-ph_{emit}}(r,z,t,\mathcal{E}+\mathcal{E}_{ph})}\end{aligned} \tag{5.47}$$

This approach neglects higher order terms where two or more phonons interact at the same time but approaches the true result given many scattering events.

Under a driving electric field, electron-phonon-photon (Bremsstrahlung) processes lead to an efficient energy gain of carriers which skews the distribution away from equilibrium. A matrix element analysis would include the matrix elements for electron-phonon scattering and absorption of photons from the field [168]. This can be simplified using a collision time approximation and Drude theory with empirical input parameters. Photons can become absorbed when a carrier is knocked from its adiabatic oscillation within the field. This occurs at any scattering event such that the input scattering rate is a combination of the carrier-phonon and carrier-carrier scattering rates added together through Matthiessen's rule, τ_{Scatt}. The average rate of energy gained by carrier through electron-phonon-photon calculated through Drude theory

$$\left[\frac{\partial \mathcal{E}}{\partial t}\right]_{epp}(r,z,t,\mathcal{E}) = \frac{(\frac{e^2 I(r,z,t)}{m' c\epsilon_0 n(r,z,t,\mathcal{E})})\tau_{scatt}(r,z,t,\mathcal{E})}{\omega_0^2 \tau_{scatt}(r,z,t,\mathcal{E})^2+1} \tag{5.48}$$

[165] where I is the laser intensity and the subscript *epp* refer to the fact that this is an electron-phonon-photon interaction. Note that this includes the refractive index, n, which varies with time and is spatially inhomogeneous due to plasma effects.

Using a similar argument to with the electron-phonon collisions, this can be converted into a change to the space-time-energy distribution by defining a proportion of carriers that move a discrete energy step corresponding to the photon energy minus the average phonon energy that scatters at the electron's initial energy. This is due to the fact that this process can only occur when the electron is disturbed from its oscillation under the field through a collision.

$$\begin{aligned}\left[\frac{\partial \rho_e}{\partial t}\right]_{epp}(r,z,t,\mathcal{E}) = \left[\frac{\partial \rho_e}{\partial \mathcal{E}}\right]_{epp}\left[\frac{\partial \mathcal{E}}{\partial t}\right]_{epp} &= -\frac{\left[\frac{\partial \mathcal{E}}{\partial t}\right]_{epp}(r,z,t,\mathcal{E})\cdot\rho_e(r,z,t,\mathcal{E})}{(\hbar\omega_0-\hbar\omega_{ph})} \\ &+\frac{\left[\frac{\partial \mathcal{E}}{\partial t}\right]_{epp}(r,z,t,\mathcal{E}-\hbar\omega_0+\hbar\omega_{ph})\cdot\rho_e(r,z,t,\mathcal{E}-\hbar\omega_0+\hbar\omega_{ph})}{(\hbar\omega_0-\hbar\omega_{ph})}\end{aligned} \tag{5.49}$$

Again, this neglects higher order terms but approximates the true change to the distribution over many collisions.

These dynamics outlined above act to redistribute the carriers across a range of energies, some giving the carrier energy and some reducing the carrier energy by transferring the it to the phonon subsystem.

Carriers above a threshold energy can relax to lower energy states through impact ionisation (also known as cascade ionisation) leading to the generation of an electron-hole pair. The reverse process of this only becomes important at very high carrier densities and causes a recombination of an electron-hole pair through the Auger effect with the excess energy being passed to a third carrier.

Both Auger and cascade processes involve three carriers but are the reverse of each other. Cascade starts with a single carrier which generates an electron-hole pair by losing energy and Auger starts with three carriers, two of which recombine by giving energy to the third. These both can be treated as three particle collisions where two

of the particles are of the same type (electron or hole) and one particle is of the other type. The initial excess energy of the electron above the threshold for cascade can be shared between the carriers in different ways leading to a distribution of final possible states. The rate of cascade processes is modelled by calculating the rate at which an electron above a threshold energy collides with the free states of the carriers from the respective bands.

$$\left[\frac{\partial \rho_e}{\partial t}\right]_{casc}(r,z,t,\mathcal{E}) = \int_{\mathcal{E}_{th}}^{\infty}\int_{\mathcal{E}_{th}-\mathcal{E}_1}^{0} \frac{\rho_e(r,z,t,\mathcal{E})}{\tau_{cc}(r,z,t)}\left(\frac{D(\mathcal{E})-\rho_e(r,z,t,\mathcal{E}_1)}{D(\mathcal{E}_1)}\right) \left(\frac{D(\mathcal{E}_2)-\rho_h(r,z,t,\mathcal{E}_2)}{D(\mathcal{E}_2)}\right) d\mathcal{E}_1\, d\mathcal{E}_2 \tag{5.50}$$

Where $\mathcal{E}_1$ is the initial hole energy, $\mathcal{E}_2$ is the initial energy of the high energy electron and $\mathcal{E}_{th}$ is threshold energy for cascade to occur, equal to $\mathcal{E}_g$. The hole energy is negative as the zero point of energy is defined as the maxima of the valence band. The terms in the first and second bracket are approximately equal to one until the density of carriers becomes very high and hence, once integrated across energy this simplifies to the cascade rate being proportional to the density of carriers for a low carrier density.

Auger processes, being the reverse of cascade, are governed by a very similar equation. by considering the density of occupied states rather than free states.

$$\left[\frac{\partial \rho_e}{\partial t}\right]_{Auger}(r,z,t,\mathcal{E}) = \int_{\mathcal{E}_{th}}^{\infty}\int_{\mathcal{E}_{th}-\mathcal{E}_1}^{0} \frac{\rho_e(r,z,t,\mathcal{E})}{\tau_{cc}(r,z,t)}\left(\frac{\rho_e(r,z,t,\mathcal{E}_1)}{D(\mathcal{E}_1)}\right) \left(\frac{\rho_h(r,z,t,\mathcal{E}_2)}{D(\mathcal{E}_2)}\right) d\mathcal{E}_1\, d\mathcal{E}_2 \tag{5.51}$$

Note that this becomes the standard formula for Auger when integrated across energy, depending upon the cube of the carrier density, with the Auger recombination parameter determined by the relation

$$C_e(r,z,t) = \frac{1}{\tau_{cc}(r,z,t) \cdot \left(\int_{-\infty}^{\infty} D(\mathcal{E})\ d\mathcal{E} \right)^2} \tag{5.52}$$

This approach, whilst more convoluted than just modelling the cascade and auger processes as linear and cubic relations, allows for the energy distribution of carriers to be calculated. In addition, separating out the energy gain of carriers from reverse Bremsstrahlung processes and the cascade process itself allows for nuance that is often missed in more basic models. Furthermore, the approach in this work highlights that at very high carrier densities, the cascade rate is no longer linearly proportional to the carrier density. Relating the constant of proportionality for the cascade and auger processes to the screened Coulomb interaction carrier-carrier scattering time also shows that the more simplistic approach is inaccurate given a large range of carrier densities as the scattering time changes significantly above a threshold carrier density.

The generation of electrons in the conduction band strongly depends upon the laser intensity. As the laser intensity is non-uniform across the focal volume, the distribution of electrons that are generated are likewise non-uniform. The non-linear generation means that the electron distribution is confined to a much smaller volume than the laser intensity. However, the electrons will spread out over time due to the non-uniform density across the volume. This spreading out can be modelled by the heat equation.

$$\left[\frac{\partial \rho_e}{\partial t} \right]_{diff} (r,z,t,\mathcal{E}) = -\nabla \cdot \left(D \nabla \rho_e(r,z,t,\mathcal{E}) \right) \tag{5.53}$$

Where D is the diffusion coefficient can be given by the Einstein relation. To first approximation, this may be good enough, however, electrons are charged particles and the laser has a strong electromagnetic field. In addition, local strain in the semiconductor will also change the electromagnetic field within the material. Therefore a full analysis of the dynamics of diffusion would require the magnetohydrodynamic

equations for a plasma and a map of the local strain field. In this model, it is assumed that the local strain is homogeneous or zero and the laser field only provides canonical momentum, in which case, the standard diffusion equation is a good approximation.

The final terms in equations 5.32 and 5.33 regard carrier recombination and excitonic formation and dissociation. Diamond is a indirect bandgap semiconductor and therefore radiative recombination is inefficient as it requires the generation of phonons to conserve momenta. Alternatively a higher energy photon can be released.

The radiative recombination rate is regulated through the screened Coulomb interaction [188] and has a constraint that carriers can only recombine given they are at the same momentum state. As momentum is being averaged over in this model, instead an empirical parameter is used; radiative recombination rates in diamond have been shown experimentally to be of $2.3\mu s$ for a starting carrier density of 1×10^{17} cm^3 [188].

$$\left[\frac{\partial \rho_e}{\partial t}\right]_{rad}(r,z,t,\mathcal{E}) = \int_{-\infty}^{0} \frac{\rho_e(r,z,t,\mathcal{E})}{\tau_{rad}(r,z,t)} \frac{\rho_h(r,z,t,\mathcal{E}_1)}{N_{carr}(r,z,t)}\, d\mathcal{E}_1 \tag{5.54}$$

The free carrier density can also be reduced through the formation of excitonic states by electrons coupling to holes through a screened Coulomb attraction.

5.2.3 Excitonic states

An electron and hole with overlapping wavefunctions can become bound through the screened Coulomb interaction and form excitonic states if their kinetic energy is less than the excitonic binding energy [171] [201]. This corresponds to the Exc terms in equations 5.32 and 5.33. The rate at which it occurs is calculated through multiplying the density of electrons and holes at a given location and a characteristic interaction timescale which depends upon the Debye length of carriers, in turn dependent on values such as the electron temperature and density. This timescale is of the same

order as the carrier-carrier scattering as both take place through the screened Coulomb interaction the same empirical parameter can be utilised for this.

$$\left[\frac{\partial \rho_{Exc}}{\partial t}\right]_{Form}(r,z,t,\mathcal{E}) = \int_{\mathcal{E}_C}^{\mathcal{E}+\mathcal{E}_x} \frac{\rho_e(r,z,t,\mathcal{E}_1)\rho_h(r,z,t,\mathcal{E}_1-\mathcal{E}-\mathcal{E}_x)}{N_{carr}(r,z,t)\cdot\tau_{cc}(r,z,t)}\, d\mathcal{E}_1 \tag{5.55}$$

Where $\mathcal{E}_X$ is the excitonic binding energy which for diamond is 80 meV [202] and $\mathcal{E}_C$ refers to the conduction band minimum and is the maximum possible energy of the bound pair. This rate is doubly dependent upon the density of free carriers as the interaction timescale is also density dependent. Single excitons in diamond are of Wannier type and remain relatively spread out over space [178], therefore excitonic binding is weak and the electron-hole pair continue to scatter phonons and other carriers somewhat independently. The density of excitons as a function of space, time and energy is given by another coupled equation.

$$\begin{aligned}\frac{d\rho_{Exc}}{dt}(r,z,t,\mathcal{E}) = &\left[\frac{\partial \rho_{Exc}}{\partial t}\right]_{Form} + \left[\frac{\partial \rho_{Exc}}{\partial t}\right]_{Exc-c} \\ +\left[\frac{\partial \rho_{Exc}}{\partial t}\right]_{Exc-ph} &- \left[\frac{\partial \rho_{Exc}}{\partial t}\right]_{Recomb} - \left[\frac{\partial \rho_{Exc}}{\partial t}\right]_{BiX} \\ &+\left[\frac{\rho_{Exc}}{\partial t}\right]_{BiX_{Diss}} + \left[\frac{\partial \rho_{Exc}}{\partial t}\right]_{BiX_{Recomb}}\end{aligned} \tag{5.56}$$

The first term corresponds to the formation of excitons, the second term corresponds to scattering processes with carriers which are similar to those described above for free carriers and thermalise the distribution also leading to dissociation of excitons back into free carriers when the exciton absorbs energy greater than the binding energy. During the pulse and shortly after the pulse, the incoming light means that excitons which form are quickly dissociated, however once the carriers and lattice form a quasi-equilibrium, most interactions lead to a loss of energy rather than a gain such that the carriers remain bound. The third term corresponds to scattering with phonons and the fourth term to excitonic recombination which takes place either

radiatively, through phonon scattering, Auger processes or existing defect trapping on timescales of nanoseconds [203]. The BiX term corresponds to the combining of excitonic states into bi-excitons, again through the screened Coulomb interaction and the final two terms regard the gain to the exciton density from the dissociation and recombination of bi-excitons. The rate at which bi-excitons form is given by

$$\left[\frac{\partial \rho_{BiX}}{\partial t}\right]_{Form}(r,z,t,\mathcal{E}) = \int_{\mathcal{E}_C-\mathcal{E}_x}^{\mathcal{E}-\mathcal{E}_C+\mathcal{E}_x+\mathcal{E}_{bx}} \frac{\rho_{Exc}(r,z,t,\mathcal{E}_1)\rho_{Exc}(r,z,t,\mathcal{E}-\mathcal{E}_1+\mathcal{E}_{bx})}{N_{carr}(r,z,t)\cdot\tau_{xx}(r,z,t)}\, d\mathcal{E}_1 \tag{5.57}$$

Where $\mathcal{E}_{bx}$ is the bi-excitonic binding energy which is 12 meV for diamond [204] and τ_{xx} is the equivalent of the carrier-carrier scattering time but just considering excitonic density. As before, a further coupled equation is defined to keep track of the density of bi-excitons as a function of space, time and energy.

$$\begin{aligned}\frac{d\rho_{BiX}}{dt}(r,z,t,\mathcal{E}) = \left[\frac{\partial \rho_{BiX}}{\partial t}\right]_{Form} + \left[\frac{\partial \rho_{BiX}}{\partial t}\right]_{BiX-c} \\ + \left[\frac{\partial \rho_{BiX}}{\partial t}\right]_{BiX-ph} - \left[\frac{\partial \rho_{BiX}}{\partial t}\right]_{Rad} + \left[\frac{\partial \rho_{BiX}}{\partial t}\right]_{STbX_{diss}}\end{aligned} \tag{5.58}$$

Again, the scattering terms include dissociation into single excitons and thermalisation. The fourth term in equation 5.58 regards radiative recombination, the rate of which are determined from [177]. There should be a fifth term in this equation along with another coupled equation corresponding to the formation of higher order multi-excitons but for simplicity these terms are neglected.

Bi-excitons are more bound than single excitons such that the lowest energy configuration of the lattice-bi-exciton system corresponds to a significantly deformed lattice and the bi-exciton trapped at a single atomic site. Upon interaction with phonons, bi-excitons will self-trap, allowing relaxation of the lattice, releasing 1.74 eV and breaking a carbon-carbon bond [178]. The density of self-trapped bi-excitonic states is given by

$$\frac{d\rho_{STbX}}{dt}(r,z,t,\mathcal{E}) = \left[\frac{\partial\rho_{STbX}}{\partial t}\right]_{Form} + \left[\frac{\partial\rho_{STbX}}{\partial t}\right]_{STbX-c} + \left[\frac{\partial\rho_{STbX}}{\partial t}\right]_{STbX-ph} - \left[\frac{\partial\rho_{STbX}}{\partial t}\right]_{Rad} - \left[\frac{\partial\rho_{STbX}}{\partial t}\right]_{FD} \tag{5.59}$$

The final term describes a hypothesised non-radiative recombination yielding the formation of a Frenkel defect which will be addressed in section 5.2.5. The higher localisation and higher energies of self-trapped multi-excitonic states mean that these act as a source of energy localisation within the crystal.

5.2.4 Lattice temperature distribution

Phonon scattering events act to cool down the carrier distributions but heat up the lattice bringing the carrier-lattice system closer to equilibrium. Melting can occur if the lattice surpasses the melting temperature (4300 K for diamond [210]) which leads to graphitic formation upon re-solidification. As graphitisation is a complicated process involving a change in the band-structure, a graphitisation threshold is defined as when the lattice goes above the melting temperature or when the carrier density goes above 9% of the atomic density [205] [206]. Above this point, the model will be inaccurate as changes to the band-structure are not considered.

The heating of the lattice is calculated through multiplying the phonon scattering rates with the average phonon energy and dividing through by the atomic density and utilise a simple heat equation model to indicate the diffusion of heat.

$$\frac{dT}{dt}(r,z,t) = \left[\frac{\partial T}{\partial t}\right]_{Scatt} + \left[\frac{\partial T}{\partial t}\right]_{Diff} \tag{5.60}$$

The first term regards lattice heating through the phonon scattering of carriers and excitons and is calculated by adding up the energy lost from the various scattering centres. For example, the temperature gain from phonon emission from electrons is given by

$$\left[\frac{\partial T}{\partial t}\right]_{Scatt_e} = \int_0^\infty \frac{\mathcal{E}_{ph}}{k_B} \frac{\rho_e(r,z,t,\mathcal{E})}{\tau_{ep_{emit}}(r,z,t,\mathcal{E})\rho_A}\, d\mathcal{E} \tag{5.61}$$

Where ρ_A is the atomic density. Similar terms exist for the other scattering terms. These scattering terms act to bring the lattice carrier system to a quasi-equilibrium state.

5.2.5 Hypothesis for Frenkel defect generation

Self-trapped multi-excitonic states allow for energy localisation and quasi-particles of high energies whilst simultaneously breaking a carbon-carbon bond through a deformation potential of $\mathcal{E}_{DP}$ =1.74 eV [178]. In order to generate a defect, 3 more bonds must be broken. One might assume that 4 bi-excitons would be required to localise to the same atomic site in order to break the 4 respective bonds, however the probability of this would scale with the fourth power of the bi-exciton density and graphitisation would occur well before there was a significant enough probability of 4 bi-excitons localising to the same site.

Simple scaling arguments suggest the breaking of 3 additional bonds should require an energy input of 3×1.74 eV = 5.22 eV however a small amount more energy is likely needed such that the vacancy-interstitial pair don't instantly recombine. The minimum potential energy of a stable Frenkel defect above a pristine lattice was calculated by Deak *et al.* through DFT to be 7.14 eV [156]. Recombination of vacancy-interstitial pairs requires a significant input of energy, 1.64 eV [207]. The energy barrier against distance between vacancy and interstitial is likely to be symmetric such that a total potential energy of $7.14 + 1.64 = 8.78$ eV is needed to form the defect.

Mauri *et al.* proposed that following self-trapping, radiative recombination of the bi-exciton would follow with a large Stokes shift of 3.23 eV on timescales of ~ 7 ns leaving a single exciton and the lattice partially distorted, leading to a localised

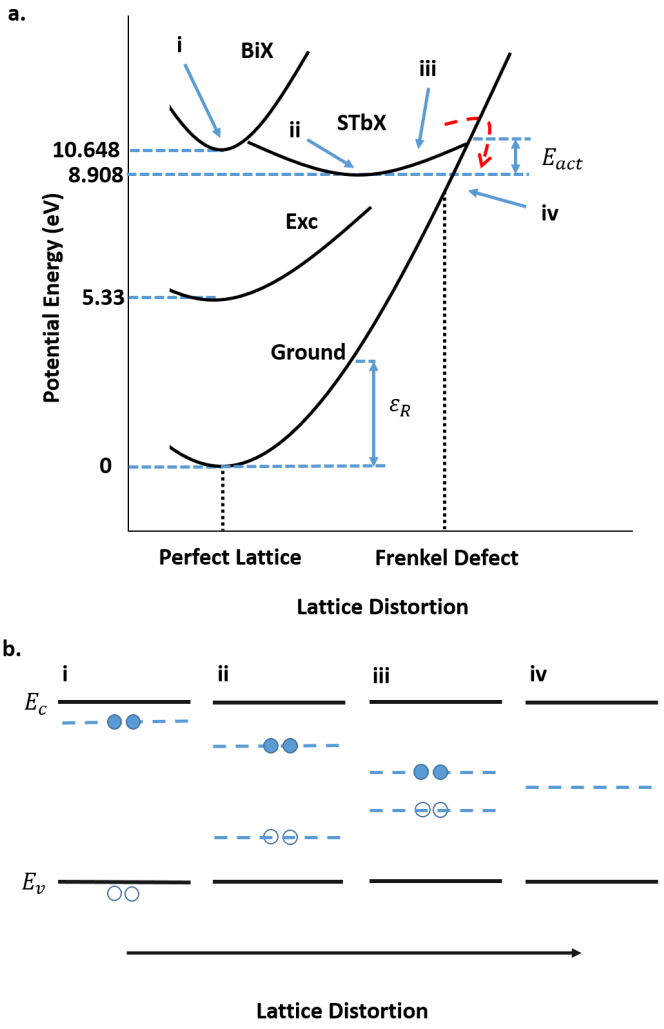


Figure 5.8 a. Schematic of the adiabatic potential energy curves of the ground state, free bi-exciton state (BiX), free exciton state (Exc), and the self-trapped bi-exciton state (STbX) against lattice distortion. The red dashed line shows possible non-radiative decay processes of the STbX's and the blue dashed lines indicate the activation energy E_{act} and relaxation energy, ϵ_R of the ground state. b. A schematic of the proposed band structure during the non-radiative recombination of the self-trapped bi-exciton. The bonding, anti-bonding states in the bandgap approach each other as the lattice is further deformed allowing non-radiative recombination.

graphitisation [178]. Here an alternative mechanism is proposed, a non-radiative recombination pathway, transferring the energy to the lattice and forming a Frenkel defect shown in Figure 5.8. The minimum potential energy of the self-trapped bi-exciton localised upon the broken bond is 8.908 eV, $(2(\mathcal{E}_C - \mathcal{E}_x) - \mathcal{E}_{bx} - \mathcal{E}_{DP})$ which is greater than the total potential energy required for Frenkel formation, therefore a non-radiative recombination yielding defect formation would lower the potential energy surface. Bang *et al.* showed that two electron-hole pairs within InGaN can non-radiatively recombine via the formation and recombination of a Frenkel pair [208] and self-trapped excitonic states have been shown to lead to the permanent formation of Frenkel defects in SiO_2 and other dielectrics [171] [175] [176]. In both cases, the deformation of the lattice leads to the formation of states within the bandgap that allow energy transfer from the electronic system to the lattice. The self-trapped bi-exciton in diamond adds two deep levels into the bandgap, a doubly occupied anti-bonding level 1.7 eV below the conduction band edge and an empty bonding level 1.6 eV above the valence band maximum, both localised on the broken bond [178]. The formation of these deep states offers a potentially efficient non-radiative recombination pathway allowing defect formation via the emission of phonons.

Non-radiative lifetimes of self-trapped bi-excitonic states are likely to be short as the carriers are already localised at the trap sites. Further deformation of the lattice pushes the deep levels towards mid-gap shown in Figure 5.8b allowing recombination through electron capture. In the high temperature approximation, electron capture is thermally activated [209] and given an energy barrier, the non-radiative recombination lifetime is given by

$$\tau_{FD}(r, z, t, \mathcal{E}) = \frac{h}{\mathcal{E}_{ph}} \exp\left(\frac{\mathcal{E}_b - (\mathcal{E} - [2(\mathcal{E}_C - \mathcal{E}_X) - \mathcal{E}_{bX} - \mathcal{E}_{DP}])}{k_B T(r, z, t)}\right) \tag{5.62}$$

where $\mathcal{E}_{ph}$ is the optical phonon energy and $\mathcal{E}_b$ is the energy barrier [208]. The

value $\mathcal{E}$ refers in this case to the energy of the self-trapped bi-exciton. The height of the energy barrier is an unknown, however, this can be made into a fitting parameter when comparing with experiment. Given a higher energy barrier, the longer the formation timescale and the more non-linear the process will become with respect to pulse energy. Given no energy barrier, this becomes the empirical phonon scattering time. A first guess of the energy barrier can be made by assuming that the shape of the self-trapped bi-exciton potential energy surface is symmetric about its minimum and that the formation energy is equal to the activation energy minus a quarter of the relaxation energy of the lattice ($\mathcal{E}_b = E_{act} - \frac{\epsilon_R}{4}$) which holds in the high temperature limit [209]. For non-radiative recombination of self-trapped bi-excitonic states in diamond, this suggests an energy barrier of 1.74 - $\frac{4.85}{4}$ = 0.5275 eV which shall be used as the initial input when comparing to experiment. The formation mechanism competes with dissociation and radiative recombination of the bi-excitonic states, the relative strengths of each being controlled by the lattice/carrier temperatures.

Another coupled equation is defined corresponding to the hypothesised density of lattice defects created by the non-radiative recombination of multi-excitonic states.

$$\frac{d\rho_{FD}}{dt}(r,z,t) = \int_{2(\mathcal{E}_C-\mathcal{E}_X)-\mathcal{E}_{bX}-\mathcal{E}_{DP}}^{2(\mathcal{E}_C-\mathcal{E}_X)-\mathcal{E}_{bx}} \frac{\rho_{STbX}(r,z,t,\mathcal{E})}{\tau_{FD}(r,z,t,\mathcal{E})}\, d\mathcal{E} \tag{5.63}$$

This equation should also include a term for the diffusion of defects which likely occurs during the pulse due to the lower activation energy than defect formation. For now, this is neglected from the analysis as only single pulses are being considered. This is a reasonable assumption since defect formation does not begin until several picoseconds after the optical pulse has passed hence there will be no defects during the initial irradiation. The recombination of Frenkel defects is also ignored, although a fixed fraction of the defects will likely recombine as soon as they form, this would appear as a scaling factor to the total number of defects formed and otherwise not alter the results of the model.

Mauri *et al.* proposed that the self-trapping of a sufficiently high density of bi-excitonic states could cluster and produce a macroscopic graphitisation due to the breaking of many single bonds [178], however utilising the assumptions above, the vast majority of bi-excitons that self-trap go on to form Frenkel defects at temperatures above 450 K as the non-radiative recombination lifetime is shorter than the radiative lifetime. In order to obtain a significant density of bi-excitons at such high temperatures, intense laser pulses generating a significant density of free carriers ($\sim 5\%\ \rho_A$) are required. Collisional heating of the lattice from such a high density of carriers means that lattice temperatures rise to above this threshold during the thermalisation of carriers with the lattice such that defect formation should be preferable over radiative recombination for high carrier densities. At lower excitation, carrier densities and the temperature do not rise as far, however, the density of self-trapped bi-excitons is also low such that both graphitisation and Frenkel formation are unlikely to occur. At very low temperatures, the formation of electron-hole plasmas and liquids should prevent lattice damage occurring as excitonic states become delocalised throughout the liquid [167]. To date, excitonic states within diamond have typically been studied at lower densities and temperatures to obtain long lived states [177] hence the probability of defect formation through their recombination has been negligible.

5.3 Limitations of the model

There are a few limitations by which this model could be improved. The conduction and valence bands are treated as continuum's and k state information is lost as it is treated as homogeneous. There may be subtle effects caused by specific momentum transfers which have not been included. A Monte Carlo simulation over all k states would be a better approach. This was not chosen for the sake of computational expense as 3 more dimensions would need to be added to each simulation. Another limitation

of the model is the fact that non-thermal melting from the shift in potential energy surfaces caused by the carrier dynamics has been ignored and instead a upper limit of carrier density is defined whereby "graphitisation occurs". The model will likely be inaccurate at high pulse energies.

The diffusion equation for carrier dynamics is overly simplistic using only the heat equation based upon the gradient in carrier density. Diffusion is likely to be affected by the strain tensor as well as magnetohydrodynamic effects. This simplification is justifiable as diffusion is a slower process the effects will be relatively small when compared with faster processes.

The rates of many terms within the coupled equations depend upon empirical scattering rates taken from the literature. These are a mixture of experimentally derived and theoretically determined parameters and many contain significant error bars. The results of this work do not claim that the laser forms a specific number of vacancies given a set of pulse parameters, instead the trends are studied, the effective non-linearity, determined given the hypothesis of multi-excitonic recombination and that this is in good agreement with the experimental results shown in the following chapter.

5.4 Summary

This chapter has described a set of coupled non-linear integro-differential equations to model how a femtosecond laser pulse interacts with a semiconductor. Parameters have been included to solve this set of differential equations for diamond. The model initially describes the focusing of the laser pulse which is followed by the generation of a dense carrier plasma through multi-photon effects. The plasma alters the laser focus and a feedback loop occurs leading to a highly dynamical generation of carriers within the focal region. A hypothesis for how the energy is transferred from the electronic

Parameter	value	ref.
Electron-Electron scattering (μ_{cc})	Equation 5.40	[200]
Electron-Phonon scattering ($\tau_{e-ph_{tot}}$)	Equation 5.44	[198]
Electron-phonon-photon scattering ($\left[\frac{\partial \mathcal{E}}{\partial t}\right]_{epp}$)	Equation 5.48	[165]
Radiative Electron-Hole recombination (τ_{rad})	2.3 μs	[188]
Radiative Exciton recombination ($\tau_{Exc_{rad}}$)	350 ns	[203]
Radiative Bi-Exciton recombination ($\tau_{BiX_{rad}}$)	7.3 ns	[177]
Radiative Self-trapped Bi-Exciton recombination ($\tau_{STbX_{rad}}$)	7 ns	[178]
Optical Phonon energy ($\mathcal{E}_{ph_o}$)	0.15 eV	[199]
Acoustic Phonon energy ($\mathcal{E}_{ph_a}$)	0.08 eV	[199]
Exciton binding energy ($\mathcal{E}_x$)	80 meV	[202]
Bi-exciton binding energy ($\mathcal{E}_{bx}$)	12 meV	[204]
Bi-exciton self-trap Deformation Potential ($\mathcal{E}_{DP}$)	1.74 eV	[178]
Lattice relaxation energy ($\mathcal{E}_R$)	4.85 eV	[178]
Thermal conductivity of diamond (σ_{th})	2200 $\mathrm{Wm^{-1}K^{-1}}$	[210]
Atomic density of diamond (ρ_A)	1.77×10^{23} $\mathrm{cm^{-3}}$	[210]

Table 5.1 Interaction parameters and constants with relevant sources

system to the atomic sub lattice via the non-radiative recombination of self-trapped bi-excitonic states is described yielding the formation of individual Frenkel defects. The highly dynamical nature of this and high density of quasi-particles required leads to a high degree of non-linearity with respect to laser intensity.

For the interaction rates the collision time approximation was used, drawing values for average interaction times from previous works (table 5.1). This approach allows carrier scattering rates to be evaluated as explicit functions of carrier energy, but averaged over momentum space. This is a reasonable approximation since carrier

scattering homogenises the momentum distribution across the Brillouin zone on femtosecond timescales.

The idea for this theoretical study into the non-linearity of laser processing was developed by myself in discussions with Jason Smith and Patrick Salter. The coupled non-linear integro-differential equations were developed and coded into MATLAB by myself. Discussions with Jason Smith, Patrick Salter, Martin Booth, Shannon Nicley and Joanna Zajac enabled clarification on various mechanisms and the hypothesis for energy transfer to Frenkel defect generation was developed by myself. The band-structure was calculated by Andrew Kirkpatrick using DFT.

Chapter Six

Non-Linearity of the Laser Writing Process - Results

6.1 Introduction

The sample was then placed into a home-built beam-scanning confocal fluorescence microscope and fluorescence was collected through an oil immersion objective lens. 2D Gaussian peaks were fitted to the confocal images of laser written sites giving a value for the brightness from the integrated intensity. The background fluorescence was measured 1 μm from the laser written points which was then subtracted from the intensity value such that the measured intensity value came solely from the laser process. Intensities measured from the ten points for each pulse energy were then averaged for a fluorescence value at that pulse energy. This gives an indication of the number of vacancies created against laser write-pulse energy.

6.2 Varying pulse energy

The initial study was to determine the dependence of Frenkel defect generation on pulse energy, with the laser writing apparatus set to its standard setup that has been

used historically. Here single 300 fs laser pulses of a 790 nm Ti:Sapphire light were focused into diamond. This study can then be used as a baseline from which changes to the parameters could be compared. The diamond sample used in this study was a type 1b single-crystal supplied by Element Six with 2 ppb nitrogen concentration. Single pulses were focused through a 1.4 NA oil immersion objective into the diamond to form an array with the pulse energy changing between rows.

Fluorescence was measured with 532 nm excitation at 1.1 mW and an oil immersion objective lens. At the fluorescence visibility threshold there was a stochastic yield of visible sites and the yield rose up to unity at the 3rd row above the visibility threshold. This could be indicative of a stochastic nature of defect formation or due to small fluctuations in the writing laser power. Figure 6.1a shows an example of a photoluminescence scan of high energy laser written sites. Spectral analysis (Figure 6.1b) and wide-field transmission imaging reveal that at higher pulse energies a significant B-band peak is observed showing the onset of graphitization with a threshold pulse energy of ~ 21 nJ. Integrated fluorescence intensity of sites against write-pulse energy is shown on a logarithmic plot in Figure 6.1c and is highly non-linear for write-pulse energies between 15 and 18 nJ, quickly saturating at higher pulse energies. For the application of colour centre generation, relatively few vacancies are desired, therefore it is the lower pulse energies that are of more interest.

It is important to note the possible sources of error that could change the shape of this graph. A difficult to characterise error is how each pulse was effected by aberrations. An SLM was used for active aberration correction over Zernike modes, however, this is unlikely to have removed all aberrations. As shown above, the laser process is highly non-linear with respect to laser intensity, therefore, a small aberration could cause a large shift on the resulting number of Frenkel defects created. However, the aberration across each array should be reasonably uniform, therefore the shape of the graph is likely to be accurate and a small aberration means that the pulse energies

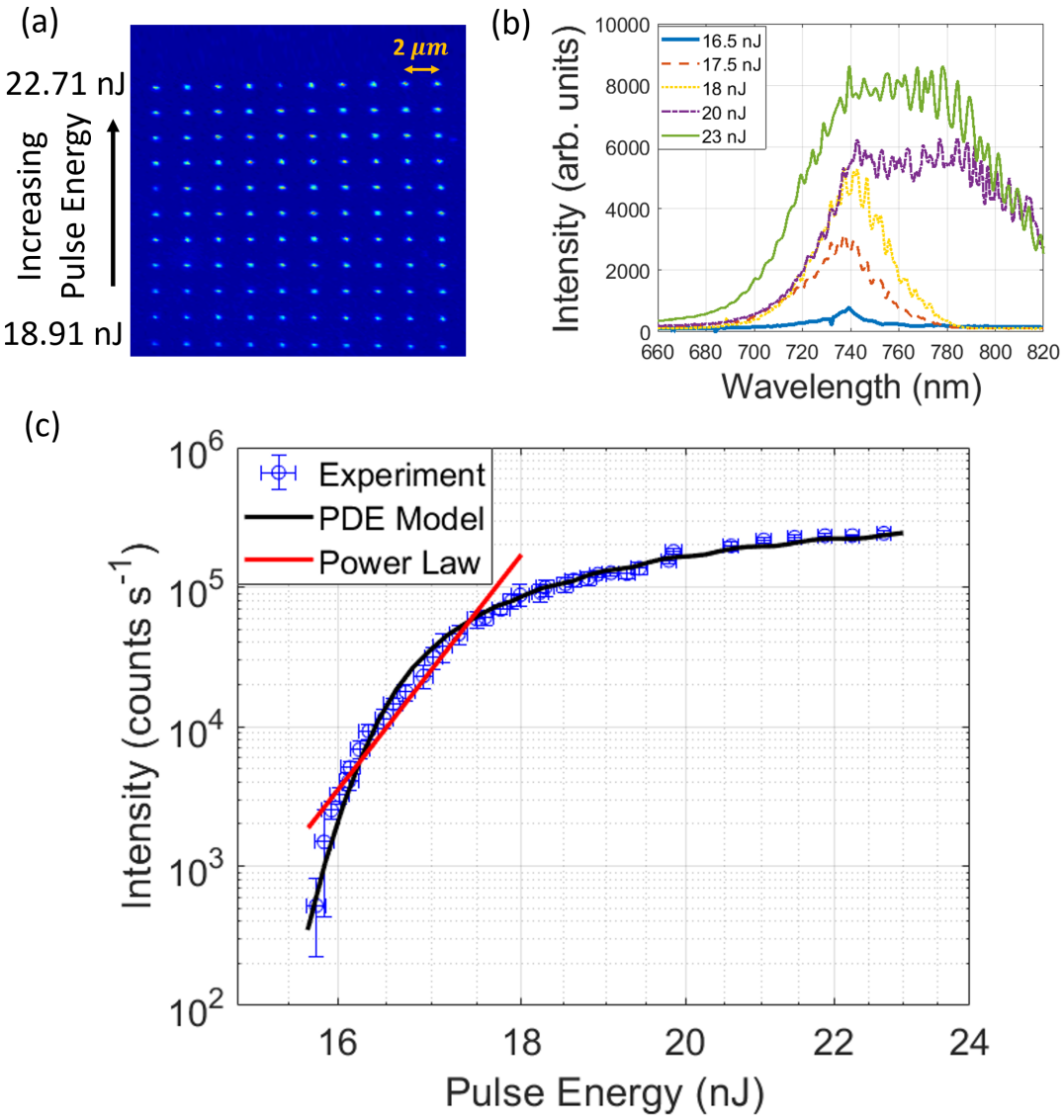


Figure 6.1 a. A confocal image of the highest energy sites in the array. b. Spectral composition of laser written sites, fluorescence is centred at a peak at 740 nm corresponding to lattice vacancies which broadens and shifts to longer wavelengths for higher pulse energies indicating further damage and graphitisation. c. The average fluorescence intensity measured from single pulses against pulse energy with the predictions from the model developed in chapter five overlaid.

are likely higher than if there were no aberrations at all. The optics used to focus the light also affect the intensity distribution of the light, therefore for a more general overview, the shape of the graph is more important than the absolute pulse energy values. For repetitions of this technique, pulse energies should be chosen in relation to the energy that is required to create visible graphite in a transmission microscope and reduce the pulse energy from there.

A power law to the 33rd power can be roughly fit to the region of the graph between 16 and 18 nJ, (shown in red) indicating that the generation is highly non-linear before saturating at the higher energies. In the multi-photon regime, photoionisation is expected to follow a power law, however this level of non-linearity is far beyond that which would be expected from photoionisation alone indicating that defect formations is likely caused by the amalgamation of several non-linear processes.

A MATLAB script was developed which modelled the coupled PDE's from chapter five (equations 5.22, 5.33, 5.34, 5.56, 5.58, 5.59, 5.60 and 5.63) and solved them numerically for diamond using the Euler finite-difference method given a range of initial conditions with empirical scattering times taken from the literature summarised in table 5.1. Simulations were calculated for a focused pulse of the laser with no additional aberrations. The rate equations were applied over the two spatial coordinates corresponding to the cylindrically symmetric focal spot, covering an axial range of 3 μm about the focal plane and a radial distance of 200 nm, which was found to be large enough that edge effects are negligible. A time-step of 0.1 fs was chosen, a pixel size of 17 nm in radius and 38 nm in depth with an energy step of 0.02 eV allowing for a reasonably fine mesh of the region of interest. Carrier concentrations are expressed as distributions over energy up to a maximum of 25 eV.

Various initial conditions corresponding to laser pulses of differing pulse energies were input into the set of coupled equations to build up data-sets to compare to experiment. As the simulations contain no aberrations or focusing losses, phenomena

will occur at lower pulse energies than during experiments. By integrating across all energy and space, the total number of electrons and defects generated by a pulse can be calculated.

$$N_e(t) = 2\pi \int_0^\infty \int_0^\infty \int_0^\infty \rho_e(r, z, t, \mathcal{E})\ r\ dr\ dz\ d\mathcal{E} \tag{6.1}$$

where N_e is the total number of electrons. The total defect number, N_{FD} is calculated by replacing ρ_e with ρ_{FD}.

Figure's 6.2a and b shows the peak density and total number of photogenerated electrons as a function of write-pulse energy along with the peak density and total number of Frenkel defects generated per pulse. The photoelectron generation curve follows a similar dependency to that from photoionisation alone as shown by Lagomarsino *et al.* [180], and in Figure 5.5, however the impact ionisation increases and smooths out the number of electrons generated. At high pulse energies there is a small uptick in the non-linearity of carriers at the centre of focus. This is because carrier densities become high enough that the carrier mobility and hence τ_{cc} rapidly decrease leading to an accelerated carrier avalanche at the centre of focus. This is rapidly saturated as Auger processes reach a quasi-equilibrium with the impact ionisation and plasma effects suppress photoionisation. Away from the centre of the focus, growth continues to occur leading to a smoothing out of the total number of carriers. It should be noted that additionally, more complex processes that are not included in the model will also take place at the higher pulse energies such as a defect induced absorption and macroscopic graphitisation. Graphitisation involves a significant modification to the band-structure such that the exact nature of this saturation in electron generation may be incorrect. This curve agrees with the experimental data of Lagomarsino *et al.* who measured the charge generated upon laser pulses of differing energies [180]. The shape of curve occurs at ~ 10 times lower pulse energies due to the use of a higher numerical aperture lens.

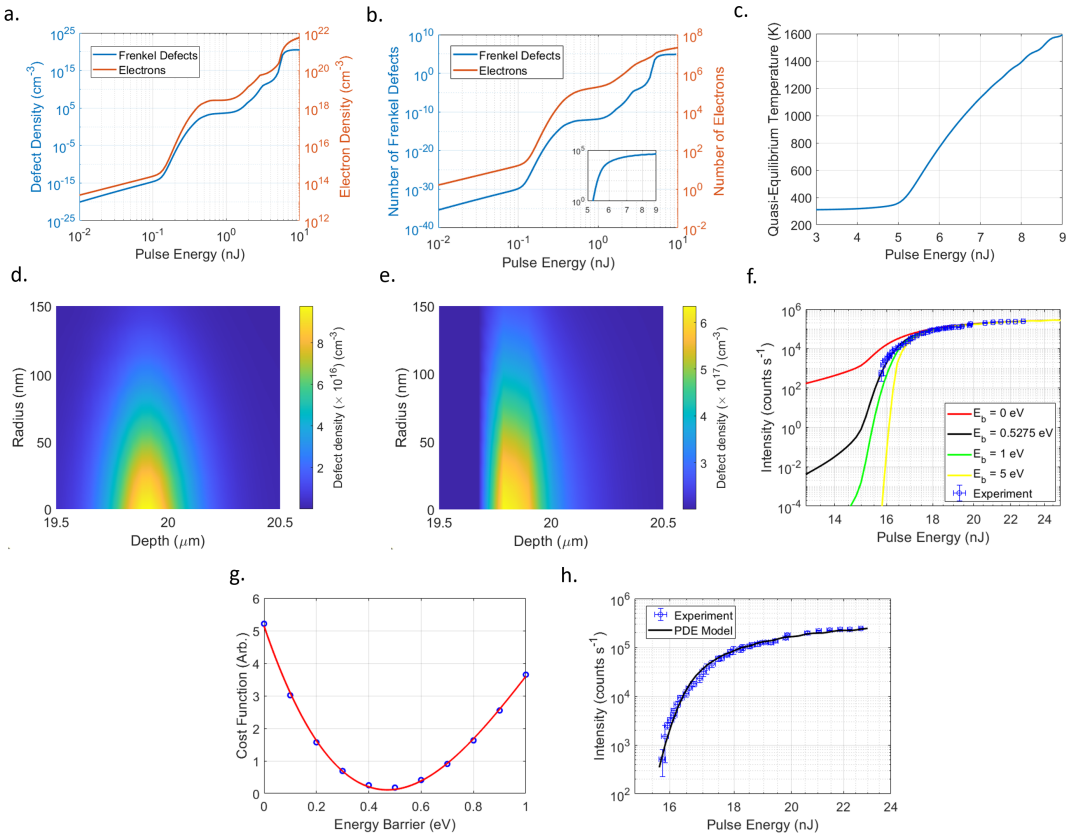


Figure 6.2 a. Maximum densities of carriers and defects generated against pulse energy. In red the number of electrons that are created against pulse energy and in blue, the simulated number of defects generated. b. Numerical integration of the coupled PDE model over energy, space and time. Inset displays the number of defects generated with probability above 1. d. Simulated spatial distribution of defects from a pulse of 5.5 nJ focused 20 μm into the diamond. The laser beam is incident from the left-hand side. c. The quasi-equilibrium temperature reached by the electron-lattice system at the centre of focus against pulse energy. d. Simulated spatial distribution of defects from a pulse of 7 nJ. f. Simulated defect vs pulse energy curves for different values of $\mathcal{E}_b$ fitted to experimental data through non-linear least squares fitting. g. Minimisation of the cost function for the energy barrier to non-radiative recombination reveals a value of $\mathcal{E}_b = 0.47 \pm 0.01$ eV fits best to the experimental data. h. Photoluminescence intensity against pulse energy for single pulses of the same pulse parameters (blue) overlaid with simulated data (black) with scaling parameters for focusing losses and conversion from number of defects to fluorescence intensity determined through non-linear parametric least squares fitting.

To calculate the defect generation rate, an energy barrier for the non-radiative recombination of self-trapped bi-excitonic states must be specified. The assumptions outlined in section 5.2.5 lead to an initial estimate of $\mathcal{E}_b = 0.5275$ eV, however this can be optimised through non-linear least squares fitting to the experimental data. In the experiments, the onset of GR1 fluorescence occurs at a pulse energy of about 16 nJ, almost three times higher than that predicted from simulation. There are a number of possible reasons for this discrepancy, including unaccounted aberrations, an underestimate of optical losses, and inaccuracies in parameters such as scattering rates and binding energies that will influence the efficiency of bi-exciton formation. This unknown scaling factor can be treated as a fitting parameter. A second scaling factor is needed in order to compare the number of Frenkel defects generated with the measured GR1 fluorescence intensity. This scaling factor is dependent on the quantum efficiency of the GR1 defects and on the efficiency of the fluorescence microscope used for the measurements. A second cost function was then defined, calculating the difference between the shape of the simulated and experimental defect curves for different values of $\mathcal{E}_b$ shown in Figure 6.2f. The sum of the squared residual distance between the experimental data and the model define a unique polynomial which is minimised at a value of $\mathcal{E}_b = 0.47 \pm 0.01$ eV shown in Figure 6.2g. Whilst the error bar on this fit is relatively small, drawing conclusions that this is the true energy barrier should be regarded cautiously as there are error bars associated with various scattering rates from the literature in many terms of the coupled equations (see table 5.1). Instead this is a best fit within the limit that the literature scattering rates are approximately correct. The fact that this value is of a similar magnitude to the initial estimate gives confidence in the model.

The defect generation curve for a value of $\mathcal{E}_b = 0.47$ is shown in Figures 6.2a and b and follows a similar pattern to that of electron generation, however the level of non-linearity is significantly increased and saturation is significantly stronger. Much

of this curve shows a defect number less than 1 which corresponds to the probability of a defect forming given a specific pulse. While these numbers are negligible and so in practice no defect generation will be seen at such low pulse energies, it is useful to plot as it shows the relationship between the electron generation and the formation of defects. The number of defects only becomes significant at the higher pulse energies therefore a zoom-in of this region with a finer resolution in pulse energy is shown in the inset of Figure 6.2b. The simulated Frenkel defect generation probability passes 1 at $\sim$ 5 nJ with a fast rise in the number of defects generated over a very small range in pulse energies which quickly saturates. This extremely steep dependence of defect formation on pulse energy occurs primarily as a result of two effects. The reduced carrier mobility not only produces an accelerated carrier avalanche but also leads to a significantly accelerated formation of excitonic states following cooling of the carriers. In addition, the quasi-equilibrium electron-lattice temperature for these pulse energies becomes significant which accelerates the non-radiative recombination of the self-trapped bi-excitons in competition with radiative processes. The quantum efficiency for Frenkel defect formation, defined as $\eta = \frac{\tau_r}{\tau_r + \tau_{FD}}$ and using equation 5.62, rises from $\sim 10^{-3}$ at room temperature to near unity at temperatures above 500 K. The quasi-equilibrium temperature reached by the carrier-lattice system at the centre of focus is shown in Figure 6.2c. At low pulse energies the maximum carrier densities are low enough that the quasi-equilibrium temperature is not significantly above the ambient temperature, however for higher pulse energies, it rises rapidly such that Frenkel defect formation will quickly become efficient over radiative recombination processes.

The rapid saturation in Frenkel defect number is again attributed to two processes. At these high pulse energies, there is a saturation to the electron density growth which becomes high enough that efficient Auger processes take equal precedence with avalanche ionisation. In addition, the non-radiative recombination of self-trapped

bi-excitons becomes efficient compared with radiative processes as the electron-lattice equilibrium temperature is high.

For comparison with experiment, the pulse energy and number of simulated defects were scaled by constants and fit as outlined above. Respective values of 2.84 and 3.47 were found for these two scaling factors, providing the fit shown in 6.2h with an R^2 of 0.9977 and adjusted R^2 of 0.9976. These scaling factors were found by first taking the base 10 logarithm of the model and experimental data such that linear regression could be used.

By integrating the coupled rate equations over energy and plotting over position, the predicted spatial distribution of defects generated is shown. Figure 6.2e shows a slice of the spatial distribution for a pulse of 5.5 nJ focused at 20 μm into the material. The distribution appears to be roughly Gaussian with a FWHM of $\sim$ 250 nm in depth and $\sim$ 50 nm in radius. Defects are centred at depths shallower than the centre of focus of the laser. This is due to the fact that the laser pulse travels downwards through the material into focus and back out, therefore electrons are generated at shallower depths first. The fast nature of the electron generation means that densities reach the plasma point before the pulse has fully reached the focal depth meaning defect generation occurs at shallower depths. The plasma then attenuates the beam such that deeper depths do not experience the same laser intensity and thus stifles the generation at focus and deeper. For higher pulse energies, there is a slight loss in the confinement with FWHM of $\sim$ 80 nm in radius and $\sim$ 250 nm axially for a 7 nJ pulse, shown in Figure 6.2f. There is also a further shift to shallower depths due to attenuation occurring at an earlier stage of the pulse propagation. This shift in depth could be compensated for by refocusing the system. These values are very similar to the measured positional accuracy of laser written NV centres shown in chapter eight [9]. Whilst not exactly a like-for-like comparison since the model does not include the annealing required to form NV centres from the Frenkel defects, the consistency

between the two gives confidence in the simulation results.

Figure 6.3 displays the simulated time dynamics for various parameters generated by an 6 nJ, 300 fs pulse at the focal point of the laser pulse, allowing the relative timings of the various processes to be observed. Electron generation occurs quickly during and following the pulse, initially via photoionisation but the majority being generated later via cascade processes. The electron concentration peaks around 0.25 ps after the peak of the pulse intensity and then decays multi-exponentially due to non-radiative recombination processes such as Auger processes and excitonic formation. Rapid carrier-carrier scattering ensures that the different carrier types are at thermal equilibrium with each other and re-ionises the majority of excitonic states that form. Immediately after the pulse the carrier temperature reaches several thousand degrees while lattice temperature remains low. Electron-phonon scattering then causes the carrier temperature to decay rapidly and the lattice temperature to increase until equilibrium is reached after around 30 ps.

The cooling of the hot carriers also triggers the increase of exciton and then bi-exciton populations, with peak populations at times of about 9 ps and 20 ps after the laser pulse. Many of these dissociate quickly back into free carriers, but some remain bound, even at high electron temperature, forming hot excitons and poly-excitons with a Boltzmann distribution at the carrier temperature. The STbX population and the resulting population of Frenkel defects then follow some 22 ps and 30 ps after the laser pulse has passed respectively. It should be noted that by this time the lattice temperature is sufficiently high that the proposed thermally activated Frenkel defect formation process will be considerably faster than radiative recombination of the STbX discussed by Mauri *et al.* [178].

Strictly speaking electron temperature only makes physical sense when the system is in equilibrium. In this highly dynamical system, the system is far from equilibrium such that plotting the carrier densities as a function of energy will give insight into

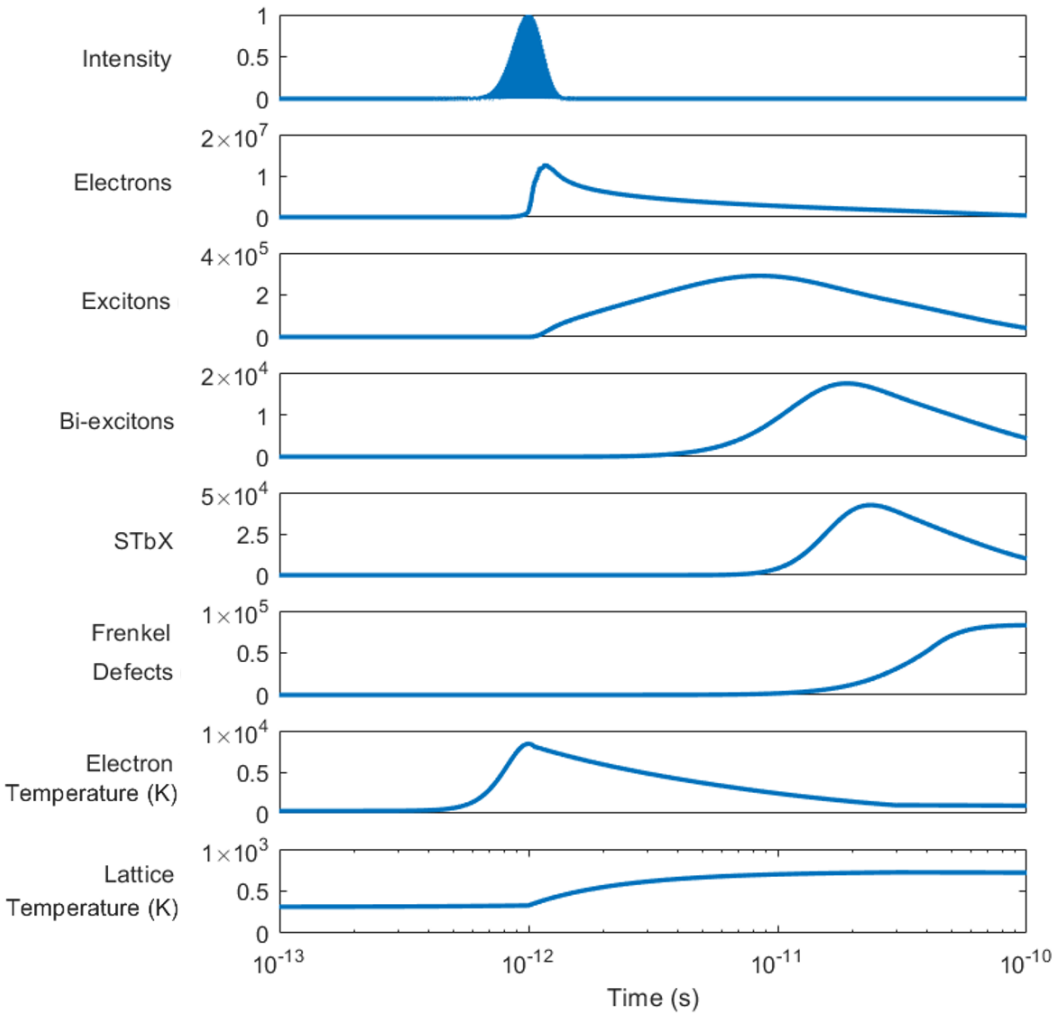


Figure 6.3 Time dependence of parameters simulated in the PDE model. The peak of the laser pulse is set to 1 ps to facilitate a logarithmic time scale capturing the range of dynamics. Through charge neutrality, the number of holes is equal to the number of electrons.

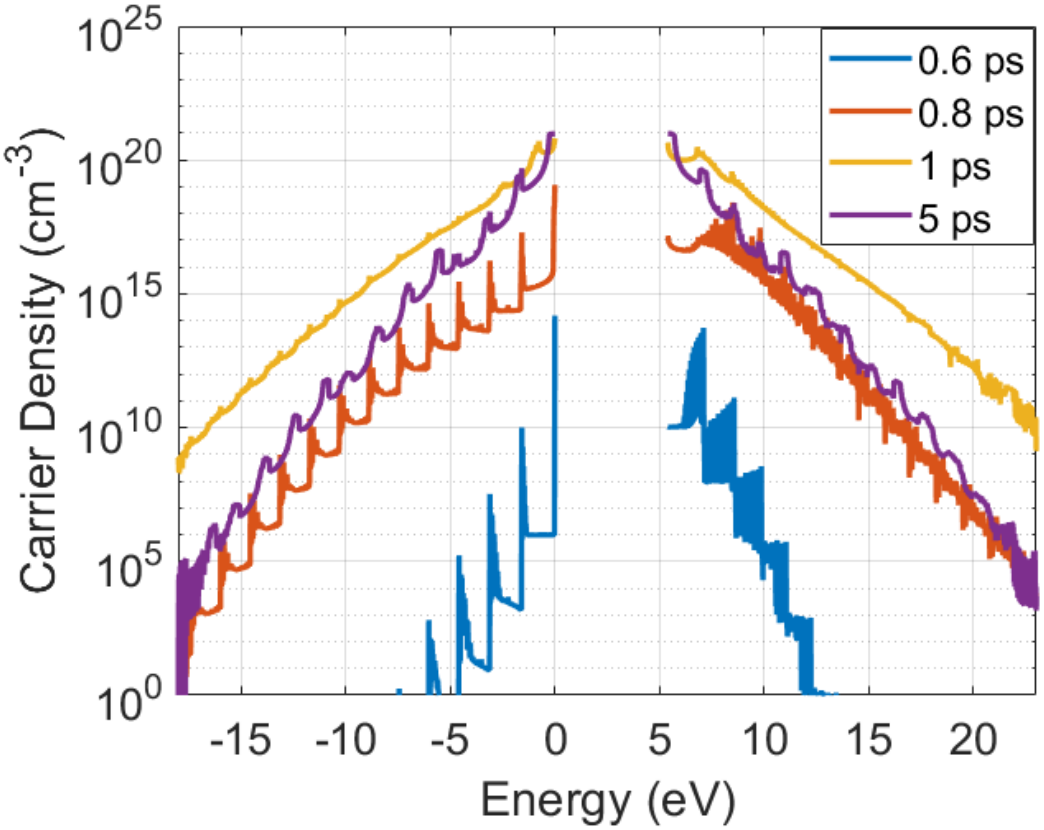


Figure 6.4 Carrier energy distribution at various times throughout the pulse where the zero of energy is the maxima of the valence band. Carriers of energy below zero are holes and carriers above zeros are electrons.

the dynamics. The energy dynamics at various times throughout and following the pulse are shown in Figure 6.4.

On a logarithmic-linear scale equilibrium carrier distributions are given by straight lines and deviation from this represents non-equilibrium dynamics. The gradient of the straight line gives an indication of the carrier temperature with shallower gradients representing higher temperatures. Initially photoionisation produces sharp deviations from equilibrium throughout. Scattering processes quickly thermalise the distribution such that an effective carrier temperature can be calculated. Carrier temperature grows quickly to thousands of degrees and that lattice temperature remains low for a much longer period. Following the pulse, carrier temperatures decay over tens of

picoseconds and thermalise with the lattice shown in Figure 6.3 with quasi-equilibrium temperatures for the carrier-lattice system given by Figure 6.2c.

6.3 Varying initial parameters

The model allows for additional exploration of the dependence of Frenkel defect generation on various pulse parameters. These parameters are also able to adjusted experimentally. Comparison of the theoretical results with experimental data over a wider range of initial conditions will enable exploration of more of the parameter space and add weight to the formation hypothesis.

6.3.1 Varying numerical aperture

The numerical aperture of the focusing lens has a drastic impact on the intensity distribution within the material. Lowering the numerical aperture will the increase the focal volume with an inverse power law relationship to the power of negative four and thus reduced the focal intensity by the same factor. Therefore the threshold pulse energy for defect creation (where the creation probability surpasses 1) should also increase significantly. Alongside lower spatial confinement, carrier diffusion is likely to play a lesser role as the spatial gradients will be lower. Experimentally, the numerical aperture of the focusing lens can be carefully controlled whilst utilising the same objective lens to maintain oil immersion by applying a blazed grating to the spatial light modulator. This allows control over the fill factor of the lens.

The change to the focal volume for a time-integrated pulse ignoring plasma effects can be seen in Figure 6.5.

Further arrays of single pulses of varying energies ranging from no visible damage upon 2000 pulses to significant graphitisation upon a single pulse were fabricated with numerical apertures ranging between 0.95 and 1.4. In addition, the set of differential

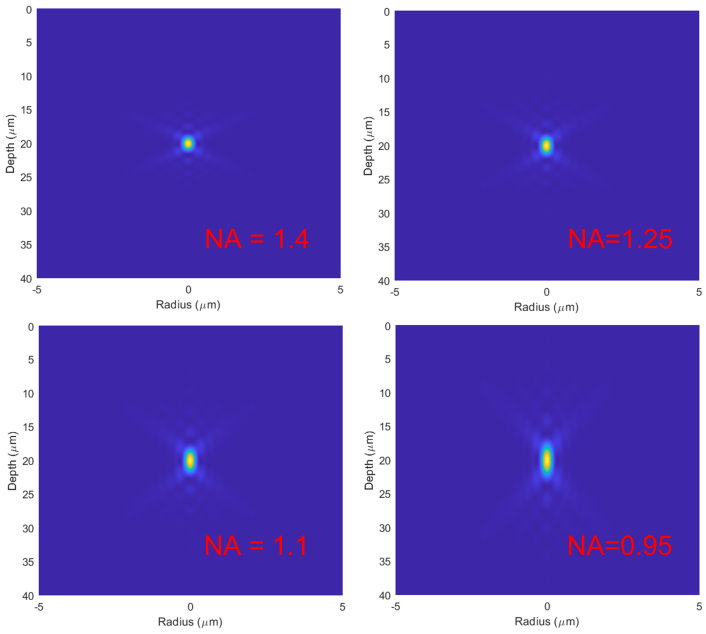


Figure 6.5 The increase in the focal volume as the numerical aperture is reduced ranging from NA = 1.4 to NA = 0.95.

equations were then solved for differing numerical apertures ranging between 0.95 and 1.4 and both experimental and simulated results are shown in Figure 6.6. As before, the shapes of the data-sets and relative distances between them are the important parameters when comparing to experiment rather than the absolute values of pulse energies due to the assumptions of perfect aberration correction and no losses of light during focusing.

The general trend that the lower the numerical aperture, the higher the threshold pulse energy, is visible in both the simulation results and the experimental data. However the required increase in pulse energy for NA = 0.95 is somewhat larger than predicted and the simulations predict a shift in the formation between numerical aperture of 1.4 and 1.25 not shown in experiment. This is possibly explained by a variation of the focal aberrations during the fabrication of these arrays as the aberration correction is very sensitive to slight changes such as sample drift, indicating that the array with NA of 1.25 had slightly less focal aberrations at the time of

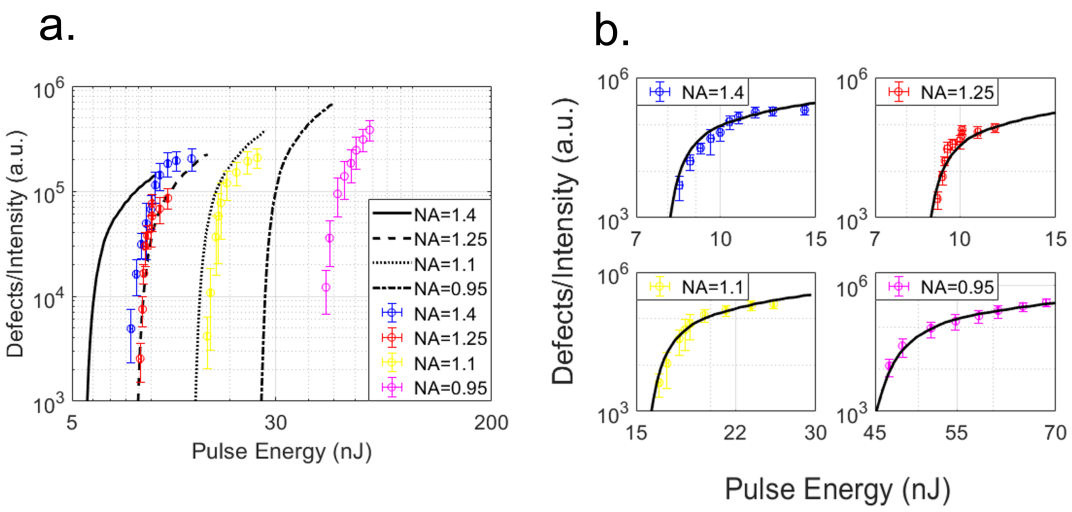


Figure 6.6 . Simulated (lines) defect generation probability as a function of pulse energy for differing numerical aperture of focus alongside experimental data (points). The numerical aperture's range from 0.95 to 1.4. b. Data and simulation for differing numerical aperture of focus overlaid to show agreement in the non-linearity. The y axis has arbitrary units (a.u).

fabrication than those around it. It could also indicate that the outermost rays passing through the objective do not contribute measurably to the peak focal intensity. Figure 6.6b shows the same experimental data with the simulation data-sets independently scaled in x and y and fit through least squares fitting as before to the experimental data for comparison of the non-linearity. The x scaling required for each dataset varied between a factor of 1.5 and 3, within the margin for error of optical aberrations. The y scaling was similar for each dataset at approximately a factor of 2 to 3. The overlaid simulations on the data show that dependence on relative pulse energy does not vary substantially with numerical aperture and the simulations fit well to the data throughout. The non-linearity of the generation does not appear to be affected by changing the numerical aperture of the focusing lens.

6.3.2 Varying pulse duration

A shorter pulse achieves the same focal intensity for a lower pulse energy but the total photoionisation is less for the same peak intensity. Phonon and carrier scattering do not change timescales depending upon pulse duration, therefore the ratio of energy gain to energy loss also changes. Impact ionisation becomes less important such that lower numbers of carriers are generated for a shorter pulse. Counter to that scattering events become less important relative to photoionisation during the pulse and defect creation occurs further after the decay of the pulse. A key difference is the onset of plasma effects in comparison to the proportion of the pulse that has passed. For short pulses, the entire pulse is contained within a short region such that the onset of plasma effects has a smaller impact than longer pulses whereby plasma effects can start to take affect whilst a large portion of the pulse is still to pass. Further arrays of single Ti:Sapphire pulses with pulse durations ranging between 120 fs to 1 ps were fabricated into the electronic grade material. Again, pulse energies were chosen with a minimum of 2000 pulses doing no visible damage and a maximum of a single pulse creating significant graphitisation. The effect of varying the pulse duration between 120 fs and 1 ps is shown in Figures 6.7a and b where, as with the numerical aperture, panel b includes a re-scaling of the individual simulation data-sets to provide best fits to the experimental data. The x scaling required for each dataset varied between a factor of 1.2 and 3, within the margin for error of optical aberrations. The y scaling was similar for each dataset at approximately a factor of 2.

The general trend shown in both experimental data and the simulation results is for shorter pulses to require higher pulse energies for defect generation. This is because, although shorter pulses achieve the same focal intensity for a lower pulse energy, they generate fewer carriers from the initial photoionisation at the same intensity and fewer carriers are generated through the secondary route of free carrier absorption

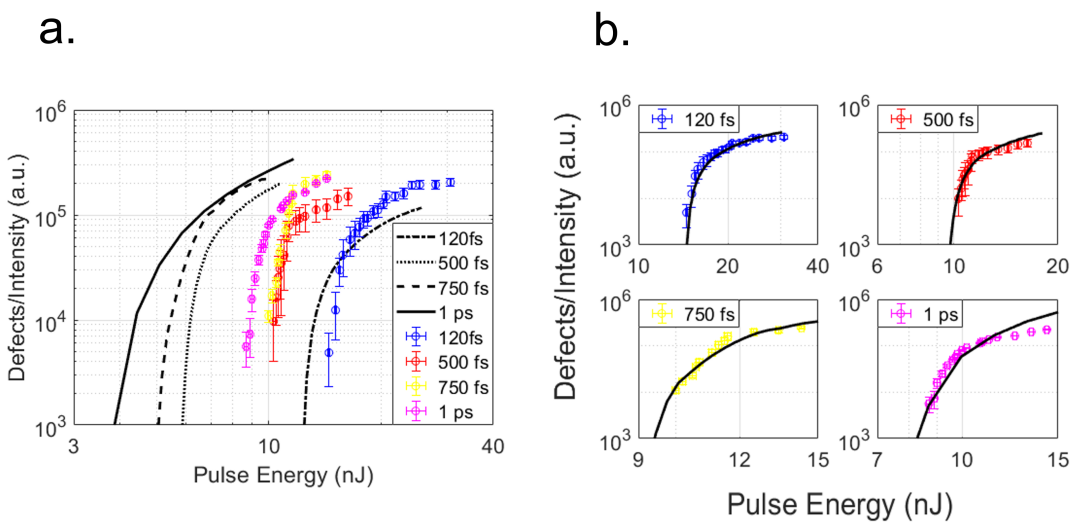


Figure 6.7 a. Simulated (lines) defect generation probability as a function of pulse energy for differing pulse durations alongside experimental data (points). The pulse durations range from 120 fs to 1 ps. b. The data and simulation for differing pulse durations are overlaid to compare the non-linearity.

and subsequent impact ionisation. This reduced carrier density per pulse also means that shorter pulses have a lower chance of graphitising giving a larger window between defect creation switch on and graphitisation allowing for more margin for error in the fabrication of defects. This trend is in qualitative agreement with Kurita *et al.* who showed that a train of shorter lasers pulse has a significantly lower chance of causing graphitisation than an equivalent train of long pulses [144] [213]. The work of Kurita *et al.* is multiple pulse processing where defects that have been formed likely influence the absorption profile of the laser for later pulses, whereas the work of this chapter is single pulse processing, however the two show agreement in the reduced probability of graphitisation. Potential future work could utilise shorter duration pulses in the fabrication of colour centres through laser processing due to this larger window.

The effect of this change is particularly marked in the results of the simulation for the 120 fs pulse, where the threshold for Frenkel defect generation is a factor of two larger than that for the 500 fs pulse. In the experiment only a 30% increase in

threshold is observed, which may indicate that the pulse envelope for the shortest pulses is less well-approximated by the Gaussian distribution used in the model. Experimentally, the observed non-linearity is again relatively unchanged; in contrast the model predicts a noticeable reduction in non-linearity for the longest pulses. The reduction in non-linearity observed in the model arises due to the competition between impact ionisation and Auger processes at the high carrier densities leading to a diminishing increase in maximum carrier density with an increase in pulse energy. In addition, the longer pulses are more affected by attenuation from plasma effects. The efficiency of impact ionisation or the attenuation is potentially over estimated in the model.

6.3.3 Varying wavelength

The light-matter interactions, generation of carriers, defects and damage by a pulse will be very sensitive to the wavelength of the light used. The photon energy is different which leads to differing photoionisation behaviour with a shorter wavelength giving a lower photoionisation non-linearity and achieving higher photoionisation yields at lower intensities. The change in wavelength also gives rise to a change in the focal volume, therefore a shorter wavelength requires less pulse energy to achieve the same peak intensity. This leads to a lowered threshold for defect creation, however, the reduced photoionisation non-linearity also leads to a lower effective threshold for graphitisation due to a higher carrier density being reached at a lower intensity.

A further array was fabricated using a frequency doubled Ytterbium laser outputting 170 fs 515nm pulsed light which broadens to $\sim$ 300 fs at the back focal plane of the objective lens for the effect of writing wavelength on fabrication to be tested experimentally. Changing the input wavelength from infrared (790 nm) to green (515 nm) allows for a tighter focus by a factor of 2.38 achieving 2.38 times higher focal

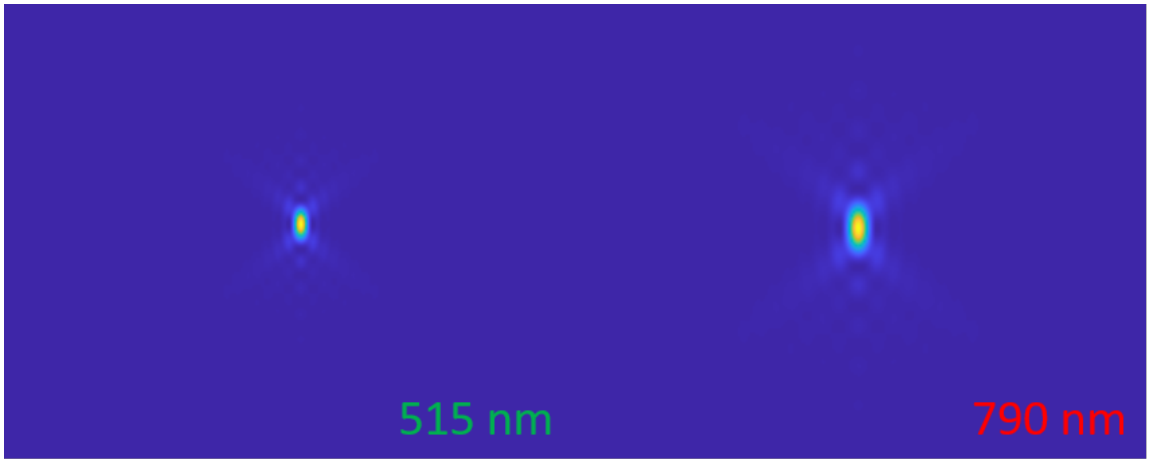


Figure 6.8 time-integrated focal volumes for light of 515 nm and 790 nm with no focal aberrations and no plasma effects. The reduced wavelength allows for a significant reduction in the focal volume leading to a 2.38 times increase in focal intensity for the same pulse energy.

intensities for the same pulse energy, the formation of defects should therefore occur at lower pulse energies. A time-integrated slice of the tighter focus assuming no plasma effects is shown in Figure 6.8.

In addition, the photon energy is larger for 515 nm light which leads to differing photoionisation behaviour. Less photons (three photons rather than five at the Γ point) are required to allow the transition of valence electrons across the bandgap and the canonical momentum gained at a particular pulse energy is greater due to the increased focal intensity, yielding a lower photoionisation non-linearity and achieving greater photoionisation yields at lower intensities. Cascade effects are also increased due to the larger photon energy producing a faster energy gain within the conduction band and the higher intensities from the tighter focus. These effects lead to a lowered threshold for defect creation, however, the reduced photoionisation non-linearity also leads to a lower effective threshold for graphitisation due to a higher carrier densities being reachable at a lower intensity.

As a different laser was used, different optics were used for adaptive aberration control and directing the light into the back focal plane of the objective lens. It should

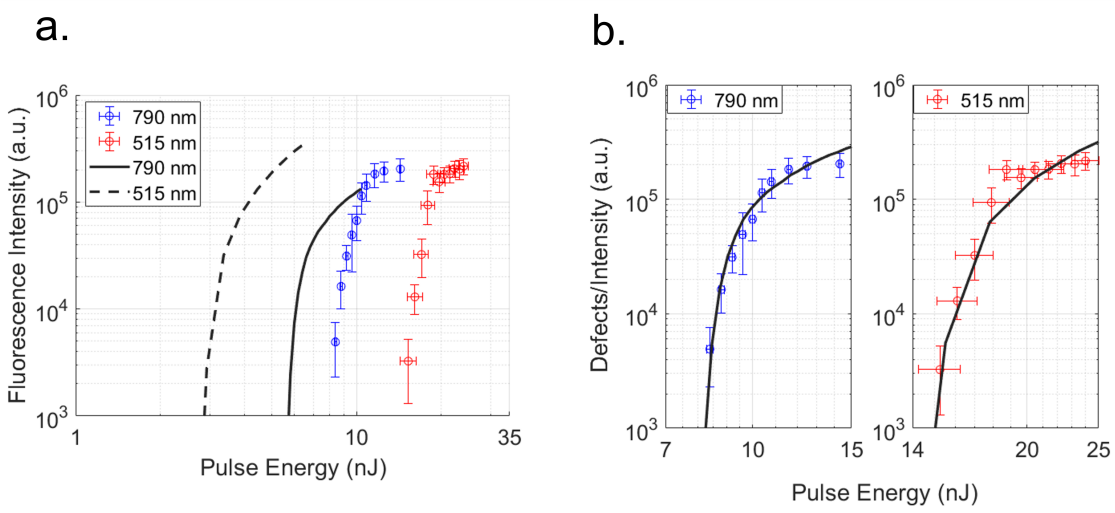


Figure 6.9 Simulated (lines) defect generation probability as a function of pulse energy for differing writing wavelengths alongside experimental data (points). The two wavelengths tested are 790 nm and 515 nm. The right-hand figure shows data and simulation for differing writing wavelengths overlaid with the simulation independently scaled in x and y to a best fit to compare the non-linearity.

be noted that the alignment of the green laser to the spatial light modulator proved difficult, thus there is likely some uncorrected aberrations in the array generated with this laser. Due to these aberrations, defect and damage formation are likely to occur at higher pulse energies than could be achieved given an optimised setup. In addition, the rotating wave-plate used to control the pulse energy for this system developed a recoil meaning there may be a small variation in pulse energy between sites that were repeated at the same pulse energy. Figure 6.9 shows simulated and experimental data-set for the wavelength dependence of defect generation.

The reduced photoionisation non-linearity and tighter focusing leads to simulated defect generation occurring at lower pulse energies than with the longer wavelength. This is in contrast with the experimental results that show that the shorter wavelength has a higher threshold pulse energy for defect creation. The difference is likely due to aberrations during the focusing of the 515 nm laser as there was some difficulty in

the alignment of the SLM. This experiment should be repeated with a less aberrated focal beam. The right-hand figure shows the simulated non-linearity curves scaled independently in x and y to best fit the experimental data in order to compare the trend with experiment. The simulation predicts small decrease in the non-linearity for the shorter wavelength that doesn't appear in experiment. The reason for this discrepancy is potentially due to the large error bars on the experimental data or an over estimation of plasma effects that lead to attenuation and a reduction in the degree of non-linearity.

6.3.4 Varying nitrogen content

The generation of defects within the diamond material is likely influenced by existing defects within the material. Deviations from a periodic lattice lead to the formation of states within the forbidden bandgap and likely significantly change photoionisation behaviour. In addition, these mid-gap states will act as traps for charge carriers through the Shockley-Read-Hall effect leading to a significant speed up of carrier recombination and potentially changing the potential energy surface required for further defect formation. In addition, they will change the absorption profile of the incoming beam. This is important for multiple pulsing experiments where the deviations from the periodic lattice are Frenkel defects, or for processing into a doped material where the deviations are dopant atoms. This is why it is often possible to generate graphite with a few pulses of a below threshold graphitisation pulse energy.

The samples used in this study were all type 1b single-crystal diamonds. A sample of concentration 1.8 ppm was supplied by DeBeers with the diamond cut and polished along a (110) surface. The other two samples used were supplied by Element Six with one sample being an electronic grade sample of 2 ppb nitrogen concentration as above, while the other was of concentration 150 ppb, both samples were (100) oriented. Prior

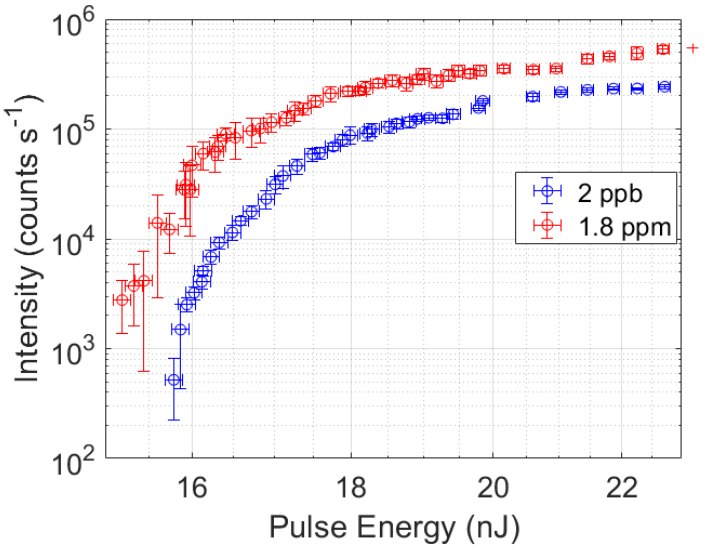


Figure 6.10 Dependence of the fluorescence behaviour of laser written Frenkel defects in diamond with the concentration of nitrogen within the material.

to the fabrication of vacancies within the diamond, cross-polar images were taken to study the relative strain within each sample with the selected region of fabrication chosen as that which had the lowest amount of relative strain. The experimental procedure was repeated for each of the samples and fluorescence intensity measured from the corresponding laser written sites. The background fluorescence from the 150 ppb sample was too high such that laser written sites appeared dark, therefore this sample was neglected from the analysis. Figure 6.10 displays the pulse energy relationship of the fluorescence intensity for the 2 ppb and 1.8 ppm sample.

Higher nitrogen content appears to shift the graph to lower pulse energies and to greater fluorescence intensities suggesting that the dopant allows for an easier formation route as the dopant atoms will naturally act as scattering centres and concentrators of laser energy.

In addition, spectral analysis reveals that some sites within the array of higher nitrogen contain a mix of vacancies and NV. It is plausible that the laser creates a vacancy as nearest neighbor to a substitutional nitrogen atom, the chance of which is

one thousand times higher moving from ppb to ppm. NV centres are much brighter than Frenkel defects, hence will dominate fluorescence intensity at low pulse energies. Indeed, the lowest pulse energies that fluorescence was observed yielded mainly no fluorescence and the small percentage that fluorescence had a significant fluorescence intensity and spectral features containing NV centres.

This parameter was not explored theoretically as the presence of nitrogen within the diamond lattice changes the band-structure and Fermi level and likely changes the absorption profile of the incoming laser pulse. There are many unknowns here which would need to tied down in order to solve the differential equations for a doped diamond material.

6.3.5 Modelling focal aberrations

In the above analysis, the focal aberrations were assumed to be zero to simplify the analysis. However, in the experimental apparatus perfect aberration correction is realistically impossible which is why scaling parameters were required to compare the model to experiment as described earlier.

It is possible to simulate focal aberrations by applying a phase shift $\phi(x, y)$ to the intensity at the back focal plane of the objective lens. An arbitrary aberration can be described by a superposition of orthonormal modes on a unit disk. Due to the large mismatch in refractive index, the most likely aberration to appear experimentally is the spherical aberration (for example if the wrong amount of correction was applied.). A spherical aberration can be simulated in the same way one might appear in experiment, by scaling the phase applied to the SLM, ϕ_{SLM} such that it no longer exactly cancels out the inherent spherical aberration from focusing into a high refractive index material, ϕ_{Sph}. This way a spherical aberration of arbitrary size can be studied.

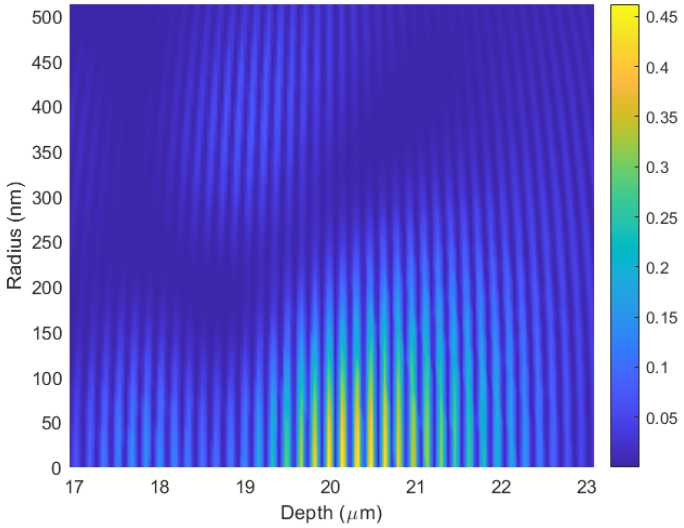


Figure 6.11 Instantaneous light energy density distribution given a focal depth at 20 μm but spherical aberration correction set to 15 μm yielding a positive spherical aberration.

$$\phi(x,y) = \phi_{Defocus}(x,y) + \phi_{Sph}(x,y) + \phi_{SLM}(x,y) \tag{6.2}$$

This aberrated phase can be substituted into the wave equation governing the propagation yielding the aberrated intensity distribution. Through comparison of the peak intensities from the aberrated beam and the perfectly focused beam, the Strehl ratio can be calculated. Figure 6.11 shows the effect of a positively spherically aberrated beam where $\phi_{SLM} = -0.75\phi_{Sph}$. This is the distribution considering no carrier generation and plasma effects.

The positive spherical aberration pushes the focal depth deeper, vastly extends the axial extent of the pulse and reduces the peak intensity by over a factor of 2. This will impact the defect generation two-fold, the reduction in spatial confinement and symmetry will reduce the positional accuracy and control of the generation and the threshold pulse energy will significantly increase due to the reduction in peak focal intensity. This explains why uncorrected or poorly corrected focuses achieve no damage regardless of high pulse energies and why absolute pulse energy is not the best

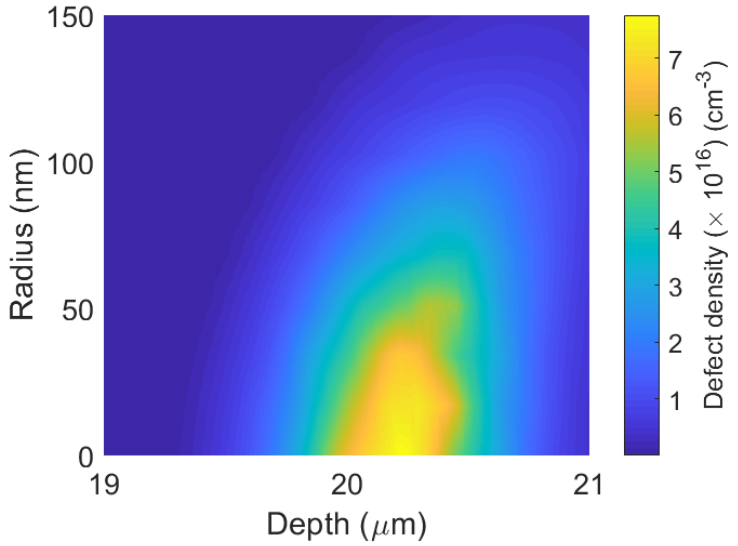


Figure 6.12 The distribution of Frenkel generated following a positively spherically aberrated pulse of pulse energy 12 nJ. Here the spherical aberration correction applied to the SLM had an amplitude of $-0.75\phi_{Sph}$. The effect is to shift the generation to a deeper depth and a higher pulse energy is required to attain generation. In addition, the generation appears to gain a tail to deeper depths at larger radii caused by a similar asymmetry in the focused light.

metric for determining how much modification to the material will be achieved ahead of time. Instead a better way to determine the pulse energies to use for a particular experiment is find the pulse energy required to graphitise the diamond and minimise through iterative aberration correction. Following this reduce the pulse energy in small increments.

Inputting an aberrated initial focus into the set of coupled differential equations can give information on the sensitivity of processing to a more realistic laser pulse. Figure 6.12 displays the distribution of Frenkel defects from an initial pulse set with $\phi_{SLM} = -0.75\phi_{Sph}$. Here the pulse energy is increased such that the peak intensity is matched that of the unaberrated case, in this case a pulse energy of 12 nJ.

The effect of the spherically aberrated focal volume is to shift the generation to a deeper depth and a higher pulse energy is required to attain generation of defects.

Careful application of these aberrations could potentially be utilised in practice to combat the shift to shallower depths caused by the plasma attenuation. In addition, the generation appears to reach deeper depths at larger radii meaning that the generation will no longer be caused by a similar asymmetry in the focused light.

It is rare that the correction will be out to such a degree as shown above. For a smaller spherical aberration, the reduction in focal intensity and spatial asymmetry will be lower however, there is also likely small aberrations from other sources such as misalignment of the beam path. These are possible to correct for by adding phase patterns to the SLM but it is unlikely that the correction will be perfect. A realistic Strehl ratio experimentally is of order $\sim$ 0.8 - 0.9.

Other common aberrations that may occur are astigmatism and coma. These arise if the light passes through or reflects off an optic at an angle to the optic axis or if the optic is slightly asymmetric. Applying the relevant Zernike polynomials to the phase pre-focusing allows for modelling of the aberrated light intensity distribution. As these aberrations contain an azimuthal component, the resulting intensity distribution is no longer cylindrically symmetric and a third dimension is needed to describe the full distribution. The addition of another dimension makes the full coupled partial differential equation model too computationally expensive to solve numerically, therefore to study the effect of these aberrations, I will calculate the no-plasma 3D light intensity distribution at peak time for various aberrated beams and measure the Strehl ratio as a function of the aberration amplitude. This can be tentatively thought of as the inverse of the pulse energy increase required for defect formation.

The phase that leads to an astigmatism can be described by

$$\phi_{astig}(r,\theta) = r^2 \sin(2\theta + \Delta\theta) \tag{6.3}$$

and coma,

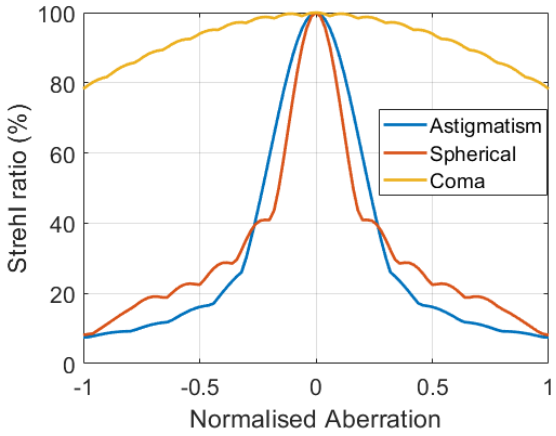


Figure 6.13 Strehl ratio against applied aberration amplitude for astigmatism, spherical and coma aberrations.

$$\phi_{coma}(r,\theta) = (3r^3 - 2r)\sin(\theta + \Delta\theta) \tag{6.4}$$

The axes which these are aligned can be adjusted by adjusting the phase in the sine functions. Figure 6.13 shows how the Strehl ratio changes given different amplitudes of each of these aberrations as well as spherical aberration.

All three are symmetrically peaked functions that quickly cause a significant drop in focal intensity given a small level of aberration. As the laser writing process is highly non-linear with respect to focal intensity, it is clear to see how a small aberration can alter a pulse from causing graphitisation to having no effect on the diamond. This effect is only compounded if the aberration is a superposition of more than one mode. The coma aberration may not appear to have too much of an effect on the Strehl ratio, however, it causes a significant deviation in the lateral positioning of the focus, vastly reducing positional accuracy. Aberration control is not only important for controlling the number of defects generated but also for the positional control of the fabrication.

6.4 Summary

This chapter has described an experimental study and theoretical into the non-linearity of the laser processing from a single pulse. Single pulses of femtosecond laser light were focused deep into the material following aberration correction yielding the formation of Frenkel defects. The defect gives a fluorescent signature at 740 nm; the intensity of fluorescence measured from the focal region gives a metric for the number of defects that are generated. Laser and material parameters such as pulse energy, pulse duration, numerical aperture and dopant concentration were carefully varied and the change to the response of the crystal was quantified by comparing the fluorescence intensity. Due to the low quantum efficiency of the vacancy fluorescence cycle, visible fluorescence is only possible when many vacancies are present. For the generation of colour centres such as the nitrogen vacancy centre, relatively few vacancies are desired as any additional defects couple to the spin and reduce the spin coherence lifetime. In this study, vacancies were generated from well below this threshold to well above this threshold to understand the dynamics of formation and how this changes with laser parameters. It is clear that the single pulse laser writing process is highly non-linear and the threshold for defect generation is highly dependent upon the laser parameters however the level of non-linearity appears only weakly dependent upon laser parameters.

The theoretical model developed in chapter five appears to explain most of the experimental data. The coupled differential equation model describes an ultra-low pulse energy regime for ultra-fast laser processing in diamond in which fabrication within the material displays further non-linearity with respect to focal intensity than the electron generation. Plasma effects are critical in explaining the highly non-linear generation observed with respect to pulse energy. For very low pulse energies, not enough carriers are generated in the initial photoionisation for plasma effects to become

important, such that most of the energy passes straight through the material. In contrast, a higher energy pulse generates a significant number of initial carriers which leads to a strong plasma absorption which in turn generates further carriers. For these pulses a significant proportion of the light becomes absorbed. For the highest energy pulses a sufficient density of plasma is generated that part of the beam is reflected back and therefore will not pass through the focus. This goes someway to explaining the saturation alongside the fact that the number of defects generated becomes of a similar order to the number of electrons. It also highlights the importance of finely controlled aberration correction during the experimental procedure. In addition, for all but the lowest energy pulses, the simulated spatial distribution of defects is shifted to shallower depths than the initial focal depth due to beam attenuation. This is potentially crucial information for improving the precision of laser fabrication inside transparent media.

This hypothesis is also consistent with the experimental results that vacancies (and therefore colour centres post an annealing step) are often found in the surrounding area of high damage regions. The surrounding region from that high damage region will have received a lower energy density irradiation and thus will be in the sweet-spot for vacancy generation.

Yurgens *et al.* recently showed that the use of a truncated hemispherical cubic zirconia solid immersion lens (t-SIL) could drastically reduce the threshold write-pulse energy for vacancy creation and allow for generation of colour centres close to the diamond surface [147]. They used single 35 fs, 800 nm pulses focused through a 0.9 numerical aperture air lens into the t-SIL and achieved vacancy creation at pulse energies down to 5.8 nJ. Without the use of the t-SIL, they were unable to generate vacancies up to the pulse energy limit of their laser (52 nJ). The reason for this drastic reduction in pulse energy threshold is likely due to a higher spatial confinement of the laser focus by the t-SIL allowing for much higher focal intensities at low pulse energies

than the traditional optical methods used in this work.

Single pulse laser writing for this study was performed by myself and Patrick Salter and fluorescence characterisation was conducted by myself and Rajesh Patel. Numerical integration of the differential equations in MATLAB and fitting of the model to experimental data was undertaken by myself. Discussions with Jason Smith, Patrick Salter and Joanna Zajac were undertaken on the presentation of data.

Chapter Seven

Enhancement of Silicon Vacancy Ensembles

7.1 Introduction

In order to be useful for quantum technologies, Frenkel defects need to be converted into colour centres, often consisting of X-vacancy where X is a dopant atom. This has been demonstrated in the past for nitrogen vacancy (NV) centres via thermal annealing where vacancies diffuse by random walk and reach a substitutional nitrogen atom [6]. Another interesting colour centre is the SiV centre.

The different structure of this defect is interesting in the context of this work as the formation processes involved may differ from those of NV centres which have been studied previously. Therefore, laser processing of a silicon doped sample may give some insight into both the formation mechanisms and the fundamental laser interaction with the material. In addition, expanding the laser processing to engineer group IV colour centres will help pave the way to the development of a solid-state quantum technology and cement laser processing as one of the predominant engineering techniques. A major challenge of engineering this centre is that the SiV centre is a lower potential energy state than substitutional silicon so obtaining a sample with a sufficiently low

dopant level introduced during growth to be able to distinguish single defect creation is challenging. In this regard silicon is normally added to samples post growth via implantation techniques and indeed the majority of studies into this defect rely upon implanted centres.

Recently, laser ablation of silicon nanoballs above the surface of the diamond has demonstrated the ability to generate near surface SiV^- centres, however with little to no positional control and a stochastic yield [86].

7.2 Method

The diamond sample used in this study was a 110 silicon doped type 1b diamond supplied by DeBeers with a significant SiV^- photoluminescence background. The sample background fluorescence comes in bands of bright and dark (Figure 7.1) corresponding to significant dislocations within the sample and at interfaces between differing levels of silicon dopant incorporated during growth of the crystal. These bright and dark bands are identified via spectroscopy to contain significant numbers of SiV^-.

Single pulses of 300 fs Ti:Sapphire light were focused 10 μm into the material generating an array with 5 μm pitch where the pulse energy varied between rows. Pulse energies were chosen such that the highest energy pulses graphitised upon 2 successive pulses and the lowest energy pulses produced no visible damage upon irradiation of 2000 pulses. Some of these sites were processed within the bright band regions and some within the dark-band regions. Twenty repeats were written at each pulse energy to build up statistics. The sample was then globally annealed in a nitrogen environment for 3 hours at 1000 °C to enable diffusion of laser generated vacancies and healing of laser damage. A second array was laser written into the diamond but not annealed.

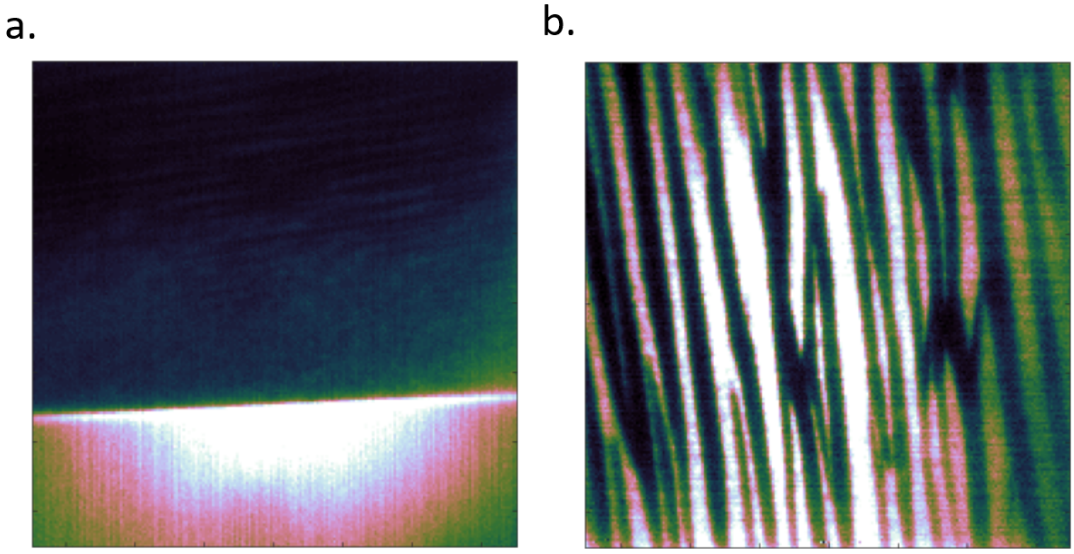


Figure 7.1 Bright and dark bands within the sample. a. A differential update of the dopant level during growth leads to a significant difference in fluorescence intensity across the interface. b. Strata of differing fluorescence intensity in the sample background corresponding to dislocations leading to variations in the density of SiV^- ensembles.

Following this, fluorescence was collected between 590 nm and 900 nm at liquid helium temperature (4 - 17 K) and room-temperature with 532 nm excitation. Excitation at 660 nm and 915 nm were also performed to measure whether there was any SiV^0 present. Photon autocorrelation measurements were carried out on laser-written sites using the Hanbury-Brown and Twiss method using single photon avalanche photodiodes with timing resolution $\sim$ 500 ps. Photoluminescence excitation (PLE) spectroscopy was used to probe the ZPL's of the annealed SiV^- ensembles at temperature T = 4.2 K. To determine the concentrations of non-fluorescent defects within the bulk material, electron paramagnetic resonance (EPR) spectroscopy was performed.

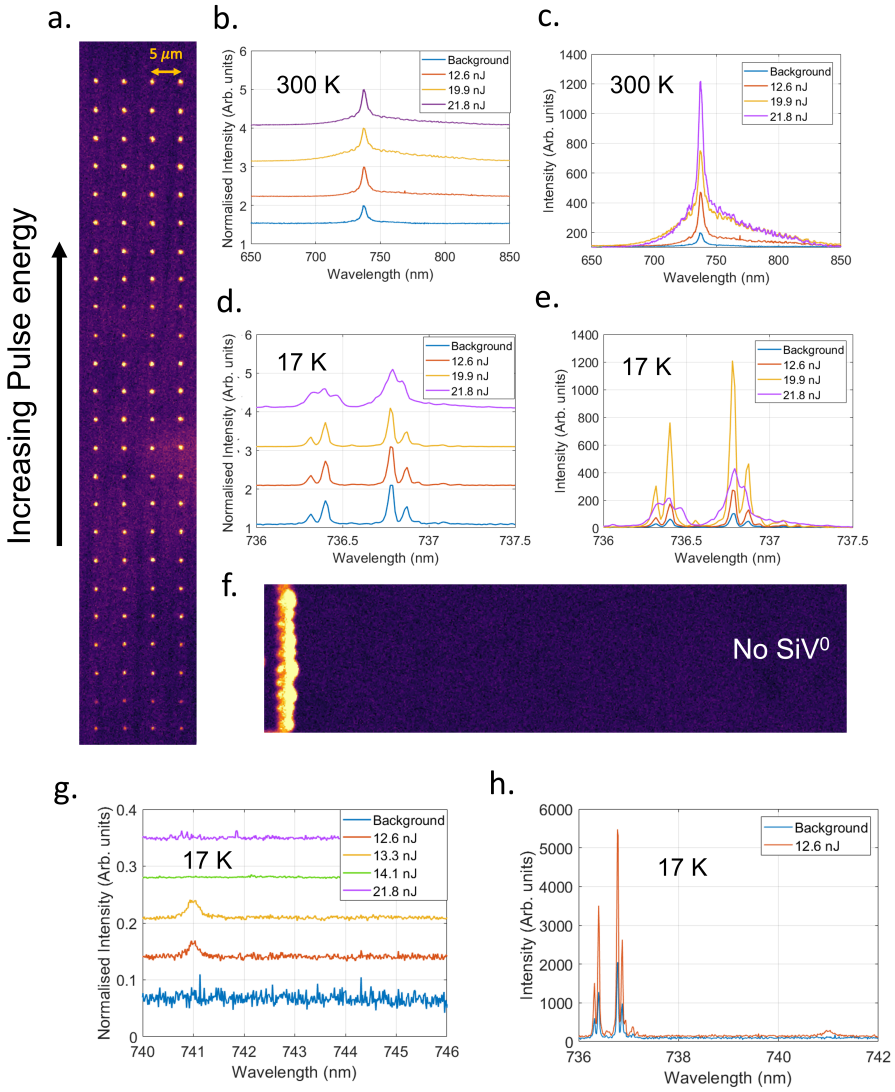


Figure 7.2 a. An image of the laser written array with no anneal taken at 532 nm excitation, 20 repeats were generated for each pulse energy. Background fluorescence is ensemble SiV^-. b. Normalised room-temperature spectra of laser written sites under an excitation wavelength of 532 nm. c. Room-temperature spectra of laser written sites. d. Normalised spectroscopy undertaken at low temperature under an excitation wavelength of 532 nm. e. Low temperature spectroscopy of the SiV^- lines for various pulse energies. f. An image of the array taken with 915 nm excitation. Laser written sites remain dark, graphitic markers are bright. g. Low temperature spectroscopy of the GR1 line for various pulse energies. h. A fluorescence spectrum of a laser written site and background indicating a near 3 times enhancement in the density of SiV^- and a small GR1 peak at 741 nm.

7.3 Results

Figure 7.2a shows a photoluminescence image of an array immediately after laser writing. Auto-correlation measurements reveal no anti-bunching indicating that these are ensembles. This is to be expected given the large SiV^- background of the sample. Room-temperature spectroscopy (Figure's 7.2b and 7.2c) carried out with an excitation wavelength at 532 nm reveals a significant increase in brightness of the 737 nm line from all processed sites which broadens at the higher pulse energies ($>$ 19 nJ). Low write-pulse energy sites fluoresce intensely at 737 nm with no broadening compared to the background. Low temperature spectroscopy of the unannealed sites reveals that the 4 spectral lines of the SiV^- all brighten significantly following a single laser pulse. At high pulse energies (21.8 nJ), these broaden and become distorted, however at lower pulse energies ($<$ 20 nJ) a significant enhancement is seen without broadening or distorting of the spectral lines. These spectra provide compelling evidence that laser writing is able to generate dense SiV^- ensembles from a single pulse without the need for an annealing step. However single pulse laser writing is known to produce Frenkel defects [6] [7] and other damage (voids/sp^2 hybridised carbon) [29] [174]. Figure 7.2f shows the same region of the sample illuminated with 915 nm excitation. No fluorescent sites can be seen except for the laser written graphitic marker lines. This indicates that there is no SiV^0 within the laser written sites. A small GR1 peak at 741 nm is observed for the lower pulse energy sites which disappears for pulse energies above 14 nJ (Figure 7.2g). The peak at 741 nm and the broadening of the SiV^- lines at higher pulse energies indicates that the laser is producing vacancies and other damage alongside increasing the density of the SiV^-. Figure 7.2h displays a spectrum and background inclusive of the the SiV lines and GR1 peak showing enhancement of the SiV signature by approximately a factor of 3. The GR1 peak is reduced compared to expected levels [7], indicating that there may be some quenching process taking place.

Following a global thermal anneal at 1000 °C for 3 hours, room-temperature spectroscopy at 532 nm (Figure's 7.3a and 7.3b) revealed the signature SiV^- peak at 737 nm alongside varying amounts of NV fluorescence dependent upon the write-pulse energy indicating that some of the vacancies which formed during the laser writing process had diffused to reach substitutional nitrogen within the crystal. Low temperature spectroscopy (Figures 7.3c and 7.3d) reveals no broadening of the SiV^- line even at the higher pulse energies indicating that any additional laser damage has been annealed away. In addition, the GR1 peak at 741 nm disappeared. This indicates that the additional laser damage generated was annealed away and some was converted into NV ensembles. Figure 7.3e indicates that the anneal slightly reduces the intensity of the SiV^- sites, although still a significant enhancement above the background, but also removes the GR1 peak, "healing" some of the additional laser damage.

PLE spectroscopy reveals laser written SiV ensembles with a spectral line-shape matching that of the sample background with a small tail to higher frequencies and roughly twice the background count rate (Figure 7.3f). Whilst these line-shapes likely contain multiple overlapping centres, a bi-Gaussian was fit with a spectral linewidth of 3.489 GHz at a central frequency of 406.712 THz and of 7.617 GHz at a frequency of 406.72 THz. The background SiV ensemble is similarly fit with a bi-Gaussian distribution with a spectral linewidth of 3.557 GHz at 406.712 THz and of 7.518 GHz at 406.72 THz. This shows that the laser process does not broaden the ensemble linewidth indicating that additional unwanted damage to the diamond is minimal and linewidths are likely limited by the inhomogeneity of the diamond. These linewidths are of a similar order to CVD grown SiV^- ensembles within the literature [71] [72]. Individual SiV^- peaks could potentially be distinguished through hole burning [72] [214].

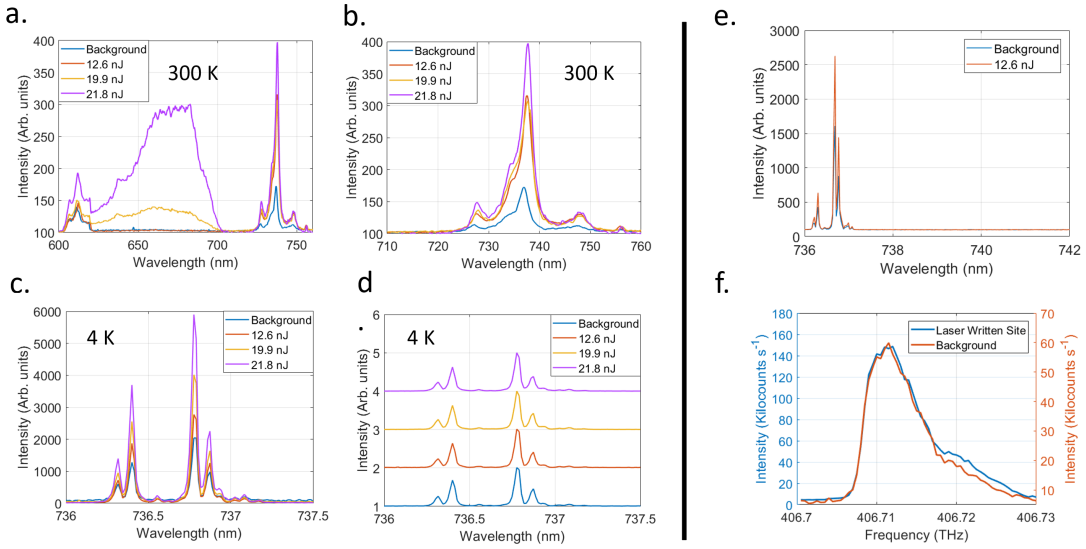


Figure 7.3 a. Room-temperature spectra of laser written and annealed sites of increasing pulse energies under an excitation wavelength of 532 nm. b. Room-temperature spectra of the zero-phonon line of the laser written and annealed sites. c. Examples of spectra taken at 4 K from a laser written and annealed site d. Normalised examples of spectra taken at 4 K from a laser written and annealed site to highlight that no broadening occurs e. A fluorescence spectrum of a laser written site and background post an annealing step indicating that the near 3 times enhancement in the density of SiV^- remains and the GR1 peak has disappeared. f. Photoluminescence excitation spectroscopy of a laser written site and the sample background.

7.4 Discussion

The enhancement of the 737 nm SiV^- ZPL by a single laser pulse with no thermal anneal suggests that the formation mechanism for these centres is different from the traditional laser writing formation mechanism. Evidence for the formation of Frenkel defects during the single pulse is seen, but also significant enhancement of the SiV^- signal. This indicates that more SiV's are being generated within the pulse which strongly suggests a mechanism different from the creation and diffusion of lattice vacancies. The observation of SiV^- generation without thermal annealing tentatively suggest a mechanism involving laser-induced dissociation of "passivated" SiV complexes rather than the recombination of thermodynamic unstable substitutional silicon and

vacancies. The exact nature of these passivated defects requires further investigation but may provide a path towards SiV-background free samples by enhancing their formation further during growth. DFT suggests many stable complexes have no allowed optical transitions, however, both SiV-H and SiV_2-H have allowed optical transitions in the infrared with the latter being associated with the experimentally identified WAR3 EPR centre [215] [216]. Furthermore, the abundance of H during CVD growth suggests the formation of a significant amount of SiVH-X defects [215]. Si-N complexes may also be able to explain the enhancement of SiV^- from a single laser pulse [217]. If the conglomerate is a Si-N complex, the laser processing may be breaking the bonds between them generating SiV^- centres and substitutional nitrogen alongside lattice vacancies. This would correlate with the formation of NV centres seen upon annealing. Bulk EPR spectroscopy was performed to determine whether these defect complexes exist, the results shown in Figure 7.4. These results put upper limits on the bulk concentrations of various defect complexes within the material.

Concentrations of 5 $\pm$1 ppb for SiV^0, and 99 $\pm$ 10 ppb for N_s^0 dominated the EPR signals. The concentration of both SiV-H^0 and SiV2-H^0 are both below the limit detectable by EPR ($\sim$ 0.5 ppb). Signals corresponding to Si-N complexes are not seen. These very low concentrations suggest that these defects are not the conglomerates being broken up during laser irradiation as the enhancement of SiV^- ensembles from the laser irradiation occurs at all irradiated sites above a pulse energy of 15 nJ. A potential defect that have not been ruled out by photoluminescence and EPR spectroscopy is the SiV^{2-} [217]. DFT studies suggest that SiV^{2-} does not fluoresce or produce an EPR signal making it difficult to observe [218]. Upon laser irradiation of a SiV^{2-}, the extra electron would become photoionised and join the plasma generated by the laser pulse and potentially become trapped by nearby Frenkel defects that form during irradiation leading to a significant gain in the density of SiV^- ensembles. Therefore, we hypothesise that the laser generates a cluster of Frenkel defects as before

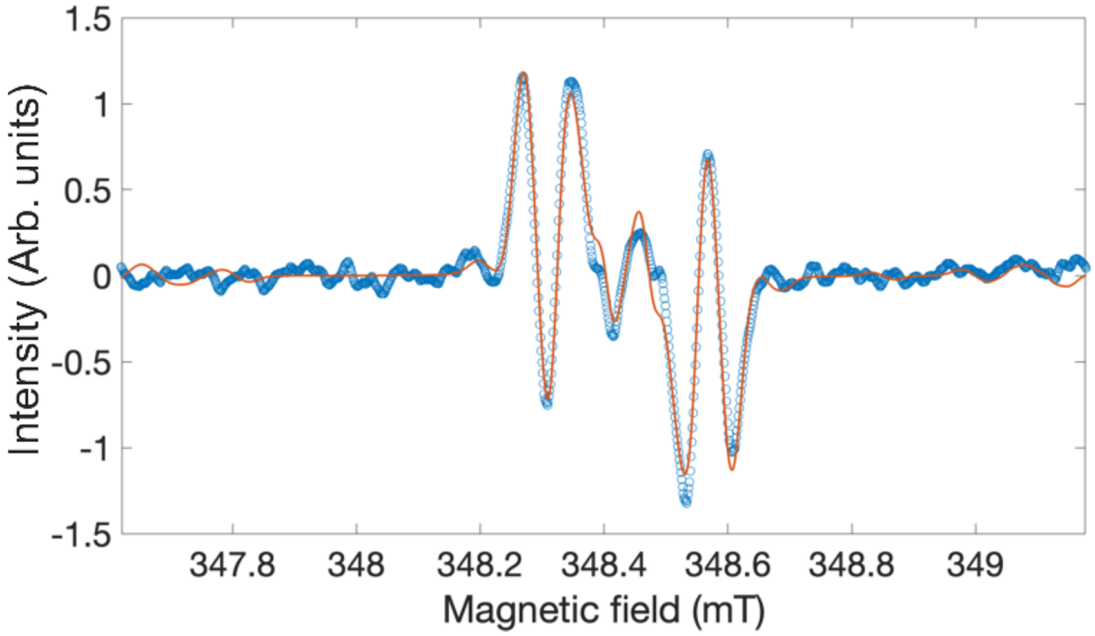


Figure 7.4 Bulk electron paramagnetic resonance spectroscopy of the silicon doped diamond material showing the first derivative of the absorption spectrum against magnetic field strength. Four peaks are identified indicating relative concentrations of N_s^0 and SiV^0. Crucially signals corresponding to hydrogen related complexes are not seen.

[7], after which the following reaction takes place.

$$SiV^{2-} + SiV^{-} + V^{0} \rightarrow 2 \times SiV^{-} + V^{-} \tag{7.1}$$

Negatively-charged vacancies (ND1 defects) are invisible in photoluminescence except in large quantities. This charge trapping would explain the apparent low levels of GR1 produced by the laser at the higher pulse energies. Further evidence that this is a charge state switching driven formation can be seen when switching between excitation wavelengths. Figure 7.5a displays the photoluminescence count rate from a laser written site following immediate switching of the excitation wavelength from 532 nm to 660 nm. The count-rate immediately increases, the opposite effect can be seen when switching from 660 nm to 532 nm.

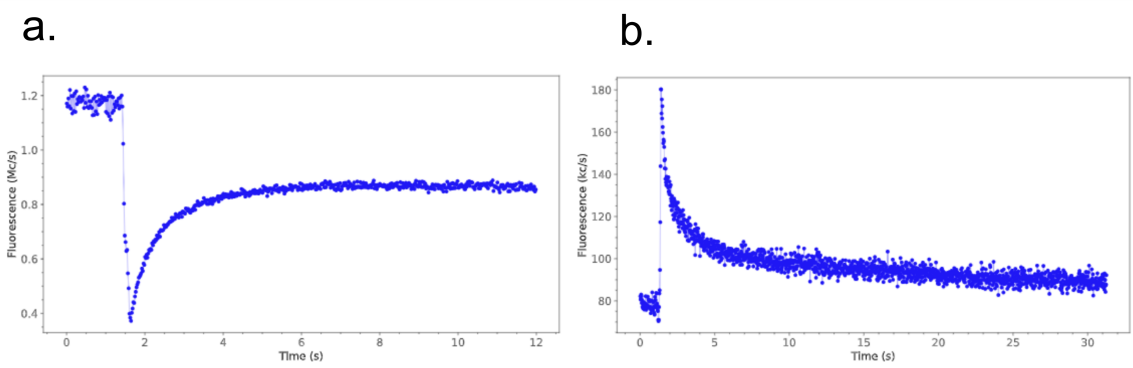


Figure 7.5 a. Time trace of fluorescence intensity of a laser written site following switching of the excitation wavelength from 532 nm to 660 nm. b. Time trace of fluorescence intensity of a laser written site following switching of the excitation wavelength from 660 nm to 532 nm

The stability of the SiV^{2-} centre will be highly dependent upon the Fermi level. EPR measurements indicate that the average nitrogen concentration throughout the sample is roughly 100 ppb which shouldn't be high enough to enable stable SiV^{2-}. However, the dopant levels were altered in discrete steps during growth such that locally the nitrogen level may be high enough to allow this. Some laser writing sites were processed at the interface between two dopant levels. The exact concentrations of nitrogen in each region are unknown. Figure 7.6 shows how the behaviour of the laser written sites changes going into a region with a lower level of dopant.

The interface has a significant effect on the visibility and contrast of laser written sites relative to the background. With 532 nm excitation, the region below the line appears bright and laser written sites cannot be seen. With 660 nm, the region appears dark and sites appear in high contrast. In the region below the interface, spectroscopy reveals no significant enhancement of the SiV^- ZPL and significant broadening, in contrast with large enhancement and no broadening above the interface, indicating that the process is highly dependent upon the amount of dopant in the material and Fermi level. The different excitation lasers are also likely driving differing

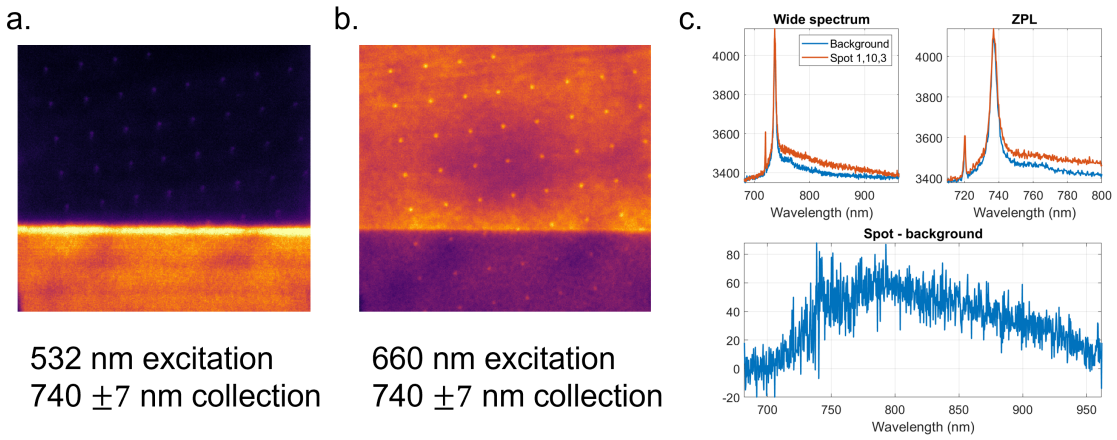


Figure 7.6 Laser written points on either side of an interface between differing levels of dopant. Top of Figure's a and b show the region with higher nitrogen and silicon dopant and below the line is a region of lower dopant. a. Excitation in 532 nm with a narrow bandpass filter around the SiV^- zero-phonon line. b. Excitation in 660 nm with a narrow bandpass filter around the SiV^- ZPL. c. Spectroscopy take in the region of low dopant with 660 nm excitation and no collection filtering.

charge dynamical behaviours hence the differing contrast and photochromic behaviour. Further investigation is necessary to determine the full charge dynamical behaviours including potentially systematically laser writing into different levels of dopant and with a new sample where the dopant levels are known. As the dopant levels are not uniform throughout the sample, both hypotheses of conglomerate defects being broken up and charge state switching cannot be ruled out. Some work on the charge switching between negative, neutral and double negative charge states of the SiV centre has been investigated in ref. [219].

Photoluminescence spectroscopy of the annealed sites reveals that the linewidths of the laser written SiV ensembles are comparable with that of the background from the crystal. This suggests that the laser produces only small amounts of additional damage and any extra damage surrounding the ensembles is healed during the annealing step and does not majorly disturb the optical coherence.

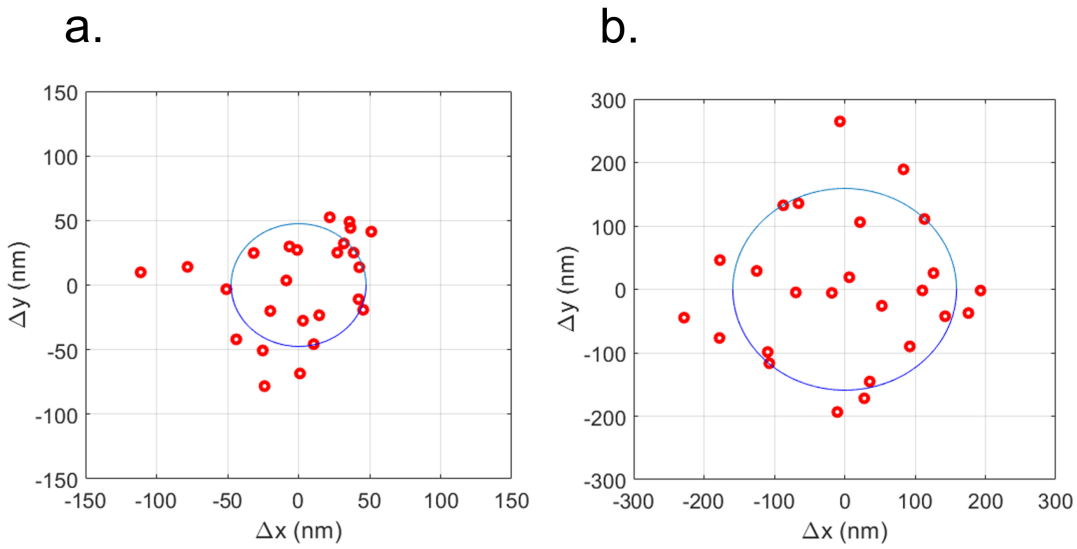


Figure 7.7 Positional accuracy of the laser processing. The positional data is convoluted with the point-spread-function of the microscope as these are ensemble centres, therefore this is an upper limit rather than the true positioning. a. 25 centroids of laser written sites pre-anneal. b. 25 centroids post anneal. Shown in blue is the FWHM least likelihood fitting of the 2D Gaussian function that best fits the centroids.

As these centres are not singles, a positional accuracy map based upon fitting a grid to a fluorescence image does not give an accurate representation as the positional data will be convoluted with the point-spread-function of the microscope. However from analysing the photoluminescence images, an upper limit for the deviation of formation from the target location can be estimated. By fitting 2D Gaussian functions to the photoluminescence image, the centroid of each laser written site could be found. Comparing these locations with respect to a target grid, an upper limit to the positional accuracy convoluted with the point-spread-function of the microscope could be found. The target grid was fitted with respect to the fluorescence image through least squares fitting of scaling, skew and rotation in x and y. Figure 7.7 reveals the residual distances of the centroids from the target grid pre and post anneal shown in red.

A maximum likelihood analysis using the 2D Gaussian probability distribution

$$P(\Delta x, \Delta y, \sigma) = \frac{1}{2\pi\sigma^2} e^{-\frac{(\Delta x^2+\Delta y^2)}{2\sigma^2}} \tag{7.2}$$

reveals a lateral FWHM deviation of $\sigma = 47.49 \pm 5.2$ nm for the unannealed centres and $\sigma = 159 \pm 17.1$ nm for the annealed centres maximise the value of P. In the following chapter, it is found that the positional accuracy of single colour centres generated through the non-linear laser processing is of order ~ 50 nm laterally [9] reducing to ~ 200 nm following an annealing stage [6]. I conservatively estimate that the positional accuracy here is of a similar order. Direct laser writing of SiV^- allows for much greater positional control than through laser ablation of silicon nanoballs with accuracies of a similar order to those obtained through ion implantation. An advantage over ion implantation is the ability to generate centres deep within the bulk and in 3D structures [29] with minimal damage. Furthermore, this work suggests that this method can be used to create or enhance the density of narrow dense SiV ensembles, for example interesting for quantum memory applications [220] from Si-doped diamond without degrading their spectral properties. In-situ laser annealing, such as that discussed in the following chapter, could potentially be used to delve into the dynamics of the formation process and optimise the enhancement of SiV^- ensembles [9].

7.5 Summary

In summary, it has been demonstrated that direct laser writing can be used to generate dense SiV ensembles of optical coherence equal to that of grown in centres with a positional accuracy that is only limited by the precision of the non-linear laser process. A tentative hypothesise is postulated that the formation mechanism differs from that of previous direct laser writing work and involves the dissociation of SiV^{2-} into SiV^-

by means of a change to the local charge environment from the formation of lattice vacancies. The extra electron is hypothesised to become trapped by the nearby vacancy converting into V^-, explaining the reduced level of GR1 emission. This mechanism is highly dependent upon the local Fermi level surrounding the emitter and writing into regions of lower dopant reveal no enhancement.

This processing method has scope for generating dense colour centre ensembles for quantum memory applications as well as offering a probe into material parameters and understanding the physics of defect complexes within wide bandgap materials. In addition, with a lower level of dopant in the starting crystal, there is potential for the formation of single SiV^- centres deep in the bulk using this method.

Single pulse laser writing in this chapter was conducted by myself and Patrick Salter. Room-temperature spectroscopy was undertaken by myself, Yu-Chen Chen, Helen Witkowska and Ben Green. Low temperature spectroscopy and PLE was undertaken by myself, Jonas Becker, Laiyi Weng, Zhin Mai, Shannon Nicley, Andrew Kirkpatrick, Helen Witkowska and Ben Green. EPR spectroscopy was undertaken by Ben Green. Data analysis including positional accuracy, spectral and PLE fitting were conducted by myself. Data analysis of EPR signals was undertaken by Ben Green. Discussions on the mechanism behind SiV formation were conducted by myself, Shannon Nicley, Jonas Becker and Ben Green.

Chapter Eight

Deterministic Engineering of Single Colour Centres

8.1 Introduction

Traditionally, colour centre engineering techniques have required a thermal anneal within a furnace to allow diffusion of vacancies to dopants to form colour centres. The thermal anneal yields a stochastic generation of colour centres entirely dependent on the random walk of vacancies during the anneal. Some sites yield no centres and some yield many centres. This stochastic nature means that the number of colour centres produced per site is determined by Poissonian statistics such that the maximum probability of creating a single centre at a given site is $\sim 37\%$.

In addition, the positioning accuracy of the resultant centres is determined by the vacancy diffusion length during annealing in a furnace. For previous laser generated single colour centres, the positioning accuracy is limited to a few hundred nanometres laterally and nearing a micron axially [6]. The development of a quantum device which could utilise single colour centres requires a significant improvement of the single centre yield and the positional accuracy such that millions of centres can be generated as an array and control hardware can be built around each site.

8.2 Laser annealing

In chapters five and six, it was found that a regime exists where a significant amount of energy can be deposited into the lattice during laser processing whilst the probability for lattice damage or defect creation remains negligible. The energy barrier required to allow diffusion of vacancies and interstitial carbon is significantly lower than that required to generate a defect [155]. Therefore there is likely a regime where a laser pulse can facilitate the diffusion of pre-existing vacancies without generating more. It is likely that this diffusion process also occurs through the relaxation of photo-generated carriers and is likely to be non-linear as well. In addition, the local heating by the laser will mean that the diffusion length is non-uniform across the focal volume giving preferential diffusivity closer to the centre of the region. Within this regime, a pulse of the laser allows for random motion of vacancies and interstitial carbon atoms confined within the non-linear reduced focal volume of the laser. In the same way that a furnace anneal allows for recombination of many Frenkel pairs and dissociation of a few which can go on to form centre, a low energy laser pulse can achieve a similar effect. A train of these pulses allows for a local annealing of the crystal facilitating the conversion from vacancies to colour centre's once a vacancy approaches a dopant atom. The local annealing could also facilitate the healing of excess damage around the centre.

A new fabrication technique emerges whereupon a single pulse of the laser, a "seed pulse", is used to generate Frenkel pairs within the material as before, but then this is followed by a train of lower energy pulses, "diffusion pulses", facilitating diffusion and recombination of Frenkel pairs alongside the formation of colour centres. This process is outlined in Figure 8.1

An initial test of utilising this technique to form NV centres was conducted by Patrick Salter and Yu-Chen Chen whereby a set number of lower energy pulses were incident upon the same region as the high energy pulse. The diamond material selected

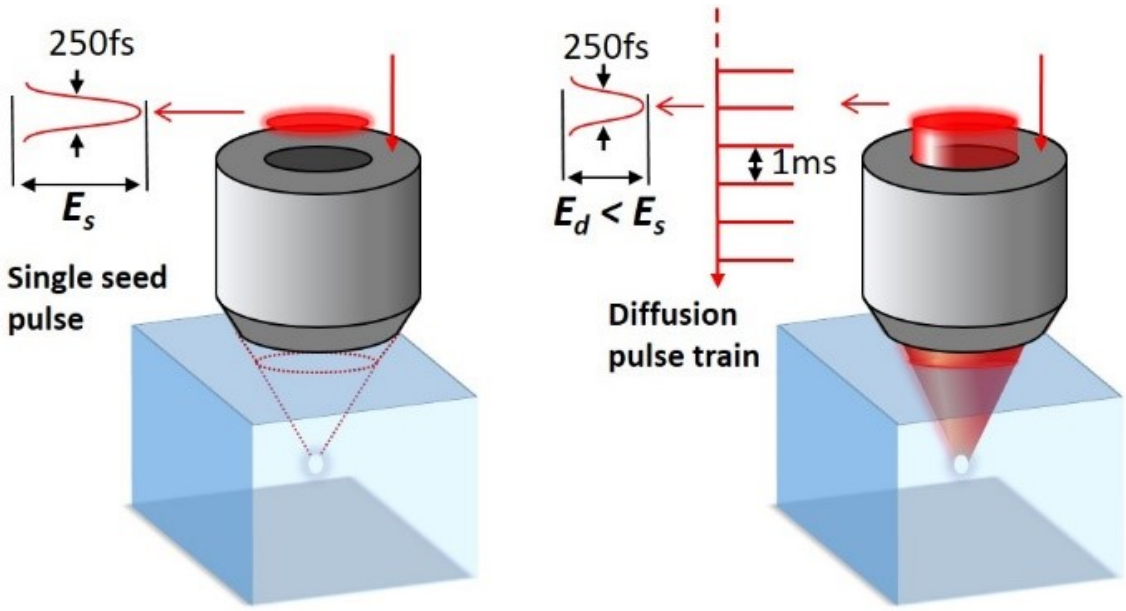


Figure 8.1 Schematic of the laser-writing and laser-annealing process. A single seed pulse is used to generate vacancies in the crystal, followed by a pulse train at lower energy to locally anneal the diamond.

for this study was nitrogen rich ($\sim$ 1.8 ppm) as based upon global annealing studies, one could expect vacancies to diffuse by only tens of nanometers before sample drift would have some effect on the processing. The pulse energies for seed and diffusion pulses were varied to gather information about how this affected the diamond material. Photoluminescence spectroscopy undertaken by Yu-Chen Chen revealed that most sites appeared either dark or graphitised due to either too much or two little energy being deposited into the material with a small number ($\sim$ 10%) displaying single and ensemble NV fluorescence determined through autocorrelation measurements. A second fabrication study was undertaken by myself and Patrick Salter at the pulse energies that had displayed highest likelihood of NV formation from the first test (17.5 nJ seed and 11.5 nJ pulse train) and varied the number of pulses within the pulse train with 30 repeats for each set of laser parameters. Table 8.1 displays the parameters that were varied during this study.

Sites with no seed pulse produced no visible fluorescence during confocal imaging.

Array	Number of seed (17.5 nJ) pulses	Number of diffusion (11.5 nJ) pulses
A	1	1000
B	1	2000
C	1	4000
D	1	6000
E	1	8000
F	1	10000
G	1	0
H	0	10000

Table 8.1 Number of seed and diffusion pulses used to investigate how number of pulses affects the probability of NV formation. 30 repeats were conducted for each.

Nineteen of the sites with no diffusion pulses produced no fluorescence and eleven sites produced a peak at 740 nm indicative of vacancy formation. Therefore the seed pulse generated a number of vacancies at and around the visibility threshold, known from previous studies to give the highest yield of single colour centres upon annealing [6].

The sites which included both a seed pulse and diffusion pulses showed a stochastic mix of no fluorescence, vacancies, graphite, single and ensemble NV determined through photoluminescence spectroscopy and autocorrelation measurements. Most processed sites produced no fluorescence and a large percentage were graphitised identifiable through a broad peak indicative of large amounts of damage. A small percentage of sites revealed a peak at 740 nm indicating that there were still vacancies present. The array showing the highest yield of centres (Array F) is shown in Figure 8.2. The sites sit between graphitised sites for ease of orientation. Auto-correlation measurements revealed 4 sites identifiable as singles ($g^{(2)}(0) = 0.2, 0.35, 0.41, 0.43$), and 7 ensembles within this array. The ensembles can be broadly split into doubles and triples indicated by $g^{(2)}(0)$ values between $0.5 - 0.7$ and > 0.7 respectively. This

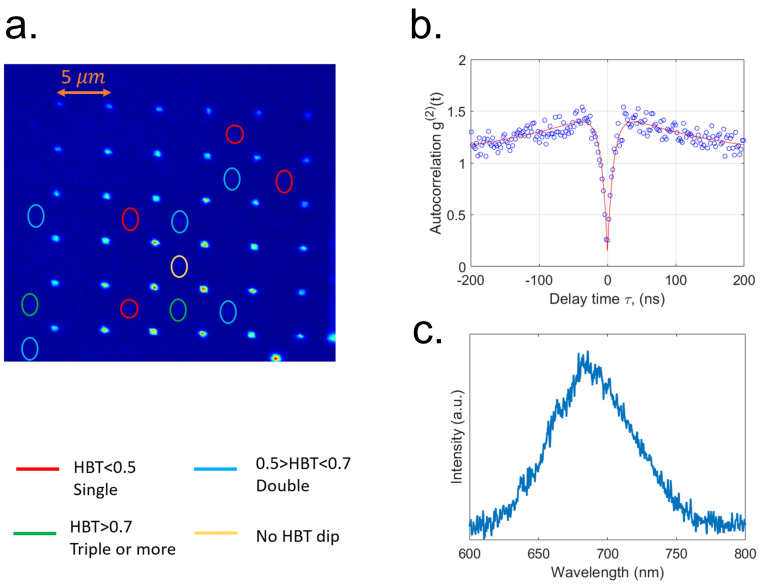


Figure 8.2 Laser written sites from the array with 1 seed pulse and 10000 diffusion pulses. Graphitic markers are placed between sites for orientation. Fluorescence was observed from 12/30 sites, 11 of which produced anti-bunching. Spectroscopy revealed these were NV^- centres and the site with no anti-bunching was a vacancy ensemble.

is not a rigorous technique but gives some indication of the statistics of generation. Sites with identifiable anti-bunching produced spectra indicating that these were NV^-.

8.3 Fluorescence feedback

The formation of single colour centres from the method outlined above is still stochastic, therefore a best single centre yield of ~ 37 % will be obtained. However, this is now a one-step process involving multiple pulses of the laser at the same location, therefore it is possible to monitor processing and form a feedback loop such that processing can be halted when the desired signal is obtained. This feedback loop allows the processing to go from Poissonian to deterministic.

NV centres fluoresce under green illumination whilst a pristine lattice does not. Vacancies also fluoresce but are much dimmer such that many thousands of vacancies

are required to achieve a fluorescence intensity comparable to a single NV. For colour centre generation, relatively few vacancies are desired such that residual damage to the lattice surrounding the NV centre is minimised. Therefore, by using photoluminescence intensity as a feedback monitor, one would anticipate the seed pulse to produce a small amount of fluorescence which jumps to a much higher intensity upon the formation of a centre.

To monitor for fluorescence whilst processing, a custom-built scanning confocal microscope that was integrated into the laser writing system, as shown in Figure 4.3 and aligned to the laser writing system such that it only detected fluorescence generated from within the focal region of the fabrication laser.

Initially, a single pulse of a high enough energy to generate a small number of vacancies was used. The pulse energy for this was chosen to be just below the visibility threshold for GR1 fluorescence with an oil immersion lens which has previously been shown to produce the best quality laser written NV centres [6]. Following this, a train of lower energy "diffusion pulses" were used at a 1 kHz repetition rate. A curious pattern of fluorescence emerges during the multi-pulse processing. A spiking of fluorescence intensity occurs, following which, the intensity stabilises. Processing can then be halted yielding the formation of a single NV centre. An example of fluorescence spiking behaviour is shown in Figure 8.3.

The origin of this fluorescence behaviour is puzzling and indicates a highly dynamical system. This will be investigated in more detail in section 8.6. Curiously, stopping the processing at the height of one of the peaks also yields the formation of a single NV centre. This suggests the NV forms relatively quickly and is then destroyed or quenched by the local environment and that stability occurs once other defects have been annealed away (either recombined or moved far enough away as to not affect the centre).

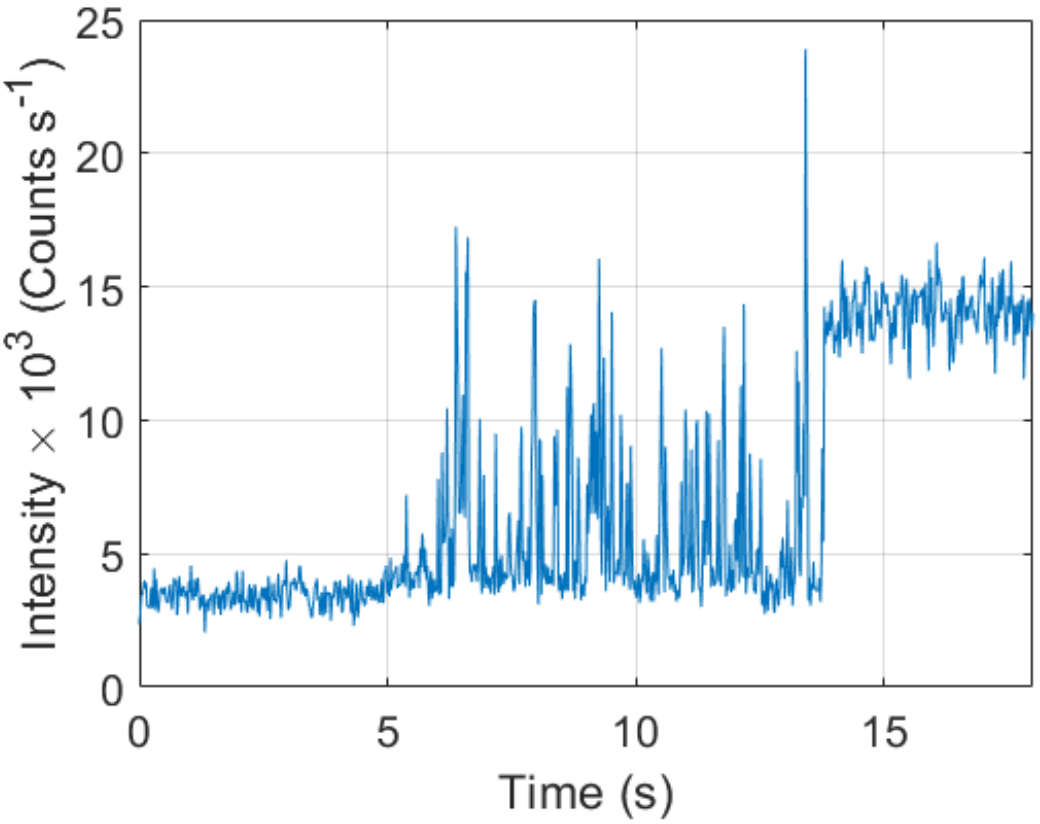


Figure 8.3 Example time-trace from the fluorescence monitor. The seed pulse occurs at time = 0, and the diffusion laser pulses begin at a time of about 5 s. The onset of a stable NV signal occurs after a further 9 s.

8.4 Characterisation

Laser annealing is able to deterministically generate single NV centres in a one-step process. Figure 8.4 shows a 5×5 array of sites generated via this technique with a spacing between sites of 2 μm. To determine the quality and fabrication control of the technique, various characterisation techniques were undertaken. Fluorescence spectroscopy was carried out on each site, and auto-correlation measurements performed through Hanbury, Brown and Twiss (HBT) interferometry. An example of a HBT measurement with baseline subtraction through the procedure outlined in chapter four, a histogram of baseline subtracted $g^{(2)}(0)$ values and an example of spectra from the laser annealed sites can be seen in Figure 8.4. The NV centres were stable in the negatively charged state, with no evidence of fluorescence from the charge-neutral state NV^0.

All 25 NV centres from the array in Figure 8.4 displayed distinct photon anti-bunching, with $g^{(2)}(0) < 0.2$. This suggests at first that all sites are single emitters, however, the site at the right-hand end of the row second from bottom was of particular interest, as this was the only site in the array to display $g^{(2)}(0) > 0.2$ when measuring photon statistics. From polarisation measurements (see following paragraph), the polarisation of the fluorescence from the site was consistent with that from two NV defects, with different in-plane orientations, that are sufficiently close not to be resolved in the confocal microscope. When measuring the photon anti-bunching with a linear excitation polarisation, it is thus possible to record $g^{(2)}(0) < 0.5$ even though a pair of NV defects are present due to poor coupling efficiency from one of the emitters into the interferometer. Following this, autocorrelation measurements were conducted on the suspected double with a circularly polarised excitation beam and a $g^{(2)}(0)$ value of 0.51. Thus, it is concluded that from the array of 25 laser process sites, 24 sites are single NV centres and one double giving a yield of 96%. In addition, 24 out of 25

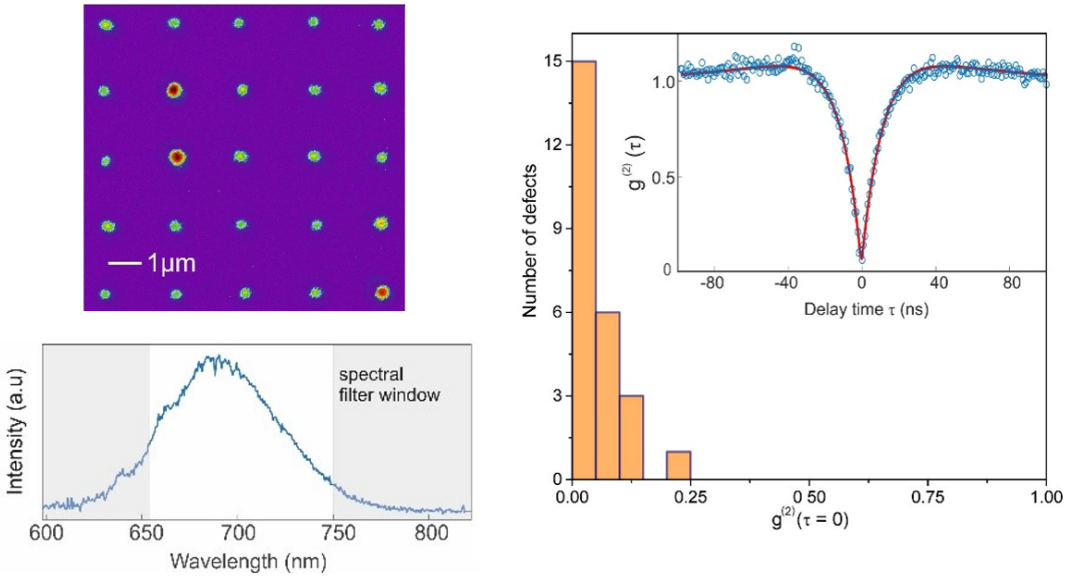


Figure 8.4 A fluorescence image of a high-yield 5×5 array of single NV centres on a 2 μm square grid alongside a histogram of $g^{(2)}(0)$ values for the array with an inset showing a typical $g^{(2)}(\tau)$ dataset corrected for background signal from the bulk crystal. Spectroscopy revealed that these centres are all NV^-, the greyed out region shows the spectral window that was monitored during processing.

and 15 out of 16 from two further arrays generated through this technique displayed $g^{(2)}(0)$ values of below 0.5 with circular excitation polarisation.

The orientation of each NV centre can be ascertained by the optical polarisation of its fluorescence, since the transition dipoles of the defect lie in the plane perpendicular to the physical axis of threefold rotational symmetry. In the sample used, the crystal plane parallel to the surface is (110) such that NV's whose axes of symmetry are oriented along the $[1\bar{1}1]$ and $[\bar{1}11]$ crystal axes lie in the plane and their fluorescence displays a high degree of linear polarisation. NV's oriented oriented along [111] and $[11\bar{1}]$, by contrast, make angles of 55^o with the image plane, so that their fluorescence is stronger but only weakly polarised.

Polarisation measurements were undertaken with a circularly polarised excitation such that all orientations are excited equally. Figure 8.5 displays polarisation measurements from NV centres in the array from Figure 8.4. It is clear that some centres produce a strong response whilst others only weakly polarise corresponding to whether the centres lie within or out of the plane of the physical axis.

The position in the image plane of each single NV centre could be accurately measured from the photoluminescence images since each was single point-source emitter. Thus, it was possible to determine the centroid of a 2D Gaussian surface fit to the measured intensity distribution, providing precision much higher than the resolution of the microscope. The standard error of the position measurements was measured to be 20 nm by repeatedly fitting three emitters over a timescale consistent with the localization measurements (approximately 20 min). The target grid was determined by performing a least-squares fit of a regular rectangular grid to the photoluminescence image using fitting parameters of offset in x and y spacing in x and y, shear, and rotation to allow for systematic and therefore correctable distortions that may have been introduced by the writing or imaging systems. Figure 8.6a shows the spatial distribution of deviations from the target grid obtained. A maximum likelihood

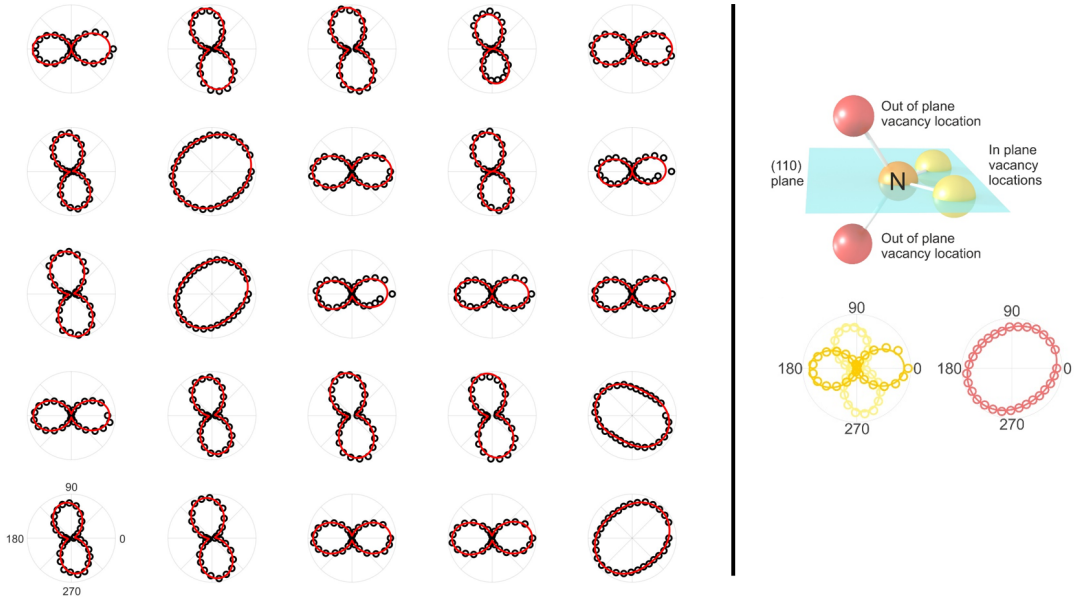


Figure 8.5 Polarisation plots of fluorescence intensity revealing the orientation of the NV centres from the 25 laser processed sites from the array shown in Figure 8.4. The schematic on the right shows the expected polarisation plots for different orientations of the NV centres within the lattice.

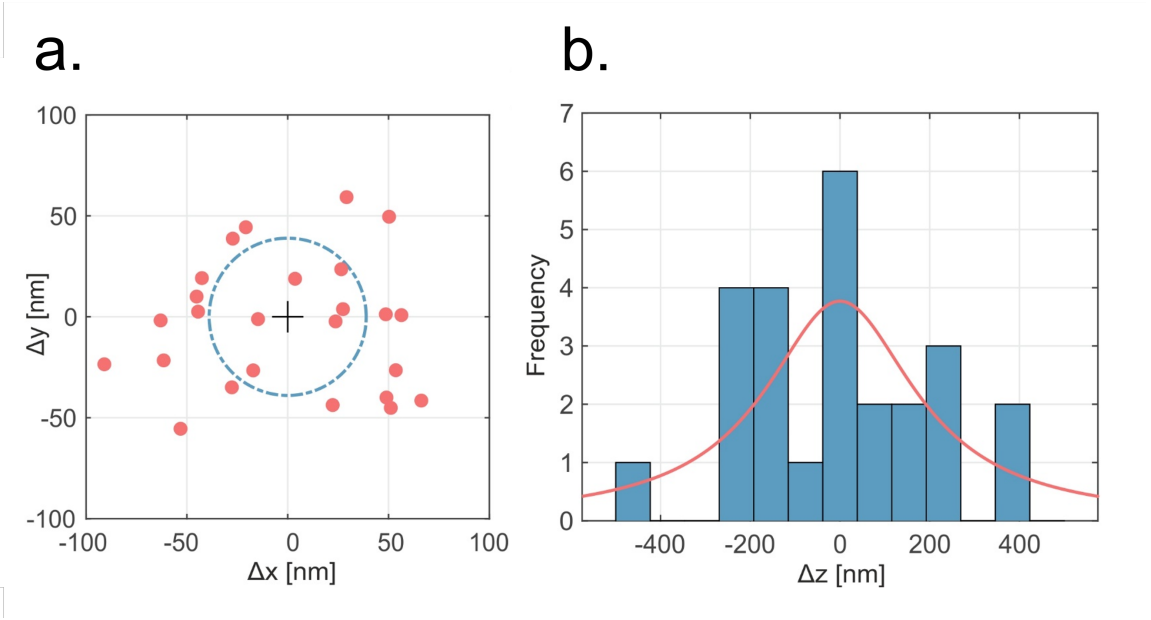


Figure 8.6 Positioning accuracy of single NV centres. a. Scatter plot of the fitted positions of the NV centres in Figure 8.4 relative to the target grid in the image plane. The dashed circle represents the deviation parameter σ for the best-fit 2D Gaussian distribution function. b. Histogram of the fitted depths of the NV centres with a best-fit Lorentzian distribution.

analysis using the 2D Gaussian probability distribution from equation 7.2 reveals a deviation parameter of $\sigma = 39 \pm 8$ nm, indicated by the circle in the figure. Quadrature subtraction of the standard error in the measurement from the measured deviation parameter revealed an in-plane deviation parameter for the fabrication technique of $\sigma_{fab} = 33 \pm 8$ nm a factor of 4.2 improvement over the in-plane positioning accuracy achieved in [6]. The modelling of the laser focus in chapter five suggested that the radius of the focused femtosecond laser beam from a 1.4 NA lens was 149 nm. Thus, the measured scatter in position relative to the targeted points was a factor of 4.5 times smaller than the transverse standard deviation of the writing laser focus.

The relative depth of each centre below the sample surface was measured with an accuracy of about 50 nm from sectional fluorescence images recorded with the confocal microscope. This axial distribution was expected to be approximately Lorentzian based on the intensity distribution of a Gaussian beam near the focus with minimal

plasma attenuation. Figure 8.6b shows the measured distribution, together with a fitted Lorentzian line shape of half-width-at-half-maximum (HWHM) of 203 ± 74 nm, from which an estimated HWHM for the fabricated NV centres of 194 ± 74 nm was calculated when the standard error for measurement was subtracted in quadrature. This depth variation is a factor of 4.3 times smaller than the calculated HWHM of the focal spot of the writing laser along the axis, the latter being equal to the Rayleigh range, $z_R = 852$ nm. This axial positioning accuracy could potentially be further improved through the use of delta doping during the growth of the crystal. Laser processing has a unique advantage over other engineering techniques in that 3D processing at an arbitrary depth can be achieved. This makes engineering into a delta doped layer with overgrowth of pure material much easier than with competing techniques.

Electron spin coherence times were recorded using Hahn echo measurements on three example color centres as $T_2 = 170$, 100, and 10 μs, as shown in Figure 8.7. This range of coherence times is likely caused by in-homogeneity in the substitutional nitrogen level and strain fields from defects, and is therefore a feature of the material used rather than being fundamental to the process. These measurements show that the process is capable of producing NV centres with coherence times long enough for quantum technology applications, and that any residual damage to the local environment of the written NV's is relatively minor. Improvement on these coherence times could be achieved through writing into lower doped material, however this would increase the fabrication time. A possible solution would be the use of delta doping to produce a high probability of diffusing to a nitrogen atom but a relatively low spin bath for long coherence times.

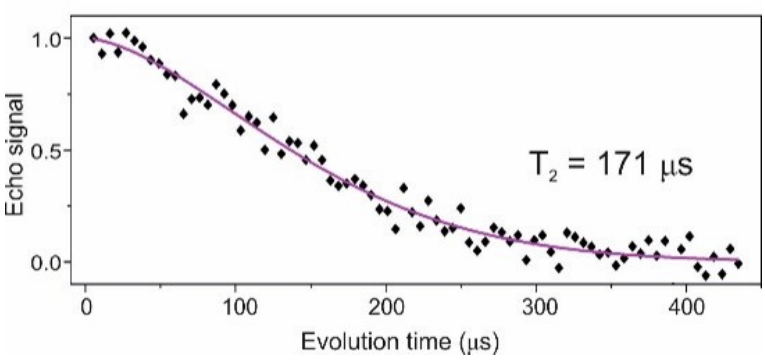


Figure 8.7 Spin coherence data from one of the laser annealed sites with a $T_2 = 171$ μs.

8.5 Advanced processing control

Continued processing of a site beyond the creation of a single NV centre can reveal rich dynamics offering additional potential for device engineering. Figure 8.8a shows an example of a fluorescence trace in which a second NV centre is formed, while Figure 8.8b shows a trace in which an NV centre is created, then destroyed, before another defect is created at a later time. Such processes allow for a degree of selection of NV properties. The simplest example is that of NV orientation in the lattice. By terminating processing when fluorescence was observed within a specific window of intensity, it was therefore possible to exercise some control over the statistical distribution of orientations in the lattice. The array in Figure 8.4 was fabricated with no selection of fluorescence intensity and 23 of the 26 NV centres (88%) created were in one of the two orientations with their axes lying in the plane of the sample, only three (12%) were created in the two orientations with their axes out-of-plane. By terminating processing only when a fluorescence signal intensity in the range 11-15 kcs^{-1} was observed, the fraction of single NV centres lying with axes out-of-plane increased to 87%. A third array in which processing was terminated when a signal of 8-11 kcs^{-1} was recorded revealed 84% of NV centres in the in-plane orientations.

It is interesting to note that when terminating processing with no preference for

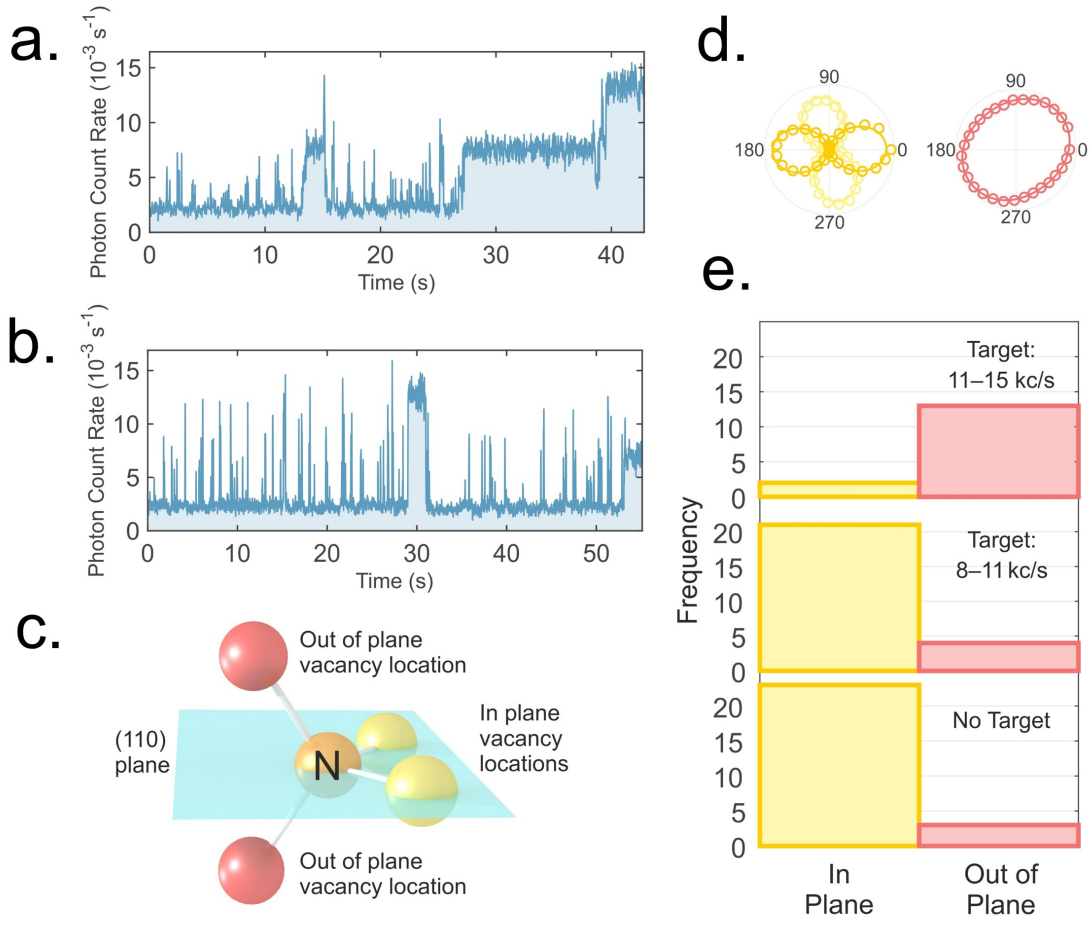


Figure 8.8 Advanced control of NV properties. (A) Fluorescence monitor trace showing creation of two NV centres at a processing site. (B) Trace showing the creation and destruction of an NV centre (time = 28-30 seconds) followed by selection of the second defect created. (C) Schematic of the four orientations of NV centres relative to the (110) image plane. (D) Example polarisation data-sets from in-plane and out-of-plane NV centres. (E) Histograms of orientations of defects in array under different termination conditions.

the fluorescence intensity gives a statistically significant chance of creating centres laying in-plane. The reason for this is unknown, however it is potentially possible that different orientations with respect to the crystal growth direction will have differing energy barriers to formation. In addition the formation process is highly dynamic and highly non-linear. Some quirk of the process may also lead to a preferential formation direction, perhaps strain within the underlying material. Further arrays generated later did not show this statistical significance, lending credence to the hypothesis of a local strain effect.

The ability to generate centres with a high positional accuracy on demand allows for highly intricate patterns of single colour centres to be generated within the material. This could be purely for aesthetic purposes such as advertising a brand name or for technological reason such as generating centres around electrodes or other control hardware. An example displaying the flexibility of this technique can be seen in Figure 8.9 where the logo for the Networked Quantum Information Technologies Hub (NQIT) is written from single NV centres into the material at 20 μm depth.

8.6 Fluorescence spiking study

During laser annealing, a spiking in the fluorescence coming from the irradiated spot was observed. Spectral analysis of this fluorescence has revealed that it is attributed to NV^- defects forming within the lattice and quickly being destroyed or quenched. Understanding this fluorescence behaviour is key to optimising processing and understanding the science behind the formation. At first, I assumed that the spiking was attributed to charge state switching of a formed centre between the neutral and negative charge states, however monitoring for fluorescence over a wavelength window corresponding to NV^0 revealed no spiking and no fluorescence was observed until the diamond graphitised.

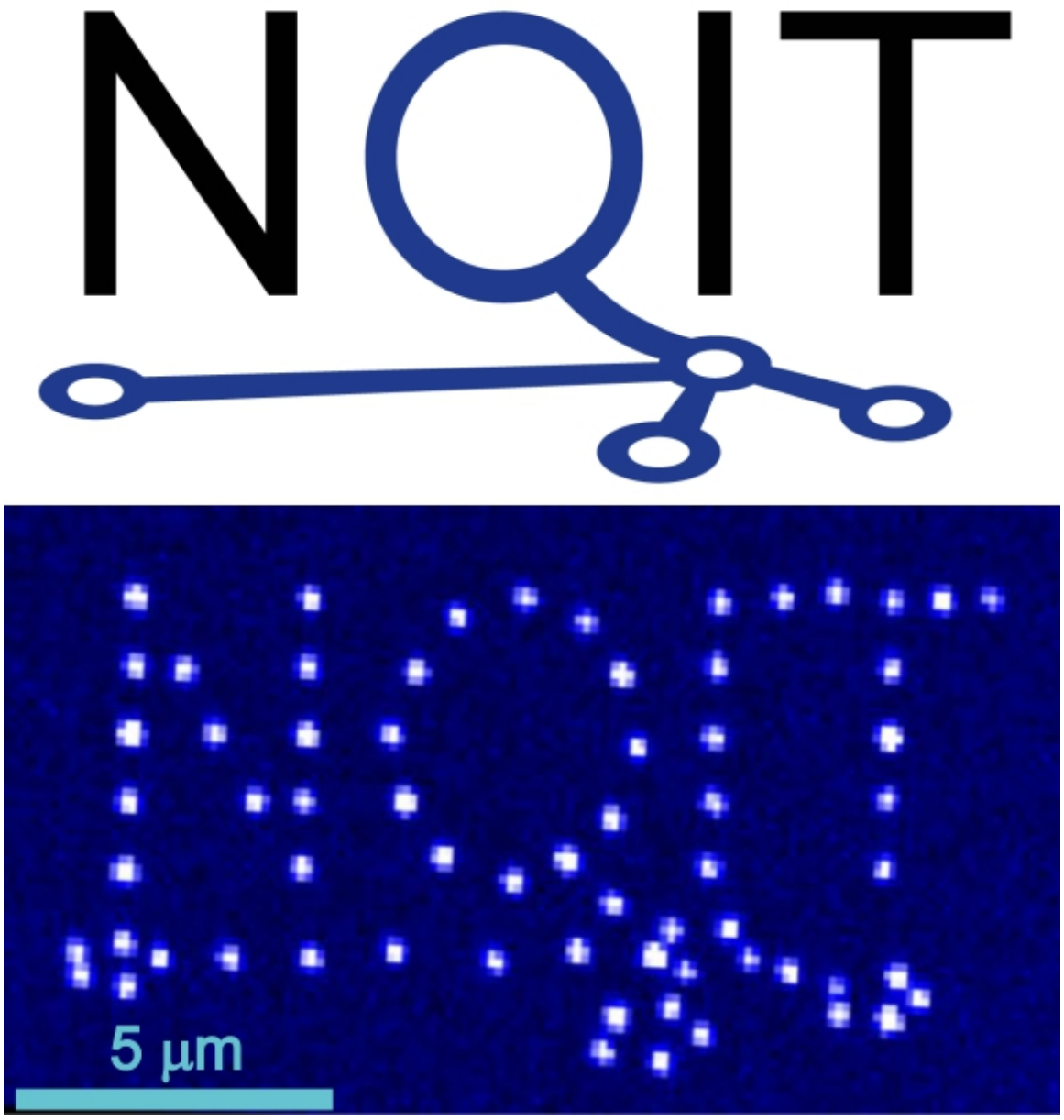


Figure 8.9 Fluorescence from single nitrogen vacancy defects in diamond produced using laser annealing. The Networked Quantum Information Technologies Hub (NQIT) is part of the UK National Quantum Technologies programme.

The spiking was then attributed to the creation and destruction of NV^- centres driven through strain fields. The vacancy is a point of lattice depletion so it is surrounded by a region of tensile strain while the split-interstitial and substitutional nitrogen add bulk to the lattice and so are surrounded by regions of compressive strain. Strain fields behave like electrostatic fields due to charges – same-sign fields correspond to repelling forces between the defects and opposite-sign fields correspond to attractive forces – such that the vacancy is attracted to both the substitutional nitrogen and to the interstitial, while the interstitial is repelled by the nitrogen. Frenkel defects created far from a nitrogen may either recombine or dissociate while for those created near to a nitrogen the vacancy will tend to locate between the interstitial and the nitrogen, whereby its diffusive motion results in occasional but unstable binding to the nitrogen, and the observed intermittent NV fluorescence. The NV complex does not provide a strong attractive force to the interstitial, so that the interstitial may diffuse far enough away to no longer interact, whereupon the vacancy remains bound to the nitrogen and stable NV fluorescence is observed. This is shown in Figure 8.10.

Further investigation by Andrew Kirkpatrick and Guangzhao Chen via DFT reveal that this picture is overly simplistic as the strain fields display more complex behaviour and the exact formation mechanism is still up for debate with the current hypothesis at the time of writing being that nearby interstitial defects hybridise the NV orbitals and quench fluorescence.

The dynamical behaviour is indicative of the vacancy performing many "hops" between lattice sites during the annealing pulses leading to a diffusion via a random walk. The mechanisms that facilitate these hops are unknown, potentially being facilitated by a thermal heating of the lattice under irradiation in a similar manner to a global anneal in a furnace. Alternatively, the hops could originate directly from the laser process itself either through the trapping of carriers much like the hypothesis for the formation of Frenkel defects outlined in chapter five, or through a different

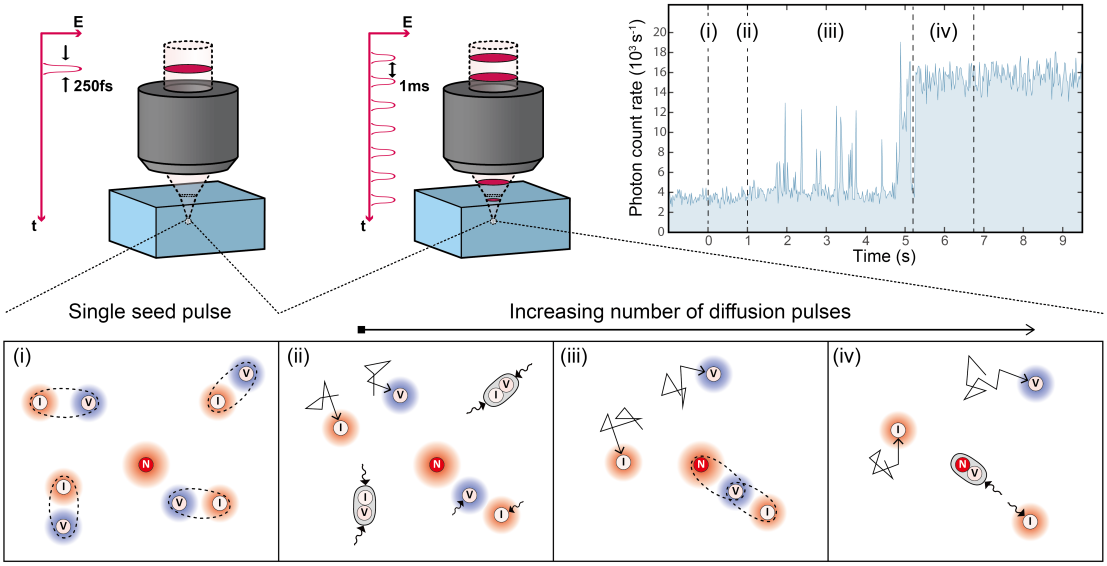


Figure 8.10 Diffusion dynamics of point defects in NV centre creation. The proposed mechanism for creation of stable NV centres occurs in four stages. (i) Intense seed pulse from laser generates Frenkel defects. (ii and iii) lower energy pulses at 1 kHz cause diffusion and recombination of Frenkel defects – some Frenkel defects align with substitutional nitrogen impurities whereby vacancy binds occasionally to nitrogen and intermittent NV fluorescence is observed. (iv) interstitial diffuses away from NV pair and stable fluorescence is observed.

mechanism. As shown earlier, the laser promotes a large density of electrons across the bandgap into the conduction band. In the extreme case, the potential energy surface is raised significantly leading to an ultra-fast non-thermal melting as the atoms can no longer hold themselves apart and quickly rearrange leading to graphitic formation upon cooling [174] [206]. However at densities below the threshold for non-thermal melting, the potential energy surface will still be raised by the generated electron plasma, leading to a reduction in the energy barriers for vacancy migration.

The level to which barrier to hopping is reduced will depend both upon the density of electrons promoted to the conduction band and the energy within that band (electron temperature). The potential energy surface for the lattice (PES_L) can then be defined as the total raise in electronic energy divided by the atomic density.

$$PES_L(r,z,t)\ (\text{eV}) = \int_{\mathcal{E}_C}^{\infty} \frac{\rho_e(r,z,t,\mathcal{E})}{\rho_A}\mathcal{E}\ d\mathcal{E} \tag{8.1}$$

A large increase in PES_L would lead to ultra-fast melting, identified to be when the carrier plasma reaches $\sim 9\%$ of the atomic density [174] [206]. The exact value of this will depend upon the electron temperatures reached with some sources quoting 6% of the atomic density but at much higher electron temperatures [221]. An increase in PES_L of less than this threshold would potentially lead to a stochastic chance of vacancy migration. This process would also be non-linear with a non-linearity similar to that of the electron generation but convoluted with the non-linearity of electron temperature. This work is ongoing.

Frequency study

By studying the frequency with which the fluorescence spikes as a function of pulse energy, information about the non-linearity of the laser annealing processes can be obtained. This is more complex than the non-linearity studies of previous chapters as it involves multiple laser pulses. Therefore the number of processes that are convoluted

into the measured non-linearity will be much greater making the mechanism more opaque. In addition, the spikes occur only when an NV centre is formed/unquenched. The vacancies will likely have to hop many lattice sites whilst in a dark state and the non-linearity of these lattice hops will add up such that the total non-linearity of spiking will be greater than that of a single lattice hop.

For this study, two different scenarios are considered, before and after the seed pulse. The diamond was irradiated for 60 seconds with a kHz train of 300 fs Ti:Sapphire pulses at a given energy. Following this, a seed pulse was irradiated into the diamond and then the 60-second train of pulses was repeated on the same site, post seed. During this time, fluorescence was simultaneously collected through the built-in confocal microscope. This study was then repeated for a variety of annealing pulse energies keeping the seed pulse the same energy and then repeated the process for varying seed pulse energies. An example data-set can be seen in Figure 8.11.

By counting the spikes in each of the 60-second time periods, the frequency of spiking can be found as a function of pulse energy. Counting the spikes is non-trivial as the standard deviation of photon shot noise increases with average fluorescence intensity; distinguishing a spike from photon shot noise requires an increase in the threshold jump in intensity to register a spike which scales with the average fluorescence intensity. The results of this can be seen in Figure 8.12.

The trend for both pre- and post-seed appears to be highly non-linear, however the seed appears to reduce the gradient. It also enables spiking to occur at lower pulse energies. This is likely because the seed pulse created vacancies that can be diffused, whereas the pre-seed function will be a convolution of the creation and diffusion of vacancies especially at the higher pulse energies. Likewise, as with the other non-linearity experiment, the shape of the graph is what is important with the absolute values of pulse energies required to achieve this being determined by the optics and aberrations. There appears to be no correlation between seed energy and

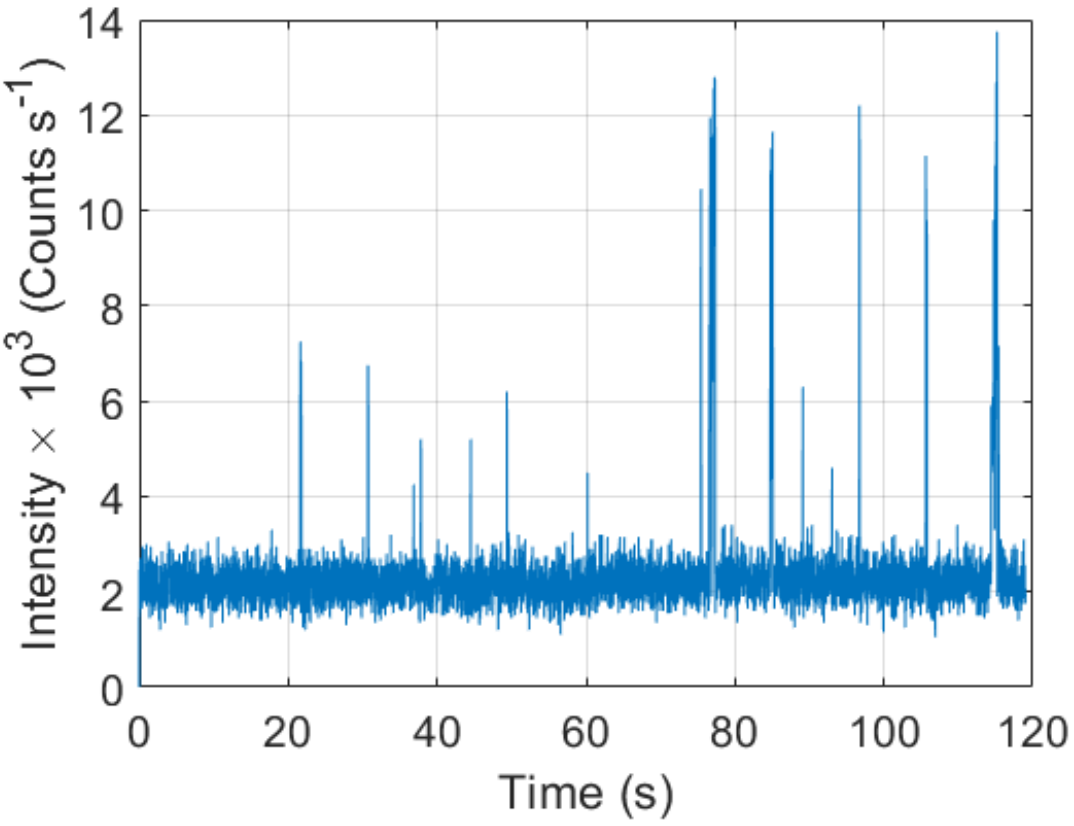


Figure 8.11 An example of a time trace of fluorescence intensity from an irradiated spot. The first 60 seconds are before a seed pulse and the latter 60 seconds are post a seed pulse.

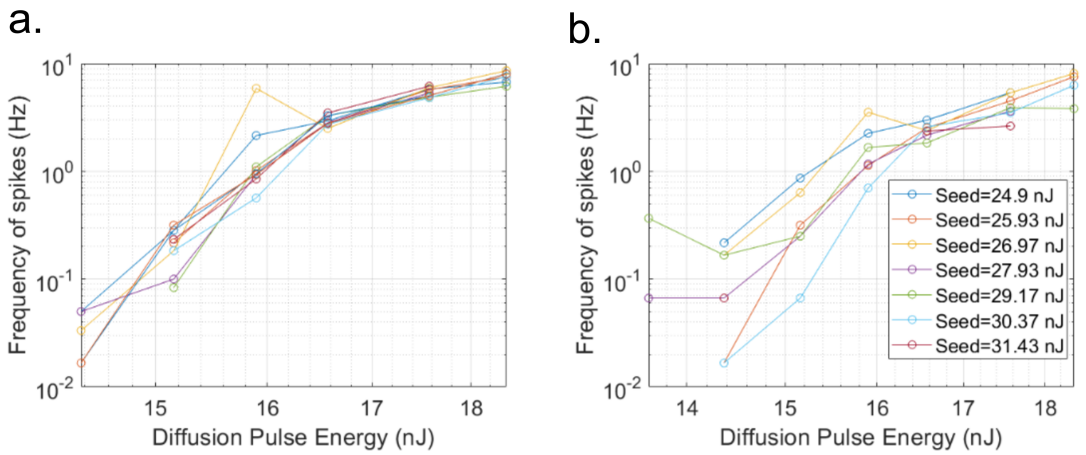


Figure 8.12 a. The frequency of spiking without a seed pulse as a function of energy. b. The frequency of spiking after a seed pulse as a function of energy

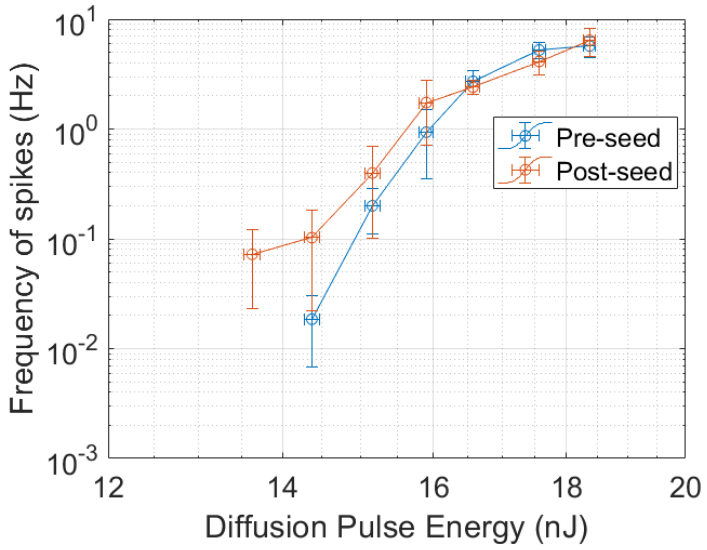


Figure 8.13 The average of spiking frequency as a function of energy, before and after a seed pulse. The seed appears to reduce the gradient of the slope and hence reduce the non-linearity. It also enables spiking to occur at lower pulse energies.

the change in shape of the curve before seed and after seed. Therefore, the data-sets can be combined and averaged over the seed energies to attain Figure 8.13. Both curves display a strong non-linearity with the data following a seed pulse having a somewhat lower level of non-linearity perhaps shifting the threshold pulse energy for diffusion of defects down to lower levels. The non-linearity is lower than from the study in chapters five and six. Fitting a straight line to the lower region of these graphs between 14 and 16 nJ reveals an approximate power law of ~ 35 for pre-seed and ~ 30 for post-seed. The pre-seed non-linearity will likely be dominated by the need to generate Frenkel defects alongside the diffusion processes whereas the post-seed will likely be an amalgamation of many defect hops which add up to a large non-linearity.

This significant non-linearity is of a similar order to that of the Frenkel defect generation outlined in previous chapters. This tentatively indicates that the diffusion of defects, creation and quenching/destruction of fluorescent colour centres also occurs through some relaxation mechanism of the photoionised carrier plasma and potentially

through the trapping and recombination of quasi-particles. Some important caveats should be highlighted. This occurs from many laser pulses and so many complex processes will take place that are convoluted in these diagrams, potentially each diffusion hop is a much lower non-linearity which adds up over many pulses. The existence of defects in the material before the laser is irradiated will also change the absorption profile of the light. These defects will also act as recombination centres for photogenerated carriers and quasi-particles changing the dynamics within and following each pulse. This recombination centre effect and changed absorption profile suggests that the non-linearity of each diffusion event will be lower and the high non-linearity emerges due to the many pulses required to achieve fluorescent spiking. To expand the model developed in earlier chapters to include the diffusion would require knowledge of the absorption and capture cross-sections of various defects alongside the energy barriers for diffusion, recombination and formation of conglomerate defects such as colour centres or dislocations. This work is ongoing, with spiking frequencies being studied for variation of other laser parameters.

8.7 Proximal writing

The ability to deterministically engineer NV centres in a one-step process with a high positional accuracy allows for the generation of interesting features within the material. Some interesting quantum applications of colour centres require the centres to be placed tens of nanometres from each other such that they can communicate directly through spin-spin interactions rather than needing a photon to mediate the quantum information. A study was designed whereby an NV centre was generated via laser annealing following which the process repeated very close-by such that a second NV centre could be created within close proximity of the first. This proved challenging as by definition, the first centre lies within the region where the laser has

enough energy to allow vacancy diffusion such that there is a stochastic chance of destroying the first centre.

The process was attempted with distances between the two sites of between 50 nm and 500 nm in steps of 50 nm. It was found that for sites with distances less than 300 nm, the initial site would either be destroyed or the diamond would graphitise. At 300 nm and greater distances, it was possible to generate a second site with a stochastic chance of destroying the initial site. Post site creation, the confocal microscope attached to the writing system was used to image the sites. Figure 8.14 displays an example of 4 sites generated via multiple pulse laser processing each containing a single NV centre with a writing distance of 300 nm.

At the separation of 300 nm, the separate centres are unresolvable in the confocal microscope. The right-hand figure has an overlay showing the target locations of each site and below is a time trace of fluorescence intensity during processing. Times i, ii, iii and iv correspond to the times that each centre was generated and a, b and c correspond to the motion of the stages in steps of 100 nm away from the generated site. The start of the diffusion pulses at each location can be ascertained due to a small uptick in the fluorescence intensity and the onset of spikes. The seed pulse for the second site at just after time a, produced a noticeable step in fluorescence intensity indicating the pulse energy was slightly too high. In this case a single NV can still be created as shown, however, there will likely be a small amount of extra damage around the site which may limit its coherence properties.

The distance from the centre of focus at which diffusion and destruction behaviour can no longer occur is likely highly dependent upon the pulse parameters such as pulse energy, duration, wavelength and repetition rate and a systematic study into this could give information on the dynamical processes involved in the formation and destruction/quenching of single NV centres. When processing at distances closer than 300 nm it was the seed pulse for the second site that destroyed the initial site rather

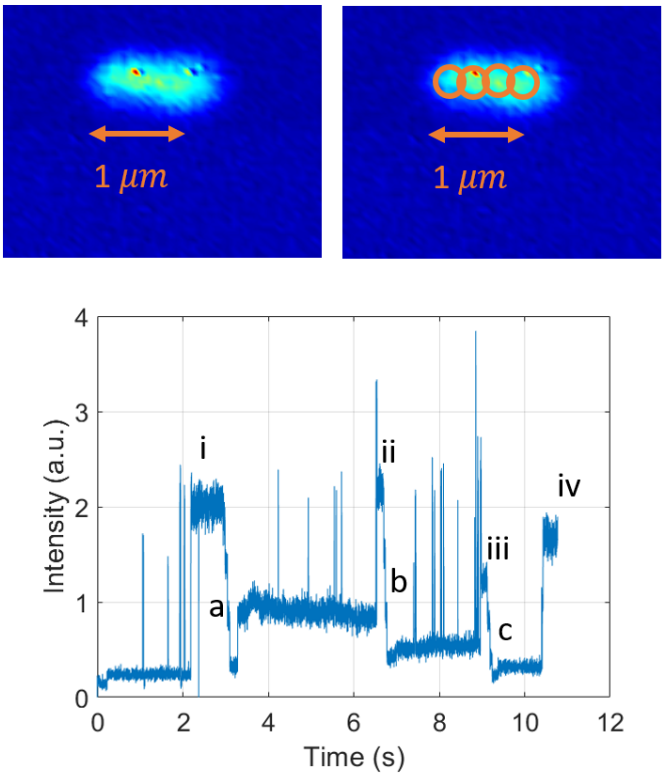


Figure 8.14 Four single NV centres generated at a distance of 300nm from each other by the deterministic laser writing technique. At this distance the centres are unresolvable as separate sites in the confocal microscope. To the right is an overlay showing the locations of each site. Below is a time trace of fluorescence intensity during processing. i, ii, iii and iv correspond to the times that each centre was generated. a, b and c correspond to the motion of the stages in steps of 100 nm. The start of the diffusion pulses at each location can be ascertained due to a small uptick in the fluorescence intensity and the onset of spikes.

than diffusion pulses, this suggests that the radius over which diffusion can occur scales with the pulse energy.

To attempt to resolve the individual colour centres generated within close proximity, stimulated emission depletion (STED) microscopy was attempted on this location within the diamond. This technique allows for imaging with a resolution below the diffraction limit by depleting the fluorescence around the region of interest allowing the central region to remain active. Unfortunately, the STED microscope used was generally used to image bright biological samples and could not detect the low photon flux of the NV centres.

8.8 Dependence on dopant level

The deterministic writing method involving a train of lower energy pulses to locally anneal the diamond proved successful in a diamond sample with ppm dopant nitrogen levels. The downside of this is that the high nitrogen content limited the spin coherence time of laser written NV centres through spin coupling with the nitrogen bath. Ideally, this technique should be used in a lower dopant material such that the spin coherence is no longer limited by the spin bath.

The experiment was repeated on an electronic grade diamond with 2 ppb of nitrogen dopant. Due to the thousandth lower dopant level, the number of hops the vacancy has to undergo to reach a nitrogen will be one thousand times greater. It can reasonably be assumed that the time required for fluorescence spiking and NV centre formation will also be one thousand times times greater. In this time frame, sample drift becomes a key parameter and a limiting step. A single pulse of 15 nJ was incident upon a region 20 μm within the sample following which the laser was set to pulse continuously at a 1 kHz repetition rate for 4000 seconds. Four spikes in the fluorescence behaviour were seen after an hour of pulsing at 1 kHz but these

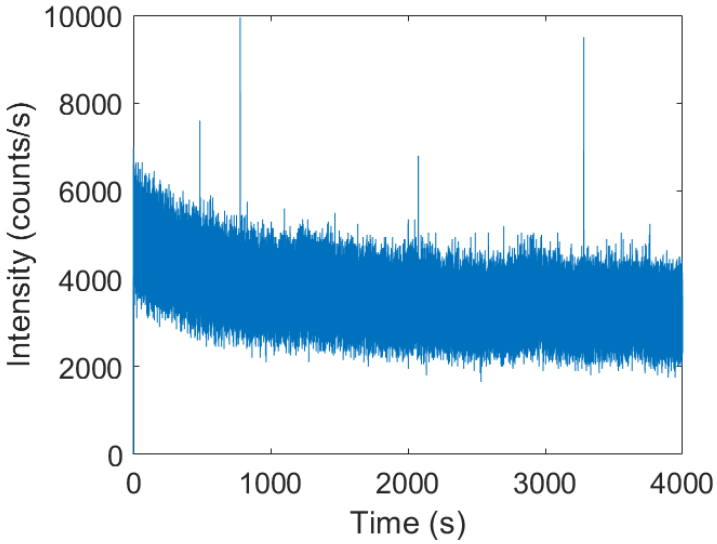


Figure 8.15 Time trace of fluorescence detected from the focal volume of the Ti:Sapphire pulsing at a repetition rate of 1 kHz.

were spikes corresponding to a single sample of the photodiode and were potentially electrical noise. Figure 8.15 displays the fluorescent response from the crystal.

Curiously the background fluorescence decays away over time, potentially due to some photo-bleaching of background light or due to sample drift. The experiment was repeated at a different location at the same depth. Interestingly, following continuous processing at 1 kHz for 30 minutes yielding two spikes in fluorescence, graphitisation occurred, potentially due to heat build up or processing at a high enough pulse energy that a small number of defects were forming upon each pulse. The background fluorescence level did not reduce during the repeat.

To combat sample drift from the large timescales required at a lower dopant level, processing with a higher repetition rate was proposed. With a MHz repetition rate, the timescale for formation of colour centres should reduce back down to seconds making this viable over long term drift. This requires a different femtosecond laser, hence there was significant delays in attempting this. A caveat to consider is that processing at a faster rate compared with kHz means that the fluorescence sampling frequency must

also change in order to still differentiate spiking behaviour. Indeed, preliminary tests of MHz processing conducted by Andrew Kirkpatrick with a fluorescence sampling frequency of 1 kHz showed a steady raised fluorescence level during processing which reduced back to background following halting emission. In this case each fluorescence sample is 1000 laser pulses, therefore it is likely that the steady raised fluorescence level is an average of the highly dynamical spiking behaviour expected. This work is ongoing.

8.9 Summary

This chapter has described a new engineering technique by which the yield of colour centres was taken from stochastic to deterministic through use of a local laser anneal and fluorescence feedback mechanism. Following the initial laser pulse to generate Frenkel defects within the diamond, the sample was irradiated by a train of lower energy pulses that had negligible chance of forming new Frenkel defects but facilitated the diffusion of the defects generated on the first pulse. By monitoring fluorescence from within the focal volume during processing, the processing could be halted once the desired defect had formed. The non-linear process of the laser mechanism ensured an improved positional accuracy over a thermal anneal by a factor of 5 and spin coherence measurements revealed that the centres were only limited by the presence of nitrogen within the sample. The fluorescence from within the focal region during processing revealed rich dynamical behaviour that was highly non-linear and the speed and one-step deterministic process allows for generation of complex 3D structures out of single colour centres and flexibility to design a device. In addition, it allows for the creation of colour centres at distances of order the diffraction limit apart deterministically. Statistical analysis of the fluorescence intensity at which a stable NV centre formed led to the realisation that the laser process potentially leads to a

preferential orientation for centres to form, the reason for which is currently unknown. Ongoing work is developing this mechanism with a faster repetition rate laser to allow for the formation of colour centres in lower dopant material in timescales shorter than the drift time of the sample as well as studying the spiking behaviour in response to different pulse parameters.

The idea to use the laser to perform a local anneal was conceived by Yu-Chen Chen with initial tests carried out by Patrick Salter, Yu-Chen Chen and myself involving a set number of lower energy pulses where the pulse energy and number of pulses in the pulse train were varied. Photoluminescence analysis of initial tests was performed by Yu-Chen Chen and myself with a small number of sites showing a single NV, a few showing multiple NV and most sites being dark or having significant graphitisation. The idea for a fluorescence feedback mechanism to monitor processing was conceived during discussions between myself, Yu-Chen Chen and Jason Smith and the confocal microscope attached to the laser writing system was designed and built by myself, Sam Johnson and Laiyi Weng. Laser annealing with fluorescence feedback with varying pulse energies and photoluminescence characterisation of laser written sites including spectral analysis, HBT and polarisation measurements were carried out and optimised by myself. Spin coherence measurements of laser annealed NV's were carried out by Shazeaa Ishmael, Yashna Lekhai and Colin Stephen and positional accuracy measurements carried out by Colin Stephen. Data analysis of characterisation data was performed by myself, Jason Smith, Sam Johnson and Shannon Nicley. Processing beyond the creation of an NV showing the ability to destroy or generate multiple centres on demand was conceived and carried out by myself. The frequency of spiking study was conceived and performed by myself with help from Shannon Nicley on the data analysis and the proximal writing study was carried out by myself with STED imaging done by Aurelien Barbotin and myself. Ongoing experimental work into the spiking behaviour is being conducted by Andrew Kirkpatrick and Patrick Salter

and ongoing theoretical work through DFT modelling is being conducted by Andrew Kirkpatrick and Guangzhao Chen.

Chapter Nine

Conclusion and Future Outlook

9.1 Conclusion

Femtosecond laser engineering has enabled the generation of high-quality colour centres within diamond with a high positional accuracy. This thesis has expanded upon previous work enabling a greater understanding of the processes involved through the development of a coupled partial differential equation model in conjunction with experimental studies. It reveals a rich and dynamical behaviour during laser processing and allows for studies of interesting material science phenomena. A hypothesis for the mechanisms behind Frenkel defect formation involving a thermally activated non-radiative recombination of self-trapped bi-excitonic states that emerge following relaxation of photoionised electron-hole pairs, has been presented and fit to experiment. A total of ~ 8 eV is shown to be needed for defect formation where the majority comes from relaxation of excited quasi-carriers and 0.41 eV comes from a thermal activation. The non-linearities of photoionisation, quasi-carrier formation and carrier mobility combine to achieve an effective non-linearity of ~ 40 with respect to focal intensity and pulse energy over a range of approximately 2 nJ. This quickly saturates to a significantly lower non-linearity for higher pulse energies. For higher pulse energies, more complex behaviour such as ultra-fast melting and graphitisation will occur which

are neglected in this analysis. The extremely high non-linearity at low pulse energies provides a switch-on behaviour approximately a step-function over which processes start to occur. The model also suggests a region of pulse energy in which a lot of energy is deposited into the material but the probability of forming defects or other laser damage is minimal. This suggests the possibility of using the laser pulses as a way to diffuse existing defects within the focal region.

Based off the idea that the laser can deposit lots of energy into the material with minimal chance of generating new defects, a new experimental technique emerges that uses the laser to locally anneal the diamond via a train of low energy pulses, allowing diffusion of the vacancies without the need for a global anneal. By making use of the fluorescence properties of the colour centres in conjunction with the local laser anneal, a feedback loop was formed allowing for the yield of generated centres to go from Poissonian to deterministic. The non-linear nature of this allows for positional accuracies much greater than the diffraction limit of the diffusing laser and five times greater than the positional accuracies achieved using a global thermal anneal. This is a key step in developing a solid-state based quantum technology where the engineering of regular defect arrays will be crucial to couple to photonic systems.

Monitoring the fluorescence behaviour during the processing reveals rich dynamical behaviour where a lot of interesting physics may lie. The "spiking" behaviour of fluorescence provides a window into the highly non-equilibrium dynamics of the system and also appears to be significantly non-linear to a similar order to that of Frenkel formation. This tentatively suggests that the mechanism for diffusion and the creation and quenching/destruction of colour centres similarly relies on quasi-carrier recombination or some process from the photoionised plasma but further investigation is needed.

In addition, laser engineering of diamond material doped with silicon has enabled the generation of dense SiV ensembles showing that laser engineering is able to generate

a wider range of colour centres than in previous studies. These ensembles formed upon a single laser pulse without any anneal by furnace or laser. This suggests a potentially new route to colour centre formation through the breaking up of conglomerate defects or photoionisation of an existing defect into a different charge state and also offers a lot of potential for understanding the material science and physics of high intensity laser interaction.

9.2 Future Outlook

The use of a femtosecond laser to generate and diffuse vacancies could potentially offer a new window into conducting material science. It allows for a non-destructive method into probing material properties within the bulk and in conjunction with the partial differential equation model could potentially give information about energy barriers to defect formation and vacancy migration within wide bandgap semiconductors. In addition, due to the highly dynamic nature of this process, it allows for the generation of some interesting states of matter and the study of dynamical systems. The focus of this thesis has been on defect generation for quantum technologies, however, the study of defects in materials is of interest in a broad range of fields. For example, bulk diamond is used as a high energy particle detector at CERN. High energy particles will produce defects within the material upon impact and cause significant radiation damage. Understanding defect formation and dynamics will be of paramount importance in understanding the signals generated upon particle detection and calculating the lifetime of a detector to radiation damage. More generally, defect formation and dynamics within materials is of interest for an array of reasons such as radiation damage in fusion reactors. Future work could look into utilising the ultra-fast laser process as a probe into defect dynamics within various transparent materials. The formation of dense exciton plasmas also means that the laser processing

could be used to study quantum behaviours in highly dynamical systems. It would be intriguing to attempt laser writing at low temperature, potentially generating electron-hole liquids. If the hypothesised mechanism for Frenkel defect formation, the formation of defects at low temperatures would not occur.

The hypothesis that Frenkel defects form from the non-radiative recombination of multi-excitonic states suggests that a more efficient mechanism for defect engineering would involve direct excitation of excitons rather than requiring relaxation from free carriers. This could possibly be achieved using an ultra-fast x-ray source and would allow for formation of defects at a lower focal intensity putting less emphasis on aberration control. Further experimental evidence for this hypothesis could be achieved by monitoring for photoluminescence indicative of excitonic states. These will be within the blue region of the spectrum and will be short-lived. A study of the amount of excitonic photoluminescence as a function of pulse energy would potentially be able to verify the loss of radiative quantum efficiency due to defect formation. This would be complicated slightly by the increase in excitonic states for higher energy pulses.

Many of the mechanisms that occur during femtosecond laser irradiation of the bulk diamond material are still not understood and indeed, this thesis has opened up as many questions as it has answered. The spiking behaviour during multiple pulse processing currently defies explanation. A good next step to understanding this is to vary laser parameters and measure the change in response of the fluorescence spiking. During chapter eight, I showed that the spiking is highly non-linear with respect to the diffusing pulse energy. This experiment could be repeated with differing pulse durations, wavelengths and repetition rates. In addition, the theoretical framework developed could be expanded to include multiple pulse processing. This would likely require additional DFT modelling to determine the energy barriers for defects to hop between lattice sites and to calculate the orbitals of the formed centre to discover if

fluorescence is still possible.

The development of a solid-state spin qubit based quantum computer has to date been held back by the ability to engineer spin qubits, on demand, in regular arrays and the ability to extract the quantum information into photonic networks for entanglement. This thesis addresses the first of these two stumbling blocks leaving the only barrier to this technology being the extraction of quantum information efficiently. Proof of principle techniques for enhancing the efficiency have been shown by building micro-structures around the emitter, but this has again been hampered by the fact that until recently, spin qubits are distributed irregularly so enhancement of more than a few has proved challenging. Now that spin qubits can be generated on demand, more regular micro-structures can be made allowing scaling and steps towards the development of a quantum device.

Further work could look into refining the laser processing of SiV centres, perhaps with a lower level of silicon dopant within the starting material, as well as attempting to tie down the mechanism and attempting laser annealing on the current sample. A systematic study of laser writing into different levels of dopant silicon and nitrogen could reveal more dynamics and formation of different stable charge states, confirming or disproving the hypothesis outlined in chapter seven. Processing of other group IV colour centres would also be a great next step, as these currently appear the most promising candidates to replace NV centres as the foremost diamond spin qubit. Laser engineering of spins in other materials such as silicon carbide or gallium nitride could also be attempted which may lead to insight into the processing and bring solid-state quantum technologies a step closer to reality.

REFERENCES

[1] X. Rong, J. Geng, F. Shi, Y. Liu, K. Xu, W. Ma, F. Kong, Z. Jiang, Y. Wu, J. Du, Experimental fault-tolerant universal quantum gates with solid-state spins under ambient conditions, Nat. Commun. 6, 8748 (2015).

[2] C. Simon, M. Afzelius, J. Appel, A. Boyer de la Giroday, S. J. Dewhurst, N. Gisin, C. Y. Hu, F. Jelezko, S. Kröll, J. H. Müller, J. Nunn, E. S. Polzik, J. G. Rarity, H. De Riedmatten, W. Rosenfeld, A. J. Shields, N. Sköld, R. M. Stevenson, R. Thew, I. A. Walmsley, M. C. Weber, H. Weinfurter, J. Wrachtrup, R. J. Young, Quantum Memories, Eur. Phys. J. D 58, 1–22 (2010).

[3] F. Jelezko, T. Gaebel, I. Popa, M. Domhan, A. Gruber, J. Wrachtrup, Observation of Coherent Oscillation of a Single Nuclear Spin and Realization of a Two-Qubit Conditional Quantum Gate, Phys. Rev. Lett. 93, 130501 (2004).

[4] Englund, D. et al. Deterministic coupling of a single nitrogen vacancy centre to a photonic crystal cavity. Nano Lett. 10, 3922–3926 (2010)

[5] Haque A, Sumaiya S, An Overview on the Formation and Processing of Nitrogen-Vacancy Photonic centres in Diamond by Ion Implantation. Journal of Manufacturing and Materials Processing, 1, 6, (2017).

[6] Y. C. Chen, P. Salter, S. Knauer, L. Weng, A. C. Frangeskou, C. J. Stephen, S. N. Ishmael, P. R. Dolan, S. Johnson, B. L. Green, G. W. Morley, M. E. Newton, J.

G. Rarity, M. J. Booth, J. M. Smith, Laser writing of coherent colour centres in diamond, Nature Photonics, Volume 11, Issue 2, pp. 77-80 (2017).

[7] B. Griffiths, A. Kirkpatrick, S. S. Nicley, R. L. Patel, J. M. Zajac, G. W. Morley, M. J. Booth, P. S. Salter, J. M. Smith, Microscopic processes during ultra-fast laser generation of Frenkel defects in diamond, Phys. Rev. B 104, 174303 (2021).

[8] B. Griffiths, L. Weng, H. Witkowska, Y. C. Chen, Z. Mai, A. Kirkpatrick, S. S. Nicley, B. L. Green, J. N. Becker, M. J. Booth, P. S. Salter, J. M. Smith, Generation of dense silicon vacancy ensembles in diamond with narrow linewidth through direct laser writing, in preparation.

[9] Y. C. Chen, B. Griffiths, L. Weng, S. S. Nicley, S. N. Ishmael, Y. Lekhai, S. Johnson, C. J. Stephen, B. L. Green, G. W. Morley, M. E. Newton, M. J. Booth, P. S. Salter, J. M. Smith, Laser writing of individual nitrogen-vacancy defects in diamond with near-unity yield, Optica, Vol. 6, Issue 5, pp. 662-667 (2019).

[10] F. Arute, K. Arya, R. Babbush, *et al.* Quantum supremacy using a programmable superconducting processor. Nature 574, 505–510 (2019).

[11] Y. Wu, W. S Bao, S. Cao, F. Chen, M. C. Chen, X. Chen, T. H. Chung, H. Deng, Y. Du, D. Fan, M. Gong, C. Guo, C. Guo, S. Guo, L. Han, L. Hong, H. L. Huang, Y. H. Huo, L. Li, N. Li, S. Li, Y. Li, F. Liang, C. Lin, J. Lin, H. Qian, D. Qiao, H. Rong, H. Su, L. Sun, L. Wang, S. Wang, D. Wu, Y. Xu, K. Yan, W. Yang, Y. Yang, Y. Ye, J. Yin, C. Ying, J. Yu, C. Zha, C. Zhang, H. Zhang, K. Zhang, Y. Zhang, H. Zhao, Y. Zhao, L. Zhou, Q. Zhu, C. Y. Lu, C. Z. Peng, X. Zhu, J. W. Pan, Strong quantum computational advantage using a superconducting quantum processor, arXiv:2106.14734

[12] M. Mø"ller, C. Vuik, On the impact of quantum computing technology on future developments in high-performance scientific computing. Ethics Inf Technol 19, 253–269 (2017).

[13] B. Schumacher, Quantum coding. Physical Review A. 51 (4): 2738–2747, (1995).

[14] A. M. Dalzell, A. W. Harrow, D. E. Koh, R. L. La Placa, How many qubits are needed for quantum computational supremacy?, Quantum 4, 264 (2020).

[15] R. Laflamme, C. Miquel, J. Paz, W. H. Zurek, Perfect Quantum Error Correcting Code, Phys. Rev. Lett. 77, 198 (1996).

[16] L Stephenson, D Nadlinger, B Nichol, P Drmota, T Ballance, K Thirumalai, J Goodwin, D Lucas, C Ballance, High-rate high-fidelity entanglement of qubits across an elementary quantum network, Physical Review Letters American Physical Society 124 (2020)

[17] H. Zhong, H. Wang, Y. Deng *et al*, Quantum computational advantage using photons, Science, Vol. 370, Issue 6523, pp. 1460-1463 (2020).

[18] G. Wolfowicz, F.J. Heremans, C.P. Anderson, *et al*. Quantum guidelines for solid-state spin defects. Nat Rev Mater (2021).

[19] M. Atature, D. Englund, N. Vamivakas, S. Y Lee, J. Wrachtrup, Material platforms for spin-based photonic quantum technologies, Nature Reviews Materials volume 3, pages38–51 (2018).

[20] G. Davies, S. C. Lawson, A. T. Collins, A. Mainwood, and S. J. Sharp, Vacancy-related centres in diamond, Phys. Rev. B 46, 13157–13170 (1992).

[21] I. Aharonovich and E. Neu. Diamond Nanophotonics. Advanced Optical Materials, 2(10):911–928, (2014).

[22] L. Childress, M. V. Gurudev Dutt, J. M. Taylor, A. S. Zibrov, F. Jelezko, J. Wrachtrup, P. R. Hemmer, M. D. Lukin, Coherent Dynamics of Coupled Electron and Nuclear Spin Qubits in Diamond, Science 314, 281 (2006).

[23] S-Y. Lee, M. Widmann, T. Rendler, M. W. Doherty, T. M. Babinec, S. Yang, M. Eyer, P. Siyushev, B. J. M. Hausmann, M. Loncar, Z. Bodrog, A. Gali, N. B. Manson, H. Fedder, J. Wrachtrup, Readout and control of single nuclear spin with meta-stable electron spin ancilla, Nature Nanotechnology, Volume 8, Issue 7, pp. 487-492, (2013).

[24] M. K. Bhaskar, R. Riedinger, B. Machielse, D. S. Levonian, C. T. Nguyen, E. N. Knall, H. Park, D. Englund, M. Lončar, D. D. Sukachev, M. D. Lukin, Experimental demonstration of memory-enhanced quantum communication, Nature 580, 60, (2020)

[25] S. D. Barrett, P. Kok, Efficient, high fidelity quantum computation using matter qubits and linear optics, Phys. Rev. A. 71 6 06031 (2005).

[26] C. Cabrillo, J. I. Cirac, P. Garcia-Fernandez, P. Zoller, Creation of entangled states from distant atoms by interference, Phys. Rev. A. 59 2 1025-1033 (1999).

[27] B. Hensen, H. Bernien, A. E. Dr'eau, A. Reiserer, N. Kalb, M. S. Blok, J. Ruitenberg, R. F. L. Vermeulen, R. N. Schouten, C. Abella'n, W. Amaya, V. Pruneri, M. W. Mitchell, M. Markham, D. J. Twitchen, D. Elkouss, S. Wehner, T. H. Taminiau, R. Hanson. Loophole-free bell inequality violation using electron spins separated by 1.3 kilometres. Nature, 526(7575):682–686, (2015).

[28] M. Pompili, S. L. N. Hermans, S. Baier, H. K. C. Beukers, P. C. Humphreys, R. N. Schouten, R. F. L. Vermeulen, M. J. Tiggelman, L. dos Santos Martins, B. Dirkse, S. Wehner, R. Hanson, Realization of a multi-node quantum network of remote solid-state qubits, Science, 372, 259-264 (2021).

[29] R. D. Simmonds, P. S. Salter, A. Jesacher, M. J. Booth, Three dimensional laser microfabrication in diamond using a dual adaptive optics system, Opt. Express 19, 24122–24128 (2011).

[30] P. S. Salter, M. J. Booth, Adaptive optics in laser processing. Light Sci Appl 8, 110 (2019).

[31] M. W. Doherty, N. B. Manson, P. Delaney, F. Jelezko, J. Wrachtrup, and L. C. L. Hollenberg. The nitrogen-vacancy colour centre in diamond. Physics Reports, 528(1):1–45, (2013)

[32] S. Tamura, G. Koike, A. Komatsubara, T. Teraji, S. Onoda, L. P. McGuinness, L. Rogers, B. Naydenov, E. Wu, L. Yan, F. Jelezko, T. Ohshima, J. Isoya, T. Shinada, T. Tanii. Array of bright silicon-vacancy centres in diamond fabricated by low-energy focused ion beam implantation. Applied Physics Express, 7 (11):115201, (2014).

[33] N. Bar-Gill, L. Pham, A. Jarmola, D. Budker, R. Walsworth, solid-state electronic spin coherence time approaching one second, Nat. Commun. 4 1743, (2013).

[34] G. Balasubmarmanian, P. Neumann, D. Twitchen, M. Markham, R. Kolesov, N. Mizuochi, J. Isoya, J. Achard, J. Beck, J. Tissler, V. Jacques, P. R. Hemmer, F. Jelezko, J. Wrachtrup, Ultralong spin coherence time in isotropically engineered diamond, Nat. Mater, 8 5 383-387 (2009).

[35] J. Walker, Optical absorption and luminescence in diamond, Reports on Progress in Physics, Volume 42, Issue 10, pp. 1605-1659, (1979).

[36] G. Thiering, Study of quantum bits in diamond from first principles, BMe Research Grant (2018).

[37] L. Du Preez. Electron paramagnetic resonance and optical investigations of defect centres in diamond. University of Witwatersrand, PhD thesis, (1965).

[38] J. H. N. Loubser and J. A. Van Wyk. Electron spin resonance in annealed type 1b diamond. Diamond Res, 11:4–7, (1977).

[39] N. B. Manson, X-F. He, P. T. H. Fisk. Raman heterodyne detected electron-nuclear-double-resonance measurements of the nitrogen vacancy centre in diamond. Optics letters, 15(19):1094–1096, (1990).

[40] X-F. He, P. T. H. Fisk, N. B. Manson. Autler–townes effect of the photoexcited diamond nitrogen-vacancy centre in its triplet ground state. Journal of applied physics, 72(1):211–217, (1992).

[41] N. B. Manson, X-F. He, P. T. H. Fisk. Raman heterodyne studies of the nitrogen-vacancy centre in diamond. Journal of luminescence, 53(1-6):49–54, (1992).

[42] X-F. He, N. B. Manson, P. T. H. Fisk. Paramagnetic resonance of photoexcited n-v defects in diamond. i. level anticrossing in the 3 a ground state. Physical Review B, 47(14):8809, (1993).

[43] D. P. DiVincenzo, The physical implementation of quantum computation. Fortschritte der Physik, 48(9-11):771–783, (2000).

[44] L. Rondin, J-P. Tetienne, J. F. Roch, P. Maletinsky, V. Jacques, Magnetometry with nitrogen-vacancy defects in diamond, Reports on Progress in Physics, Volume 77, Issue 5, (2014).

[45] E. Van Oort, N. B. Manson, M. Glasbeek. Optically detected spin coherence of the diamond NV centre in its triplet ground state. Journal of Physics C: solid-state Physics, 21(23):4385, (1988).

[46] A. Gruber, A. Drabenstedt, C. Tietz, L. Fleury, J. Wrachtrup, C. Von Borczyskowski. Scanning confocal optical microscopy and magnetic resonance on single defect centres. Science, 276(5321):2012–2014, (1997).

[47] C. Kurtsiefer, S. Mayer, P. Zarda, Harald Weinfurter. Stable solid-state source of single photons. Physical review letters, 85(2):290, (2000).

[48] A. T. Collins, M. F. Thomaz, M. I. B. Jorge, Luminescence decay time of the 1.945eV centre in type Ib diamond, Journal of Physics C, 16 (11) 2177, (1983).

[49] B. Scharfenberger, W. Munro, K. Nemeto, Coherent Control of an NV centre with one adjacent Carbon 13, New Journal of Physics, 16, 9, (2014).

[50] H.-J Wang, C. S. Shin, C. E. Avalos, S. J. Seltzer, D. Budker, A. Pines, V. S. Bajaj. Sensitive magnetic control of ensemble nuclear spin hyperpolarisation in diamond. Nat. Commun. 4, 1940, (2013)

[51] I. Popa, T. Gaebel, M. Domhan, C. Wittmann, F. Jelezko, J. Wrachtrup. Energy levels and decoherence properties of single electron and nuclear spins in a defect centre in diamond. Physical Review B, 70(20):201203, (2004).

[52] C. E. Bradley, J. Randall, M. H. Abobeih, R. C. Berrevoets, M. J. Degen, M. A. Bakker, M. Markham, D. J. Twitchen, T. H. Taminiau, A Ten-Qubit Solid-State Spin Register with Quantum Memory up to One Minute, Phys. Rev. X 9, 031045 (2019).

[53] H. P. Bartling, M. H. Abobeih, B. Pingault, M. J. Degen, S. J. H. Loenen, C. E. Bradley, J. Randall, M. Markham, D. J. Twitchen, T. H., Coherence and entanglement of inherently long-lived spin pairs in diamond, arXiv:2103.07961, (2021).

[54] P. Tamarat, T. Gaebel, J. R. Rabeau, M. Khan, A. D. Greentree, H. Wilson, L. C. L. Hollenberg, S. Prawer, P. Hemmer, F. Jelezko, J. Wrachtrup. Stark shift control of single optical centres in diamond. Physical review letters, 97(8): 083002, (2006).

[55] A. Batalov, V. Jacques, F. Kaiser, P. Siyushev, P. Neumann, L. J. Rogers, R. L. McMurtrie, N. B. Manson, F. Jelezko, J. Wrachtrup. Low temperature studies of the excited-state structure of negatively charged nitrogen-vacancy color centres in diamond. Physical Review Letters, 102(19):195506, (2009).

[56] E. Togan, Y. Chu, A. S. Trifonov, L. Jiang, J. Maze, L. Childress, M. V. G. Dutt, A. S. Sorensen, P. R. Hemmer, A. S Zibrov, M. D. Lukin, Quantum entanglement between an optical photon and a solid-state spin qubit, Nature 466 (7307) 730-734 (2010).

[57] J. P. Hadden, J. P. Harrison, A. C. Stanley-Clarke, L. Marseglia, Y-L. D. Ho, B. R. Patton, J. L. O'Brien, J. G. Rarity. Strongly enhanced photon collection from diamond defect centres under microfabricated integrated solid immersion lenses. Applied Physics Letters, 97(24):241901, (2010).

[58] S. Johnson, P. Dolan, T. Grange, A. A. P. Trichet, G. Hornecher, Y. C. Chen, L. Weng, G.M. Hughes, A.A.R Watt, A. Auffeves, J.M. Smith, Tunable Cavity coupling of the zero-phonon line of nitrogen vacancy defects in diamond, New Journal of Physics, 17, 12, 12203 (2015)

[59] M. Ruf, M. J. Weaver, S. B. Van Dam, R. Hanson, Resonant Excitation and Purcell Enhancement of Coherent Nitrogen-Vacancy centres Coupled to a Fabry-Pérot Micro-Cavity, Phys. Rev. Applied 15, 024049, (2021).

[60] C. Bradac, W. Gao, J. Forneris, M. E. Trusheim, I. Aharonovich, Quantum nanophotonics with group IV defects in diamond, Nature Communications volume 10, Article number: 5625 (2019).

[61] G. Thiering, A. Gali, Ab Initio Magneto-Optical Spectrum of Group-IV Vacancy Color centres in Diamond, Phys. Rev. X 8, 021063 (2018).

[62] T. Iwasaki, Y. Miyamoto, T. Taniguchi, P. Siyushev, M. H. Metsch, F. Jelezko, M. Hatano, Tin-Vacancy Quantum Emitters in Diamond, Phys. Rev. Letters, 119, 253601 (2017).

[63] T. Schröder, M. E, Trusheim, M. Walsh, L. Li, J. Zheng, M. Schukraft, A. Sipahigil, R. E. Evans, D. D. Sukachev, C. T. Nguyen, J. L. Pacheco, R. M. Camacho, E. S. Bielejec, M. D. Lukin, D. Englund, Scalable focused ion beam creation of nearly lifetime-limited single quantum emitters in diamond nanostructures Nat Commun. Vol 8: 15376, (2017).

[64] C. Hepp, T. Muller, V. Waselowski, J. N. Becker, B. Pingault, H. Sternschulte, D. Steinmuller-Nethl, A Gali, J.R. Maze, M. Atture, C. Becher, Electronic structure of the silicon vacancy color centre in diamond, Phys Rev Lett 112 3 036405 (2014).

[65] E. Neu, D. Steinmetz, J. Riedrich-Moller, S. Gsell, M. Fischer, M. Schreck, C. Becher, Single photon emission from silicon-vacancy colour centres in chemical vapour deposition nano-diamonds on iridium, New Journal of Physics, 13(2):025012, (2011).

[66] A. T. Collins, L. Allers, C. J. H. Wort, G. A. Scarsbrook. The annealing of radiation damage in de beers colourless cvd diamond. Diamond and Related Materials, 3(4-6):932–935, (1994).

[67] U. Jantzen, A. B. Kurz, D. S. Rudnicki, C. Schafermeier, K. D. Jahnke, U. L. Andersen, V. A. Davydov, V. N. Agafonov, A. Kubanek, L. J. Rogers, F. Jelezko, Nanodiamonds carrying silicon-vacancy quantum emitters with almost lifetime limited linewidths. New Journal of Physics, 18(7):073036, (2016).

[68] K. Li, Y. Zhou, A. Rasmita, I. Aharonovich, W. B. Gao. Nonblinking emitters with nearly lifetime-limited linewidths in cvd nanodiamonds. Physical Review Applied, 6(2):024010, (2016).

[69] C. Arend, J. N. Becker, H. Sternschulte, D. S. Nethl, C. Becher. Photoluminescence excitation and spectral hole burning spectroscopy of silicon vacancy centres in diamond. Physical Review B, 94(4):045203, (2016).

[70] A. Sipahigil, K.D. Jahnke, L.J. Rogers, T. Teraji, J. Isoya, A.S. Zibrov, F. Jelezko, M.D. Lukin, Indistinguishable photons from separated silicon vacancy centres in diamond, Phys Rev Lett 113 (11) 113602, (2014).

[71] T. Müller, C. Hepp, B. Pingault, E. Neu, S. Gsell, M. Schreck, H. Sternschulte, D. Steinmüller-Nethl, C. Becher, M. Atatüre, Optical signatures of silicon-vacancy spins in diamond, Nature Communications Vol 5, 3328 (2014).

[72] L Nicolas, T. Delord, P. Huillery, C. Pellet-Mary, G. Hetet, Sub-GHz Linewidth Ensembles of SiV centres in a Diamond Nanopyramid Revealed by Charge State Conversion, ACS Photonics, 6, 10, 2413–2420, (2019).

[73] S. Lindner, A. Bommer, A. Muzha, A. Krueger, L. Gines, S. Manda, O. Williams, E. Londero, A. Gali and C. Becher, Strongly inhomogeneous distribution of spectral properties of silicon-vacancy color centres in nanodiamonds, New J. Phys. 20 115002 (2018).

[74] J. I. Zhang, H Ishwata, T. M. Babinec, M. Radulaski, K. Muller, K.G. Lagoudakis, C. Dory, J. Dahl, R. Edgington, V. Souliere, G. Ferro, A.A. Fokin, P.R. Schriener, Z.-X. Shen, N.A. Melosh, A. Vuckovic, Hybrid group IV nanophotonic structures incorperating diamond silicon vacancy color centres, Nano Lett 16, 212-217, (2012).

[75] J. N. Becker, J. Gorlitz, C. Arend, M. Markham, C. Becher. Ultrafast all-optical coherent control of single silicon vacancy colour centres in diamond. Nature Communications, 7:13512, (2016).

[76] B. Pingault, J. N. Becker, H. Carsten, H. Schulte, C. Arend, C. Hepp, T. Godde, A. I. Tartakovskii, M. Markham, C. Becher, Mete Atatüre, All-Optical Formation of Coherent Dark States of Silicon-Vacancy Spins in Diamond, Phys. Rev. Lett. 113, 263601 (2014).

[77] L. J. Rogers, K. D. Jahnke, M. H. Metsch, A. Sipahigil, J. M. Binder, T. Teraji, H. Sumiya, J. Isoya, M. D. Lukin, P. Hemmer, F. Jelezko, All-Optical Initialization, Readout, and Coherent Preparation of Single Silicon-Vacancy Spins in Diamond, Phys. Rev. Lett. 113, 263602 (2014).

[78] J. N. Becker, B. Pingault, D. Groß, M. Gundogan, N. Kukharchyk, M. Markham, A. Edmonds, M. Atatüre, P. Bushev, C. Becher, All-Optical Control of the Silicon-Vacancy Spin in Diamond at Millikelvin Temperatures, Phys. Rev. Lett. 120, 053603 (2018).

[79] B. Pingault, D-D. Jarausch, C. Hepp, L. Klintberg, J. N. Becker, M. Markham, C. Becher, M. Atatüre, Coherent control of the silicon-vacancy spin in diamond, Nat Commun 8, 15579, (2017).

[80] J. N. Becker, E. Neu, Semiconductors and Semimetals: chapter Seven - The silicon vacancy centre in diamond Vol 103, pp.201-235 (2020).

[81] V.S. Vavilov, A. A. Gippius, A. M. Zaitsev, B. V. Derjaguin, B. V. Spitsyn, A. E. Aleksensko, Investigation of the cathodoluminescence of epitaxial diamond films, Sov. Phys-Semicond. 14 1078, (1981).

[82] C. D. Clark, H. Kanda, I. Kiflawi, G. Sittas, Silicon Defects in Diamond, Phys. Reb. B 51 16681-88, (1995).

[83] J. P. Goss, R. Jones, S. J. Breuer, P. R. Briddon, S. Oberg, The Twelve Line 1.682 eV Luminescence centre in Diamond and the Vacancy-Silicon Complex Phys. Rev. Lett. 77, 3041 (1996).

[84] C. Wang, C. Kurtsiefer, H. Weinfurter, B. Burchard, Single photon emission from SiV centres in diamond produced by ion implantation, J. Phys. B: At. Mol. Opt. Phys. 39 37, (2005).

[85] B. L. Green, S. Mottishaw, B. G. Breeze, A. M. Edmonds, U. F. S. D'Haenens-Johansson, M. W. Doherty, S. D. Williams, D. J. Twitchen, M. E. Newton, The neutral silicon-vacancy centre in diamond: spin polarization and lifetimes, Phys. Rev. Lett. 119, 096402 (2017)

[86] Y. Rong, K. Cheng, Z. Ju, C. Pan, Q. Ma, S. Liu, S. Shen, B. Wu, T. Jia, E. Wu, H. Zeng, Bright near-surface silicon vacancy centres in diamond fabricated by femtosecond laser ablation, Opt. Lett. 44, 3793-3796 (2019).

[87] B. L. Green, M. W. Doherty, E. Nako, N. B. Manson, U. F. S. D'Haenens-Johansson, S. D. Williams, D. J. Twitchen, and M. E. Newton, Electronic structure of the neutral silicon-vacancy centre in diamond, Phys. Rev. B 99, 161112(R) (2019).

[88] U. F. S. D'Haenens-Johansson, A. M. Edmonds, B. L. Green, M. E. Newton, Optical properties of the neutral silicon split-vacancy centre in diamond, Phys. Rev. B 84, 245208 (2011).

[89] B. C. Rose, D Huang, Z.H. Zhang, P. Stevenson, A. M. Tyryshkin S. Sangtawesin, Observation of an environmentally insensitive solid-state spin defect in diamond, Science, Vol. 361, Issue 6397, pp. 60-63, (2018).

[90] A. Gali and J. R. Maze, Ab initio study of the split silicon-vacancy defect in diamond: Electronic structure and related properties, Phys. Rev. B 88, 235205, (2013).

[91] P. Siyushev, M. H. Metsch, A. Ijaz, J. M. Binder, M. K. Bhaskar, D. D. Sukachev, A. Sipahigil, R. E. Evans, C. T. Nguyen, M. D. Lukin, P. R. Hemmer, Y. N. Palyanov, I. N. Kupriyanov, Y. M. Borzdov, L. J. Rogers, F. Jelezko, Optical and microwave control of germanium-vacancy centre spins in diamond, Phys. Rev. B 96, 081201(R), (2017).

[92] T. Iwasaki, F. Ishibashi, Y. Miyamoto, Y. Doi, S. Kobayashi, T. Miyazaki, K. Tahara, K. D. Jahnke, L. J. Rogers, B. Naydenov, F. Jelezko, S. Yamasaki, S. Nagamachi, T. Inubushi, N. Mizuochi, M. Hatano, Germanium-Vacancy Single Color centres in Diamond, Scientific Reports Vol 5, 12882 (2015).

[93] M. K. Bhaskar, D. D. Sukachev, A. Sipahigil, R. E. Evans, M. J. Burek, C. T. Nguyen, L. J. Rogers, P. Siyushev, M. H. Metsch, H. Park, F. Jelezko, M. Loncar, and M. D. Lukin, Quantum Nonlinear Optics with a Germanium-Vacancy Color centre in a Nanoscale Diamond Waveguide, Phys. Rev. Lett. 118, 223603 (2017)

[94] J. Görlitz, D. Herrmann, G. Thiering, P. Fuchs, M. Gandil, T. Iwasaki, T. Taniguchi, Michael Kieschnick, J. Meijer, M. Hatano, A. Gali, C. Becher, Spectro-

scopic investigations of negatively charged tin-vacancy centres in diamond, New J. Phys. 22 013048, (2020).

[95] M. E. Trusheim, B. Pingault, N. H. Wan, M. Gündoğan, L. De Santis, R. Debroux, D. Gangloff, C. Purser, K. C. Chen, M. Walsh, J. J. Rose, J. N. Becker, B. Lienhard, E. Bersin, I. Paradeisanos, G. Wang, D. Lyzwa, A. R-P. Montblanch, G. Malladi, H. Bakhru, A. C. Ferrari, I. A. Walmsley, M. Atatüre, D. Englund, Transform-Limited Photons From a Coherent Tin-Vacancy Spin in Diamond, Phys. Rev. Lett. 124, 023602, (2020).

[96] R. Debroux, C. P. Michaels, C. M. Purser, N. Wan, M. E. Trusheim, J. A. Martínez, R. A. Parker, A. M. Stramma, K. C. Chen, L. de Santis, E. M. Alexeev, A. C. Ferrari, D. Englund, D. A. Gangloff, M. Atatüre, Quantum control of the tin-vacancy spin qubit in diamond, preprint, arXiv:2106.00723 (2021).

[97] M. E. Trusheim, N. H. Wan, K. C. Chen, C. J. Ciccarino, J. Flick, R. Sundararaman, G. Malladi, E. Bersin, M. Walsh, B. Lienhard, H. Bakhru, P. Narang, D. Englund, Lead-related quantum emitters in diamond, Phys. Rev. B 99, 075430, (2019).

[98] Y.I, Sohn, S. Meesala, B. Pingault, H. A. Atikian, J. Holzgrafe, M. Gündoğan, C. Stavrakas, M. J. Stanley, A. Sipahigil, J. Choi, M. Zhang, J. L. Pacheco, J. Abraham, E. Bielejec, M. D. Lukin, M. Atatüre, M. Lončar, Controlling the coherence of a diamond spin qubit through its strain environment, Nature Communications volume 9, Article number: 2012 (2018).

[99] J. R. Weber, W. F. Koehl, J. B. Varley, A. Janotti, B. B. Buckley, C. G. Van de Walle, and D. D. Awschalom, Quantum computing with defects, PNAS 107 (19) 8513-8518, (2010).

[100] C. P. Michaels, J. A. Martínez, R. Debroux, R. A. Parker, A. M. Stramma, L. I. Huber, C. M. Purser, M. Atature, D. A. Gangloff, Multidimensional cluster states using a single spin-photon interface coupled strongly to an intrinsic nuclear register, arXiv:2104.12619, (2021).

[101] B. M. Chernobrod and G. P. Berman. "Spin microscope based on optically detected magnetic resonance." J. Appl. Phys., 97, 014903–014903 (2005).

[102] R. L. Patel, L. Q. Zhou, A. C. Frangeskou, G. A. Stimpson, B. G. Breeze, A. Nikitin, M. W. Dale, E. C. Nichols, W. Thornley, B. L. Green, M. E. Newton, A. M. Edmonds, M. L. Markham, D. J. Twitchen, G. W. Morley, Sub-nanotesla magnetometry with a fibre-coupled diamond sensor, Phys. Rev. Applied 14, 044058 (2020).

[103] L. V. H. Rodgers, L. B. Hughes, M. Xie, P. C. Maurer, S. Kolkowitz, A. C. Bleszynski Jayich, N. P. de Leon, Materials challenges for quantum technologies based on color centers in diamond, arXiv:2106.12100, (2021).

[104] F. P. Bundy, H. T. Hall, R. H. Wentorf, Man-made Diamonds, Nature 176 (4471) 51-55, (1955).

[105] J. M. Smith, S. A. Meynell, A. C. Bleszynski Jayich, J. Meijer, Colour centre generation in diamond for quantum technologies, Nanophotonics, 8(11), 1889-1906.(2019)

[106] J. J. Gracio, Q. H. Fan, J. C. Madaleno, Diamond Growth by Chemical Vapour Deposition, Journal of Physics, 43 37 (2010).

[107] J. F. Barry, J. M. Schloss, E. Bauch, M. J. Turner, C. A. Hart, L. M. Pham, R. L. Walsworth, Sensitivity optimization for NV-diamond magnetometry, Rev. Mod. Phys. 92, 015004, (2020).

[108] R. Abbascian, H, Zhu, C. Clarke, High Pressure-high temperature growth of diamond crystals using split sphere apparatus, diamond and related Materials, 14 11-12 1916-1919, (2005).

[109] J. Schwartz, S. Aloni, D. Olgetree, T. Schenkel, Effects of low energy electron irradiation on the formation of nitrogen vacancy centres in single crystal diamond, New Journal Phys. 14 4 043024 (2012).

[110] J. Michl, T. Teraji, S. Zaiser, I. Jakobi, G. Waldherr, F. Dolde, P. Neumann, M. W. Doherty, N. B. Mason, J. Isoya, J. Wrachtrup, Perfect alignment and preferential orientation of nitrogen vacancy centres during chemical vapour deposition diamond growth on (111) surfaces, Appl Physics Lett 104(11) 113107, (2014)

[111] K. Groot-Berning, N. Raatz, I. Dobrinets, M. Lesik, P. Spinicelli, A. Tallaire, J. Achard, V. Jacques, J. F. Roch, A. M. Zaitsev, J. Meijer, S. Pezzagna, Passive charge state control of nitrogen-vacancy centres in diamond using phosphorous and boron doping, Physica Status Solidi (A) Applications and Materials 211(10), (2014).

[112] T. Lühmann, R. John, R. Wunderlich, J. Meijer, S. Pezzagna, Coulomb-driven single defect engineering for scalable qubits and spin sensors in diamond, Nature Comm. volume 10, 4956 (2019).

[113] E. D. Herbschleb, H. Kato, Y. Maruyama, T. Danjo, T. Makino, S. Yamasaki, I. Ohki, K. Hayashi, H. Morishita, M. Fujiwara, N. Mizuochi, Ultra-long coherence times amongst room-temperature solid-state spins, Nature Comm. Vol 10, 3766 (2019).

[114] Y. Tao, C. Degen, Facile Fabrication of single crystal diamond nano-structures with ultra high aspect ratio, Adv. Materials 25 (29) 3962-3967, (2013).

[115] T. N. Tran Thi, B. Fernandez, D. Eon, E. Gheeraert, J. Hartwig, T. A. Lafford, A. Perrat-Mabilon, C. Peaucelle, C. Olivero, E. Bustarret, Ultrasmooth single crystal diamond surfaces resulting from implantation and liftoff processes, Physica status solidi A 208 (9) 20157-2061 (2011).

[116] A. J. Armini, S. N. Bunker, M. B. Spitzer, Non-mass analysed ion implantation equipment for high volume solar cell production, Proc 16th IEEE Photovoltaic Specialist Conference, San Diego California pp 895-899 (1982).

[117] S. Pezzagna, B. Naydenov, F Jelezko, J Wrachtrup, J Meijer, Creation efficiency of NV centres in diamond, New J Phys, 12 (6) 065017 (2010).

[118] J. Meijer, B. Burchard, M. Domhan, C. Wittmann, T. Gaebel, I. Popa, F. Jelezko, and J. Wrachtrup, Generation of single colour centres by focused nitrogen implantation, Appl. Phys. Lett. 87, 261909 (2005).

[119] C. Santori, P. Barclay, K. C. Fu, R. Beausoleil, Vertical distribution of nitrogen-vacancy centres in diamond formed by ion implantation and annealing, Phys. Rev. B 79 125313, (2009).

[120] G.E. Anner. Ion Implantation. In: Planar Processing Primer. Springer, Dordrecht. (1990)

[121] A. G. Alekseev, V. N. Amosov, A. V. Krasil'nikov, S. N. Tugarinov, V. V. Frunze, and A. Yu Tsutskikh. Transformation of gr1 defects in annealed natural type iia diamonds. Technical Physics Letters, 26(6):496–498, (2000).

[122] S. Sangtawesin, T. O. Brundage, Z. J. Atkins, J. R. Petta, Highly tunable formation of nitrogen-vacancy centers via ion implantation, Appl. Phys. Lett. 105, 063107 (2014).

[123] T. Shinada, S. Okamoto, T. Kobayashi, I. Ohdomari. Enhancing semiconductor device performance using ordered dopant arrays, Nature, 437:1128–31, (2005).

[124] A. E. Rugar, H. Lu, C. Dory, S. Sun, P. J. McQuade, Z. X. Shen, N. A. Melosh, J. Vuckovic, Generation of Tin-Vacancy Centers in Diamond via Shallow Ion Implantation and Subsequent Diamond Overgrowth, Nano Lett. 2020, 20, 3, 1614–1619, (2020).

[125] T. Gaebel, M. Domham, I. Popa, C. Whittman, P. Neumann, F. Jelezko, J.R. Rabeau, N. Stavrias, A.D. Greentree, S. Prawer, J. Meijer, J. Twamley, P.R. Hemmer, J.Wrachtrup, Room Temperature Coherent Coupling of single spins in diamond, Nat Physics 2 (6) 408-413 (2006).

[126] M. Haruyama, S. Onoda, T. Higuchi, W. Kada, A. Chiba, Y. Hirano, T. Teraji, R. Igarashi, S. Kawai, H. Kawarada, Y. Ishii, R. Fukuda, T. Tanii, J. Isoya, T. Ohshima, O. Hanaizumi, Triple nitrogen-vacancy centre fabrication by $C_5N_4H_n$ ion implantation

[127] A. Stacey, D. Simpson, T. Karle, B. Gibson, V. Acosta, Z. Huang, K. Fu, C. Santori, R. Beausoleil, L. McGuiness, K. Ganesan, S. Tomljenovic-Hanic, A. Greentree, S. Prawer, Near-Surface Spectrally Stable Nitrogen Vacancy Centres Engineered in Single Crystal Diamond, Adv. Materials 24 3333-3338, (2012).

[128] Y. Zhou, Z. Mu, G. Adamo, S. Bauerdick, A. Rudzinski, I. Aharonovich, W-B. Gao, Direct writing of single germanium vacancy centre arrays in diamond, New J. Phys. 20 125004 (2018).

[129] I. Kiflawi, A. T. Collins, K. Iakoubovskii and D. Fisher, Electron irradiation and the formation of vacancy–interstitial pairs in diamond, J. Phys.: Condens. Matter 19 046216 (2007).

[130] P. Hovington, D. Drouin, R. Gauvin, CASINO: A new Monte Carlo code in C language for electron beam inter-action part I: description of the program. Scanning 19:1–14., (1997).

[131] C. A. McLellan, B. A. Myers, S. Kraemer, K. Ohno, D. D. Awschalom, and A. C. Bleszynski Jayich, Patterned formation of highly coherent nitrogen-vacancy centres using a focused electron irradiation technique, Nano Lett. 16, 2450–2454 (2016).

[132] Eichhorn TR, McLellan CA, Jayich AC. Optimizing the formation of depth-confined nitrogen vacancy centre spin ensembles in diamond for quantum sensing, Phys. Rev. Materials 3, 113802, (2019).

[133] J. P. Hadden, V. Bharadwaj, B. Sotillo, S. Rampini, R. Osellame, J. D. Witmer, H. Jayakumar, T. T. Fernandez, A. Chiappini, C. Armellini, M. Ferrari, R. Ramponi, P. E. Barclay, S. M. Eaton, Integrated waveguides and deterministically positioned nitrogen vacancy centres in diamond created by femtosecond laser writing, Opt. Lett. 43, 3586-3589 (2018).

[134] R. Gattass, E. Mazur, Femtosecond laser micromachining in transparent materials, Nature Photon 2, 219–225 (2008).

[135] C. B. Schaffer, A. Brodeur, E. Mazur. Laser-induced breakdown and damage in bulk transparent materials induced by tightly focused femtosecond laser pulses. Measurement Science and Technology, 12(11):1784, (2001).

[136] N. A. Vainos. Laser growth and processing of photonic devices. Cambridge, Woodhead, (2012).

[137] Y. Liu, G. Chen, M. Song, X. Ci, B. Wu, E. Wu, H. Zeng. Fabrication of nitrogen vacancy color centres by femtosecond pulse laser illumination. Optics express, 21(10):12843–12848, (2013).

[138] P. Sprangle, J. R. Penano, B. Hafizi. Propagation of intense short laser pulses in the atmosphere. Physical Review E, 66(4):046418, (2002).

[139] Neff M, Kononenko TV, Pimenov SM, Romano V, Lüthy W, Konov VI. Femtosecond laser writing of buried graphitic structures in bulk diamond. Appl Phys A 97:543–7, (2009)

[140] V. Bharadwaj, O. Jedrkiewicz, J. P. Hadden, B. Sotillo, M. R. Vázquez, P. Dentella, T.T. Fernandez, A. Chiappini, A. N. Giakoumaki, T. Le Phu, M. Bollani, M. Ferrari, R. Ramponi, P. E. Barclay, S. M. Eaton, Femtosecond laser written photonic and microfluidic circuits in diamond, J. Phys. Photonics 1 022001, (2019)

[141] S. Lagomarsino, M. Bellini, C. Corsi, S. Fanetti, F. Gorelli, I. Liontos, G. Parrini, M. Santoro, S. Sciortino, Electrical and Raman-imaging characterization of laser-made electrodes for 3D diamond detectors. Diam Relat Mater; 43:23–8, (2014).

[142] A. Courvoisier, M. J. Booth, and P. S. Salter, Inscription of 3D waveguides in diamond using an ultrafast laser, Appl. Phys. Lett. 109, 031109 (2016).

[143] S. M. Pimenov, A. A. Khomich, B. Neuenschwander, B. Jaggi, V. Romano. Picosecond-laser bulk modification induced enhancement of nitrogen-vacancy luminescence in diamond, Proc. SPIE 8967, Laser Applications in Microelectronic and Optoelectronic Manufacturing (LAMOM) XIX, 89670B, (2014).

[144] T. Kurita, N. Mineyuki, Y. Shimotsuma, M. Fujiwara, N. Mizuochi, M. Shimizu, K. Miura, Efficient generation of nitrogen-vacancy centre inside diamond with shortening of laser pulse duration, Appl Phys Lett 2018;113:211102. (2018).

[145] C. J. Stephen, B. L. Green, Y. N. D. Lekhai, L. Weng, P. Hill, S. Johnson, A. C. Frangeskou, P. L. Diggle, Y.-C. Chen, M. J. Strain, E. Gu, M. E. Newton, J. M. Smith, P. S. Salter, G. W. Morley, Deep Three-Dimensional Solid-State Qubit Arrays with Long-Lived Spin Coherence, Phys. Rev. Applied 12, 064005 (2019).

[146] B. Sotillo, V. Bharadwaj, J. P. Hadden, S. Rampini, A. Chiappini, T. T. Fernandez, C. Armellini, A. Serpengüzel, M. Ferrari, P. E. Barclay, R. Ramponi, S. M. Eaton, Visible to Infrared Diamond Photonics Enabled by Focused Femtosecond Laser Pulses, Micromachines, 8, 60, (2017).

[147] V. Yurgens, J. A. Zuber, S. Flagan, M. De Luca, B. J. Shields, I. Zardo, P. Maletinsky, R. J. Warburton, and T. Jakubczyk, Low charge-noise nitrogen-vacancy centres in diamond created using laser writing with a solid-immersion lens, ACS Photonics 2021, 8, 6, 1726–1734, (2021).

[148] S. Castelletto, J. Maksimovic, T. Katkus, T. Ohshima, B. C. Johnson, S. Juodkazis, Color centres Enabled by Direct Femto-Second Laser Writing in Wide Bandgap Semiconductors, Nanomaterials, Vol 11, Issue 1, pp. 72 (2021).

[149] S. Castelletto, A. F. M. Almutairi, K. Kumagai, T. Katkus, Y. Hayasaki, B. C. Johnson, and S. Juodkazis, Photoluminescence in hexagonal silicon carbide by direct femtosecond laser writing, Opt. Lett. 43, 6077–6080 (2018).

[150] U. Saleem, M. D. Birowosuto, S. Hou, A. Maurice, T. B. Kang, E. H. T. Teo, M. Tchernycheva, N. Gogneau, and H. Wang, "Light emission from localised point defects induced in GaN crystal by a femtosecond-pulsed laser," Opt. Mater. Express 8, 2703–2712 (2018).

[151] Y. C. Chen, P. S. Salter, M. Niethammer, M. Widmann, F. Kaiser, R. Nagy, N. Morioka, C. Babin, J. Erlekampf, P. Berwian, M. J. Booth, J. Wrachtrup, Laser Writing of Scalable Single Color centres in Silicon Carbide, Nano Lett., 19, 4, 2377–2383 (2019).

[152] R. Buividas, I. Aharonovich, G. Seniutinas, X. W. Wang, L. Rapp, A. V. Rode, T. Taniguchi, and S. Juodkazis, Photoluminescence from voids created by femtosecond-laser pulses inside cubic-BN, Opt. Lett. 40, 5711–5713 (2015).

[153] V. Kononenko, I. Vlasov, E. Zavedeev, A. Khomich, V. Konov, Correlation between surface etching and NV centre generation in laser irradiated diamond, Applied Phys. A. 124:226 (2018).

[154] V. V. Kononenko, I. I. Vlasov, V. M. Gololobov, T. V. Kononenko, T. A. Semenov, A. A. Khomich, V. A. Shershulin, V. S. Krivobok, V. I. Konov, Nitrogen-vacancy defects in diamond produced by femtosecond laser nanoablation technique, Appl. Phys. Lett. 111, 081101 (2017).

[155] D. J. Twitchen, D. J. Twitchen, D. C. Hunt, C. Wade, M. E. Newton, J. M. Baker, T. R. Anthony, and W. F. Banholzer, The production and annealing stages of the self-interstitial (R2) defect in diamond, Physica B 273, 644–646 (1999).

[156] P. Deak, B. Aradi, M. Kaviani, T. Frauenheim, A. Gali, Formation of NV centres in diamond: A theoretical study based on calculated transitions and migration of nitrogen and vacancy related defects, Phys. Rev. B 89, 075203, (2014).

[157] X. Hu, Y. Dai, R. Li, H. Shen, X. He, The diffusion of Vacancies near a diamond (001) surface, solid-state Comm. 122 1 45-48 (2002).

[158] M. Newton, B. Campbell, D. Twitchen, J. Baker, T.Anthony, Recombination-enhanced diffusion of self-interstitial atoms and vacancy-interstitial recombination in diamond, Diamond, Relat. Materials, 11, 618, (2002).

[159] Y. C. Chen, Laser Writing of Coherent Colour Centres in Diamond, DPhil Materials, University of Oxford, (2017).

[160] S. Subedi, V. Fedorov, S. Mirov, M. Markham, Spectroscopy of GR1 centers in synthetic diamonds, Optical Materials Express Vol. 11, Issue 3, pp. 757-765 (2021).

[161] Y. Chu, N.P. de Leon, B.J. Shields, B. Hausmann, R. Evans, E. Togan, M. J. Burek, M. Markham, A. Stacey, A.S. Zibrov, A. Yacoby, D.J. Twitchen, M. Loncar, H. Park, P. Maletinsky, M.D. Lukin, Coherent Optical Transitions in Implanted Nitrogen Vacancy Centers, Nano Lett. 14, 4, pp.1982–1986, (2014).

[162] N. A. Dobrinets, V. G. Vins, A. M. Zaitsev, HPHT-Treated Diamonds, Springer Series in Materials Science, Volume 181

[163] T. V. Kononenko, M. Meier, M. S. Komlenok, S. M. Pimenov, V. Romano, V. P. Pashinin, V. I. Konov, Microstructuring of diamond bulk by IR femtosecond laser pulses, Appl. Phys. A 90, 645–651 (2008).

[164] L. V. Keldysh. Ionization in the field of a strong electromagnetic wave. Sov. Phys. JETP, 20(5):1307–1314, (1965).

[165] P. K. Kennedy, A First-Order Model for Computation of Laser-Induced Breakdown Thresholds in Ocular and Aqueous Media: Part I-Theory, IEEE Journal of Quantum Electron, Vol. 31, No. 12, p. 2241. (1995).

[166] T. Apostolova, Y. Hahn, Modeling of laser-induced breakdown in dielectrics with subpicosecond pulses, Journal of Applied Physics 88, 1024 (2000).

[167] L. V. Keldysh, The electron-hole liquid in semiconductors, Contemporary Physics, 27:5, 395-428, (1986)

[168] A. Kaiser, B. Rethfeld, M. Vicanek, G. Simon, Microscopic processes in dielectrics under irradiation by subpicosecond laser pulses, Phys. Rev. B 61, 11437 (2000).

[169] K. Plamann, F. Aptel, C. L. Arnold, A. Courjaud, C. Crotti, F. Deloison, F. Druon, P. Georges, M. Hanna, J-M. Legeais, Ultrashort pulse laser surgery of the cornea and the sclera, J. Opt. 12 084002, (2010).

[170] L. L. Taylor, R. E. Scott, J. Qiao, Integrating two-temperature and classical heat accumulation models to predict femtosecond laser processing of silicon, Opt. Mat. Express 8(3) 648-658 (2018).

[171] S. S. Mao, F. Quere, S. Guizard, X. Mao, R. E. Russo, G. Petite, P. Martin. Dynamics of femtosecond laser interactions with dielectrics. Applied Physics A, 79(7):1695–1709, (2004).

[172] N. Medvedev, H. O. Jeschke, B. Ziaja, Nonthermal phase transitions in semiconductors induced by a femtosecond extreme ultraviolet laser pulse, New J. Phys. 15 015016, (2013).

[173] H. O. Jeschke, M. E. Garcia, and K. H. Bennemann, Microscopic analysis of the laser-induced femtosecond graphitization of diamond, Phys. Rev. B 60, R3701(R) (1999).

[174] C. Z. Wang, K. M. Ho, M. D. Shirk, P. A. Molian, Laser-Induced Graphitization on a Diamond (111) Surface, Phys. Rev. Lett. 85, 4092 (2000).

[175] N. Itoh, T. Shimizu-Iwayama, T. Fujita. Excitons in crystalline and amorphous SiO2: formation, relaxation and conversion to Frenkel pairs. J Non Cryst Solids ;179:194–201 (1994).

[176] T. T. Williams, K. S. Song, W. L. Faust, C. H. Leung, Off-centre self-trapped excitons and creation of lattice defects in alkali halide crystals. Phys Rev B ;33:7232–40 (1986).

[177] J. Omachi, T. Suzuki, K. Kato, N. Naka, K. Yoshioka, M. Kuwata-Gonokami, Observation of Excitonic N-Body Bound States: Polyexcitons in Diamond, Phys. Rev. Lett. 111, 026402 (2013)

[178] F. Mauri, R. Carr, First-Principles Study of Excitonic Self-Trapping in Diamond, Phys. Rev. Lett. 75, 3166 (1995).

[179] D. Delgado, R. Villa, Statistical Molecular Dynamics study of displacement energies in diamond, Journal of Nuclear Mater. 419, 32–38 (2011).

[180] S. Lagomarsino, S. Sciortino, B. Obreshkov, T. Apostolova, C. Corsi, M. Bellini, E. Berdermann, C. J. Schmidt, Photoionisation of monocrystalline CVD diamond irradiated with ultrashort intense laser pulse, Phys. Rev. B Vol 93, 085128, (2016).

[181] M. Barbiero, S. Castelletto, M. Gu, Multi-focal laser fabrication of nitrogen vacancy centres in a bulk diamond, OSA Continuum 3(12), 3416-3423,9 (2020).

[182] A. Guenther, Laser induced damage in optical materials, CRC Press (2019)

[183] S. V. Popruzhenko, Keldysh theory of strong field ionization: history, applications, difficulties and perspectives, J. Phys. B: At. Mol. Opt. Phys. 47 204001, (2014).

[184] V. E. Gruzdev, Photoionization rate in wide bandgap crystals, Phys. Rev. B 75, 205106, (2007).

[185] K. W. Böer, U. W. Puhl, Semiconductor Physics. Springer, Cham. (2018).

[186] S. I. Kudryashov, R. A. Khmelnitskii, P. A. Danilov, N. A. Smirnov, A. O. Levchenko, O. E. Kovalchuk, M. V. Uspenskaya, E. A. Oleynichuk, M. S. Kovalev, Broadband and fine-structured luminescence in diamond facilitated by femtosecond laser driven electron impact and injection of "vacancy-interstitial" pairs, Optics Letters Vol. 46, Issue 6, pp. 1438-1441 (2021).

[187] J. L. Deziel, L. J. Dube, C. Varin, Dynamical rate equation model for femtosecond laser-induced breakdown in dielectrics, Phys. Rev. B. 104, 045201 (2021).

[188] E. I. Lipatov, D. E. Genin, D. V. Grigor'ev, V. F. Tarasenko Luminescence - An Outlook on the Phenomena and their Applications, chapter 9: Recombination Radiation in the diamond (2016).

[189] Piprek J. chapter 3 - Carrier Transport, Semiconductor Optoelectronic Devices, Academic Press, (2003).

[190] Brown, R. Hanbury; Twiss, R.Q., A new type of interferometer for use in radio astronomy, Philosophical Magazine. 45 (366): 663–682 (1954).

[191] A. Jesacher, M. J. Booth, Parallel direct laser writing in three dimensions with spatially dependent aberration correction, Opt. Express 18, 21090-21099 (2010).

[192] Goodman, J. W. Introduction to Fourier optics. New York: McGraw-Hill (1996).

[193] M. Kolesik, J. V. Moloney, Nonlinear optical pulse propagation simulation: From Maxwell's to unidirectional equations, Phys. Rev. E 70, 036604, (2004).

[194] M. Combescot, J. Bok, Electron-hole plasma generation and evolution in semiconductors, Journal of Luminescence, Vol 30, 1–4, pp. 1-17 (1985).

[195] Y. R. Shen, The Principles of Nonlinear Optics. New York: Wiley, (1984).

[196] S. J. Clarke, M. Segall, C. J. Pickard, P. J. Hasnip, M. Probert, K. Refson, M. C. Payne Z Kristallogr Cryst Mater., Vol. 220, Issue 5-6, pp. 567-570 (2004)

[197] P. Perdew, M. Ernzerhof, J. Chem. Phys., Vol. 105, Issue 22, pp. 9982-9985 (1996)

[198] N. Tandon, J. D. Albrecht, L. R. Ram-Mohan, Electron–phonon coupling and associated scattering rates in diamond, Diamond and Related Materials, Vol. 56, pp. 1-5, (2015).

[199] B. Monserrat, R. J. Needs, Comparing electron-phonon coupling strength in diamond, silicon, and silicon carbide: First-principles study, Phys. Rev. B 89, 214304 (2014).

[200] M. Kozak, F. Trojanek, P. Maly, Optical study of carrier diffusion and recombination in CVD diamond, Phys. Status Solidi A 210, No. 10, (2013).

[201] P. E. Selbmann, In: Hess K. (eds) Hot Carriers in Semiconductors. Springer, Boston, MA. pp. 19-22 (1996).

[202] C. D. Clark, P. J. Dean and P. V. Harris, Intrinsic edge absorption in diamond, Proc. R. Soc. London, Ser. A, 277, 312. (1964).

[203] H. Morimoto Y. Hazamaa, K Tanaka, N. Naka, Exciton lifetime and diffusion length in high-purity chemical-vapor-deposition diamond, Diamond and Related Materials, Vol 63, pp.47-50 (2016).

[204] H. Katow, J. Usukura, R. Akashi, K. Varga, S. Tsuneyuki, Numerical investigation of triexciton stabilization in diamond with multiple valleys and bands, Phys. Rev. B Vol 95, 125205 (2017).

[205] S. M. Bennington, R. I. Bewley, T. E. Weller, Using tip enhanced femtosecond lasers to create graphite nanostructures on diamond, STFC Central Laser facility, Annual Report 2008/2009 pp204.

[206] P. Stampfli, K. H. Bennermann, Theory for the instability of the diamond structure of Si, Ge, and C induced by a dense electron-hole plasma, Physical Review B (Condensed Matter and Materials Physics) 42, 7163 (1990).

[207] S. Salustro, Y. Nöel, C. M. Zicovich-Wilson, P. Olivero, R. Dovesi, The V + I defects in diamond: An ab initio investigation of the electronic structure, of the Raman and IR spectra, and of their possible recombination, J. Chem. Phys. 145, 184701 (2016).

[208] J. Bang, Y. Y. Sun, J-H. Song, S. B. Zhang, Carrier-induced transient defect mechanism for non-radiative recombination in InGaN light-emitting devices, Scientific Reports volume 6, Article number: 24404 (2016)

[209] A. Shenk, A model for the field and temperature dependence of Shockley-Read-Hall lifetimes in silicon. Solid-State Electronics, vol. 35, no. 11, p. 1585-1596. (1992).

[210] D. Saada, Diamond and graphite properties, PhD thesis, Israel Institute of Technology (2000).

[211] C. D. Clark, J. Walker, The Neutral Vacancy in Diamond, Proceedings of the Royal Society A, Vol. 334, Issue 1597, (1973).

[212] K. Iakoubovskii, S. Dannefaer, A. Stesmans, Evidence for vacancy-interstitial pairs in Ib-type diamond, Physical Review B. 71 (23): 233201. (2005)

[213] T. Kurita, Y. Shimotsuma, M. Fujiwara, M. Fujie, N. Mizuochi, M. Shimizu, K. Miura, Direct writing of high-density nitrogen-vacancy centres inside diamond by femtosecond laser irradiation, Appl. Phys. Lett. 118, 214001 (2021)

[214] C. Arend, J. N. Becker, H. Sternschulte, D. Steinmüller-Nethl, C. Becher, Photoluminescence excitation and spectral hole burning spectroscopy of silicon vacancy centres in diamond, Physical Review B 94 (4), 045203 (2016).

[215] G. Thiering, A. Gali, Complexes of silicon, vacancy, and hydrogen in diamond: A density functional study, Physical Review B 92, 165203 (2015).

[216] U. F. S. D'Haenens-Johansson, A. M. Edmonds, and M. E. Newton, EPR of a defect in CVD diamond involving both silicon and hydrogen that shows preferential alignment, Phys. Rev. B 82, 155205 (2010).

[217] B. G. Breeze , C. J. Meara, X. X. Wu, C. P. Michaels, R. Gupta, P. L. Diggle, M. W. Dale, B. L. Cann, T. Ardon, U. F. S. D'Haenens-Johansson, I. Friel, M. J. Rayson, P. R. Briddon, J. P. Goss, M. E. Newton, B. L. Green, Doubly charged silicon vacancy centre, Si-N complexes, and photochromism in N and Si codoped diamond,Phys. Rev. B, 101, 184115 (2020).

[218] A. Gali, J. R. Maze, Ab initio study of the split silicon-vacancy defect in diamond: Electronic structure and related properties, Phys. Rev. B 88, 235205, (2013).

[219] A. Gardill, I. Kemeny, M. C. Cambria, Y. Li, H. T. Dinani, A. Norambuena, J. R. Maze, V. Lordi, S. Kolkowitz, Probing charge dynamics in diamond with an individual color center, arXiv:2106.05405, (2021).

[220] C. Weinzetl, J. Görlitz, J. N. Becker, I. A. Walmsley, E. Poem, J. Nunn, C. Becher, Coherent Control and Wave Mixing in an Ensemble of Silicon-Vacancy centres in Diamond, Physical Review Letters 122 (6), 063601 (2019).

[221] M. Kempkes, T. Zier, K. Singer, M. E. Garcia, Ultrafast nonthermal NV center formation in diamond, Carbon, 174, 524-530, (2021).

APPENDIX

Appendix A

PDE Model

Outlined below is a summary of equations utilised in the coupled partial differential equation model defined in Chapter 5. Scattering rates taken from the literature are outlined in table 5.1.

A.1 Light intensity distribution

The differential equation governing the light intensity distribution is given by

$$\frac{dI}{dt}(r,z,t) = \left[\frac{\partial I}{\partial t}\right]_0 + \left[\frac{\partial I}{\partial t}\right]_{eh} \tag{A.1}$$

The first term comes from the initial focus assuming that the light does not interact with the material.

$$\left[\frac{\partial I}{\partial t}\right]_0 (r,z,t) = \frac{I_0(r,z,t+dt) - I_0(r,z,t)}{dt} \tag{A.2}$$

where

$$I_0(x,y,z,t) = I_V(x,y,z) \cdot I_t\left(t + \frac{\omega_0 n^2 (z_0 - z)}{c^2 \phi(x,y)}\right) \tag{A.3}$$

$$I_V(x,y,z) = \int_{-\infty}^{\infty}\int_{-\infty}^{\infty} I(k_x,k_y)_{BFP} e^{i\phi(x,y)(z-z_0)} e^{-i(k_x x + k_y y)}\, dk_x\, dk_y \tag{A.4}$$

$$\phi(x,y) = \phi_{Ab}(x,y) + \phi_{SLM}(x,y) \tag{A.5}$$

$$I(k_x,k_y)_{BFP} = \begin{cases} 1 & \text{if } k_x^2 + k_y^2 \leq R_{pupil} \\ 0 & \text{otherwise} \end{cases} \tag{A.6}$$

$$I_t(t) = E(t)^2 \tag{A.7}$$

$$E(t) = \mathrm{Re}\left[\exp\left[\frac{-(t-\mu)^2}{2\sigma^2} \right] e^{i\omega_0 t} \right] \tag{A.8}$$

The second term in equation A.1 comes from the changes to the distribution when interactions are considered including phase shifts, attenuation and reflections.

$$\left[\frac{\partial I}{\partial t}\right]_{eh}(r,z,t) = \left(\left[\frac{\partial E}{\partial t}\right]_{eh}(r,z,t) \right)^2 \cdot \frac{cn_2\epsilon_0}{2} \tag{A.9}$$

$$\begin{aligned} \left[\frac{\partial E}{\partial t}(r,z,t)\right]_{eh} = {} & E_0\left(r,z,t + \int_0^z \frac{\Delta\phi(r,Z,t)(Z-z)n_2}{c}\, dZ\right)\left(\prod_0^z \exp\left[-\alpha(r,Z,t)\frac{\omega_0}{c}\right]\right) \\ & - \int_0^\infty \int_z^\infty R(r,z,t) E\left(X,Z,t - \frac{n_2 n_r(r,z,t)\sqrt{(r-X)^2+(z-Z)^2}}{c}\right) \\ & \left(\frac{dr^2}{(r-X)^2+(z-Z)^2}\right) dX dZ - E_0(r,z,t) \end{aligned} \tag{A.10}$$

$$\Delta\phi(r,z,t) = \frac{\omega_0(n_2 - (n_2 n_r(r,z,t)))}{c\phi(r)} \tag{A.11}$$

$$\alpha(r,z,t) = \kappa_r\left(r + \int_0^z \Delta\phi(r,z,t)(Z-z)\, dZ, z, t + \int_0^z \frac{\Delta\phi(r,z,t)(Z-z)n_2}{c}\, dZ\right) \tag{A.12}$$

$$R(r,z,t) = \left| \frac{n_2 n_r(r,z,t) - n_2 n_r(r,z-dz,t)}{n_2 n_r(r,z,t) + n_2 n_r(r,z-dz,t)} \right|^2 \tag{A.13}$$

and

$$n_r(r,z,t) = \sqrt{\mathrm{Re}[\epsilon_r(r,z,t)]^2 \cdot \mathrm{Im}[\epsilon_r(r,z,t)]^2} + \frac{\mathrm{Re}[\epsilon_r(r,z,t)]}{2} \tag{A.14}$$

$$\kappa_r(r,z,t) = \sqrt{\mathrm{Re}[\epsilon_r(r,z,t)]^2 \cdot \mathrm{Im}[\epsilon_r(r,z,t)]^2} - \frac{\mathrm{Re}[\epsilon_r(r,z,t)]}{2} \tag{A.15}$$

$$\mathrm{Re}[\epsilon_r(r,z,t)] = \frac{\omega_p(r,z,t)^2\tau_{coll}^2}{1+(\omega_0^2\tau_{coll}^2)},\ \mathrm{Im}[\epsilon_r(r,z,t)] = \frac{\omega_p(r,z,t)^2\tau_{coll}}{\omega_0(1+(\omega_0^2\tau_{coll}^2))} \tag{A.16}$$

$$\omega_p(r,z,t) = \sqrt{\frac{(\rho_e(r,z,t)+\rho_h(r,z,t))\cdot e^2}{m\epsilon_0}} \tag{A.17}$$

A.2 Carrier density distributions

The second differential equation concerns the density of electrons in the conduction band. An identical equation exists for the valence band holes with ρ_e replaced by ρ_h and integral limits are replaced by the range of energies that holes occupy $\mathcal{E} = -\infty$ to $\mathcal{E} = 0$.

$$\begin{aligned}\frac{d\rho_e}{dt}(r,z,t,\mathcal{E}) = &\left[\frac{\partial\rho_e}{\partial t}\right]_{PI} + \left[\frac{\partial\rho_e}{\partial t}\right]_{cc} + \left[\frac{\partial\rho_e}{\partial t}\right]_{e-ph} + \left[\frac{\partial\rho_e}{\partial t}\right]_{epp} \\ &+ \left[\frac{\partial\rho_e}{\partial t}\right]_{Casc} - \left[\frac{\partial\rho_e}{\partial t}\right]_{Auger} - \left[\frac{\partial\rho_e}{\partial t}\right]_{Rad} \\ &+ \left[\frac{\partial\rho_e}{\partial t}\right]_{Diff} - \left[\frac{\partial\rho_e}{\partial t}\right]_{Exc} + \left[\frac{\partial\rho_e}{\partial t}\right]_{Exc_{Diss}}\end{aligned} \tag{A.18}$$

The first term regards the photoionisation (PI) of electrons into the conduction band.

$$\left[\frac{\partial\rho_e}{\partial t}\right]_{PI}(r,z,t,\mathcal{E}^C) = \sum_{V=1,\ C=1}^{\infty} \frac{2\omega_0}{9\pi}\left(\frac{\omega_0 m}{\hbar\gamma_1}\right)^{\frac{3}{2}} Q(\gamma,x)\exp\left[-\pi\langle x+1\rangle\frac{K(\gamma_1)-E_i(\gamma_1)}{E_i(\gamma_2)}\right] \tag{A.19}$$

where

$$\gamma = \frac{\omega_0}{\omega_t} = \frac{\omega_0}{e}\left(\frac{m' cn\epsilon_0 \mathcal{E}_V^C(t)}{I_{eff}(r,z,t)}\right)^{\frac{1}{2}} \tag{A.20}$$

$$\gamma_1 = \frac{\gamma}{\sqrt{1+\gamma^2}} \tag{A.21}$$

$$\gamma_2 = \frac{\gamma_1}{\gamma} \tag{A.22}$$

$$x = \frac{2\mathcal{E}_V^C(t)}{\pi\gamma_1\hbar\omega_0} E_i(\gamma_2) \tag{A.23}$$

$$Q(\gamma, x) = \sqrt{\frac{\pi}{2K(\gamma_2)}} \sum_{n=0}^{\infty} \exp\left[-\pi n \frac{K(\gamma_1) - E_i(\gamma_1)}{E_i(\gamma_2)}\right] \Phi\left[\sqrt{\frac{\pi^2(2\langle x+1\rangle - 2x) + n)}{2K(\gamma_2)E_i(\gamma_2)}}\right] \tag{A.24}$$

$$I_{eff}(r,z,t) = Re\big[E(r,z,t)\cdot D(t)\big]\frac{c}{n} \tag{A.25}$$

$$D(t) = \epsilon_0 E(r,z,t) + P(t) \tag{A.26}$$

$$P(t) = (n^2-1)E_0 \exp\left[\frac{(t-\mu)^2}{(2\sigma)^2}\right]\Big(\exp[i\omega t] + B\exp[3i\omega t] + C\exp[5i\omega t]\Big) \tag{A.27}$$

and $\mathcal{E}_V^C(t)$ is calculated by finding the energy difference between the conduction bands and the shifted valence bands as a function of time and the subscript and superscript V and C refer to between which valence and conduction bands the transition occurs over. E_i and K are elliptical integrals of the first and second kind, Φ indicates the Dawson integral and $\mathcal{E}^C$ is the energy of the conduction band at the momentum value at which transition occured. The bandstructure is calculated through density functional theory and the valence bands are shifted by a momentum $p(t)$ given by

$$p(t) = \hbar k = p_0 + e|A(t)| \tag{A.28}$$

where

$$A(t) = -\int E(t)\ dt \tag{A.29}$$

The zero of energy is defined as the maxima of the valence bands therefore hole energies appear negative.

The carrier-carrier (cc) scattering term is given by

$$\left[\frac{\partial \rho_e}{\partial t}\right]_{cc}(r,z,t,\mathcal{E}) = \frac{1}{\tau_{cc}(r,z,t)}\left[\int_{\mathcal{E}_C}^{\infty}\int_{\mathcal{E}_C}^{\infty}\frac{\rho_e(r,z,t,\mathcal{E}_1)}{\mathcal{E}_1+\mathcal{E}_2-\mathcal{E}_C}\frac{\rho_e(r,z,t,\mathcal{E}_2)}{N_{carr}(r,z,t)}\ d\mathcal{E}_1\ d\mathcal{E}_2 - \rho_e(r,z,t,\mathcal{E})\right] \text{ for } \mathcal{E} \leq \mathcal{E}_1+\mathcal{E}_2-\mathcal{E}_C \tag{A.30}$$

Under the condition that

$$\rho_e(r,z,t,\mathcal{E}) + \left[\frac{\partial \rho_e}{\partial t}\right]_{cc}(r,z,t,\mathcal{E})\cdot\Delta t < D(\mathcal{E}) \tag{A.31}$$

where

$$\tau_{cc}(r,z,t) = \mu_{cc}(r,z,t)\cdot\frac{m}{e} \tag{A.32}$$

$$\mu_{cc}(r,z,t) = \frac{aT(r,z,t)^{\frac{2}{3}}}{N_{carr}(r,z,t)\ln(1+bT(r,z,t)^2(1\times10^{-4}\cdot N_{carr}(r,z,t))^{-\frac{2}{3}})} \tag{A.33}$$

Electron phonon ($e-ph$) collisions are described by

$$\left[\frac{\partial \rho_e}{\partial t}\right]_{e-ph}(r,z,t,\mathcal{E}) = -\frac{\rho_e(r,z,t,\mathcal{E})}{\tau_{ep_{tot}}(r,z,t,\mathcal{E})} + \frac{\rho_e(r,z,t,\mathcal{E}-\mathcal{E}_{ph})}{\tau_{e-ph_{abs}}(r,z,t,\mathcal{E}-\mathcal{E}_{ph})} + \frac{\rho_e(r,z,t,\mathcal{E}+\mathcal{E}_{ph})}{\tau_{e-ph_{emit}}(r,z,t,\mathcal{E}+\mathcal{E}_{ph})} \tag{A.34}$$

where

$$\tau_{e-ph_{emit}}(r,z,t,\mathcal{E}) = \tau_{e-ph_{tot}}(\mathcal{E})\frac{T_e(r,z,t)+T_L(r,z,t)}{T_e(r,z,t)} \tag{A.35}$$

$$\tau_{e-ph_{abs}}(r,z,t,\mathcal{E}) = \tau_{e-ph_{tot}}(\mathcal{E})\frac{T_e(r,z,t)+T_L(r,z,t)}{T_L(r,z,t)} \tag{A.36}$$

$$\tau_{e-ph_{tot}}(\mathcal{E}) = \frac{1}{aD(\mathcal{E})} \tag{A.37}$$

Electron-phonon-photon (*epp*) collisions (reverse Bremsstrahlung processes) are given by

$$\left[\frac{\partial \rho_e}{\partial t}\right]_{epp}(r,z,t,\mathcal{E}) = \left[\frac{\partial \rho_e}{\partial \mathcal{E}}\right]_{epp}\left[\frac{\partial \mathcal{E}}{\partial t}\right]_{epp} = -\frac{\left[\frac{\partial \mathcal{E}}{\partial t}\right]_{epp}(r,z,t,\mathcal{E})\cdot\rho_e(r,z,t,\mathcal{E})}{(\hbar\omega_0-\hbar\omega_{ph})} + \frac{\left[\frac{\partial \mathcal{E}}{\partial t}\right]_{epp}(r,z,t,\mathcal{E}-\hbar\omega_0+\hbar\omega_{ph})\cdot\rho_e(r,z,t,\mathcal{E}-\hbar\omega_0+\hbar\omega_{ph})}{(\hbar\omega_0-\hbar\omega_{ph})} \tag{A.38}$$

where

$$\left[\frac{\partial \mathcal{E}}{\partial t}\right]_{epp}(r,z,t,\mathcal{E}) = \frac{(\frac{e^2 I(r,z,t)}{m' c\epsilon_0 n(r,z,t,\mathcal{E})})\tau_{scatt}(r,z,t,\mathcal{E})}{\omega_0^2\tau_{scatt}(r,z,t,\mathcal{E})^2+1} \tag{A.39}$$

$$\frac{1}{\tau_{scatt}(r,z,t,\mathcal{E})} = \frac{1}{\tau_{e-ph_{tot}}(\mathcal{E})} + \frac{1}{\tau_{cc}(r,z,t)} \tag{A.40}$$

Cascade (*casc*) (impact ionisation processes) are given by

$$\left[\frac{\partial \rho_e}{\partial t}\right]_{casc}(r,z,t,\mathcal{E}) = \int_{\mathcal{E}_{th}}^{\infty}\int_{\mathcal{E}_{th}-\mathcal{E}_1}^{0} \frac{\rho_e(r,z,t,\mathcal{E})}{\tau_{cc}(r,z,t)}\left(\frac{D(\mathcal{E}) - \rho_e(r,z,t,\mathcal{E}_1)}{D(\mathcal{E}_1)}\right) \left(\frac{D(\mathcal{E}_2) - \rho_h(r,z,t,\mathcal{E}_2)}{D(\mathcal{E}_2)}\right) d\mathcal{E}_1\, d\mathcal{E}_2 \tag{A.41}$$

And the reverse, Auger ($Auger$) processes are given by

$$\left[\frac{\partial \rho_e}{\partial t}\right]_{Auger}(r,z,t,\mathcal{E}) = \int_{\mathcal{E}_{th}}^{\infty}\int_{\mathcal{E}_{th}-\mathcal{E}_1}^{0} \frac{\rho_e(r,z,t,\mathcal{E})}{\tau_{cc}(r,z,t)}\left(\frac{\rho_e(r,z,t,\mathcal{E}_1)}{D(\mathcal{E}_1)}\right) \left(\frac{\rho_h(r,z,t,\mathcal{E}_2)}{D(\mathcal{E}_2)}\right) d\mathcal{E}_1\, d\mathcal{E}_2 \tag{A.42}$$

Radiative (Rad) recombination of electron-hole pairs is described by

$$\left[\frac{\partial \rho_e}{\partial t}\right]_{rad}(r,z,t,\mathcal{E}) = \int_{-\infty}^{0} \frac{\rho_e(r,z,t,\mathcal{E})}{\tau_{rad}(r,z,t)}\frac{\rho_h(r,z,t,\mathcal{E}_1)}{N_{carr}(r,z,t)}\, d\mathcal{E}_1 \tag{A.43}$$

Diffusion of electrons ($diff$) is described by

$$\left[\frac{\partial \rho_e}{\partial t}\right]_{diff}(r,z,t,\mathcal{E}) = -\nabla \cdot \big(D\nabla\rho_e(r,z,t,\mathcal{E})\big) \tag{A.44}$$

The loss to the electron density by the formation of excitons (Exc) is given by

$$\left[\frac{\partial \rho_e}{\partial t}\right]_{Exc}(r,z,t,\mathcal{E}_1) = \int_{\mathcal{E}_C}^{\mathcal{E}+\mathcal{E}_x} \frac{\rho_e(r,z,t,\mathcal{E}_1)\rho_h(r,z,t,\mathcal{E}_1-\mathcal{E}-\mathcal{E}_x)}{N_{carr}(r,z,t)\cdot\tau_{cc}(r,z,t)}\, d\mathcal{E}_1 \tag{A.45}$$

And the gain to the density from exciton dissociation (Exc_{Diss}) is given by

$$\left[\frac{\partial \rho_e}{\partial t}\right]_{Exc_{Diss}}(r,z,t,\mathcal{E}) = \frac{1}{\tau_{cc}(r,z,t)}\left[\int_{\mathcal{E}_C-\mathcal{E}_x}^{\mathcal{E}_C}\int_{\mathcal{E}_C}^{\infty}\frac{\rho_e(r,z,t,\mathcal{E}_1)}{\mathcal{E}_1+\mathcal{E}_2-\mathcal{E}_C}\frac{\rho_{Exc}(r,z,t,\mathcal{E}_2)}{N_{carr}(r,z,t)}\,d\mathcal{E}_1\,d\mathcal{E}_2 - \rho_e(r,z,t,\mathcal{E})\right] + \frac{\rho_{Exc}(r,z,t,\mathcal{E}-\mathcal{E}_{ph})}{\tau_{e-ph_{abs}}(r,z,t,\mathcal{E}-\mathcal{E}_{ph})} \text{ for } \mathcal{E}_C \le \mathcal{E} \le \mathcal{E}_1+\mathcal{E}_2-\mathcal{E}_C \tag{A.46}$$

A.3 Excitonic density distribution

Electrons and holes can combine to form excitons. A fourth differential equation governing excitonic density is shown below.

$$\begin{aligned}\frac{d\rho_{Exc}}{dt}(r,z,t,\mathcal{E}) = &\left[\frac{\partial \rho_{Exc}}{\partial t}\right]_{Form} + \left[\frac{\partial \rho_{Exc}}{\partial t}\right]_{Exc-c} \\ +\left[\frac{\partial \rho_{Exc}}{\partial t}\right]_{Exc-ph} &- \left[\frac{\partial \rho_{Exc}}{\partial t}\right]_{Recomb} - \left[\frac{\partial \rho_{Exc}}{\partial t}\right]_{BiX} \\ &+\left[\frac{\rho_{Exc}}{\partial t}\right]_{BiX_{Diss}} + \left[\frac{\partial \rho_{Exc}}{\partial t}\right]_{BiX_{Recomb}}\end{aligned} \tag{A.47}$$

The first term describing the formation of excitons ($Form$) is given by

$$\left[\frac{\partial \rho_{Exc}}{\partial t}\right]_{Form}(r,z,t,\mathcal{E}) = \int_{\mathcal{E}_C}^{\mathcal{E}+\mathcal{E}_x}\frac{\rho_e(r,z,t,\mathcal{E}_1)\rho_h(r,z,t,\mathcal{E}_1-\mathcal{E}-\mathcal{E}_x)}{N_{carr}(r,z,t)\cdot\tau_{cc}(r,z,t)}\,d\mathcal{E}_1 \tag{A.48}$$

Scattering with carriers is described by

$$\left[\frac{\partial \rho_{Exc}}{\partial t}\right]_{Exc-c}(r,z,t,\mathcal{E}) = \frac{1}{\tau_{cc}(r,z,t)}\left[\int_{\mathcal{E}_C-\mathcal{E}_x}^{\mathcal{E}_C}\int_{\mathcal{E}_C}^{\infty}\frac{\rho_e(r,z,t,\mathcal{E}_1)}{\mathcal{E}_1+\mathcal{E}_2-\mathcal{E}_C}\frac{\rho_{Exc}(r,z,t,\mathcal{E}_2)}{N_{carr}(r,z,t)}\,d\mathcal{E}_1\,d\mathcal{E}_2 - \rho_e(r,z,t,\mathcal{E})\right] \text{ for } \mathcal{E} \le \mathcal{E}_C-\mathcal{E}_x \tag{A.49}$$

This scattering described both the thermalisation of excitons with carriers and the dissociation of them into free carriers.

Exciton-phonon ($Exc-ph$) collisions are described by

$$\left[\frac{\partial \rho_{Exc}}{\partial t}\right]_{Exc-ph}(r,z,t,\mathcal{E}) = -\frac{\rho_{Exc}(r,z,t,\mathcal{E})}{\tau_{ep_{tot}}(r,z,t,\mathcal{E})} + \frac{\rho_{Exc}(r,z,t,\mathcal{E}-\mathcal{E}_{ph})}{\tau_{e-ph_{abs}}(r,z,t,\mathcal{E}-\mathcal{E}_{ph})} + \frac{\rho_{Exc}(r,z,t,\mathcal{E}+\mathcal{E}_{ph})}{\tau_{e-ph_{emit}}(r,z,t,\mathcal{E}+\mathcal{E}_{ph})} \tag{A.50}$$

Where again, phonon scattering leads to both thermalisation with the lattice and dissociation back into free carriers.

Recombination of excitons (*Recomb*) occurs through a mixture of processes but for simplicity a rate equation is defined with a time constant from the literature.

$$\left[\frac{\partial \rho_{Exc}}{\partial t}\right]_{Recomb}(r,z,t,\mathcal{E}) = \frac{\rho_{Exc}(r,z,t,\mathcal{E})}{\tau_{Exc_{Recomb}}(r,z,t) N_{carr}(r,z,t)} \tag{A.51}$$

The exciton density is also reduced by the formation of bi-excitons (BiX)

$$\left[\frac{\partial \rho_{Exc}}{\partial t}\right]_{BiX}(r,z,t,\mathcal{E}_1) = \int_{\mathcal{E}_C-\mathcal{E}_x}^{\mathcal{E}-\mathcal{E}_C+\mathcal{E}_x+\mathcal{E}_{bx}} \frac{\rho_{Exc}(r,z,t,\mathcal{E}_1)\rho_{Exc}(r,z,t,\mathcal{E}-\mathcal{E}_1+\mathcal{E}_{bx})}{N_{carr}(r,z,t)\cdot\tau_{xx}(r,z,t)}\, d\mathcal{E}_1 \tag{A.52}$$

And the exciton density is increased by the dissociation of bi-excitons.

$$\left[\frac{\partial \rho_{Exc}}{\partial t}\right]_{BiX_{Diss}}(r,z,t,\mathcal{E}) = \frac{1}{\tau_{cc}(r,z,t)}\left[\int_{\mathcal{E}_C}^{\infty}\int_{2(\mathcal{E}_C-\mathcal{E}_x)-\mathcal{E}_{bx}}^{2(\mathcal{E}_C-\mathcal{E}_x)} \frac{\rho_e(r,z,t,\mathcal{E}_1)}{\mathcal{E}_1+\mathcal{E}_2-\mathcal{E}_C} \frac{\rho_{BiX}(r,z,t,\mathcal{E}_2)}{N_{carr}(r,z,t)}\, d\mathcal{E}_2\, d\mathcal{E}_1 - \rho_{Exc}(r,z,t,\mathcal{E})\right] + \frac{\rho_{BiX}(r,z,t,\mathcal{E}-\mathcal{E}_{ph})}{\tau_{e-ph_{abs}}(r,z,t,\mathcal{E}-\mathcal{E}_{ph})} \text{ for } \mathcal{E}_C-\mathcal{E}_x \le \mathcal{E} \le \mathcal{E}_1+\mathcal{E}_2-\mathcal{E}_C \tag{A.53}$$

Increase to the exciton density through the recombination of bi-excitons can be modelled by

$$\left[\frac{\partial \rho_{Exc}}{\partial t}\right]_{BiX_{Recomb}}(r,z,t,\mathcal{E}) = \frac{\rho_{BiX}(r,z,t,\mathcal{E}+\mathcal{E}_C-\mathcal{E}_x-\mathcal{E}_{bx})}{\tau_{BiXrad}(r,z,t)N_{carr}(r,z,t)} \tag{A.54}$$

A.4 Bi-excitonic density distribution

A fifth partial differential equation governs the density of bi-excitons (BiX).

$$\begin{aligned}\frac{d\rho_{BiX}}{dt}(r,z,t,\mathcal{E}) = &\left[\frac{\partial \rho_{BiX}}{\partial t}\right]_{Form} + \left[\frac{\partial \rho_{BiX}}{\partial t}\right]_{BiX-c} \\ -&\left[\frac{\partial \rho_{BiX}}{\partial t}\right]_{BiX-ph} - \left[\frac{\partial \rho_{BiX}}{\partial t}\right]_{Rad} + \left[\frac{\partial \rho_{BiX}}{\partial t}\right]_{STbX_{diss}}\end{aligned} \tag{A.55}$$

The formation term ($Form$) is given by

$$\left[\frac{\partial \rho_{BiX}}{\partial t}\right]_{Form}(r,z,t,\mathcal{E}) = \int_{\mathcal{E}_C-\mathcal{E}_x}^{\mathcal{E}-\mathcal{E}_C+\mathcal{E}_x+\mathcal{E}_{bx}} \frac{\rho_{Exc}(r,z,t,\mathcal{E}_1)\rho_{Exc}(r,z,t,\mathcal{E}-\mathcal{E}_1+\mathcal{E}_{bx})}{N_{carr}(r,z,t)\cdot\tau_{xx}(r,z,t)}\, d\mathcal{E}_1 \tag{A.56}$$

where

$$\tau_{xx}(r,z,t) = \mu_{xx}(r,z,t)\cdot\frac{m}{e} \tag{A.57}$$

$$\mu_{xx}(r,z,t) = \frac{aT(r,z,t)^{\frac{2}{3}}}{\rho_{Exc}(r,z,t)\ln(1+bT(r,z,t)^2(1\times10^{-4}\cdot\rho_{Exc}(r,z,t))^{-\frac{2}{3}})} \tag{A.58}$$

Scattering with carriers is described by

$$\left[\frac{\partial \rho_{BiX}}{\partial t}\right]_{BiX-c}(r,z,t,\mathcal{E}) = \frac{1}{\tau_{cc}(r,z,t)}\Bigg[\int_{\mathcal{E}_C-\mathcal{E}_x}^{\mathcal{E}_C}\int_{\mathcal{E}_C}^{\infty}\frac{\rho_{BiX}(r,z,t,\mathcal{E}_1)}{\mathcal{E}_1+\mathcal{E}_2-\mathcal{E}_C}\frac{\rho_e(r,z,t,\mathcal{E}_2)}{N_{carr}(r,z,t)}\,d\mathcal{E}_2\,d\mathcal{E}_1 - \rho_e(r,z,t,\mathcal{E})\Bigg] \text{ for } \mathcal{E} \leq 2(\mathcal{E}_C-\mathcal{E}_x)-\mathcal{E}_{bx} \tag{A.59}$$

This scattering described both the thermalisation of bi-excitons with carriers and the dissociation of them into single excitons.

Bi-exciton-phonon ($BiX-ph$) collisions are described by

$$\left[\frac{\partial \rho_{BiX}}{\partial t}\right]_{BiX-ph}(r,z,t,\mathcal{E}) = -\frac{\rho_{BiX}(r,z,t,\mathcal{E})}{\tau_{ep_{tot}}(r,z,t,\mathcal{E})} + \frac{\rho_{BiX}(r,z,t,\mathcal{E}-\mathcal{E}_{ph})}{\tau_{e-ph_{abs}}(r,z,t,\mathcal{E}-\mathcal{E}_{ph})} + \frac{\rho_{BiX}(r,z,t,\mathcal{E}+\mathcal{E}_{ph})}{\tau_{e-ph_{emit}}(r,z,t,\mathcal{E}+\mathcal{E}_{ph})} \tag{A.60}$$

Absorption of phonons leads to dissociation into free excitons and emission of phonons leads to the formation of self-trapped bi-excitons.

Radiative recombination of bi-excitons is described by

$$\left[\frac{\partial \rho_{BiX}}{\partial t}\right]_{BiX_{Rad}}(r,z,t,\mathcal{E}) = \frac{\rho_{BiX}(r,z,t,\mathcal{E})}{\tau_{BiXrad}(r,z,t)N_{carr}(r,z,t)} \tag{A.61}$$

The bi-exciton density is also increased by the dissociation of self-trapped bi-excitons back into free bi-excitons

$$\left[\frac{\partial \rho_{BiX}}{\partial t}\right]_{STbX_{Diss}}(r,z,t,\mathcal{E}) = \frac{1}{\tau_{cc}(r,z,t)}\Bigg[\int_{\mathcal{E}_C}^{\infty}\int_{2(\mathcal{E}_C-\mathcal{E}_x)-\mathcal{E}_{bx}-\mathcal{E}_{DP}}^{2(\mathcal{E}_C-\mathcal{E}_x)-\mathcal{E}_{bx}}\frac{\rho_e(r,z,t,\mathcal{E}_1)}{\mathcal{E}_1+\mathcal{E}_2-\mathcal{E}_C}\frac{\rho_{STbX}(r,z,t,\mathcal{E}_2)}{N_{carr}(r,z,t)}\,d\mathcal{E}_2\,d\mathcal{E}_1 - \rho_{BiX}(r,z,t,\mathcal{E})\Bigg] + \frac{\rho_{STbX}(r,z,t,\mathcal{E}-\mathcal{E}_{ph})}{\tau_{e-ph_{abs}}(r,z,t,\mathcal{E}-\mathcal{E}_{ph})} \tag{A.62}$$
$$\text{for } 2(\mathcal{E}_C-\mathcal{E}_x)-\mathcal{E}_{bx} \leq \mathcal{E} \leq \mathcal{E}_1+\mathcal{E}_2-\mathcal{E}_C$$

A.5 Self-trapped bi-excitonic density distribution

A sixth partial differential equation models the density of self-trapped bi-excitons.

$$\frac{d\rho_{STbX}}{dt}(r,z,t,\mathcal{E}) = \left[\frac{\partial\rho_{STbX}}{\partial t}\right]_{Form} + \left[\frac{\partial\rho_{STbX}}{\partial t}\right]_{STbX-c} + \left[\frac{\partial\rho_{STbX}}{\partial t}\right]_{STbX-ph} - \left[\frac{\partial\rho_{STbX}}{\partial t}\right]_{Rad} - \left[\frac{\partial\rho_{STbX}}{\partial t}\right]_{FD} \tag{A.63}$$

The formation term ($Form$), is derived from the phonon scattering when phonons are emitted by the free bi-excitons.

$$\left[\frac{\partial\rho_{STbX}}{\partial t}\right]_{Form}(r,z,t,\mathcal{E}) = \frac{\rho_{BiX}(r,z,t,\mathcal{E}+\mathcal{E}_{ph})}{\tau_{e-ph_{emit}}(r,z,t,\mathcal{E}+\mathcal{E}_{ph})} \tag{A.64}$$

Scattering of self-trapped bi-excitons with carriers is described by

$$\left[\frac{\partial\rho_{STbX}}{\partial t}\right]_{STbX-c}(r,z,t,\mathcal{E}) = \frac{1}{\tau_{cc}(r,z,t)}\left[\int_{\mathcal{E}_C-\mathcal{E}_x}^{\mathcal{E}_C}\int_{\mathcal{E}_C}^{\infty}\frac{\rho_{STbX}(r,z,t,\mathcal{E}_1)}{\mathcal{E}_1+\mathcal{E}_2-\mathcal{E}_C}\frac{\rho_e(r,z,t,\mathcal{E}_2)}{N_{carr}(r,z,t)}\,d\mathcal{E}_2\,d\mathcal{E}_1 - \rho_e(r,z,t,\mathcal{E})\right] \text{ for } \mathcal{E} \le 2(\mathcal{E}_C-\mathcal{E}_x)-\mathcal{E}_{bx}-\mathcal{E}_{DP} \tag{A.65}$$

This scattering described both the thermalisation of the self-trapped bi-excitons with carriers and the dissociation of them into free bi-excitons.

Self-trapped bi-exciton-phonon ($STbX-ph$) collisions are described by

$$\left[\frac{\partial\rho_{STbX}}{\partial t}\right]_{STbX-ph}(r,z,t,\mathcal{E}) = -\frac{\rho_{STbX}(r,z,t,\mathcal{E})}{\tau_{ep_{tot}}(r,z,t,\mathcal{E})} + \frac{\rho_{STbX}(r,z,t,\mathcal{E}-\mathcal{E}_{ph})}{\tau_{e-ph_{abs}}(r,z,t,\mathcal{E}-\mathcal{E}_{ph})} + \frac{\rho_{STbX}(r,z,t,\mathcal{E}+\mathcal{E}_{ph})}{\tau_{e-ph_{emit}}(r,z,t,\mathcal{E}+\mathcal{E}_{ph})} \tag{A.66}$$

For high energy self-trapped bi-excitons, absorption of phonons leads to dissociation into free bi-excitons.

Radiative recombination of self-trapped bi-excitons is described by

$$\left[\frac{\partial \rho_{STbX}}{\partial t}\right]_{STbX_{Rad}}(r,z,t,\mathcal{E}) = \frac{\rho_{STbX}(r,z,t,\mathcal{E})}{\tau_{STbXrad}(r,z,t)N_{carr}(r,z,t)} \tag{A.67}$$

The reduction in self-trapped bi-exciton density by the formation of Frenkel defects is given by

$$\left[\frac{\partial \rho_{STbX}}{\partial t}\right]_{FD}(r,z,t,\mathcal{E}) = \frac{\rho_{STbX}(r,z,t,\mathcal{E})}{\tau_{FD}(r,z,t,\mathcal{E})} \tag{A.68}$$

where

$$\tau_{FD}(r,z,t,\mathcal{E}) = \frac{h}{\mathcal{E}_{ph}} \exp\left(\frac{\mathcal{E}_b - (\mathcal{E} - [2(\mathcal{E}_C - \mathcal{E}_X) - \mathcal{E}_{bX} - \mathcal{E}_{DP}])}{k_B T(r,z,t)}\right) \tag{A.69}$$

A.6 Defect density distribution

A seventh partial differential equation governs the density of Frenkel defects. As diffusion and recombination of defects are not considered, this equation only has one term, the formation of defects.

$$\frac{d\rho_{FD}}{dt}(r,z,t) = -\int_{2(\mathcal{E}_C-\mathcal{E}_x)-\mathcal{E}_{bx}-\mathcal{E}_{DP}}^{2(\mathcal{E}_C-\mathcal{E}_x)-\mathcal{E}_{bx}} \left[\frac{\partial \rho_{STbX}}{\partial t}\right]_{FD}(r,z,t,\mathcal{E})\, d\mathcal{E} \tag{A.70}$$

A.7 Lattice temperature distribution

The eighth and final partial differential equation governs the temperature of the lattice.

$$\frac{dT}{dt}(r,z,t) = \left[\frac{\partial T}{\partial t}\right]_{Scatt} + \left[\frac{\partial T}{\partial t}\right]_{Diff} \tag{A.71}$$

The first term in this equation regards the lattice exchanging energy with different populations via scattering and can be modelled as

$$\begin{aligned}\left[\frac{\partial T}{\partial t}\right]_{Scatt} &= \left[\frac{\partial T}{\partial t}\right]_{Scatt_e} + \left[\frac{\partial T}{\partial t}\right]_{Scatt_h} \\ + \left[\frac{\partial T}{\partial t}\right]_{Scatt_{Exc}} &+ \left[\frac{\partial T}{\partial t}\right]_{Scatt_{BiX}} + \left[\frac{\partial T}{\partial t}\right]_{Scatt_{STbX}}\end{aligned} \tag{A.72}$$

where

$$\left[\frac{\partial T}{\partial t}\right]_{Scatt_e} = \int_{\mathcal{E}_C}^{\infty} \frac{\mathcal{E}_{ph}}{k_B} \frac{\rho_e(r,z,t,\mathcal{E})}{\tau_{ep_{emit}}(r,z,t,\mathcal{E})\rho_A}\, d\mathcal{E} - \int_{\mathcal{E}_C}^{\infty} \frac{\mathcal{E}_{ph}}{k_B} \frac{\rho_e(r,z,t,\mathcal{E})}{\tau_{ep_{abs}}(r,z,t,\mathcal{E})\rho_A}\, d\mathcal{E} \tag{A.73}$$

The other scattering terms are identical to $\left[\frac{\partial T}{\partial t}\right]_{Scatt_e}$ but with ρ_e replaced with the density of other populations and the integral limits changed to the minimum and maximum energies of the scattering populations.

The diffusion of heat is modelled by the heat equation with a proportionality constant determined by the thermal conductivity of diamond.

$$\left[\frac{\partial T}{\partial t}\right]_{Diff} = -\sigma_{th}\nabla^2 T \tag{A.74}$$